Interface-resolved simulations of dense particulate flows

Studies on sedimentation and slurry pipe flow

Shajahan, M.T.

DOI
10.4233/uuid:e76f59d3-6c81-417e-90bd-b5270a2c55ad

Publication date
2024

Document Version
Final published version

Citation (APA)
Shajahan, M. T. (2024). *Interface-resolved simulations of dense particulate flows: Studies on sedimentation and slurry pipe flow*. [Dissertation (TU Delft), Delft University of Technology].
https://doi.org/10.4233/uuid:e76f59d3-6c81-417e-90bd-b5270a2c55ad

Important note
To cite this publication, please use the final published version (if applicable).
Please check the document version above.

INTERFACE-RESOLVED SIMULATIONS OF DENSE PARTICULATE FLOWS

STUDIES ON SEDIMENTATION AND SLURRY PIPE FLOW

INTERFACE-RESOLVED SIMULATIONS OF DENSE PARTICULATE FLOWS

STUDIES ON SEDIMENTATION AND SLURRY PIPE FLOW

Proefschrift

ter verkrijging van de graad van doctor
aan de Technische Universiteit Delft,
op gezag van de Rector Magnificus prof. dr. ir. T. H. J. J. van der Hagen
voorzitter van het College voor Promoties,
in het openbaar te verdedigen op
donderdag 29 februari 2024 om 10:00 uur

door

Tariq SHAJAHAN

Master of Science in Aerospace Engineering
Technische Universiteit Delft, Nederland
geboren te Sengottai, India

Dit proefschrift is goedgekeurd door de promotoren.

promotor: Dr. ir. Wim-Paul Breugem
promotor: Prof. dr. ir. Christian Poelma

Samenstelling promotiecommissie:

Rector Magnificus,	voorzitter
Dr. ir. W. P. Breugem,	Technische Universiteit Delft, promotor
Prof. dr. ir. C. Poelma,	Technische Universiteit Delft, promotor
Onafhankelijke leden:	
Prof. dr. ir. W. S. J. Uijttewaal,	Technische Universiteit Delft
Prof. dr. ir. Johan T. Padding,	Technische Universiteit Delft
Prof. dr. ir. Hans Kuipers,	Technische Universiteit Eindhoven
Prof. Dr. -Ing. Bernhard Vowinckel,	Technische Universität Dresden
Dr. ir. G. H. Keetels,	Technische Universiteit Delft
Overige leden:	
Prof. dr. ir. B. J. Boersma,	Technische Universiteit Delft

The numerical simulations were carried out on the Dutch national supercomputers Cartesius and Snellius with the support of SURF (www.surf.nl). This work is part of the research programme Topsector Water with Number ALWTW.2016.050, which is (partly) financed by the Dutch Research Council (NWO).

Keywords: sediment transport, slurry flow, transport regimes, flow transition, secondary flow, turbulence modulation, multiparticle interactions, dense suspensions, sedimentation, path instabilities, wake-trapping, drafting-kissing-tumbling, kinematic waves, direct numerical simulation, immersed boundary method, soft-sphere collision model, high-performance computing

Printed by: Gildeprint

ISBN 978-94-6496-054-9

An electronic version of this dissertation is available at
http://repository.tudelft.nl/.

To my mother Nigar

CONTENTS

SUMMARY

Dense suspension flows, both in the natural environment and industrial settings, are complex phenomena with significant implications. From rivers shaping landscapes to industrial processes involving slurry transport, these flows hold a prominent position in numerous sectors. This thesis delves into a specific facet of these intricate flows: slurry transport within horizontal pipes. Slurry, a mixture of solid particles and a viscous fluid, presents a challenging arena due to its dynamic nature, encompassing multiple flow regimes and diverse phenomena that govern its behavior. This research seeks to unravel the complexities of slurry transport, presenting a comprehensive analysis using interface-resolved Direct Numerical Simulation (DNS). In the context of slurry transport (also referred to as sediment transport), a horizontal pipe is a conduit where particles suspended in a viscous fluid are transported. The dynamics of this transport are governed by several dimensionless numbers, each highlighting distinct aspects of the flow. Prominently, in this work we explore the role of the Reynolds number (Re) which encapsulates the balance between inertial and viscous forces, the Galileo number (Ga) which characterizes the competition between inertial and viscous effects in particle settling under gravity, and concentration of particles which has an influence on particle-particle and particle-fluid interactions. Key flow dynamics that determine the behaviour of the flow include turbulent mixing, gravitational settling of particles, and shear-induced particle migration due to particle-stress gradients. Practical applications of slurry transport are numerous, spanning industries such as mining, agriculture, and chemical processing. Slurry transport is of particular relevance to the dredging industry in the Netherlands to maintain its inland waterways and for land reclamation projects. However, pipeline operators grapple with issues ranging from pressure drop and the prevention of bed formation to the control of excessive pipe abrasion, silting risks, and production instability. These challenges stem from the intricate interplay of particle behavior, fluid dynamics, and pipeline geometry.

Studying dense suspensions, particularly in the context of slurry transport, presents unique challenges. The sheer range of particle sizes, interparticular interactions, and fluid-particle interactions in such flows require specialized approaches. Interface-resolved DNS provides a sophisticated computational method employed to capture the coupling between particles and the fluid medium. This approach goes beyond conventional approaches, for example a point-particle representation, by modeling finite-size particles, considering their interactions with the surrounding fluid in a more realistic manner. Interface-resolved DNS approach not only unravels the intricate physics of slurry flow but also serves as a tool to validate closure models used in continuum-based Computational Fluid Dynamics (CFD) simulations. These CFD models utilize a continuum approach, employing local volume-averaging and Reynolds-averaging to obtain macroscopic mass and momentum balances.

The primary objective of this research is to develop a comprehensive framework that leverages particle-resolved Direct Numerical Simulation (DNS) to unravel the 3D instationary flow physics of sediment transport within a horizontal pipe, encompassing all scales, from a microscale of individual particles to the macroscale of the pipe. This framework will be validated, and the research aims to identify governing parameters to characterize sediment transport. Towards that end, the sediment transport problem is downscaled by lowering Ga to achieve entrainment of particles in the flow even at moderate Re, thus facilitating an investigation of all transport regimes. In the subsequent sections, this thesis explores two distinct but interconnected studies: understanding sediment transport through sedimentation dynamics and exploring slurry transport regimes through quantitative sediment transport analysis. These studies contribute to a holistic understanding of the challenges, intricacies, and potential solutions in managing dense suspension flows, unraveling the complexities that shape both natural landscapes and industrial processes.

- **Understanding Sediment Transport through Sedimentation Dynamics**
  Sediments in a slurry are prevented from sedimenting and are maintained in suspension by the process of turbulent mixing and shear-induced migration. We explore sedimentation in the absence of an externally forced flow as a prelude to our investigation of slurry transport. Sedimentation involves the settling of particles suspended within a fluid medium, offering valuable insights into the mechanics behind particle movement, deposition, and erosion. This comprehensive exploration strives to unravel the complex interplay between key factors like flow inertia, particle interactions, and concentration, all of which contribute to a deeper understanding of sediment transport dynamics. The study's primary focus centers on sedimentation within non-colloidal suspensions, specifically involving spheres in a viscous fluid medium. This study probes the intricate connection between flow inertia, as quantified by Ga, and concentration-dependent particle interactions. With increasing Ga, the particle trajectory of a single settling particle in free space transforms from predictable vertical descent into an oblique trajectory, and subsequently into oscillations, and chaotic movements. Despite this influence on individual settling particles, the research reveals a stronger influence of concentration in determining the spatial distribution of a collection of suspended particles. At dilute concentrations particles arranged themselves into coherent vertical alignments resembling intricate trains, possibly due to particles drafting other particles vertically. At slightly higher concentrations, drafting-kissing-tumbling (DKT) interactions lead to the formation of horizontally oriented particle pairs. At dense concentrations, particles adopt a seemingly random distribution akin to "hard-sphere" arrangements, yet traces of DKT instabilities persist. In all cases, hindered settling at a reduced speed is observed as compared to a single settling sphere. Further, as reported in literature, the well-known Richardson-Zaki relation for the mean sedimentation velocity was applicable only at dense concentrations. Additionally, the study explores the phenomenon of kinematic waves, shedding light on the link between localized disturbances like DKT and the macroscopic fluctuations in the con-

centration distribution of the suspension. A model was proposed to explain the scaling relation for the particle velocity spectra based on the inertial response of the particles to small-scale flow perturbations. Further, the velocity spectra suggests that kinematic waves may trigger DKT instabilities, while conversely DKT instabilities may be responsible for the onset of kinematic waves. By investigating the influence of concentration and flow inertia, the study lays a foundation for understanding the intricate processes governing sedimentation, with implications across various scientific and engineering domains. This understanding bridges the gap between theory and application, providing insight into sediment transport and related processes.

- **Advancing Slurry Pipeline Efficiency through Quantitative Sediment Transport Analysis**
  Efficient sediment transport holds paramount importance across industries reliant on slurry pipelines. This study is focused on particle-laden flows within slurry pipelines, with the objective of exploring the dynamics of three broad sediment transport regimes. This was achieved through a combination of experiments in a slurry flow loop and interface-resolved DNS. The DNS results generally agreed well with experimental findings, even when considering experimental uncertainties in liquid bulk velocity and Ga. In the fixed-bed regime, a distinct sharp and flat interface separated the overlying flow from the stationary bed, marked by a regular packing of spheres in concentric rings. Over the fixed bed, the flow resembled turbulent flow in a channel with a non-circular cross-section and rough walls, featuring a secondary flow pattern of Prandtl's second kind. In the sliding-bed regime, the interface between the sliding bed and overlying flow was diffuse, with particle layering within the bed. Secondary flow patterns existed both above and within the sliding bed, closely linked to the spatial particle distribution. Finally, the suspended-flow regime was characterized by a dense particle core, with variations in particle distribution influenced by Reynolds and Galileo numbers, demonstrating the effects of gravity and shear-induced migration. Turbulent mixing and particle stresses played dominant roles in momentum transfer across different flow conditions and strata within slurry pipe flow. Moreover, the friction factor for each regime aligned well with predictions from existing models in literature. This research provides insight for optimizing slurry pipeline operations. The correlation between non-dimensional parameters coupled with quantifiable insights into flow behavior, constructs a comprehensive roadmap for efficient sediment transport and prolonged pipeline functionality. Insights from this work provides recommendations that may minimize pipe wall wear, maximize solid flux, and thus enhance efficiency while reducing maintenance costs. The emphasis on interfacial, particle, and turbulent stresses along with a detailed dilineation of recirculation patterns, offers practical guidance in operating slurry pipelines.

Although grounded in computational simulations, these findings hold real-world applicability, empowering operators with insight into diverse conditions, anticipate challenges, and refine strategies. Ultimately, this work empowers informed decision-

making, augments pipeline reliability, and fosters efficiency and cost-effectiveness in not only slurry transportation systems, but also in broader engineering applications such as in mining and mineral processing, oil and gas industry, wastewater treatment, chemical processing, pulp and paper industry, food and beverage production and power generation.

SAMENVATTING

Dichte suspensiestromen, zowel in de natuurlijke omgeving als in industriële omgevingen, zijn complexe verschijnselen met aanzienlijke implicaties. Van rivieren die landschappen vormgeven tot industriële processen waarin suspensies voorkomen: deze stromingen nemen een prominente plaats in in tal van sectoren. In dit proefschrift wordt dieper ingegaan op een specifiek facet van deze ingewikkelde stromingen: slurrytransport binnen horizontale leidingen. Slurry, een mengsel van vaste deeltjes en een stroperige vloeistof, vormt een uitdagende arena vanwege zijn dynamische aard, die meerdere stromingsregimes en diverse fenomenen omvat die het gedrag ervan bepalen. Dit onderzoek heeft tot doel de complexiteit van slurrytransport te ontrafelen, door een uitgebreide analyse te presenteren met behulp van interface-opgeloste Direct Numerical Simulation (DNS). In het kader van baggertransport (ook wel sedimenttransport genoemd) is een horizontale leiding een leiding waarin deeltjes gesuspendeerd in een stroperige vloeistof worden getransporteerd. De dynamiek van dit transport wordt bepaald door verschillende dimensieloze getallen, die elk verschillende aspecten van de stroming benadrukken. Prominent onderzoeken we in dit werk de rol van het Reynoldsgetal (Re) dat de balans tussen traagheid en visceuze krachten weerspiegelt, en het Galileo-getal (Ga) dat de competitie tussen traagheid en stroperige effecten karakteriseert bij het bezinken van deeltjes onder de zwaartekracht, en de concentratie van deeltjes die invloed heeft op de deeltjes-deeltjes en deeltjes-vloeistof interacties. Belangrijke stromingsdynamieken die het gedrag van de stroming bepalen, zijn onder meer turbulente menging, bezinking door zwaartekracht van deeltjes en door schuifkracht geïnduceerde deeltjesmigratie als gevolg van deeltjesspanningsgradiënten. Praktische toepassingen van slurrytransport zijn talrijk en omvatten industrieën zoals mijnbouw, landbouw en chemische verwerking. Slurrytransport is van bijzonder belang voor de baggerindustrie in Nederland voor het onderhoud van de binnenwateren en voor landaanwinningsprojecten. Exploitanten van pijpleidingen worstelen echter met problemen variërend van drukval en het voorkomen van bedvorming tot het beheersen van overmatige slijtage van pijpleidingen, risico's op verzanding en productie-instabiliteit. Deze uitdagingen komen voort uit het ingewikkelde samenspel van deeltjesgedrag, vloeistofdynamica en pijplijngeometrie.

Het bestuderen van dichte suspensies, vooral in de context van slurrytransport, brengt unieke uitdagingen met zich mee. Het enorme bereik aan deeltjesgroottes, interparticulaire interacties en vloeistof-deeltjes interacties in dergelijke stromen vereisen gespecialiseerde benaderingen. Interface-resolved DNS biedt een geavanceerde rekenmethode die wordt gebruikt om de koppeling tussen deeltjes en het vloeibare medium vast te leggen. Deze benadering gaat verder dan conventionele benaderingen, bijvoorbeeld een puntdeeltjesrepresentatie, door deeltjes van eindige grootte te modelleren, waarbij hun interacties met de omringende vloeistof op een meer realisti-

sche manier worden bekeken. Interface-opgeloste DNS-aanpak ontrafelt niet alleen de ingewikkelde fysica van slurrystroming, maar dient ook als hulpmiddel voor het valideren van sluitingsmodellen die worden gebruikt in continuümgebaseerde Computational Fluid Dynamics (CFD) simulaties. Deze CFD-modellen maken gebruik van een continuümbenadering, waarbij gebruik wordt gemaakt van lokale volumemiddeling en Reynoldsmiddeling om macroscopische massa- en momentumbalansen te verkrijgen.

Het primaire doel van dit onderzoek is het ontwikkelen van een alomvattend raamwerk dat gebruik maakt van deeltjesopgeloste Directe Numerieke Simulatie (DNS) om de 3D instationaire stromingsfysica van sedimenttransport binnen een horizontale pijp te ontrafelen, dat alle schaalniveaus omvat, van een microschaal van individuele deeltjes tot de macroschaal van de pijp. Dit raamwerk zal worden gevalideerd en het onderzoek heeft tot doel de bepalende parameters te identificeren om sedimenttransport te karakteriseren. Met dat doel voor ogen wordt het sedimenttransportprobleem verkleind door Ga te verlagen om het meesleuren van deeltjes in de stroom te bereiken, zelfs bij gematigde Re, waardoor een onderzoek naar alle transportregimes wordt vergemakkelijkt. In de volgende paragrafen onderzoekt dit proefschrift twee afzonderlijke, maar onderling verbonden onderzoeken: het begrijpen van sedimenttransport door middel van sedimentatiedynamiek en het verkennen van slurrytransportregimes door middel van kwantitatieve sedimenttransportanalyse. Deze onderzoeken dragen bij aan een holistisch begrip van de uitdagingen, complexiteiten en mogelijke oplossingen bij het beheersen van dichte suspensiestromen, waardoor de complexiteiten worden ontrafeld die zowel natuurlijke landschappen als industriële processen vormgeven.

- **Begrip van Sedimenttransport via Sedimentatiedynamiek**
  De neiging van gesuspendeerde deeltjes in een slurry om te sedimenteren wordt tegengegaan door turbulente menging en schuifkracht-geinduceerde migratie. We onderzoeken sedimentatie in afwezigheid van een van buitenaf geforceerde stroming als opmaat voor ons onderzoek naar slurrytransport. Sedimentatie omvat het bezinken van deeltjes die in een vloeibaar medium zijn gesuspendeerd, wat waardevolle inzichten biedt in de mechanismen achter deeltjesbeweging, afzetting en erosie. Deze uitgebreide verkenning streeft ernaar de complexe wisselwerking tussen sleutelfactoren zoals stromingsinertie, deeltjesinteracties en concentratie te ontrafelen, die allemaal bijdragen aan een dieper begrip van de dynamiek van sedimenttransport. De primaire focus van het onderzoek ligt op sedimentatie in niet-colloïdale suspensies, met name op bollen in een stroperig vloeibaar medium. Deze studie onderzoekt het ingewikkelde verband tussen stromingsinertie, zoals gekwantificeerd door Ga, en concentratieafhankelijke deeltjesinteracties. Met toenemende Ga transformeert het deeltjestraject van een enkel bezinkend deeltje in de vrije ruimte van voorspelbare verticale afdaling naar een schuin traject, en vervolgens in oscillaties en chaotische bewegingen. Ondanks deze invloed op individuele bezinkende deeltjes laat het onderzoek een sterkere invloed van concentratie zien bij het bepalen van de ruimtelijke verdeling van een verzameling zwevende deeltjes. Bij verdunde concentraties rangschikten deeltjes zichzelf in coherente verticale uitlijningen die

op ingewikkelde treinen leken, mogelijk doordat deeltjes andere deeltjes verticaal aanzuigen. Bij iets hogere concentraties leiden drafting-kissing-tumbling (DKT)-interacties tot de vorming van horizontaal georiënteerde deeltjesparen. Bij dichte concentraties nemen deeltjes een schijnbaar willekeurige verdeling aan, vergelijkbaar met 'harde-bol' verdelingen, maar toch blijven er sporen van DKT-instabiliteit bestaan. In alle gevallen wordt een gehinderde bezinking bij verminderde snelheid waargenomen in vergelijking met een enkele bol die bezinkt in de vrije ruimte. Verder was, zoals gerapporteerd in de literatuur, de bekende Richardson-Zaki-relatie voor de gemiddelde sedimentatiesnelheid alleen toepasbaar bij dichte concentraties. Daarnaast onderzoekt de studie het fenomeen van kinematische golven, waardoor licht wordt geworpen op het verband tussen gelokaliseerde verstoringen zoals DKT en de macroscopische fluctuaties in de concentratieverdeling van de suspensie. Er werd een model voorgesteld om waargenomen schalingsrelaties voor de deeltjessnelheidsspectra te verklaren op basis van de traagheidsrespons van de deeltjes op kleinschalige stromingsverstoringen. Verder suggereren de snelheidsspectra dat kinematische golven DKT-instabiliteiten kunnen veroorzaken, terwijl omgekeerd DKT-instabiliteiten verantwoordelijk kunnen zijn voor het ontstaan van kinematische golven. Door de invloed van concentratie en stromingsinertie te onderzoeken, legt het onderzoek een basis voor het begrijpen van de ingewikkelde processen die sedimentatie beheersen, met implicaties voor verschillende wetenschappelijke en technische domeinen. Dit inzicht overbrugt de kloof tussen theorie en toepassing en biedt inzicht in sedimenttransport en gerelateerde processen.

- **Verbetering van de Efficiëntie van Slurryleidingen via Kwantitatieve Analyse van Sedimenttransport**
  Efficiënt sedimenttransport is van het allergrootste belang in industrieën die afhankelijk zijn van slurrypijpleidingen. Deze studie is gericht op met deeltjes beladen stromen in slurrypijpleidingen, met als doel de dynamiek van drie brede sedimenttransportregimes te onderzoeken. Dit werd bereikt door een combinatie van experimenten in een van experimenten aan slurrytransport in een recirculerend stromingskanaal en interface-opgeloste DNS. De DNS-resultaten kwamen over het algemeen goed overeen met experimentele bevindingen, zelfs als we rekening houden met experimentele onzekerheden in de vloeistofbulksnelheid en Ga. In het regime met een vast bed scheidde een duidelijk scherp en vlak grensvlak de bovenliggende stroom van het stationaire bed, gemarkeerd door een regelmatige pakking van bollen in concentrische ringen. Boven het vaste bed leek de stroming op turbulente stroming in een kanaal met een niet-cirkelvormige dwarsdoorsnede en ruwe wanden, met een secundair stromingspatroon van Prandtl's tweede soort. In het regime met een glijdend bed was het grensvlak tussen het glijdende bed en de bovenliggende stroming diffuus, met deeltjeslagen in het bed. Secundaire stromingspatronen bestonden zowel boven als binnen het glijdende bed, nauw verbonden met de ruimtelijke deeltjesverdeling. Ten slotte werd het regime met volledig gesuspendeerde deeltjes gekenmerkt door een dichte deeltjeskern, met variaties in de deeltjesverdeling beïnvloed door Reynolds- en Galileo-getallen, wat de effecten van zwaartekracht en door schuifkracht geïndu-

ceerde migratie aantoont. Turbulente menging en deeltjesspanningen speelden een dominante rol bij de impulsoverdracht over verschillende stromingsomstandigheden en lagen binnen de stroming van slurryleidingen. Bovendien kwam de frictiefactor voor elk regime goed overeen met voorspellingen uit bestaande modellen in de literatuur. Dit onderzoek biedt inzicht voor het optimaliseren van het operationeel gebruik van slurryleidingen in de praktijk. De correlatie tussen niet-dimensionale parameters, gekoppeld aan kwantificeerbare inzichten in stromingsgedrag, construeert een uitgebreide routekaart voor efficiënt sedimenttransport en langdurige functionaliteit van pijpleidingen. De inzichten uit dit werk bieden aanbevelingen die de slijtage van de pijpwand kunnen minimaliseren, de sedimentflux kunnen maximaliseren en zo de efficiëntie kunnen verbeteren en tegelijkertijd de onderhoudskosten kunnen verlagen. De nadruk op grensvlak-, deeltjes- en turbulente spanningen, samen met een gedetailleerde karakterisering van recirculatiepatronen, biedt praktische handvatten voor het exploiteren van slurrypijpleidingen.

Hoewel ze gebaseerd zijn op computersimulaties, zijn deze bevindingen toepasbaar in de echte wereld, waardoor operators inzicht krijgen in diverse omstandigheden, kunnen anticiperen op uitdagingen en strategieën kunnen verfijnen. Uiteindelijk maakt dit werk geïnformeerde besluitvorming mogelijk, vergroot het de betrouwbaarheid van pijpleidingen en bevordert het de efficiëntie en kosteneffectiviteit in niet alleen slurrytransportsystemen, maar ook in bredere technische toepassingen zoals in de mijnbouw en de verwerking van mineralen, de olie- en gasindustrie, de behandeling van afvalwater, chemische verwerking, pulp- en papierindustrie, voedsel- en drankproductie en energieopwekking.

1

INTRODUCTION

The dynamics of dense particulate suspensions affects the mechanics of many industrial and naturally occurring phenomena. In industry, engineers aim to develop models that can simulate the physics of industrial processes such as transport of domestic waste in sanitation systems [5], coal in mining [26, 27], debris in drilling [96], and organic materials in the food process industry [102]. Another example is air traffic which may be significantly impacted by the aggregation and sedimentation of volcanic ash (see Fig. 1.1a) that may critically depend on aggregation and sedimentation processes [50, 114]. Insights into the dispersion of aerosols [122] and droplet dispersion while coughing [146, 36, 75] may benefit the health sector. Sedimentation tanks (see Fig. 1.1b) are a common component of water treatment processes and are effective in removing suspended solids from water. Dredging, a process of transporting a slurry (a multiphase mixture typically consisting of sand, rock, gravel and/or debris in water) and depositing them in a designated area (see Fig. 1.1c), is essential for flood protection, land reclamation, navigation, water quality maintenance, energy infrastructure support, environmental restoration, and tourism. In nature, the transport of sediments (see Fig. 1.1d) may influence the advance and retreat of tide water glaciers [22] and flooding in rivers [120]. In most of the aforementioned examples, the macroscopic behaviour that these phenomena exhibit (for example the amount of sediment transported) are governed by the physics of small scale interactions (for example interaction between sediment particles). Hence, it is of interest to probe the dynamics of the small scale interactions to evaluate their role in how they affect the macroscopic behaviour of dense particulate suspensions.

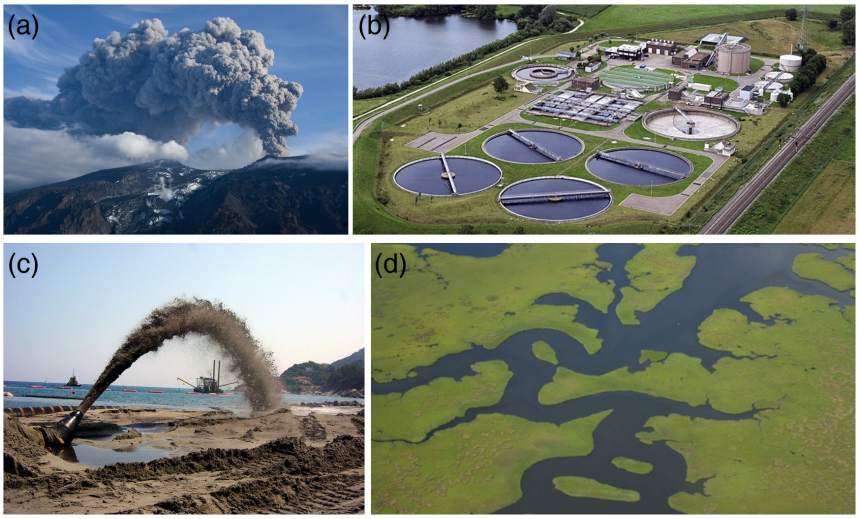

Figure 1.1: Examples of dense particulate systems: (a) dispersion of an ash cloud over Eyjafjallajökull, Iceland (hiticeland.com), (b) sedimentation based waste water treatment process (bioenergyconsult.com), (c) rainbowing of sediment during land reclamation (startdredging.com) and (d) Mississippi river delta (mississippiriverdelta.org).

Dredging operations for land reclamation and maintenance of the inland waterways is crucial for inland water management in the Netherlands, with a majority of its land lying below the sea level. As mentioned above, dredging operations involve transporting slurry (a mixture of sand, mud, gravel, etc., in water) in horizontal pipelines, typically at high volume concentrations (as high as 30% [121]) under turbulent conditions (see Fig. 1.2). The complex interaction between the turbulent carrier fluid and the individual particles comprised by the slurry determines the throughput, the energy input required to transport the slurry, and abrasion and wear on the pipe walls. A detailed understanding of the fundamental mechanics of slurry transport is essential for operating the slurry pipelines optimally. For example, formation of stationary deposits may block the pipe and a sliding bed layer may increase wear in pipelines, and knowing the pressure drop along the pipeline may help optimally situate booster stations to reduce the energy required to transport the slurry. In the realm of slurry flow dynamics, the intricate interplay of turbulent mixing, gravitational settling, and shear-induced particle migration determines the behavior of slurries. Turbulent mixing counteracts gravitational settling by inducing chaotic eddies and vortices, ensuring particle dispersion and suspension within the fluid. Shear-induced particle migration, driven by stress gradients, further mitigates settling tendencies for example by guiding particles from high-stress regions near flow boundaries to lower-stress regions in the flow. The synergy between these mechanisms results in diverse flow regimes such as the fixed-bed, sliding-bed, and fully-suspended (see Fig. 1.3), each delineating unique particle distribution patterns. Additionally, parameters like particle size, shape, concentration, fluid viscosity, and flow velocity intricately influence these dynamics, collectively influencing the efficiency of slurry transport, vital for the dredging industry.

Figure 1.2: (a) Transport of sediments from a dredger via horizontal pipelines over water using flotation buoys (damen.com). (b) Slurry transport pipelines (fluidflowinfo.com).

Researchers have used a combination of experimental studies, analytical models and numerical simulations to study sediment transport. It is challenging to study dense suspensions experimentally because the large concentration of particles in the suspension prevents optical access within the bulk. This can be mitigated to a certain extent by the use of index-matching suspensions, which enables the use of imaging techniques such as particle image velocimetry and laser Doppler velocimetry [148]. Other techniques such as ultrasound imaging velocimetry [134] and nuclear magnetic resonance imaging [2, 129] do provide access into the bulk of such dense suspensions, however, it remains challenging to capture the physics of these interactions at the scale of individual particles. This has motivated the use of numerical simulations in the present work to investigate the dynamics of such suspensions.

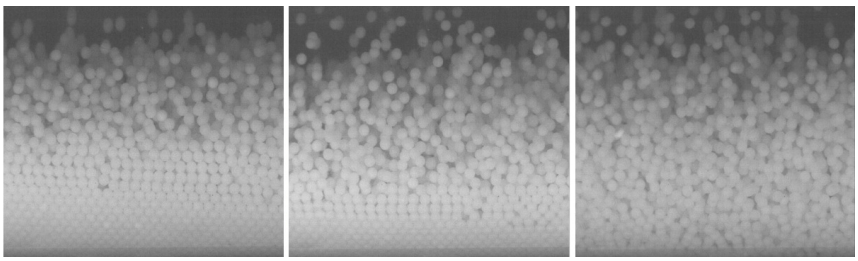

Figure 1.3: Instantaneous snapshots of slurry transport through a horizontal pipe from experiments by T. Schouten in the Dredging Engineering laboratory at TU Delft (see also chapter 4, Fig. 4.3). The flow rate is increasing from left to right, illustrating the different possible flow regimes of slurry transport: the fixed-bed regime (left), the sliding-bed regime (middle) and the fully-suspended regime (right).

The prime motivation for the present work is to further our understanding of slurry transport in horizontal pipelines, which is much needed to improve currently existing slurry flow models used in engineering. Historically, researchers began with the development of empirical and semi-empirical models. These models aimed to establish relationships between observed dynamics and operating parameters. For instance, models were developed to estimate the "limit deposit velocity", i.e., the critical flow velocity at which sediment particles start to deposit at pipe bottom, and to relate the pressure

drop along the pipeline to the power input needed for slurry transport [43, 166, 42]. These models have seen industrial applications due to their simplicity and reliance on experimental data. However, their drawbacks lie in their empirical nature, limited applicability to specific conditions, and failure to account for complex interactions such as particle collisions and non-uniform sediment beds. With more research into dynamics of transport phenomena, mechanistic layer models emerged as a significant advancement in sediment transport studies. These models aimed to describe sediment transport processes through interactions between different layers within sediment-laden flows. Wilson's layer models introduced the concept of multi-layered bed-load transport with varying grain sizes [174]. Building on this, Doron's models integrated effects like grain sorting and vertical fluxes, providing a more comprehensive view of sediment dynamics [42, 40]. While these models provided valuable insights, they faced challenges in assuming well-defined layers in natural environments and in capturing intricate interactions among layers. In the last few decades, computational fluid dynamics (CFD) has been incorporated into sediment transport modeling. Computational Fluid Dynamics (CFD) simulations facilitate a more detailed analysis of the flow regimes in slurry transport. In this context, Eulerian-based continuum models gained prominence [119]. For instance, the Two-Fluid Model treated water and sediment as separate but interpenetrating fluids [48]. The Euler-Lagrange Large Eddy Simulation (LES) provides more detail by coupling fluid behavior (represented through large eddy simulation) with the motion of individual sediment particles in a Lagrangian framework [25, 24]. However, these approaches still lack a careful representation of the particle shape and individual particle-particle interactions. Hence, the collision and lubrication interactions at the scale of an individual particle remain underrepresented.

It is apparent that a high level of detail is required to capture the dynamics of dense particulate simulations, especially in turbulent flows. To demonstrate this, consider a typical dredging pipeline with a pipe diameter $\sim 1\ m$, the kinematic viscosity of water $\sim 10^{-6}\ m^2/s$ and a flow rate $\sim 5\ m/s$, the bulk Reynolds number can be computed to be $\approx 5 \times 10^6$. Such turbulent flows, have been shown to exhibit a variety of different 3D fluctuating motions spread over length and time scales that may differ by several orders of magnitude [135]. Hence, modelling such a system warrants a high resolution to capture the broad range of length and time scales. Further, the particles are *finite sized particles*, meaning that the particles are typically significantly larger than the smallest turbulence structures in their vicinity. The smallest flow relevant scale for turbulent flow may be considered to be the Kolmogorov microscale [135]. Considering the pipeline described above, the smallest flow relevant scale may be $\sim 0.03\ mm$ (based on the bulk viscous dissipation rate in turbulent single-phase pipe flow with 1 mm wall roughness) and the size of a typical sand particle may be $\sim 1\ mm$. Hence, we can see that the size of the particle is more than 30 times larger than the smallest flow relevant scale. Moreover, inter-particular interactions such as collisions and lubrication effects between particles have a significant impact on the dynamics of the flow. The complex fluid-solid interactions and the solid-solid interactions (4-way) [49] give rise to a gamut of different interactions that are far from understood [121]. In addition to the finite size of the particles, the particles may also vary in shape, size, density and

frictional properties and thus, requiring any numerical framework to ideally capture such short-range particle-particle interactions. A careful treatment of particle-particle interactions and particle-fluid interactions is essential to accurately resolving the dynamics of dense particulate systems.

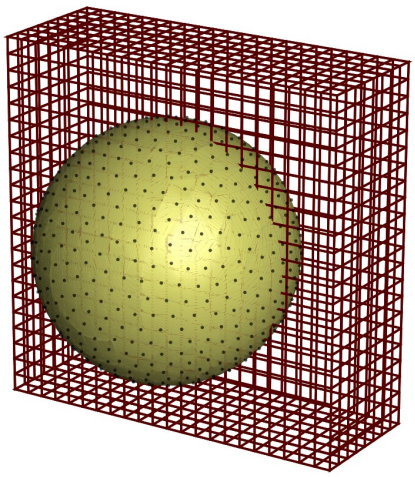

Figure 1.4: Discretization of the flow domain into a Eularian regularized grid and a Lagrangian grid over the surface of an individual particle [18].

Interface-resolved Direct Numerical Simulations (DNS) offer a distinct advantage over other Computational Fluid Dynamics (CFD) approaches by capturing fine-scale turbulence, particle-particle interactions, and fluid-particle interfaces accurately. This approach captures the complex interplay between the fluid and particle behaviour at a microscale by explicitly tracking the interface between the different phases. Interface-resolved Direct Numerical Simulations (DNS) have been applied to study sediment transport dynamics, for example: particle-laden turbulent channel flow [156], sediment interaction with open-channel flow [132], particle dynamics in turbulent plane channel flow [104], particle clustering in isotropic turbulence [115], and particle dispersion in decaying isotropic turbulence [49], providing insights into particle concentration, dispersion, and clustering mechanisms in turbulent environments. However, interface-resolved DNS has not yet been applied to study slurry transport of finite-sized heavy particles under turbulent conditions in horizontal pipelines. One key aspect of interface-resolved DNS is its application to particle-fluid coupling, a fundamental challenge in understanding the behavior of particles within a fluid. One prominent framework for such coupling is the IBM (Immersed Boundary Method) which seamlessly integrates the motion of finite-size particles into the fluid flow by imposing forces at the interface points, enabling a more realistic representation on particles [160]. Here, the flow domain is descretized into a fixed Eularian regular grid and a uniform Lagrangian grid over the surface of and translates with each individual particle (see Fig. 1.4). Furthermore, accurate collision models, integrated within the interface-resolved

DNS framework, allow for a faithful representation of these interactions, ensuring a comprehensive understanding of the system's behavior.

The primary objective of this research is to develop a comprehensive framework that leverages particle-resolved Direct Numerical Simulation (DNS) to unravel the 3D instationary flow physics of sediment transport within a horizontal pipe, encompassing all scales, from a microscale of individual particles to the macroscale of the pipe. This framework will be validated, and the research aims to identify governing parameters to characterize sediment transport. Towards that end, the sediment transport problem is downscaled by lowering Ga to achieve entrainment of particles in the flow even at moderate Re, thus facilitating an investigation of all transport regimes. For our studies we use an interface-resolved immersed boundary method described by Breugem [18]. This implementation of the method has been applied to a number of particle-laden flow problems over the last decade and has demonstrated significant accuracy in capturing the essential physics of dense particulate suspensions [133, 105, 132, 150]. This in addition to an improved contact model described by Costa et al. [29] where long-range and short-range hydrodynamic interactions, and solid-solid collision and lubrication effects are accounted for to ensure that particle-particle interactions are well resolved. This makes this method ideally suited to be applied in the investigation of sedimentation and sediment transport. Interface-resolved DNS not only provides insights into the underlying physics of slurry flows but also serves as a robust tool for validating closure models used in Computational Fluid Dynamics (CFD) simulations based on continuum approaches. In continuum modeling, local volume-averaging and ensemble/Reynolds-averaging techniques are employed to obtain macroscopic descriptions of flow properties. These techniques facilitate the reconstruction of macroscopic momentum balances, particle stress distributions, and other macroscopic variables from the resolved microscale interactions. By comparing results from interface-resolved DNS with predictions from continuum models, researchers can validate and improve the accuracy of CFD simulations and closure models used, enhancing the predictive capability of these models in a broader range of scenarios. Hence, interface-resolved DNS, particularly in the context of slurry flows, enables a detailed examination of microscale interactions that significantly impact macroscopic behaviors. This approach not only sheds light on the complex dynamics of multiphase systems but also provides a means to validate and enhance continuum-based closure models, bridging the gap between micro and macro scales in the slurry transport phenomena.

We focus on the sedimentation of suspensions in the inertial regime as a prelude to studying the dynamics of the sediment transport. Understanding the underlying physics of sedimentation is crucial for predicting the movement of these particles in a fluid and subsequently for modeling sediment transport phenomena [38]. Hence, to supplement our understanding of slurry transport we first focus on sedimentation of non-colloidal suspensions of spheres in viscous and Newtonian fluids (see Fig. 1.5). In the next chapters, we present and discuss results on particle sedimentation and horizontal slurry pipe transport. A short introduction to these chapters is given below:

- Sedimentation, the process of particles settling under gravity or centrifugal forces, plays a pivotal role in understanding slurry transport dynamics [11]. As particles are transported through a fluid medium, they experience various forces including gravitational settling, fluid drag, and turbulent fluctuations. In this work, we study sedimentation dynamics of non-colloidal suspensions of spheres in a viscous and Newtonian fluid, with a specific emphasis on the influence of flow inertia (expressed through the Galileo number) on the suspension microstructure and settling behavior in chapters 2 and 3. In the Stokes regime, characterized by small particles settling at low velocities, sedimentation has been extensively studied [3]. However, the behavior of larger particles such as coarse sand grains ($\sim 1\ mm$) settling at higher velocities, known as the inertial regime, is equally important and presents distinct challenges [161]. The Stokes regime involves gentle settling, where the drag force of the fluid dominates over particle inertia. This leads to predictable, well-behaved settling paths and wake dynamics [70], at least for highly dilute suspensions where particle-particle interactions are negligible. In contrast, the inertial regime introduces complexities due to the interplay of fluid and particle inertia, often resulting in chaotic motion, vortex shedding, and irregular wake interactions.

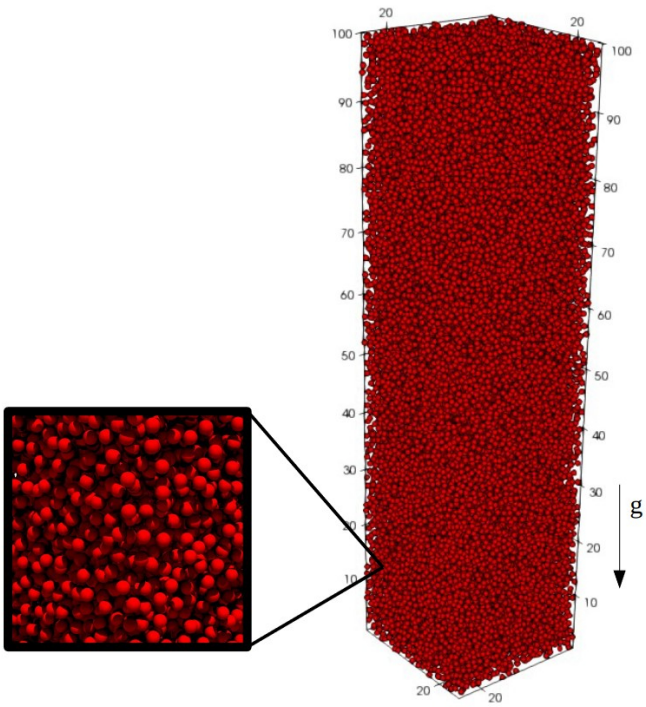

Figure 1.5: Instantaneous snapshot of a dense sedimenting suspension of non-colloidal spheres at a volume concentration of 30% under the influence of gravity. The numbers represent the domain size in particle diameter, and the arrow indicates the direction of gravity.

The research explores the different concentration regimes, each characterized by distinct particle arrangements: the dilute concentration regime with vertical trains, the moderate concentration regime with horizontal particle pairs, and the dense concentration regime with a pseudo-random distribution. A central research question guiding this study is how the sedimentation behavior evolves across different concentration regimes (dilute, moderate, and dense) and Galileo numbers. This entails an exploration of how wake trapping, drafting-kissing-tumbling (DKT) phenomena, and multiparticle effects contribute to the observed particle arrangements and settling dynamics. Furthermore, we aim to understand how these interactions transform as the concentration increases, and how these changes manifest in the fluctuations and correlations of particle velocities. By addressing these interconnected questions, we provide insights into the intricate mechanisms governing the sedimentation behavior of particle suspensions and illuminate the ways in which inertia influences these complex dynamics.

Figure 1.6: Experimental slurry loop in the Dredging Engineering laboratory at TU Delft, used for the experiments by T. Schouten. The experimental results are compared with results from interface-resolved DNS in chapter 4.

- The sedimentation study sets the stage for understanding slurry transport in a horizontal pipe discussed in chapter 4. In pursuit of a deeper comprehension of the flow dynamics, we embarked on a comprehensive investigation encompassing both experiments and interface-resolved Direct Numerical Simulations (DNS) centered on slurry flow within a horizontal pipe. This study aims to explore the behavior of slurry flows within three basic transport regimes, namely

fixed-bed, sliding-bed or fully-suspended regime. The complex dynamics observed in each of these regimes is determined by the bulk liquid Reynolds number (Re), the Galileo number (Ga), the solid bulk concentration (ϕ_b), the particle-to-fluid density ratio (ρ_p/ρ_f), the particle/pipe diameter ratio (D_p/D_{pipe}), and parameters related to direct particle interactions such as the Coulomb coefficient of sliding friction (μ_c).

This research was part of a bigger research program on "Modelling of turbulent hyperconcentrated sediment transport in horizontal pipes" with involvement of one other PhD student, T. Schouten, under supervision of Dr. G. Keetels and late Prof. C. van Rhee[†] of the Dredging Engineering Laboratory at TU Delft. This research was funded by the Topsector Water Programme of the Dutch Research Council (NWO), with co-funding from the dredging companies Van Oord and Boskalis. The experiments described in chapter 4 were performed by T. Schouten as part of a collaborative research with the aim to compare experiments with interface-resolved DNS of slurry pipe flow under the same flow conditions (see Fig. 1.6). The experiments were conducted in a slurry flow loop having a pipe with a diameter (D_{pipe}) of 4 cm. Our observations entailed monitoring the pressure drop along the pipeline, characterizing solid concentration distributions within the cross-flow plane via Electrical Resistance Tomography (ERT), and employing a high-speed camera to visualize the flow dynamics. The slurry itself was composed of polystyrene spheres suspended in water with a particle diameter (D_p) of 2 mm, a particle-to-fluid density ratio close to 1.02, Ga in the range of 40-45, and solid bulk concentrations ranging from 26% to 33%. To explore diverse flow regimes, we manipulated the flow rate, thereby varying the Reynolds number (Re) within the range of 3272 to 13830. This study represents a pioneering effort in employing interface-resolved DNS for simulating the fundamental transport regimes inherent to slurry pipe flow.

Questions that we would like to answer through this research are: how well do interface-resolved DNS simulations align with experimental data when it comes to capturing the dynamics of slurry pipe flow in various transport regimes? To what extent do modified empirical models accurately predict friction factors across different slurry transport regimes, and what are the contributing factors to any deviations? What are the mechanisms underlying secondary flow patterns within slurry flows across different transport regimes, and how do these patterns affect the overall momentum balance and frictional behavior of the system?

Following the introduction in chapter 1, we study sedimentation dynamics of non-colloidal suspensions of spheres in a viscous and Newtonian fluid in chapters 2 and 3. The characteristics of slurry transport regimes are discussed in chapter 4. Finally, concluding remarks and recommendations for future work are provided in chapter 5.

2

INFLUENCE OF CONCENTRATION ON SEDIMENTATION OF A DENSE SUSPENSION IN A VISCOUS FLUID[1]

Macroscopic properties of sedimenting suspensions have been studied extensively and can be characterized using the Galileo number (Ga), solid-to-fluid density ratio (π_p) and mean solid volume concentration ($\bar{\phi}$). However, the particle-particle and particle-fluid interactions that dictate these macroscopic trends have been challenging to study. We examine the effect of concentration on the structure and dynamics of sedimenting suspensions by performing direct numerical simulation based on an Immersed Boundary Method of monodisperse sedimenting suspensions of spherical particles at fixed Ga = 144 (corresponding to a particle Reynolds number for a single settling particle Re_T = 186), π_p = 1.5, and concentrations ranging from $\bar{\phi}$ = 0.5% to $\bar{\phi}$ = 30%. Our simulations reproduce the macroscopic trends observed in experiments and are in good agreement with semi-empirical correlations in literature. From our studies, we observe, first, a change in trend in the mean settling velocities, the dispersive time scales and the structural arrangement of particles in the sedimenting suspension at different concentrations, indicating a gradual transition from a dilute regime ($\bar{\phi} \lesssim 2\%$) to a dense regime ($\bar{\phi} \gtrsim 10\%$). Second, we observe the vertical propagation of kinematic waves as fluctuations in the local horizontally-averaged concentration of the sedimenting suspension in the dense regime.

2.1. INTRODUCTION

Sedimentation is the collective settling of particles suspended in a viscous fluid under the influence of gravity. It plays a major role in a multitude of industrial processes

[1] This chapter has been published as: T. Shajahan and W.-P. Breugem. Influence of concentration on sedimentation of a dense suspension in a viscous fluid. *Flow, Turbulence and Combustion*, 105:537-554, 2020.

such as slurry transport, water treatment plants, land reclamation projects and fluidized beds. It also plays a prominent role in the dynamics of environmental processes such as volcanic eruptions, sediment transport in rivers and rain.

2

Researchers have employed a multitude of techniques to study the dynamics of sedimenting suspensions [64, 33]. Sedimentation of monodisperse suspensions of non-colloidal particles can be fully characterized using the Galileo number $Ga = \sqrt{(\pi_p - 1) g D_p^3 / \nu_f^2}$, solid-to-fluid density ratio $\pi_p = \rho_p / \rho_f$ and mean solid volume concentration $\bar{\phi}$, where $\mathbf{g}$ is the gravitational acceleration, ρ_p and ρ_f are the density of the solid and fluid, respectively, ν_f is the dynamic viscosity of the fluid and D_p is the diameter of the particle. For concentrations $\bar{\phi} > \mathcal{O}(1\%)$, the settling of particles is *hindered* due to the increased vertical hydrostatic pressure gradient over the suspension, a net upward motion of the fluid and the nearby presence of other neighboring particles in their vicinity [34]. As a result the average settling velocity of dense suspensions decreases for increasing concentration. In literature many semi-empirical laws have been proposed for the average settling velocity of a suspension (V_S) as function of the terminal settling velocity of a single particle (V_T) and bulk concentration [62]. A popular correlation is the one proposed by Richardson and Zaki [141, 142] which predicts the average settling velocity of dense suspensions with good accuracy. Based on their experiments they demonstrated that the average settling velocity of a suspension exhibits a power-law relation in the bulk void fraction:

$$V_s = V_T (1 - \bar{\phi})^n, \tag{2.1}$$

where the exponent n is a function of the terminal particle Reynolds number $Re_T = V_T D_p / \nu_f$. Richardson and Zaki determined n and V_T by fitting Eq. 2.1 to their experimental results for various concentrations in the dense regime (typically $\bar{\phi} > 10\%$) [141]. However, in later studies it was found that Eq. 2.1 underestimates the settling velocity for $\bar{\phi} < 10\%$. The value of V_T obtained from fitting Eq. 2.1 to the dense regime appears to underestimate the actual value of V_T for a single settling particle. Yin and Koch [182] therefore proposed to multiply Eq. 2.1 with a certain correction factor of typically $0.86 - 0.92$ when the actual value of V_T is used. Furthermore, Garside and Al-Dibouni [62] proposed an empirical and implicit logistic curve equation for the (relative) settling velocity that agrees well with experimental data over the entire range of $\bar{\phi}$, including the regime of $\bar{\phi} < 10\%$.

While Richardson and Zaki consistently found that the settling velocity of dense suspensions is always smaller than the settling velocity of a single sphere, it was recently found that very dilute suspensions may show enhanced settling velocities for certain Ga and π_p. This has been connected to stable vertical columnar structures within which particles settle at enhanced velocities. Heitkam et al. [71] observed in their experiments at very low Reynolds number an increase of the sedimentation velocity of particles confined in circular capillaries. Experimental observation of columnar structures in dilute particle suspensions in homogenous turbulence was reported by Nishino and Matsuhita [127]. These columnar structures were also observed recently in a Direct Numerical Simulation (DNS) study by Uhlmann and Doychev [162]. They

found that at $Ga = 178$ and $\pi_p = 1.5$ a dilute suspension with $\bar{\phi} = 0.5\%$ settles faster than a single particle at the same Ga and π_p values. A single settling particle experiences instabilities in its wake as a function of Ga and π_p. As a result the path the particle travels may not be rectilinear and aligned with the direction of gravity. Path instabilities experienced by a single settling particle as a function of Ga and π_p have recently been studied in detail [163, 82]. At $Ga \approx 178$ and $\pi_p \approx 1.5$ a particle has a relatively long planar wake and settles at a slightly oblique trajectory. Uhlmann and Doychev suggested that the lateral motion and the elongated wakes of particles settling in close proximity to one another may lead to one particle being captured in the wake of another particle, which subsequently may result in the formation of columnar structures in which particles settle at enhanced velocities. The exact mechanism of this phenomenon is not fully understood yet. An enhanced settling velocity was also found later in experiments by Huisman et al. [77], who investigated concentrations up to $\bar{\phi} = 0.1\%$ at Ga varying between 110 and 310 and $\pi_p = 2.5$. However, in their experiments vertical clustering was observed even at Ga and π_p values where in case of a single particle no path instabilities were expected.

At dense concentrations, suspensions exhibit instabilities in the form of vertically propagating, horizontally oriented kinematic waves and shocks. Kynch theory provides an expression for the velocities of the kinematic shocks and waves as a function of concentration and sedimentation volume flux [98]. The development and propagation of these waves have been researched extensively in the context of fluidized beds [99, 85, 10, 79]. However, it has been challenging to relate the development of these instabilities to individual particle-particle and particle-fluid interactions.

The development of non-intrusive experimental techniques without the need for optical access has been able to provide insight into the dynamics of sedimenting suspensions [153, 173]. In addition, with the availability of computational resources and efficient numerical methods, it has been possible to provide a detailed account of the behavior of individual particles in these suspensions. In-depth descriptions of computational methods used to study particle laden flows are provided by Prosperetti and Tryggvason [137] and more recently by Maxey [116].

In this work, we aim to provide a description of gravity-driven monodisperse sedimentation of dense suspensions in a viscous fluid. The main questions we would like to address are: (1) how are the macroscopic properties of a dense sedimenting suspension related to particle-particle and particle-fluid interactions? and (2) how is this influenced by the concentration? We have performed DNS of gravity-driven sedimenting suspensions of non-colloidal spherical particles in a triply periodic computational domain, with the solid volume concentration varying from $\bar{\phi} = 0.5\%$ to $\bar{\phi} = 30\%$ at a fixed $Ga = 144$ and $\pi_p = 1.5$. The choice of Ga and π_p was motivated by a numerical study of Uhlmann and Dušek [163] of a single settling particle in which they considered the same Ga and π_p values. At a comparable $Ga = 121$, in the DNS performed by Uhlmann and Doychev [162] no significant particle clustering was reported. This was confirmed by the DNS performed by Fornari et al. [56] at $Ga = 144$ and concentrations

$\bar{\phi} = 0.5\%$ and $\bar{\phi} = 1\%$. While the previous works of Uhlmann and Doychev and Fornari et al. focussed on the dynamics of very dilute suspensions $\bar{\phi} < \mathcal{O}(1\%)$, we focus our analysis on the influence of concentration on the dynamics of sedimenting suspensions with an emphasis on dense suspensions for which $\bar{\phi} > \mathcal{O}(1\%)$.

We use an interface-resolved DNS based on an Immersed Boundary Method for the fluid/solid coupling [18]. In addition, a soft-sphere collision model described by Costa et al. [29] is used for frictional particle collisions. We first describe the computational method and provide validation of the method. Next, we study the particle-particle and particle-fluid interactions by investigating the mean structural configurations and the average flow field around a particle as a function of concentration. Lastly, we focus our attention on investigating macroscopic trends in the average settling velocity, dispersion of particles within the suspension and development of kinematic waves.

2.2. COMPUTATIONAL SETUP

2.2.1. GOVERNING EQUATIONS

Fully resolved DNS is carried out in a triply periodic rectangular domain filled with a viscous fluid in which immersed non-colloidal spherical particles are allowed to settle under gravity. The two phases in the simulation (fluid and particulate) are treated independently and coupled through a no-slip boundary condition enforced on the surface of the particle. The solution to the fluid phase is computed on a fixed Eulerian mesh and the moving surface of the particle is represented using a Lagrangian mesh that translates with the particle. For the fluid/solid coupling the Immersed Boundary Method (IBM) of Breugem [18] is used. In this method the no-slip/no-penetration condition at the particle/fluid interface is approximately enforced by (1) interpolating the provisional velocity in the fractional-step integration scheme from the Eulerian to the Lagrangian mesh, (2) calculating the force required to correct the fluid velocity to the local particle velocity, and (3) spreading this force from the Lagrangian to the Eulerian mesh. The principle of the IBM is that the no-slip/no-penetration condition is not imposed in a direct manner, but that force is locally added to the right-hand side of Eq. 2.3 in a thin spherical shell around each particle surface to enforce this condition by good approximation. This approach is a blend of the regularized δ-function approach proposed by Peskin [130] and the direct-forcing approach of Fadlun et al. [53] initially described by Uhlmann [160] and later improved to obtain second-order accuracy by Breugem [18].

The fluid phase is governed by the incompressible Navier-Stokes equations and the particle interactions are governed by the Newton-Euler equations. The governing equations are made dimensionless using reference scales, $l_{ref} = D_p$, $u_{ref} = \sqrt{gD_p}$, $t_{ref} = l_{ref}/u_{ref}$ and $a_{ref} = u_{ref}^2/l_{ref}$. The fluid phase in the simulation is advanced in time by solving the incompressible Navier-Stokes equations, given by:

$$\nabla \cdot \mathbf{u} = 0, \tag{2.2}$$

$$\left(\frac{\partial \mathbf{u}}{\partial t} + \nabla \cdot \mathbf{uu}\right) = -\nabla p_h - \nabla p + \frac{\sqrt{\pi_p - 1}}{Ga}\nabla^2 \mathbf{u}, \tag{2.3}$$

where $\mathbf{u}$ is the velocity, p is the modified pressure (total pressure - p_h). Here, ∇p_h is the contribution to the hydrostatic pressure gradient from the submerged weight of the particles. For a homogenous suspension with concentration $\bar{\phi}$, $\nabla p_h = (\pi_p - 1)\bar{\phi}\,\tilde{\mathbf{g}}$ and the gravitational acceleration g is non-dimensionalized as $\tilde{\mathbf{g}} = \mathbf{g}/|\mathbf{g}|$. The penultimate term in Eq. 2.3 becomes singular for $\pi_p = 1$, but note that this corresponds to the case in which particles are not settling at all. The translational and angular velocities of monodisperse spherical particles are determined from the Newton-Euler equations, given by:

$$\pi_p \frac{d\mathbf{u}_p}{dt} = \frac{6}{\pi}\Big(\oint_{\partial V} (\boldsymbol{\tau}\cdot\mathbf{n})\,dA + (\frac{\pi}{6})(\pi_p - 1)(1-\bar{\phi})\tilde{\mathbf{g}} + \mathbf{F}_c\Big), \tag{2.4}$$

$$\pi_p \frac{d\boldsymbol{\omega}_p}{dt} = \frac{60}{\pi}\Big(\oint_{\partial V} \mathbf{r}\times(\boldsymbol{\tau}\cdot\mathbf{n})\,dA + \mathbf{T}_c\Big), \tag{2.5}$$

where $\mathbf{u}_p$ and $\boldsymbol{\omega}_p$ are the translational and rotational velocity of the particle, $\boldsymbol{\tau} = -p\mathbf{I} + [\sqrt{\pi_p - 1}/Ga](\nabla\mathbf{u} + \nabla\mathbf{u}^T)$ is the stress tensor for a Newtonian fluid with $\mathbf{I}$ the unit tensor, $\mathbf{r}$ is the position vector with respect to the particle centroid, $\mathbf{n}$ is the outward normal directed from the surface (∂V) of the particle and $\mathbf{F}_c$ and $\mathbf{T}_c$ are the force and torque acting on the particle from inter-particle collisions. We consider non-colloidal particles in our simulations and hence the inter-particular interactions exclude electrostatic and Van der Waals forces. Brownian motion is neglected as well.

2.2.2. COLLISION MODEL AND LUBRICATION CORRECTION

A soft-sphere collision model described by Costa et al. [29] is used to model frictional particle collisions. The collision model simulates a spring-damper interaction by allowing partial overlap between colliding entities. The collision force consists of a normal and tangential component. The normal repulsive component is represented by a spring-dashpot model,

$$F_n = -k_n\delta_n - \eta_n u_n, \tag{2.6}$$

where k_n and η_n represent the stiffness and damping coefficient, respectively, and δ_n and u_n are the overlap distance and the relative velocity between the particles in the normal direction respectively. The tangential force component is modeled with a spring-dashpot model in the stick regime and Coulomb's friction model in the slip regime,

$$F_t = \min(||-k_t\delta_t - \eta_t u_t||, ||-\mu_c F_n||), \tag{2.7}$$

where k_t, η_t and μ_c are the stiffness, damping coefficient in the tangential direction and the coefficient of sliding friction respectively, and δ_t and u_t are the overlap distance and the relative velocity between the particles in the tangential direction. $k_{n,t}$ and $\eta_{n,t}$ are determined from the reduced mass of the particles, the dry coefficient of restitution and a preset collision time [29]. In our simulations $e_{n,dry} = 0.97$, $e_{t,dry} = 0.10$ and $\mu_c = 0.15$ based on experimental data for oblique glass particle-wall collisions in an aqueous glycerine solution [29, 84].

Lubrication effects are automatically accounted for in our DNS, although underresolved at inter-particle distances smaller than a grid cell. When prior to a collision the

distance between the particles is lower than a threshold of the order of the mesh size and the particles are not colliding yet, a lubrication force correction is added to the rhs of Eq. 4.3a. The (dimensional) lubrication correction is given by,

$$\Delta F_{lub} = -3\pi\nu_f\rho_f D_p u_n[\lambda(\epsilon) - \lambda(\epsilon_{\Delta x})] \tag{2.8}$$

where $\epsilon = 2\delta_n/D_p$ and $\epsilon_{\Delta x}$ is the threshold gap between two particles, and λ is the Stokes amplification factor given by Jeffrey [81]. The collision model has been validated against several benchmark experiments and the results show a good quantitative agreement [29].

2.2.3. NUMERICAL METHOD

The Navier-Stokes equations are solved by a fractional step approach and a three-step Runge-Kutta scheme is used for integration in time. The spatial discretization uses second-order central finite differences on a uniform, staggered and isotropic grid. The Eulerian mesh employs a Cartesian coordinate system where the y-axis is aligned with the vertical direction. Gravity is the only external force acting on the system and it is directed vertically downwards in the negative y-direction. The domain size was chosen to minimize the effect of periodic boundary conditions. The time taken for fluctuations in particle velocities to decorrelate was determined by computing the auto-correlation of particle velocities in each component direction, shown in Fig. 2.9. A vertical decorrelation distance was calculated as a product of the vertical decorrelation time scale and the mean settling velocity of the suspension. The evolution of the settling velocity of suspensions at different concentrations is shown in Fig. 2.1. We have checked *a posteriori* that the domain size in each direction was several times larger than the decorrelation distance, see fourth and last column in Table 3.2. The domain size for all the simulations (except $\bar{\phi} = 0.5\%$) was fixed at $25D_p \times 100D_p \times 25D_p$. The domain size for the case $\bar{\phi} = 0.5\%$ was chosen to be $37.5D_p \times 200D_p \times 37.5D_p$ in order to account for a longer decorrelation distance and to increase the number of particles for statistical convergence. A grid resolution of $D_p/\Delta x = 16$ was chosen for our simulations and validation for it is provided in the next section. An illustration of the computational domain with particles is shown in Fig. 4.2. The domain size, mean solid volume concentration, number of particles and observation time for calculating the statistics is provided in Table 3.2.

At the start of the simulation, particles in the domain are initialized at random locations within the domain with zero velocity and allowed to settle under gravity. The fluid is initialized over the entire domain with zero velocity as well. After an initial transient of about $t = 50\sqrt{D_p/g}$ the particles settle at the mean settling velocity, after which statistics are collected. At every time step the hydrostatic pressure gradient in Eq. 2.3 is implicitly imposed from the requirement that the overall bulk flow (particle and fluid) has to be zero. This mimics the presence of a bottom wall in a batch sedimentation process.

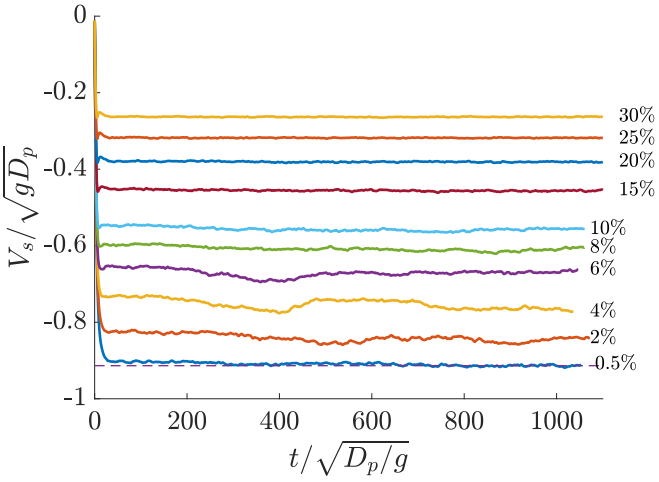

Figure 2.1: Evolution of the mean settling velocity of suspensions at different concentrations at $Ga = 144$ and $\pi_p = 1.5$. The dashed line corresponds to the settling velocity of a single particle.

Table 2.1: Physical parameters in the DNS: global solid volume fraction $\bar{\phi}$, size of the computational domain L_α (in the coordinate direction x_α), the number of particles N_p, T_{obs} is the duration of the observation interval over which statistics were calculated and the product $V_s\tau_L$ is the decorrelation distance. The Galileo number $Ga = 144$ and density ratio $\pi_p = 1.5$ in all simulations.

Case	$\bar{\phi}$	N_p	$L_x \times L_y \times L_z$	$T_{obs}/\sqrt{D_p/g}$	$(V_s\tau_L)/D_p$
A	0.005	2686	$37.5D_p \times 200D_p \times 37.5D_p$	1096	46.79
B	0.02	2388	$25D_p \times 100D_p \times 25D_p$	1072	14.29
C	0.04	4775	$25D_p \times 100D_p \times 25D_p$	1036	9.91
D	0.06	7163	$25D_p \times 100D_p \times 25D_p$	1046	7.72
E	0.08	9549	$25D_p \times 100D_p \times 25D_p$	1060	6.01
F	0.1	11937	$25D_p \times 100D_p \times 25D_p$	1060	3.80
G	0.15	17903	$25D_p \times 100D_p \times 25D_p$	1143	3.46
H	0.20	23871	$25D_p \times 100D_p \times 25D_p$	1154	2.55
I	0.25	29838	$25D_p \times 100D_p \times 25D_p$	1144	2.56
J	0.30	35806	$25D_p \times 100D_p \times 25D_p$	1134	1.97

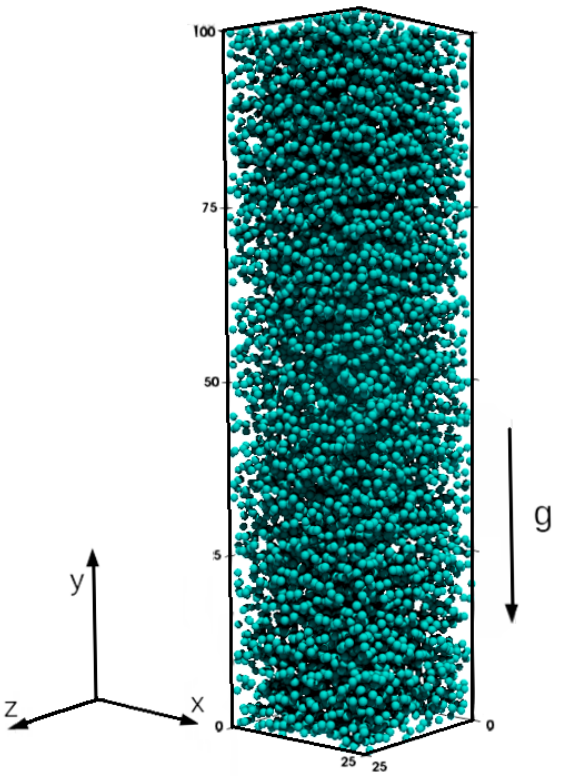

Figure 2.2: Computational domain used in the simulations with domain size $L_z = L_x = 25D_p$ and $L_y = 100D_p$ and solid volume concentration $\bar{\phi} = 10\%$ with $n_p = 11937$ particles.

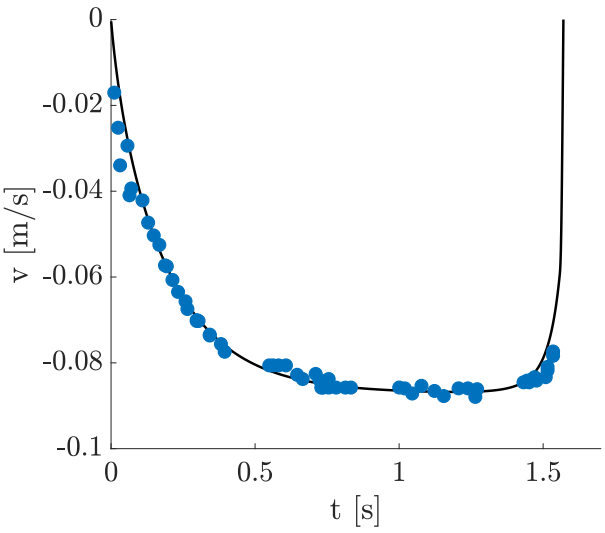

Figure 2.3: Comparison of the results of a nylon sphere settling in silicon oil using DNS (black line) and experimental results of Ten Cate et al. (blue dots) [157].

2.2.4. VALIDATION

The present numerical code is validated against experimental results by Ten Cate et al. [157] for settling of a sphere in a viscous fluid at $Re_T = 11.6$. The experiment was performed in a container of dimensions $100 \times 100 \times 160\ mm^3$. The fluid used in the experiment is silicon oil with a density of $962\ kg/m^3$ and dynamic viscosity $0.113 kg/ms$ and the solid used is a nylon sphere with density $1120\ kg/m^3$ and diameter of $15\ mm$, which corresponds to $Ga = 19.85$ or $Re_T = 11.6$ and $\pi_p = 1.16$. The numerical simulation was set up to be similar to the experiment. A no-slip, no-penetration boundary condition is imposed on all 6 walls of the container. In Fig. 2.3, the solid line represents the computed result from the DNS and the blue dots represent the experimental data. The numerical results are found to be in good agreement with the experimental data.

In addition, we performed a DNS of a single settling particle at $Ga = 144$ and $\pi_p = 1.5$. A moving frame of reference with inflow/outflow conditions was used in the vertical direction and periodic boundary conditions were imposed in the horizontal directions. The domain size is $5.33D_p$ in the horizontal direction and $16D_p$ in the vertical direction. The grid resolution was uniform with $D_p/\Delta x = 16$. The results were compared against spectral/spectral-element simulations by Uhlmann and Dušek [163] for a similar case in a cylindrical domain with a diameter of $5.34D_p$. Our terminal settling velocity was close to the one of Uhlmann and Dušek with an error of 0.45%. The particle was found to settle in a rectilinear fashion as expected. The vertical velocity field relative to the particle is shown in Fig. 2.6 (a). The terminal Reynolds number, $Re_T = V_T D_p/\nu_f$, is 186. This is also very close to the expected value of 184.5 obtained from Abraham's correlation for the drag coefficient [1], indicating a negligible effect of

the lateral domain size. The DNS has also been validated against several different flows previously [18, 29].

2.3. RESULTS

2.3.1. SNAPSHOTS OF INSTANTANEOUS PARTICLE DISTRIBUTION AND VELOCITY

From our simulations, we observe a distinct change in the structure and dynamics of sedimenting suspensions at different concentrations. We support our observations with a number of statistical correlations that demonstrate this change. Instantaneous snapshots of the computational domain at three different solid volume concentrations are shown in Fig. 2.4. We observe different structural arrangements of particles as the solid volume concentration is increased. At $\bar{\phi} = 2\%$ we observe a tendency for vertical aggregation of particles. This can be observed in the trains of particles that settle significantly faster compared to the average settling velocity of the suspension, indicated by the red colored particles at the flanks of the domain. On moving to the denser solid volume concentrations of $\bar{\phi} = 10\%$ and $\bar{\phi} = 20\%$ the particles exhibit a seemingly random distribution, however it is hard to discern any structural trends from visual inspection alone. At $\bar{\phi} = 10\%$ and $\bar{\phi} = 20\%$ we observe a trace amount of particles traveling upwards (i.e., $V/V_s < 0$, $V > 0$ and $V_s < 0$). The distribution of colors (velocities), indicate the presence of fairly large scale structures in the sedimenting suspensions at $\bar{\phi} = 10\%$ and $\bar{\phi} = 20\%$.

2.3.2. PARTICLE-CONDITIONED AVERAGE PARTICLE DISTRIBUTION

The local average distribution of particles in the vicinity of each particle is studied by computing the particle-conditioned average. A solid phase-indicator function is defined over the entire domain. This function is defined to have a value of 1 within solid particles and 0 elsewhere. By averaging the solid phase-indicator function in the vicinity of each particle, the local particle-conditioned average is obtained.

The particle-conditioned average in a vertical plane passing through the center of the particle for different solid volume concentrations is shown in Fig. 2.5. The yellow colors in the plot indicate regions of higher than average concentration and the blue regions indicate regions of lower than average concentration. In Fig. 2.5, we observe that the regions away from the center of the particle show a concentration equal to the mean solid volume concentration. For $\bar{\phi} = 0.5\%$ we notice that there is a tendency for vertical aggregation of particles indicated by the cone-shaped profiles in the vertical direction. We also observe a significantly lower than average concentration of particles in the regions adjacent to the vertical columns. In the case of $\bar{\phi} = 10\%$, we notice that there is a slightly higher concentration of particles adjacent to the reference particle in the horizontal direction, but this anisotropy in particle arrangement is restricted to distances less than $2D_p$. This suggests the increased probability of a particle to settle adjascent to a neighboring particle in the horizontal direction.

In the case of $\bar{\phi} = 30\%$, we notice first, spherical contours around the particle at

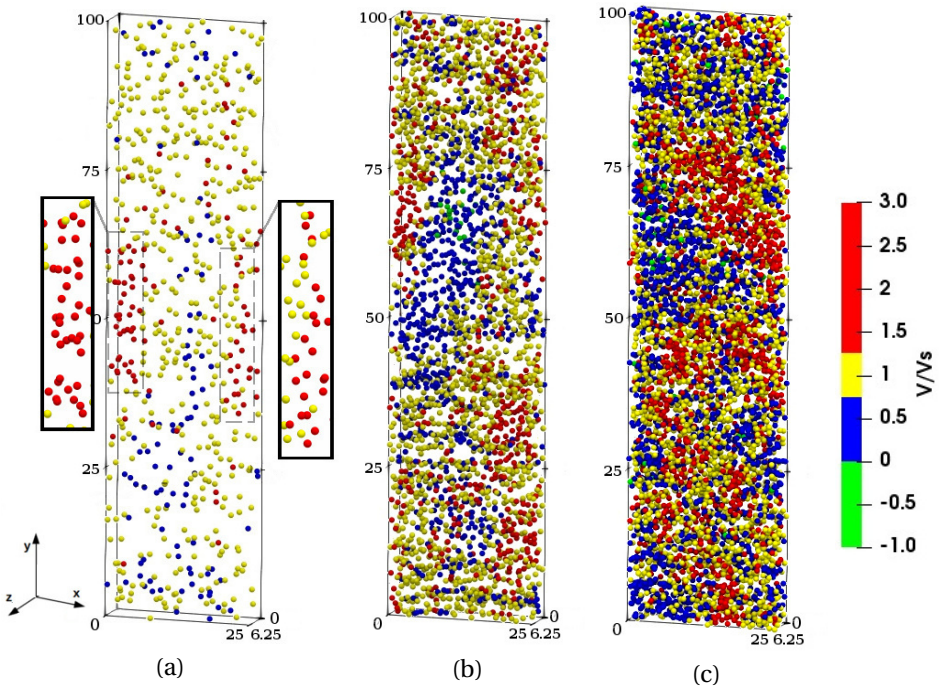

Figure 2.4: Instantaneous snapshot of a thin slab of the computational domain at solid volume concentrations (a) $\bar{\phi} = 2\%$, (b) $\bar{\phi} = 10\%$ and (c) $\bar{\phi} = 20\%$. The slab thickness is 6.25 particle diameters. Particles are colored discreetly by their vertical velocity scaled with the mean sedimenting velocity ($V_s < 0$) of the suspension. The vertical trains of particles in the instantaneous snapshot for the case $\bar{\phi} = 2\%$ are outlined using rectangles in (a). Positive values of V/V_s indicate that particles are settling along the direction of gravity, i.e vertically downwards.

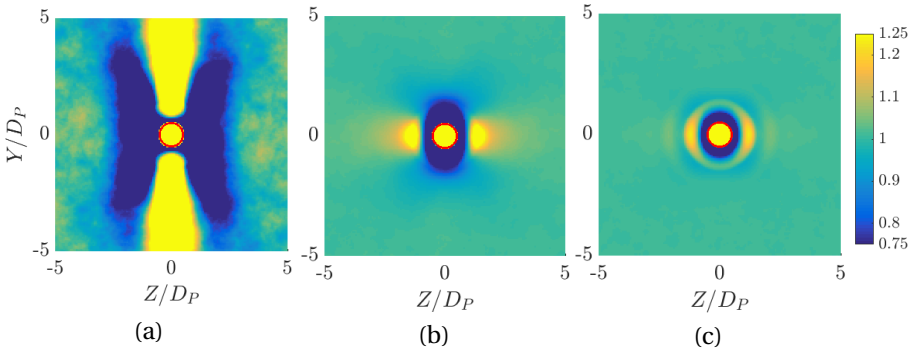

Figure 2.5: Averaged solid volume concentration conditioned on particle positions (scaled by the global solid volume concentration of the suspensions) for different solid volume concentrations: (a) $\bar{\phi}$ = 0.5%, (b) $\bar{\phi}$ = 10% and (c) $\bar{\phi}$ = 30%.

radii of $1.16D_p$ and $2.09D_p$ and second, a slightly higher concentration in the horizontal direction. However, this effect is much weaker as compared to $\bar{\phi}$ = 10%. The concentric circles near the reference particle can be explained by the kinematic constraint that particles cannot overlap with the reference particle; this effect fades away within a few particle diameters. This results in a largely uniform hard sphere like distribution. A similar arrangement was also observed in the dense regime of sedimenting spherical particles at $Re_T \ll 1$, shown using a radial distribution function by Guazzelli and Morris [64], and using a pair probability distribution function by Yin and Koch [182] at $\bar{\phi}$ = 20% for $Re_T = 10$.

2.3.3. AVERAGE FLOW FIELD AROUND A PARTICLE

The average vertical flow field around a particle relative to the mean settling velocity of the suspensions is determined by computing the average vertical fluid flow field in two mutually perpendicular vertical planes centered around each particle. The mean settling velocity of the suspension is subtracted from the flow field to obtain the velocities relative to the particle's frame of reference. The mean is computed over all particles in the suspension and at 5 different instants in time over the course of the simulation. The averaged flow fields for the concentrations $\bar{\phi}$ = 2% and $\bar{\phi}$ = 30% as shown in Fig. 2.6 (b) and (c) respectively. For comparison, the instantaneous flow field around a single particle is shown in Fig. 2.6 (a) using a simulation with inflow/outflow conditions described in section 2.2.4. Comparing Fig. 2.6 (b) and (c), we observe that the extent of the wake at $\bar{\phi}$ = 30% is much smaller than at $\bar{\phi}$ = 2%, while the latter is similar to the wake structure of a single particle. The presence of other neighboring particles in close proximity to the reference particle disrupts the formation of elongated wakes at $\bar{\phi}$ = 30%. This limits the influence of particle-fluid interactions and suggests a dominance of particle-particle interactions (lubrication and collisions), while the opposite holds for $\bar{\phi}$ = 2% as the wake in this case is similar to the case of a single settling particle.

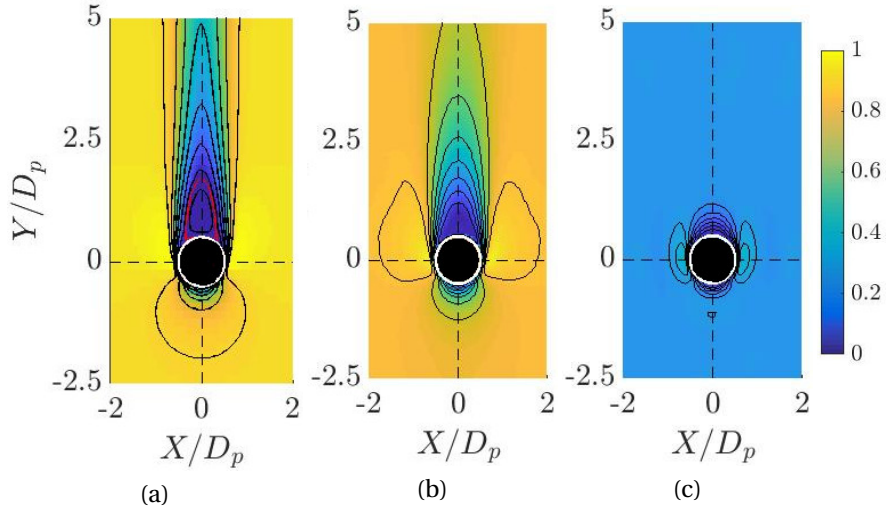

Figure 2.6: (a) Relative vertical flow field around a settling particle for an isolated single particle (the red contour marks the location where the vertical fluid velocity $V_f = 0$, which indicates the extent of the recirculation region), (b) averaged flow field relative to a particle for a suspension with $\bar{\phi} = 2\%$, (c) Idem for $\bar{\phi} = 30\%$. Colors and contour lines in each figure span from 0 to the terminal settling velocity V_T for the single particle and the mean settling velocity V_s for concentrations $\bar{\phi} = 2\%$ and $\bar{\phi} = 30\%$.

2.3.4. PARTICLE VELOCITY STATISTICS

From literature, it is known that the settling velocity of a suspension decreases with the increasing solid volume concentration, with the exception of very dilute suspensions at specific Ga and π_p such as mentioned in the introduction. For dense suspensions the settling velocity can be described by Eq. 2.1 suggested by Richardson and Zaki [141]. Our simulations reproduce a similar trend for the solid volume concentrations simulated. We observe that Eq. 2.1 is valid for suspensions at solid volume concentrations $\bar{\phi} > \mathcal{O}(10\%)$, while Richardson and Zaki underpredicts settling velocity at lower concentrations; the deviation increases for lower concentration in agreement with previous studies mentioned in the introduction section. In our DNS suspensions at lower solid volume concentrations show a deviation from this trend and settle faster than that predicted by the power-law relation. This can be seen in the double logarithmic plot of the settling velocity as a function of concentration, shown in Fig. 2.7.

The red dot in the figure is the terminal settling velocity $V_T = 0.91\sqrt{gD_p}$ of a single particle settling under gravity. Richardson and Zaki determined $V_{T,ext}$ of a particle settling under gravity by extrapolating Eq. 2.1 to a suspension at infinite dilution i.e. $\bar{\phi} = 0\%$ [141]. We compute $V_{T,ext} = 0.76\sqrt{gD_p}$ (indicated in blue in Fig. 2.7) in our DNS using the same approach and the corresponding $Re_T = 154.3$. Note that $V_{T,ext}$ computed using this approach is different from the real V_T of a single settling particle (indicated by the red dot in Fig. 2.7). From fitting Eq. 2.1 to the results for $\bar{\phi} \geq 10\%$ we find that $n = 3.0$. Richardson and Zaki performed their experiments in 2 different pipes and found a clear dependency of the exponent n on the ratio of the particle to tube

diameter. For $Re_T = 154.3$ their proposed correlation for n varies between $n = 2.69$ for $D_{pipe}/D_p = \infty$ and $n = 3.12$ for $D_{pipe}/D_p = 25$ [141]. In our simulations the ratio of particle diameter to the lateral extent of the domain is equal to 25. Note, however, that we make use of periodic boundary conditions, so we expect that the value from our DNS is in between these limits. This is indeed the case as our measured value for $n = 3$ is in between the 2 limits mentioned before : $2.69 < n < 3.12$.

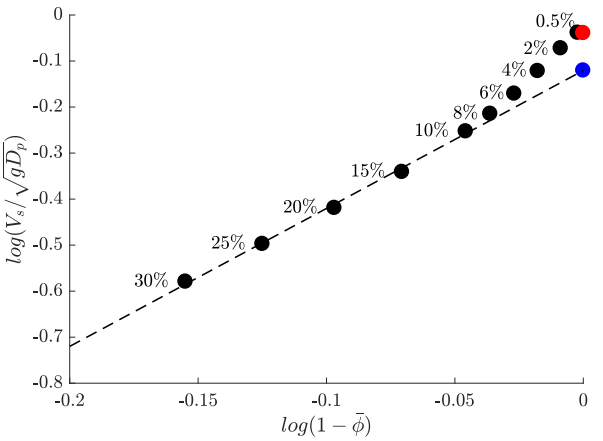

Figure 2.7: Double-logarithmic plot of settling velocities of suspensions at different $\bar{\phi}$. The red dot indicates the terminal settling velocity V_T of a single settling particle and the blue dot indicates the terminal settling velocity V_T of a single settling particle computed from fitting the power relation proposed by Richardson and Zaki [141] and given in Eq. 2.1 to the settling velocities for $\bar{\phi} \geq 10\%$.

2.3.5. PARTICLE DISPERSION STATISTICS

The dispersion of the particles in the suspension is measured from the mean square displacement of the particle as a function of time. The expression to compute the mean square displacement is given by:

$$\overline{Y^2}(\tau) = \overline{(Y(t+\tau) - Y(t) - V_s\tau)^2}, \tag{2.9}$$

where, Y is the displacement, τ is time interval over which the displacement is measured and t is the simulation time over which the mean is computed. The term $-V_s\tau$ is a correction for the mean vertical displacement over a time interval τ. The overline represents an average over t, the time over which statistics were computed and over the displacements of all the particles in the vertical direction. The expression for the mean square displacement provided in Eq. 2.9 is analogous for the lateral directions, but without $-V_s\tau$ term. Einstein predicted ballistic and diffusive transport at short and long times, respectively, for Brownian motion of small particles [47]. Similarly, for sedimenting suspensions the particles are in the ballistic regime for short times, where the mean square displacement scales quadratically with time, while for long times they are in diffusive regime, where the mean square displacement scales linearly with time. In turbulent flows dispersion of a passive scalar also displays ballistic and diffusive regime

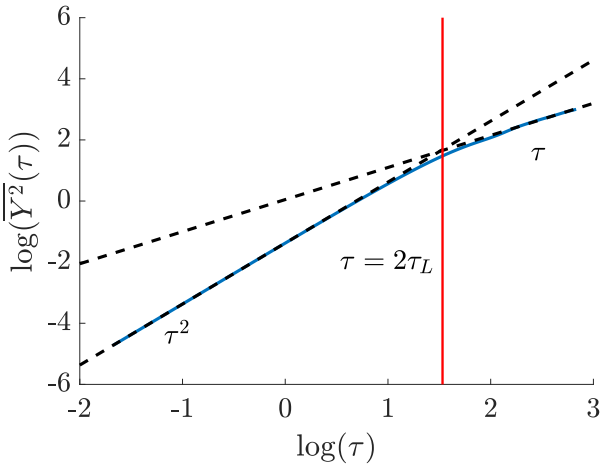

Figure 2.8: Double logarithmic plot of mean square displacement at $\bar{\phi} = 2\%$. The slopes indicate the scaling of the mean square displacement with time. The red line indicates the integral time scale τ_L.

as shown by Taylor [60] similar to Einstein's theory of Brownian motion. The time scale $\tau = 2\tau_L$[2] at which the two regimes (indicated by the linear and quadratic fits) intersect is twice the integral time scale. This is indicated by the red line in Fig. 2.8 for the case of $\bar{\phi} = 2\%$. It marks the transition from the ballistic to the dispersive regime. The integral time scale is a measure of the typical time over which the particle velocity decorrelates with itself or, alternatively, is a typical diffusive time scale. The integral time scale associated with each solid volume concentration is computed and expressed as a function of $\bar{\phi}$ in Fig. 2.9. It can be observed from this plot that the rate of diffusion increases with increasing concentration up to $\bar{\phi} \sim 0.06$ and 0.1 in the horizontal and vertical direction, respectively, while it remains nearly constant for higher concentrations. The dispersive time scale for the vertical direction is larger than for the lateral directions. Because of symmetry, the dispersive time scales for the x and z directions should be identical. This can indeed be observed, except for some discrepancies in the smallest concentrations related to some lack of statistical convergence.

2.3.6. KINEMATIC WAVES

Kynch theory [98] of sedimentation makes use of two assumptions. First, the concentration of a sedimenting suspension is assumed to be uniform in the lateral directions. This enables the distribution of the local concentration of the sedimenting suspension to be expressed as a function of vertical position and time $\phi(y,t)$. Second, the settling velocity of the suspension is assumed to be quasi-steady only dependent on the local

[2] Note: In the article published in *Flow, Turbulence and Combustion* on 15 June 2020, it was incorrectly reported that $\tau = \tau_L$. Here, it has been corrected to state that $\tau = 2\tau_L$.

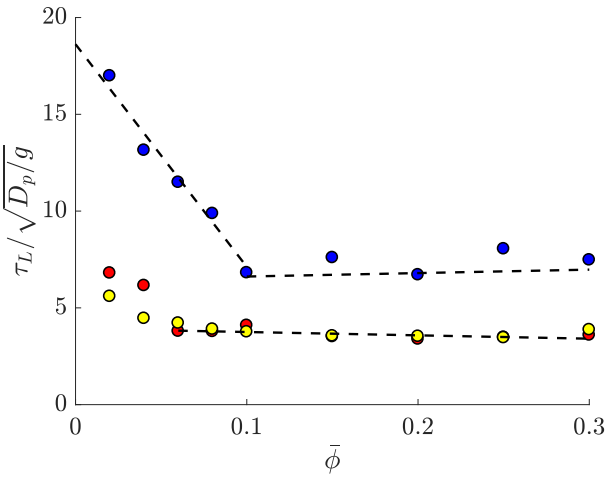

Figure 2.9: Integral time scale expressed as a function of solid volume concentration. The blue circles indicate the integral time scale in the vertical direction and the red and yellow circles are the integral time scales in the lateral directions.

concentration. Using these assumptions, mass conservation requires that:

$$\frac{\partial \phi}{\partial t} + V_{KW}\frac{\partial \phi}{\partial y} = 0, \tag{2.10}$$

with the kinematic wave velocity $V_{KW} = \partial(\phi V_s)/\partial\phi$, where ϕV_s represents the vertical volume flux of solids in the suspension. Based on the correlation provided by Richardson and Zaki given in Eq. 2.1, the mean sedimentation flux can be computed analytically using the above expressions, given by:

$$\bar{\phi} V_s = V_T \bar{\phi}(1-\bar{\phi})^n. \tag{2.11}$$

A comparison of the sedimentation flux computed from this theoretical expression and the measured value from our DNS, is shown in Fig. 2.10. The results are found to be in good agreement.

Due to the strong dependence of sedimentation on the solid volume concentration, local fluctuations in the solid volume concentration are expected to trigger small amplitude kinematic waves. These appear as vertically propagating fluctuations in the local solid volume concentration. To study this, we calculate the plane-averaged solid volume concentration as function of the vertical height and time. This is shown in Fig. 2.11 for the case $\bar{\phi} = 20\%$. From this space/time plot, we observe local fluctuations in the vertical concentration profile around the global solid volume concentration (indicated by the blue and yellow bands) that show a wave-like pattern that propagates downwards, though at a lower velocity than the average settling velocity.

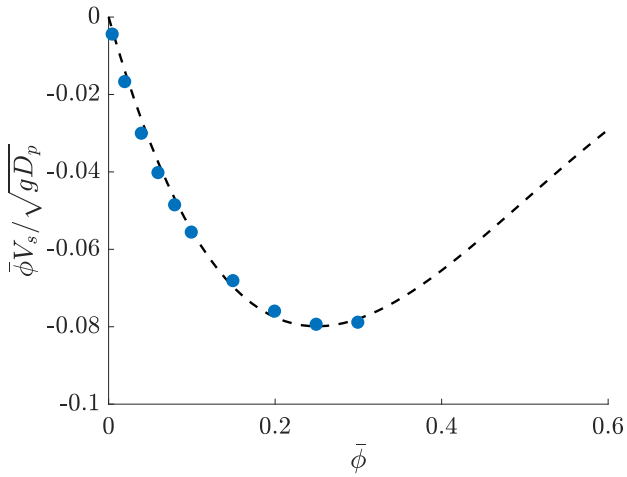

Figure 2.10: Comparison of solid volume flux of a sedimenting suspension as a function of concentration between theory (black dashed line) with the measured sedimentation flux from DNS (blue dots) at particle Reynolds number $Re_T = 154.3$.

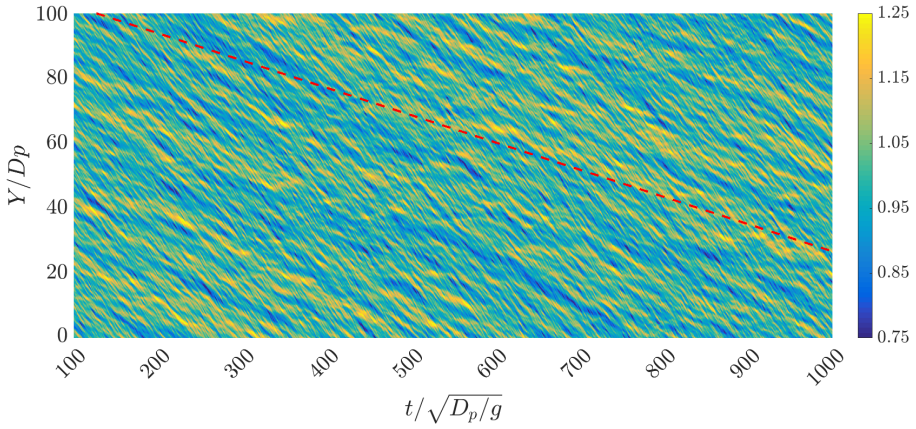

Figure 2.11: Space/time plot of the plane-averaged solid volume concentration $\phi(y,t)$ as a function of height and time. The colors represent the local volume concentration scaled with the global solid volume concentration ($\bar{\phi} = 20\%$). The red dashed line indicates kinematic wave velocity determined from the space/time autocorrelation.

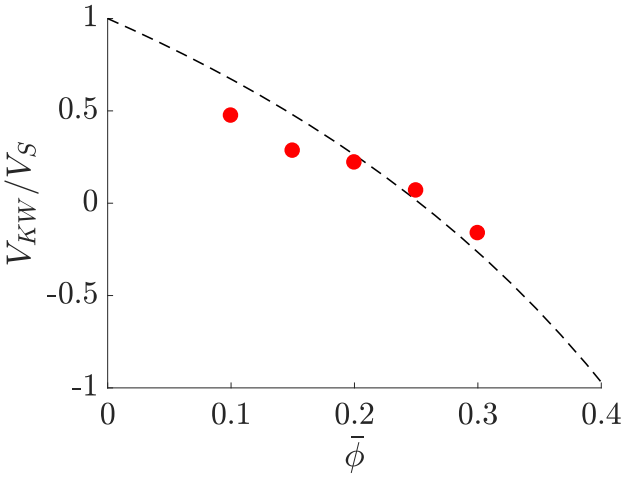

Figure 2.12: Comparison of kinematic wave velocity of a sedimenting suspension as a function of concentration between theory (black dashed line) with the measured sedimentation flux from DNS (red dots).

In order to measure the velocity of the wave-like structures in the sedimenting suspension, we performed an autocorrelation of the plane averaged solid volume concentration. The autocorrelation is given by:

$$\rho(\Delta y, \Delta t) = \overline{\phi'(y,t)\phi'(y+\Delta y, t+\Delta t)} \tag{2.12}$$

where $\phi'(y,t) = \phi(y,t) - \bar{\phi}$ is the fluctuation in the plane-averaged solid volume concentration. The overline represents an average over y and t. The correlations over large displacements in space and time are expected to correspond to kinematic waves. By means of a linear fit through the correlation peaks over large displacements in y and t, the velocity of the correlated structure (i.e. kinematic wave) can be determined. The velocity of the kinematic waves V_{KW} corresponding to the cases $\bar{\phi} = 10\%$ to $\bar{\phi} = 30\%$ are computed in a similar manner. From Kynch sedimentation theory, the velocity of the kinematic waves V_{KW} at a particular concentration can be determined by computing the slope of the sedimentation flux curve in Fig. 2.10, given by:

$$\frac{V_{KW}}{V_S} = \frac{1-(n+1)\bar{\phi}}{1-\bar{\phi}} \tag{2.13}$$

We compare the kinematic wave velocities at different concentrations from the DNS and theory, shown in Fig. 2.11. The measured results from the DNS follow a similar trend as predicted by the theory. Deviations between the DNS data and Eq. 2.13 may be related to dispersive effects not accounted for in Eq. 2.10 [79]

2.4. CONCLUSIONS AND DISCUSSION

Particle-particle and particle-fluid interactions influence the macroscopic properties of a sedimenting suspension and are a strong function of the global particle volume

concentration. From our results we observe for increasing concentration a gradual transition from a dilute ($\bar{\phi} \lesssim 2\%$) to a dense regime ($\bar{\phi} \gtrsim 10\%$). From the instantaneous snapshots of the suspensions at different concentrations and the particle-conditioned concentration, we notice that structural arrangement of particles is different in each regime. From the conditionally averaged particle concentrations, we observe with increasing $\bar{\phi}$ a gradual transition from a preference for vertical particle aggregation in the dilute regime to a uniform distribution in the dense regime with a slightly higher preference of a particle to settle adjacent to another particle.

A particle settling in the wake of another particle experiences less drag and hence tends to draft towards that particle. The trailing particle can either spend an extended duration of time drafting towards the leading particle or can come into contact (kissing) with the leading particle and tumble into a more stable horizontal configuration. The latter is known as the drafting, kissing and tumbling (DKT) mechanism. The former is expected in the dilute regime where the wake of a settling particle is elongated and relatively undisturbed by the presence of other particles as compared to the dense regime. This leads to vertical aggregation of particles which we observed at the most dilute concentrations considered, i.e. $\bar{\phi} = 0.5\%$ and $\bar{\phi} = 2\%$. At $\bar{\phi} > 2\%$, the slight increase in the horizontal concentration close to the reference particle observed in the particle-conditioned concentration can be explained by the DKT mechanism. The negative velocities of a few particles observed in the dense regime could be due to the presence of particle-rich and particle-poor regions that set up local convection of fluid causing a few particles in the latter region to travel upwards. Lubrication and collisions likely play an important role in the dynamics of the dense regime, though a more quantitative analysis of their influence is required.

In tandem with this change, we observe first, a deviation of the mean settling velocity from the power-law relation suggested by Richardson and Zaki [141] in the dilute regime and second, the dispersive time scales were found to decrease rapidly up to $\bar{\phi} \sim 10\%$, while they remained relatively unaltered in the dense regime. This highlights the change in dynamics from the dilute to the dense regime. Yin and Koch [182] suggested that the power-law scaling of the settling velocity is associated with a hard sphere like (random) particle distribution. In our simulation we study the structural arrangement of particles in the suspension by means of the particle-conditioned concentrations and we can confirm that the power-law scaling is indeed associated with such a distribution as observed in the dense regime. The statistically homogeneous distribution of particles could be a possible reason for the good agreement of our results with the power-law relation provided by Richardson and Zaki, while the vertical arrangement of particles in the dilute regime promotes a settling velocity higher than predicted by the power-law relation for a homogenous suspension.

We observed the presence of kinematic waves in the dense regime and we computed their velocities by means of an autocorrelation of the fluctuations in local vertical concentration of the sedimenting suspension. The results are found to be in good agreement with that predicted by Kynch theory. The origin of this agreement can be

attributed to two factors: an agreement with the assumptions of the theory and a trigger mechanism to initiate the propagation of kinematic waves. First, in the dense regime, particles exhibit a hard sphere distribution which is largely uniform and any local anisotropy in the particle concentration is limited to distances less than $2D_p$. Second, the settling velocity of the sedimenting suspensions are dependent on the local-concentration as indicated by the good agreement with the power-law relation presented by Richardson and Zaki, Eq. 2.1. We speculate that the slight increase in local horizontal concentration of particles could be the trigger that initiates the propagation of kinematic waves. Though the agreement with Kynch theory is good, the theory does not account for dispersion of particles within the suspension. It would therefore be interesting to extend this investigation to a more detailed analysis such as proposed by Jackson [79].

3

INERTIAL EFFECTS IN SEDIMENTING SUSPENSIONS OF SOLID SPHERES IN A LIQUID[1]

Particle-resolved Direct Numerical Simulations have been performed on the gravitational settling of mono-disperse solid spheres in a viscous fluid and triply periodic domain. In a comprehensive study, the bulk solid volume concentration was varied from $\phi = 0.5$ *to* 30%*. To study the effect of inertia, three different Galileo numbers were considered in the inertial regime,* $Ga = 144, 178$ *and* 210*, for which a single settling sphere exhibits distinctly different wake and path characteristics. The particle/fluid mass density ratio was fixed at 1.5. We find that for* $\phi = 2 - 30\%$ *the suspension microstructure and dynamics depend predominantly on the bulk concentration. In qualitative agreement with previous studies in literature, three different sedimentation regimes can be distinguished: (1) the dilute concentration regime for* $\phi \lesssim 2\%$ *with preferential settling of particles in vertical trains, (2) the moderate concentration regime for* $2\% \lesssim \phi \lesssim 10\%$ *with preferential settling of particles in horizontal pairs with an interparticle distance of* $\sim$ *1.5 particle diameters, and (3) the dense concentration regime for* $\phi \gtrsim 10\%$ *with a nearly random ("hard-sphere") distribution of the particles in space. The clustering of particles is dictated by, respectively, trapping of particles in the wake of other particles, a drafting-kissing-tumbling (DKT) instability by which two vertically aligned particles quickly reorient themselves into a horizontally aligned particle pair, and short-range multiparticle interactions through viscous lubrication and to a lesser extent collisions between particles. In all cases, hindered settling at a reduced speed is observed as compared to a single settling sphere. The well-known Richardson-Zaki relation for the mean sedimentation velocity appears valid only for the dense concentration regime. We provide ample evidence that in the dense regime the characteristic velocity and time scales*

[1] This chapter has been published as: T. Shajahan and W.-P. Breugem. Inertial effects in sedimenting suspensions of solid spheres in a liquid. International Journal of Multiphase Flow, 166:104498, 2023.

of particle motion are proportional to $\sqrt{gD_p}$ and $\sqrt{D_p/g}$, respectively, with g the gravitational acceleration and D_p the particle diameter. We also observe an ω^{-3} scaling of the particle velocity spectra for $\omega\sqrt{D_p/g} \gtrsim 0.4$ and we propose a model to explain this scaling behavior, based on the inertial response of the particles to small-scale flow perturbations. Kinematic waves, i.e., vertically propagating plane waves in the local concentration field, are observed in all cases, though unrelated particle motions are responsible for significant loss of the spatio-temporal coherence of the waves. The wave speed was determined from repeated space-time autocorrelations of the local concentration field and appears in reasonable agreement with Kynch sedimentation theory using the Richardson-Zaki relation. The passage of kinematic waves causes perturbations in the particle velocity at a frequency that matches well with peak frequencies in the particle velocity spectra for concentrations up to $\phi \approx 10\%$. The time-lagged crosscorrelation of the vertical and horizontal particle velocity suggests that kinematic waves may trigger DKT instabilities, while conversely DKT instabilities may be responsible for the onset of kinematic waves. Finally, we suggest that obstruction and perturbation of the particle wake by neighbouring particles could offer an explanation for the small influence of the Galileo number on the suspension behavior for $\phi = 2-30\%$.

3.1. INTRODUCTION

Sedimentation refers to the collective settling of particles under gravity or centrifugal forces. It is a commonly occurring process in nature and many industrial applications. Examples are deposition of sediments in rivers, sedimentation of volcanic ash, rainfall, settling basins in waste water treatment, land reclamation through spraying large amounts of sediments in, e.g., sea, and blood separation centrifuges. Sedimentation is also closely related to fluidisation, where an upward fluid flow exerts a hydrodynamic force on the particles such that their average settling velocity is zero and which has many applications in chemical industry. Provided that wall effects can be neglected and the particles are homogeneously fluidized, the two processes are dynamically similar, having the same relative particle/fluid velocity when the fluidisation velocity (flow rate divided by the crosssectional area of the fluidisation column) is equal to the average particle settling velocity in sedimentation [142, 9]. For many applications, it is desired to accurately predict the sedimentation or fluidisation velocity as function of particle concentration. For fluidized bed reactors, a homogeneous spatial particle distribution and strong fluid and particle mixing are typically desired too.

A large body of sedimentation literature has focused on sedimentation of small particles in the Stokes regime [33, 131, 100, 64, 69]. The complex particle-fluid and multi-particle interactions are responsible for chaotic particle behavior and limit a detailed analytical treatment of the problem except for very dilute sphere suspensions [12, 14]. Sedimentation of larger particles in the inertial regime (i.e., at a Reynolds number $Re_T > O(1)$, based on the terminal settling velocity and diameter of a single settling particle) has received comparatively less attention. The presence of inertial effects not only increases the complexity of the flow physics, detailed and well-controlled experiments are particularly challenging in this regime and it puts severe requirements on computational methods for accurate simulation of sedimentation. However, the devel-

opment of efficient methods for particle-resolved simulations [137, 116] and the ever increasing computing power have recently paved the way to study the influence of inertia on sedimentation in great detail.

In the present study we consider sedimentation of non-colloidal suspensions of spheres in a viscous and Newtonian fluid for which molecular forces such as Van der Waals and electrostatic forces as well as Brownian motion can be neglected. That is, we consider particle diameters $\gg 1\,\mu m$ and a large Péclet number related to Brownian particle motion [64]. From dimensional analysis it can be shown that the sedimentation dynamics of non-colloidal suspensions in free (unbounded) space is governed by the following three dimensionless numbers: (1) the Galileo number, $Ga = \nu_g D_p/\nu_f$, with $\nu_g = \sqrt{|\rho_p/\rho_f - 1|gD_p}$ the inertio-gravitational velocity, ρ_p the particle mass density, ρ_f the fluid mass density, g the gravitational acceleration, D_p the particle diameter, and ν_f the fluid kinematic viscosity, (2) the particle-to-fluid mass density ratio, ρ_p/ρ_f, and (3) the bulk solid volume fraction, ϕ. In literature, sometimes the terminal Reynolds number of a single settling particle is used instead of Ga to characterize the relative importance of fluid inertia over viscous forces and the two numbers are related to each other through $Re_T = \left(2/\sqrt{3C_d}\right) Ga$ with $C_d = C_d(Re_T)$ the sphere drag coefficient.

The seemingly simple case of a single sphere settling in free space exhibits already rich physics as has been explored in a number of comprehensive numerical studies [82, 192, 7] and extensive experimental campaigns [165, 76, 138]. While for $Ga \lesssim 155$, a sphere settles steadily in the vertical direction once it has reached its terminal velocity and exhibits an axi-symmetric wake, at $Ga \approx 155.6$ ($Re_T \approx 206.1$) and irrespective of the particle-to-fluid density ratio, the sphere wake undergoes a regular bifurcation and becomes planar symmetric [52], causing the particle to steadily rotate and settle down at a small inclination angle of a few degrees with respect to the vertical [192]. Upon further increasing the Galileo number, different transition scenarios exist dependent on the density ratio and thus on the influence of the fluid/solid coupling strength on the translational and rotational sphere dynamics [7]. At a density ratio around 1, the sphere undergoes a secondary Hopf bifurcation, displaying an oscillating oblique path and periodic vortex shedding from the wake. The wake then becomes irregular and transitions into a chaotic state for $Ga \gtrsim 200$, with the sphere settling on average in the vertical again, and with evidence of an intermediate periodic (vertical oscillating) state for $250 \lesssim Ga \lesssim 300$ [192, 138].

The collective settling of particles is generally characterized by hindered settling, i.e., a reduced settling speed with respect to a single settling particle. This originates on the one hand from the higher mixture mass density and thus larger Archimedes force, and on the other hand from the enhanced hydrodynamic drag on a particle from the nearby presence of other particles and the upward return flow of the fluid [9]. Hindered settling has already been studied over more than 80 years and many empirical correlations have been proposed [9, 62, 33]. Richardson and Zaki [142] proposed a simple

correlation that is widely used:

$$V_s = kV_T(1-\phi)^n, \tag{3.1}$$

where V_T is the terminal settling velocity of a single particle in free space, $n = n(Re_T, D_p/D_{pipe})$ with D_{pipe} the diameter of the sedimentation tube, and $k = 1$ for sedimentation and $log_{10}(k) = -D_p/D_{pipe}$ for fluidisation. (The difference in k value between sedimentation and fluidisation was attributed to the presence of a liquid velocity gradient near the wall in the latter; the presence of a wall breaks the similarity between the two processes.) Based on their experimental data, Richardson and Zaki proposed correlations for n, varying from $n = 4.65$ for the Stokes regime and when wall effects are negligible to $n = 2.39$ for $Re_T > 500$.

Theoretical support for Eq. (3.1) has been provided by Batchelor [12] who derived that $k = 1$ and $n = 6.55$ for a very dilute, statistically homogeneous and monodisperse suspension in the Stokes regime, while $n \approx 5.6$ when the spheres are slightly bidisperse in size at high Péclet number based on the relative sphere settling velocity [14, 34]. Garside and Al-Dibouni [62] critically evaluated Eq. (3.1) and proposed a single correlation for n, which varies from 5.1 for the Stokes regime down to 2.7 for the high-Reynolds regime. Moreover, they reported that Eq. (3.1) deviates from experimental data for concentrations below 10%, an effect most pronounced for the higher Reynolds number range. Here it should be noted that Richardson and Zaki actually didn´t do measurements for $\phi < O(5\%)$, but fitted Eq. (3.1) to the dense regime to determine n and kV_T, and divided the latter by a theoretical estimate of V_T to determine k.

The deviation of Eq. (3.1) from data for the dilute regime was noticed in many later studies [182, 54, 188, 150], with the deviation increasing for decreasing ϕ and increasing Re_T. Interestingly, based on particle-resolved simulations for $Re_T \simeq 1-20$ and $\rho_p/\rho_f = 2$, Yin and Koch [182] attributed the deviation for $\phi \lesssim 5\%$ to anisotropy of the suspension microstructure caused by inertial wake interactions between spheres, while the suspension microstructure was isotropic and exhibited a "hard-sphere" particle distribution [168, 64] for $\phi \gtrsim 5\%$ where Eq. (3.1) gave a good fit. The wake interaction between vertically oriented pairs of spheres was explained by a drafting-kissing-tumbling (DKT) phenomenon [59, 178, 80] present at finite Reynolds number. Shielded in the wake of the leading particle, the trailing particle experiences less drag and accelerates towards the leading particle ("drafting"), while simultaneously it experiences a shear-induced lift force [97]. When this lift force is not strong enough, the particles will eventually touch ("kissing"). Either way, irrespective whether actual contact is made or not, the particles will quickly move from a highly unstable vertical to a horizontal pair orientation and repel each other horizontally ("tumbling"). Yin and Koch suggested that particle tumbling is hindered by the nearby presence of other particles, explaining the observed enhanced likelihood of particle pairs to orient themselves horizontally at a distance of 2-2.5 particle diameters for $\phi = 1$ and 5% at $Re_T = 10$, while the prevalence of chaotic multi-particle interactions may explain the observed isotropic microstructure for $\phi = 20\%$. A similar tendency for horizontal particle alignment at moderate concentrations and an isotropic particle distribution for the dense regime was observed in

later studies [187, 68, 171, 149].

Compared to the isotropic microstructure in the dense regime, the enhanced drag from prevalent horizontal particle pairs in the lower concentration range may explain the steeper decrease in the sedimentation velocity with increasing concentration than expected from Eq. (3.1) [68]. Consistent with this, Yin and Koch found $k \approx 0.86-0.92$, which is thus smaller than $k = 1$ suggested by Richardson and Zaki but in agreement with $k \approx 0.8-0.9$ found from experiments [55, 54] and particle-resolved simulations [172, 171, 150]. Based on literature data and additional simulations for $Ga = 4.6-153.6$ and $\rho_p/\rho_f = 1.3-6$, Yao et al. [181] recently proposed a correlation of k in the form of an exponentially decaying function in Ga^2, which varies from $k = 0.89$ for $Ga \to 0$ to $k = 0.7$ for $Ga = 153.6$. They attributed the drop in k with increasing Ga to the influence of Ga on the frequency and lifespan of clusters that were quantified by means of Voronoï tessellation. The change in cluster formation was associated with appreciable particle wake interactions for the lowest Ga and the dominance of collisions over wake interactions for the highest Ga investigated.

Contrary to hindered settling, in several studies an increase in the settling speed has been reported for very dilute suspensions when Ga is sufficiently high [87, 86, 162, 187, 77, 57, 149]. This was first observed in particle-resolved simulations by Kajishima and Takiguchi [87] for $\phi = 0.2\%$, $Re_T = 350$ and 400 ($Ga \approx 243$ and 272) and $\rho_p/\rho_f = 8.8$ and 10, respectively, though particle rotation was ignored in their study for computational reasons. The enhanced settling speed was related to the formation of elongated vertical clusters with a lateral extent of $\sim 10D_p$ and a life time of several particle response times. They attributed the formation of clusters to wake trapping of particles in the unsteady wakes of other particles and the breakup of clusters to turbulent stresses that are intensified by the presence of clusters. Finally, their results suggest a threshold Reynolds number of around 200 ($Ga \approx 154$) for vertical cluster formation and enhanced settling. In a follow-up study, Kajishima [86] studied the effect of particle rotation and concentration on cluster formation at $Re_T = 300$ ($Ga \approx 214$) and $\rho_p/\rho_f = 8.8$. When rotation is accounted for, no vertical clusters were formed at $\phi = 0.05\%$, while clusters and an enhanced settling speed of $\sim 20\%$ was observed for $\phi = 0.1-0.4\%$. Furthermore, particle rotation was responsible for a shorter lifetime and irregular formation of clusters, which was attributed to the rotation that particles obtain in the high shear zones surrounding the clusters and the resulting Magnus lift force that tends to expel particles from the clusters.

The results of Kajishima and Takiguchi [87] and Kajishima [86] were corroborated by particle-resolved simulations of Uhlmann and Doychev [162] for $Ga = 121$ and 178, $\rho_p/\rho_f = 1.5$ and $\phi = 0.5\%$. While particles were nearly randomly distributed in space for $Ga = 121$ and settled on average at approximately the same speed as a single settling particle, elongated vertical clusters with a lateral extent of $\sim 10D_p$ were formed for $Ga = 178$ and the average settling speed was enhanced by about 12%. They attributed the formation of these vertical clusters to particle wake attraction related to the DKT mechanism, though Yin and Koch [182] invoked the same DKT mechanism to explain

the reduced likelihood of finding vertical particle pairs and the higher likelihood of finding horizontal particle pairs in their simulations at lower Ga and higher ϕ. Based on the critical Ga for transition of the wake and path of a single settling sphere from axisymmetric and vertical to plane symmetric and oblique, Uhlmann and Doychev [162] conjectured that the threshold Galileo number for the emergence of the vertical clusters is approximately 155 related to the enhanced likelihood of particles to encounter each other when they are settling in an oblique fashion. Experimental evidence of vertical cluster formation and enhanced settling was provided by Huisman et al. [77] for $Ga = 110-310$, $\rho_p/\rho_f = 2.5$ and $\phi = 0.02-0.1\%$ with a maximum speed increment of 25% found for $Ga = 170$ and $\phi = 0.05\%$. Contrary to the conjecture of Uhlmann and Doychev [162] also an enhanced settling speed of up to 19% was found for $Ga = 110$, though Huisman et al. noted that their results may have been biased by the presence of a large-scale flow circulation induced by the settling of the particles in the middle of their settling tank. Particle-resolved simulations by Zaidi et al. [187] showed significantly enhanced settling for $\phi = 0.5$ and 1%, $\rho_p/\rho_f = 2.5$ and $Re_T \geq 175$. The latter condition corresponds to $Ga \geq 138$, thus well below 155.

Table 3.1: Overview of the investigated parameter ranges in particle-resolved DNS studies of fluidisation and sedimentation in free space (no walls) of non-colloidal monodisperse spheres in the inertial regime ($Ga \gg 1$). Studies are ordered by the highest investigated Ga value. When Ga was not provided in the reference, it was estimated from Re_T using Abraham's empirical correlation for the drag coefficient [1], and vice versa when only Ga was provided. (*) Density ratio was not explicitly mentioned, but presumed here to be 2.5 based on earlier publication of the same lead author.

Literature reference	Ga	Re_T	ϕ (in %)	ρ_p/ρ_f
Climent and Maxey [28]	1.4−18.1	0.1−10	0.3−12	0.9−5
Hamid et al. [68]	0.97−18.1	0.05−10	1−40	5
Yin and Koch [183]	2.0−28.3	0.2−20	1,20	2
Yin and Koch [182]	4.6−28.5	1−20	0.5−40	2
Zaidi et al. [188]	1.4−53.4	0.1−50	0−40	2.5 (*)
Esteghamatian et al. [51]	59.4	57.9	∼ 47	10
Willen et al. [172, 171]	49.7−99.4	43.3−110.8	8.7−34.9	2−5
Shajahan and Breugem [150]	144	185.9	0.5−30	1.5
Fornari et al. [57]	144.9	188	0.5,1	1.02
Yao et al. [181]	4.6−153.6	0.95−200.0	22−43	1.3−6
Seyed-Ahmadi and Wachs [149]	70,160	72.4,210.3	1−20	2
Uhlmann and Doychev [162]	121,178	141.6,260.6	0.5	1.5
Fornari et al. [56]	19−200	10.8−276.5	0.5	1.02
Zaidi et al. [187]	4.7−214.0	1−300	0.5−5	2.5
Kajishima [86]	214.0	300	0.05−0.4	8.8
Zaidi et al. [186]	3.2−272.2	0.5−400	1−20	2.5 (*)
Kajishima and Takiguchi [87]	53.4−272.2	50−400	0.2	8.8,10
Present study	144−210	185.9−290.4	0.5−30	1.5

From the above literature discussion, it is clear that flow inertia may have a profound effect on the suspension microstructure and the flow dynamics, in particular in the lower concentration range. Compared to the moderate Ga regime, only few studies have yet addressed the effect of flow inertia for $Ga > 100$ for a wide range in ϕ, see the overview of particle-resolved Direct Numerical Simulation (DNS) studies of the inertial regime in table 3.1.

In a previous study for $Ga = 144$, $\rho_p/\rho_f = 1.5$ and ϕ varying from 0.5-30% [150], we observed three different settling regimes with a different suspension microstructure: a dilute concentration regime for $\phi \lesssim 1\%$, a moderate concentration regime for $1 \lesssim \phi \lesssim 10\%$, and a dense concentration regime for $\phi \gtrsim 10\%$, with a preference of particles to settle in vertically aligned clusters, horizontally aligned pairs and a nearly isotropic fashion, respectively. Little is yet known about how the microstructure and related flow dynamics will change when increasing Ga and how this will affect the transition between flow regimes when the concentration is varied. In the present study, we aim to gain understanding of the structure and dynamics of sedimenting suspensions by (1) examining the competing influences of wake trapping, drafting-kissing-tumbling and multiparticle interactions, and (2) by examining the influence of inertia by varying Ga for a wide range of concentrations. Partially motivated by earlier studies of Uhlmann and Dušek [163] and Uhlmann and Doychev [162], we have chosen 3 different Galileo numbers, $Ga = 144$, 178 and 210, at a fixed density ratio of $\rho_p/\rho_f = 1.5$. For a single settling particle in free space, these values are a priori expected to correspond to a steady vertical settling path at $Ga = 144$ with $Re_T \approx 184$, a steady oblique settling path at $Ga = 178$ and $Re_T \approx 240$, and an oscillating oblique or chaotic settling path at $Ga = 210$ and $Re_T \approx 293$ [192].

For our study, we employed particle-resolved DNS to simulate sedimentation of spheres in a triply periodic computational domain at $\phi = 0.5 - 30\%$ and the chosen Ga values. The case of $\phi = 0.5\%$ was simulated only for $Ga = 144$ as to check whether or not vertical particle clustering would result in an enhanced settling speed in this case as Uhlmann and Doychev [162] suggested that $Ga \gtrsim 155$ is required for this. The lowest concentration considered for $Ga = 178$ and 210 is $\phi = 2\%$ as the focus of the present study is primarily on the moderate and dense concentration regime. The DNS is based on an Immersed Boundary Method for the fluid/solid coupling [18] in combination with a soft-sphere collision model for frictional particle collisions [29]. A few results for $Ga = 144$ from our previous study [150] are included in the present study for the sake of comparison with the other Ga.

We present results for the suspension microstructure by means of particle-conditioned averages, particle statistics such as the mean and root-mean-square (rms) velocities of the particles and fluid phase, probability density functions (pdfs) of the particle velocity, and particle velocity correlations and related frequency (energy) spectra. We also examine the role of particle collisions by analysing the particle force balance. Finally, we analyse the properties of so-called kinematic waves [98, 85, 10, 99, 78], i.e., vertically propagating plane waves in the local concentration with a relatively small amplitude,

which we observed before in our previous study for $Ga = 144$ [150]. Recently, Willen et al. [172] analysed the characteristics of kinematic waves in DNS of a homogeneously fluidized bed for $Ga = 50-99$, $\rho_p/\rho_f = 2-5$ and $\phi = 8.7-34.9\%$. The wave speed was found to be in good agreement with Kynch theory [98] in combination with the Richardson-Zaki correlation, Eq. (3.1), for the sedimentation velocity. Based on a truncated spatial Fourier series reconstruction, they demonstrated the footprint of propagating concentration waves on the vertical fluid velocity. In the present study we will adopt a different method to analyse kinematic waves based on repeated space-time autocorrelations of the local concentration field, which avoids the need to apply filtering in wavenumber space. Fortes et al. [59] (p. 468) suggested that particle aggregation associated with DKT interactions may cause propagation of 'voidage cracks' in fluidisation and we will explore this idea in the present sedimentation study with regard to kinematic waves.

The remainder of this manuscript is organized as follows. In section 3.2 we provide details on the computational method and setup used in the DNS. In section 3.3 we present results for a single settling sphere at the three chosen Galileo numbers. In section 4.6 the results are discussed for sedimenting suspensions. Finally, in section 3.5 we summarize the conclusions and provide a discussion of our main findings.

3.2. COMPUTATIONAL SETUP

3.2.1. GOVERNING EQUATIONS AND COLLISION MODEL

The physics of the fluid phase and the particle dynamics are governed by the Navier-Stokes and Newton-Euler equations, respectively. We use the following inertial scales to non-dimensionalize these equations: $l_{ref} = D_p$, $u_{ref} = \sqrt{gD_p}$, $t_{ref} = l_{ref}/u_{ref}$, $p_{ref} = \rho_f u_{ref}^2$ and $a_{ref} = u_{ref}^2/l_{ref}$. The non-dimensional Navier-Stokes equations for an incompressible and Newtonian fluid are then given by:

$$\nabla\cdot\mathbf{u}_f = 0, \tag{3.2a}$$

$$\frac{\partial\mathbf{u}_f}{\partial t}+\nabla\cdot\mathbf{u}_f\mathbf{u}_f = -\nabla p_h-\nabla p+\frac{1}{\sqrt{gD_p^3/\nu_f^2}}\nabla^2\mathbf{u}_f, \tag{3.2b}$$

where $\mathbf{u}_f$ is the fluid velocity and p is the total fluid pressure excluding the contributions from the weight per unit volume of the fluid and the net weight per unit volume of the suspended particles, p_h. Note that $\sqrt{gD_p^3/\nu_f^2} = Ga/\sqrt{\rho_p/\rho_f-1}$. The gradient of p_h is equal to $\nabla p_h = \left(\rho_p/\rho_f-1\right)\phi\tilde{\mathbf{g}}$, where $\tilde{\mathbf{g}}$ is a dimensionless unit vector pointing in the direction of gravity. The linear velocity, $\mathbf{u}_p$, and the angular velocity, $\boldsymbol{\omega}_p$, of a particle are described by the Newton-Euler equations, which for non-colloidal solid spheres are given by:

$$\left(\frac{\rho_p}{\rho_f}\frac{\pi}{6}\right)\frac{d\mathbf{u}_p}{dt} = \oint_{A_p}\boldsymbol{\tau}_f\cdot\mathbf{n}\,dA+\frac{\pi}{6}\left(\frac{\rho_p}{\rho_f}-1\right)\left(1-\phi\right)\tilde{\mathbf{g}}+\mathbf{F}_c, \tag{3.3a}$$

$$\left(\frac{\rho_p}{\rho_f}\frac{\pi}{60}\right)\frac{d\boldsymbol{\omega}_p}{dt} = \oint_{A_p}\mathbf{r}\times(\boldsymbol{\tau}_f\cdot\mathbf{n})\,dA+\mathbf{T}_c, \tag{3.3b}$$

where $\boldsymbol{\tau}_f$ is the stress tensor for a Newtonian fluid defined as:

$$\boldsymbol{\tau}_f = -p\mathbf{I} + \left(1/\sqrt{gD_p^3/\nu_f^2}\right)(\nabla\mathbf{u}_f + \nabla\mathbf{u}_f^T)$$

with $\mathbf{I}$ the unit tensor, $\mathbf{r}$ is the position vector relative to the centroid of the particle, $\mathbf{n}$ is the outward-pointing unit normal on the particle surface (A_p), and $\mathbf{F}_c$ and $\mathbf{T}_c$ are the collisional force and torque, respectively. Eqs. (3.2a)-(3.3b) are coupled with each other through the no-slip/no-penetration condition at the surface of the particles:

$$\mathbf{u}_f = \mathbf{u}_p + \boldsymbol{\omega}_p \times \mathbf{r} \quad \text{at } \mathrm{A}_p\,. \tag{3.4}$$

Collisions between particles are modeled using a frictional soft-sphere collision model described in detail by Costa et al. [29]. In this model the rigid particles are allowed numerically to overlap slightly. A linear spring-dashpot model is used in which the collision force is computed from the overlap and relative velocity between the particles. The model accounts for transition from the stick to the slip regime dependent on the ratio of the tangential to the normal component of the collision force. The spring stiffness and damping coefficients for the normal and tangential collision force components are expressed in terms of four model parameters [72]: the dry normal and tangential (or rotational) coefficients of restitution, $e_{n,dry}$ and $e_{t,dry}$, respectively, the Coulomb coefficient of sliding friction, μ_c, and the collision duration, T_c. Joseph and Hunt [84] experimentally determined that $e_{n,dry} = 0.97$, $e_{t,dry} = 0.39$ and $\mu_c = 0.15$ for the oblique impact of a glass particle on a thick Zerodur (glass-like) wall in both air and an aqueous glycerine solution. We took the same values for our collision parameters with the exception of $e_{t,dry}$, which was set to 0.1; the lower value effectively promotes transition to the slip regime. The collision duration is a numerical parameter. In order to accurately resolve collisions in time, it was artificially stretched to $T_c = 8\Delta t$ with Δt the computational time step [29].

As will be explained in the section 3.2.2, the present DNS makes use of a fixed Cartesian grid for the fluid phase. Hydrodynamic interactions between particles are resolved as long as the distance between particle interfaces is larger than $O(\Delta x)$ with Δx the grid spacing; the associated interaction force and torque are included in the first term at the right-hand side of Eqs. (3.3a) and (3.3b), respectively. For distances smaller than the grid spacing, the normal interaction force between particles is increasingly underestimated as the flow in the intervening gap between the particles is not sufficiently resolved anymore. To compensate for this, a lubrication correction force is added to the right-hand side of Eq. (3.3a) when the distance between particle interfaces drops below a grid-dependent threshold value. The correction is based on an asymptotic analytical expression for the lubrication force for the normal approach between two equal solid spheres in the Stokes regime [29, 32]. As the analytical correction force approaches infinity in the limit of zero gap width, the diverging behavior is capped when the gap width drops below a threshold distance of $5 \cdot 10^{-4} D_p$, which can be associated with the typical height of roughness asperities on the surface of the particles [84].

3.2.2. NUMERICAL METHOD, INITIALISATION AND FLOW PARAMETERS

The DNS is based on the computationally efficient Immersed Boundary Method (IBM) of Breugem [18] for the particle/fluid coupling, which is a modified version of the original IBM introduced by Uhlmann [160]. The IBM makes use of two different grids: a fixed Eulerian grid for the fluid phase and a Lagrangian grid on the surface of every particle and moving with the particle. A key ingredient of the IBM is that the no-slip/no-penetration condition given by Eq. (3.4), is not imposed in a direct manner, but forces are added locally near the particle's surface to enforce this condition by good approximation. The additional IBM force, **f**, is added to the right-hand side of the fluid momentum equation (3.2b). The present IBM falls in the class of direct-forcing methods [53] and is embedded in the predictor-corrector scheme used to integrate the Navier-Stokes equations. The force is calculated using a regularized delta-function approach in which the regularized delta function proposed by Roma et al. [145] is used to first interpolate the provisional fluid velocity from the Eulerian to the Lagrangian grid, then the IBM force is computed on the Lagrangian grid such that the corrected velocity will fulfill the no-slip/no-penetration condition, and finally the IBM force is spread back from the Lagrangian to the Eulerian grid using the same regularized delta function. From the force distribution on the Lagrangian grid, the overall hydrodynamic force and torque acting on the particle are computed. The IBM contains a multi-direct forcing scheme [112] to reduce the error in the enforced no-slip/no-penetration condition caused by overlapping interpolation kernels from neighbouring Lagrangian grid points. Furthermore, the Lagrangian surface grid is slightly retracted towards the interior of the particle over a distance of $0.3\Delta x$ to compensate for the finite width of the interpolation kernels. This improves the accuracy of the overall method. The reader is referred to Breugem [18] for further details and validation of the present IBM.

The three-step Runge-Kutta method of Wray [169] is used to integrate the Navier-Stokes and Newton-Euler equations in time. The computational time step, Δt, is dynamically adjusted to ensure numerical stability. The Navier-Stokes equations are discretized in space on a fully staggered Cartesian grid. The central-differencing scheme is used to approximate spatial gradients. The computational domain is a triply periodic rectangular box. Gravity is acting in the negative y-direction.

At the start of the simulations, the particles are randomly placed in the domain subject to the criterion that they must not overlap with each other. The particles and fluid phase are initialised with zero velocity. When the particles start to fall downwards by the action of gravity, a return fluid flow co-develops by virtue of the imposed hydrostatic pressure gradient in Eq. (3.2b). Within a few tens of time units $\sqrt{D_p/g}$, the flow reaches a statistically steady state in which the average particle velocity is slightly fluctuating in time around a constant value. The imposed hydrostatic pressure gradient then balances the submerged weight of the suspension and the overall mixture (fluid+particles) velocity is zero. The zero bulk mixture velocity mimics the virtual presence of a bottom wall as in a batch sedimentation process. The statistics shown later in this manuscript have been calculated for $t > 50\sqrt{D_p/g}$ to ensure that a statistically steady state was reached in all simulations.

As mentioned in the introduction section, we performed a parametric study in which we varied the Galileo number and the bulk solid volume fraction. The particle-to-fluid mass density ratio was fixed at a value of 1.5. In total 25 different sedimentation cases have been simulated. The simulation parameters are listed in Table 3.2.

Table 3.2: Physical parameters and computational settings used in the present parametric DNS study: Ga is the Galileo number, ϕ is the global solid volume fraction, N_p is the number of particles in the computational domain, $L_x \times L_y \times L_z$ are the dimensions of the computational domain, $D_p/\Delta x$ is a measure for the grid resolution, and T_{obs} is the duration of the observation interval over which statistics were obtained.

Ga	ϕ	N_p	$L_x \times L_y \times L_z$	$D_p/\Delta x$	$T_{obs}/\sqrt{D_p/g}$
144	0.005	2686	$37.5D_p \times 200D_p \times 37.5D_p$	16	2157
	0.02	2388	$25D_p \times 100D_p \times 25D_p$	16	2134
	0.04	4775	$25D_p \times 100D_p \times 25D_p$	16	1036
	0.06	7163	$25D_p \times 100D_p \times 25D_p$	16	1046
	0.08	9549	$25D_p \times 100D_p \times 25D_p$	16	1060
	0.10	11936	$25D_p \times 100D_p \times 25D_p$	16	1060
	0.15	17903	$25D_p \times 100D_p \times 25D_p$	16	1143
	0.20	23871	$25D_p \times 100D_p \times 25D_p$	16	1154
	0.25	29838	$25D_p \times 100D_p \times 25D_p$	16	1144
	0.30	35806	$25D_p \times 100D_p \times 25D_p$	16	1134
178	0.02	2388	$25D_p \times 100D_p \times 25D_p$	24	1367
	0.04	4775	$25D_p \times 100D_p \times 25D_p$	24	684
	0.06	7163	$25D_p \times 100D_p \times 25D_p$	24	706
	0.08	9549	$25D_p \times 100D_p \times 25D_p$	24	727
	0.10	11936	$25D_p \times 100D_p \times 25D_p$	24	735
	0.15	17903	$25D_p \times 100D_p \times 25D_p$	24	753
	0.20	23871	$25D_p \times 100D_p \times 25D_p$	24	745
	0.25	29838	$25D_p \times 100D_p \times 25D_p$	24	731
	0.30	35806	$25D_p \times 100D_p \times 25D_p$	24	729
210	0.02	2388	$25D_p \times 100D_p \times 25D_p$	24	983
	0.06	7163	$25D_p \times 100D_p \times 25D_p$	24	673
	0.10	5968	$25D_p \times 50D_p \times 25D_p$	24	693
	0.20	11936	$25D_p \times 50D_p \times 25D_p$	24	693
	0.25	14919	$25D_p \times 50D_p \times 25D_p$	24	768
	0.30	17903	$25D_p \times 50D_p \times 25D_p$	24	713

Note that the domain height in case A1 was set to 200 particle diameters, which is 2-4 times larger than in the other cases. This was done for two reasons. Firstly, to improve convergence of particle statistics by increasing the number of particles in the domain for this case with the lowest bulk concentration. Secondly, to accommodate large-scale columnar structures present at this bulk concentration [150]. We checked *a posteriori* for all cases that the domain height was much larger than the estimated ver-

tical distance over which fluctuations in the vertical particle velocity are decorrelated, see Shajahan and Breugem [150] where a prior analysis is presented for $Ga = 144$. A higher grid resolution was used for $Ga = 178$ and 210 than for $Ga = 144$, in order to sufficiently resolve the flow field at the higher Galileo and hence higher Reynolds numbers. The chosen grid resolutions for the different Galileo numbers were motivated by a previous numerical study of Uhlmann and Dušek [163] in which they analysed the grid sensitivity of their DNS/IBM results for gravitational settling of a single particle at the same density ratio and for a similar range in Galileo number as considered in the present study. The grid resolution of the Lagrangian grid was chosen to match as closely as possible the resolution of the Eulerian grid, corresponding to 746 and 1721 Lagrangian grid cells for $D_p/\Delta x = 16$ and 24, respectively.

3.3. SINGLE SETTLING PARTICLE IN FREE SPACE

For each investigated Galileo number, an additional simulation was performed of a single settling particle in free space to determine the terminal settling velocity of an individual particle and to validate the DNS code. The size of the rectangular computational domain and the grid resolution are listed in Table 3.3. Prescribed inflow and convective outflow boundary conditions were applied in the vertical y-direction and periodic boundary conditions were imposed in the horizontal x and z directions. The initial centroid position of the particle was set to $x = L_x/2$, $y = 9D_p$ and $z = L_z/2$. A moving frame of reference was used in which the inflow velocity was set slightly higher than the expected terminal settling velocity of the particle. This was done in order to track the particle motion over a sufficiently long time to capture the development of possible wake and sphere path instabilities. Following the procedure used by Uhlmann and Dušek [163], during the first part of the simulation the particle was fixed in space till the flow around the particle was fully developed. Then the simulation was restarted and the particle was allowed to move freely during the second part of the simulation. The terminal settling velocity was determined from the difference between the vertical particle drift velocity and the prescribed inlet velocity.

Table 3.3: Computational settings, terminal settling velocity and terminal Reynolds number obtained from DNS of a single settling particle with a particle-to-fluid density ratio of 1.5. Ga is the Galileo number, $L_x \times L_y \times L_z$ is the domain size, $D_p/\Delta x$ is a measure for the grid resolution, $V_T/\sqrt{gD_P}$ is the normalised terminal settling velocity in the vertical direction, and Re_T is the terminal settling Reynolds number. The last three columns show Re_T obtained from, respectively, the present DNS, the spectral/spectral-element simulations of Uhlmann and Dušek [163] for their largest domain size, and the expected values using Abraham's correlation for the drag coefficient [1].

Ga	$L_x \times L_y \times L_z$	$D_p/\Delta x$	$V_T/\sqrt{gD_P}$	Re_T	Re_T ([163])	Re_T ([1])
144	$22D_p \times 30D_p \times 22D_p$	16	-0.913	185.9	185.1	184.5
178	$22D_p \times 30D_p \times 22D_p$	24	-0.953	239.8	243.0	239.8
210	$22D_p \times 30D_p \times 22D_p$	24	-0.978	290.4	-	293.3

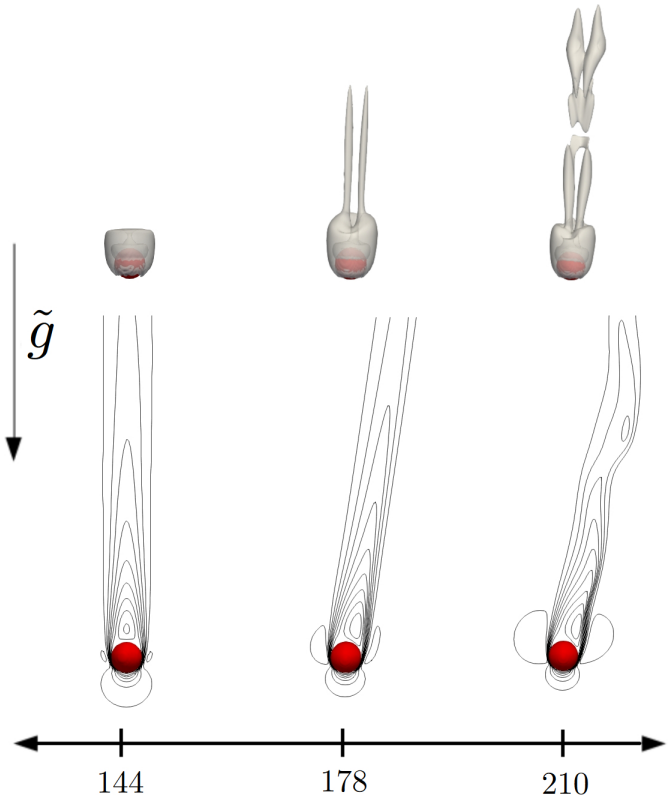

Figure 3.1: Visualisation of the instantaneous flow field around a single particle settling in free space for $Ga = 144$, 178 and 210. Top panels show the $\lambda_2 = -0.015$ isocontour of the λ_2 vortex identification criterion [83]. Bottom panels show isocontours of the relative fluid velocity ranging from $-0.2\sqrt{gD_p}$ to $1.0\sqrt{gD_p}$ (see main text for a more detailed explanation).

Similar to Uhlmann and Dušek [163], Fig. 3.1 shows visualisations of the fully developed flow field around the freely settling particle for each Galileo number. The top panels show visualisations in terms of the λ_2 vortex identification criterion [83]. For the vertical plane passing through the particle centroid and parallel to the particle velocity, the bottom panels show isocontours of the vertical fluid velocity relative to the particle. At $Ga = 144$ the particle falls steadily downwards along the vertical and exhibits an axisymmetric wake. At $Ga = 178$ the particle settles steadily along a slightly oblique trajectory at an angle of approximately 7.1° with the vertical. The wake is no longer axisymmetric, but plane symmetric, and contains two characteristic vortex threads. Consistent with the presence of a skewed wake, the particle rotates steadily along a horizontally aligned axis with an angular velocity of approximately $0.052\sqrt{g/D_p}$ (in the clockwise direction for the plane shown in Fig. 3.1). Finally, at $Ga = 210$ the particle shows periodic wake shedding with an oscillation period of $7.3\sqrt{D_p/g}$. This is accompanied by a small periodic oscillation of the inclination angle at which the particle is falling, varying in the range of $9.6 - 9.9°$. The flow visualisations for $Ga = 144$ and 178

are in good agreement with the numerical results presented by Uhlmann and Dušek [163] for the same Galileo numbers based on spectral/spectral-element simulations and simulations based on an IBM similar to the one presently used. Minor differences can be attributed to differences in domain size, grid resolution, boundary conditions and accuracy of the methods used. The case of $Ga = 210$ was not investigated by them, but they did simulate the case of $Ga = 190$, which exhibits similar oscillatory behavior.

For all three Galileo numbers, the values for the terminal settling velocity, $V_T/\sqrt{gD_p}$, and the corresponding terminal Reynolds number, $Re_T = |V_T|D_p/\nu_f$, are shown in Table 3.3. Good agreement is found with the results from the spectral/spectral-element simulations of Uhlmann and Dušek [163] for $Ga = 144$ and 178. The table also includes the expected terminal Reynolds number from the balance between the submerged weight of the particle and the steady hydrodynamic drag force using Abraham's empirical correlation for the drag coefficient [1]. Again, good agreement is found for all Ga values, which demonstrates the accuracy of our simulations for the chosen grid resolutions.

3.4. DNS RESULTS FOR SEDIMENTING SUSPENSIONS

3.4.1. INSTANTANEOUS SPATIAL PARTICLE DISTRIBUTION

Snapshots of the instantaneous spatial particle distribution are shown in Fig. 3.2 for $\phi = 6\%$, 20% and 30% for each investigated Galileo number. For a compact representation, only part of the flow domain is shown ($25D_p \times 50D_p \times 6.25D_p$). The particles are colored by their instantaneous vertical velocity normalised with the mean sedimentation velocity, V_s. A discrete colorbar is used to distinguish between four groups of particles: particles settling at a velocity higher than the mean with $v_p/V_s > 1.25$ (red color), particles settling around the mean in the range of $0.75 < v_p/V_s < 1.25$ (yellow), particles settling at a velocity less than the mean with $0 < v_p/V_s < 0.75$ (blue), and particles moving in the upward direction, $v_p/V_s < 0$ (green).

The snapshots clearly show that in all cases a large number of particles settle at a velocity significantly lower or higher than the mean. Also, the slower and faster moving particles are seemingly segregated in space and contained in relatively large-scale structures with a spatial dimension $\gg D_p$. A small amount of particles appears to move even in the upward direction. The relative fraction of upward moving particles increases with increasing bulk concentration as will be analysed in more detail in subsection 3.4.5. This likely originates from a locally strong return flow of the fluid, which may drag some particles along in the upward direction. Hydrodynamic particle interactions and particle bouncing after collisions might also cause individual particles to move instantaneously upward. Finally, we remark that no clear effect of the Galileo number can be discerned from the snapshots in contrast with the Ga-dependent wake dynamics of a single settling particle discussed in the previous section. For a more in-depth analysis of particle clustering and effects of Ga on this, we present results for the suspension microstructure by means of the particle-conditioned average concentration and flow field in the next subsection.

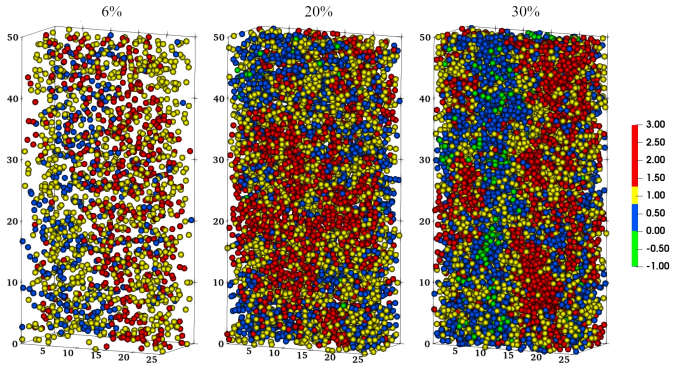

(a)

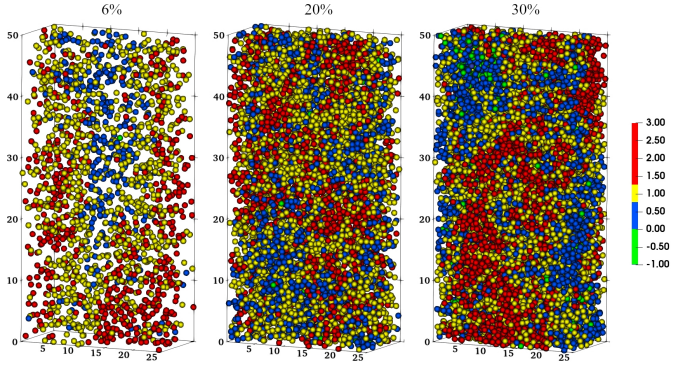

(b)

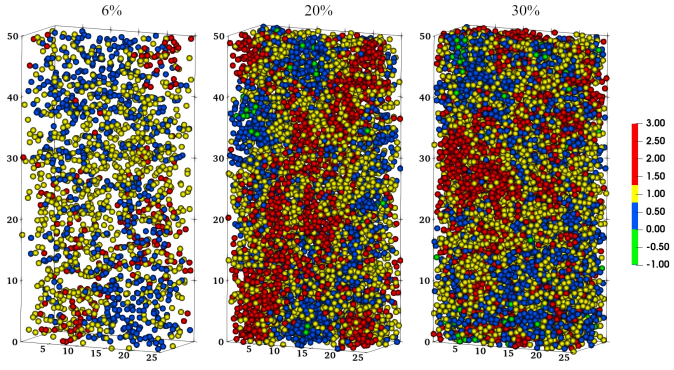

(c)

Figure 3.2: Instantaneous snapshots of the spatial particle distribution in sedimenting suspensions as function of Galileo number and bulk concentration (indicated by the numbers on top of the panels). The particles are colored by their vertical velocity normalised with the mean sedimentation velocity, v_p/V_s. Note that $v_p > 0$ (upward moving particle) corresponds to $v_p/V_s < 0$ as $V_s < 0$. ((a)) $Ga = 144$, ((b)) $Ga = 178$, ((c)) $Ga = 210$.

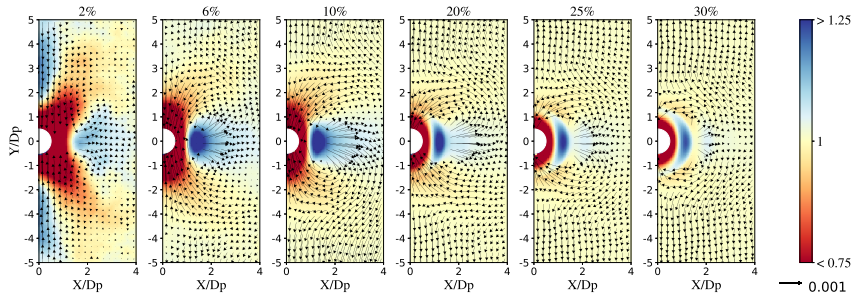

(a)

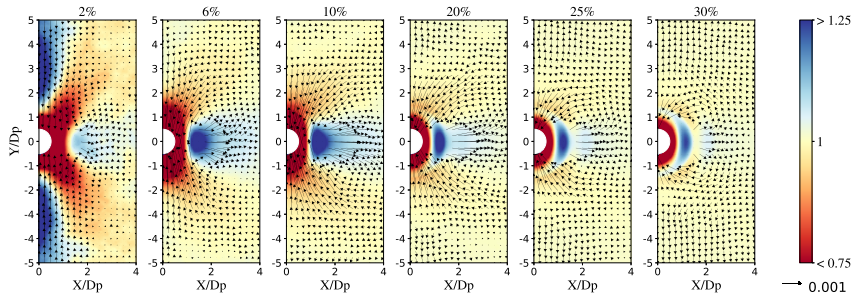

(b)

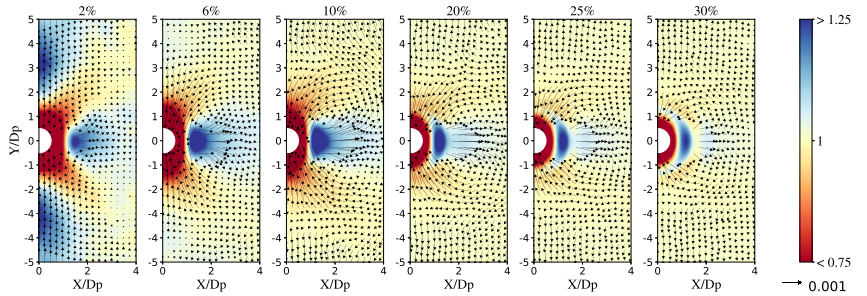

(c)

Figure 3.3: Particle-conditioned average concentration field in the vertical plane through the reference particle centroid and normalised with the bulk concentration, $\overline{\gamma}/\phi$. The vectors represent the PCA relative particle velocity field. For clarity, the vectors within a radial distance of $1.5D_p$ of the reference particle centroid have been omitted as they are much larger than the vectors further away from the reference particle. The reference vector below the color legend has a magnitude of $0.001\sqrt{gD_p}$. Because of mirror symmetry only $x/D_p \geq 0$ is shown. The concentration is increasing from left to right from $\phi = 2-30\%$. ((a)) $Ga = 144$, ((b)) $Ga = 178$, ((c)) $Ga = 210$.

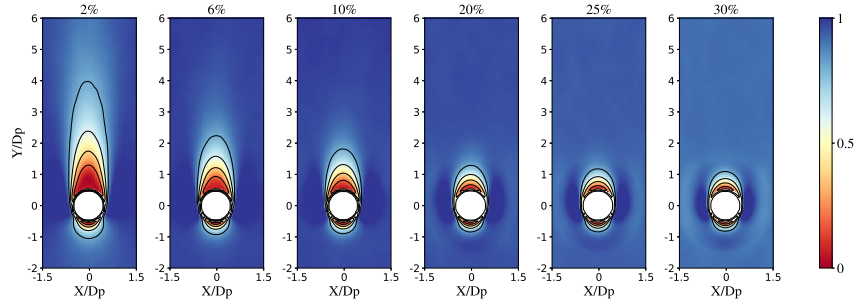

(a)

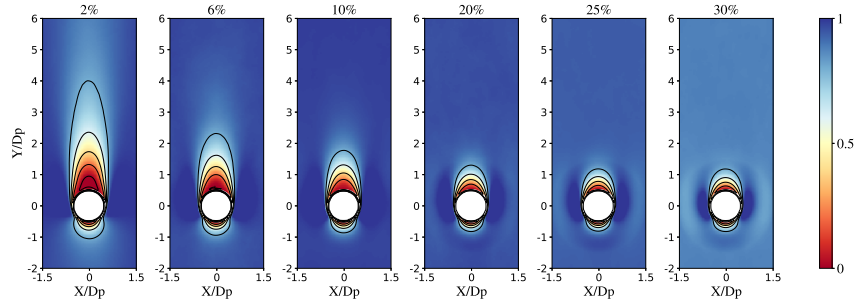

(b)

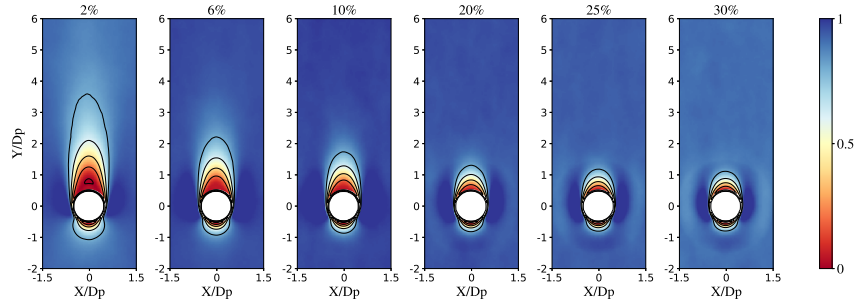

(c)

Figure 3.4: Particle-conditioned average fluid flow field in the vertical plane through the reference particle centroid and normalised with the mean relative fluid velocity, $V_r = V_s - V_f$. The solid lines are isocontours varying from 0 to 0.8 at intervals of 0.2. The concentration is increasing from left to right from $\phi = 2 - 30\%$. ((a)) $Ga = 144$, ((b)) $Ga = 178$, ((c)) $Ga = 210$.

3.4.2. SUSPENSION MICROSTRUCTURE

The particle-conditioned average (PCA) concentration field has been computed in the same way as in our previous study [150]. First, we computed the spatial distribution of the instantaneous solid phase indicator function around each particle, $\gamma(\mathbf{x} - \mathbf{x}_c, t)$, in two mutually perpendicular and vertically oriented planes passing through the particle centroid at $\mathbf{x}_c(t)$. Here we define γ as the local solid volume fraction in a grid cell,

which varies between 0 for cells located fully inside the fluid phase and 1 for cells contained fully inside particles. The 2D spatial distributions of γ were then averaged over all particles and time, and, because of statistical symmetry, also over the two mutually perpendicular planes to obtain the PCA concentration field, $\overline{\gamma}(\mathbf{x}-\mathbf{x}_c)$, where the bar denotes the statistical average. A similar procedure was used to compute the PCA relative particle and fluid velocity fields, defined by $\overline{\gamma[\mathbf{u}_p(\mathbf{x}-\mathbf{x}_c,t)-\mathbf{u}_p(\mathbf{x}_c,t)]}/\overline{\gamma}$ and $\overline{(1-\gamma)[\mathbf{u}_f(\mathbf{x}-\mathbf{x}_c,t)-\mathbf{u}_p(\mathbf{x}_c,t)]}/\overline{(1-\gamma)}$, respectively.

Figure 3.3 presents the PCA concentration field in the vertical plane through the reference particle centroid as function of bulk concentration and Galileo number. The local mean concentration is normalised with the bulk concentration to highlight regions with higher (blue) and lower (red) than average concentration. The vectors show the PCA relative particle velocity field. At first sight, the PCA concentration field does not vary much with the Galileo number and depends predominantly on the bulk concentration. At $\phi = 2\%$, we observe a clear tendency for vertical aggregation of particles. This is most pronounced at $Ga = 178$ and extends from $y/D_p \simeq 1.5-5$. At all three Galileo numbers, this is accompanied by an elevated concentration in the lateral direction around a spot centered at $x/D_p \simeq 1.5$ and fading away for larger x. At $\phi = 2\%$ particles thus show an enhanced likelihood to settle in vertical trains of several particle diameters long as well as in a pairwise side-by-side motion. The relative particle velocity field shows the tendency of vertically aligned particles to move towards the reference particle, consistent with the wake-trapping mechanism. At close encounter with the reference particle, a DKT-type instability seems to be responsible for a quick reconfiguration of vertically aligned particles towards horizontal side-by-side motion, consistent with the local pattern in the relative particle velocity and a characteristic X-shaped region near the reference particle with a lower than average concentration.

Interestingly, not shown here but discussed in Shajahan and Breugem [150], the tendency of particles to aggregate in the vertical is even much more pronounced for $\phi = 0.5\%$ and $Ga = 144$, where the particle clusters are alike the columnar structures reported by Uhlmann and Doychev [162] for $\phi = 0.5\%$ and $Ga = 178$. Contrary to $\phi = 2\%$, this is accompanied by a significantly less likelihood for particles to settle side-by-side (see Fig. 5a in [150]). We observe from Fig. 3.3 that the tendency to aggregate in the vertical quickly vanishes with increasing bulk concentration. Already at $\phi = 6\%$ the tendency has almost completely disappeared, while simultaneously the tendency for pairwise side-by-side motion has become stronger as compared to $\phi = 2\%$. Thus, $\phi = 2\%$ marks the transition from the dilute to the moderate concentration regime, with a tendency of particles to aggregate in the vertical at lower bulk concentrations by the wake-trapping mechanism and a tendency of particles to settle side-by-side in a pairwise manner at a distance of $\sim 1.5D_p$ by a DKT-type instability at moderate bulk concentrations. The breakdown of the vertical aggregates in the moderate concentration regime might be related to the increased importance of short-range particle-particle interactions at the cost of long-range hydrodynamic interactions like wake trapping. This is consistent with a more localized preferential concentration pattern and a more confined particle recirculation pattern at higher ϕ. Recall that preferential settling in

a dominant pairwise side-by-side configuration was reported before by Yin and Koch [182] for the moderate Reynolds number regime ($Re_T = 10$, $\rho_p/\rho_f = 2$) at $\phi = 1\%$ and 5% with interparticle distances of $\sim 2.5D_p$ and $\sim 2D_p$, respectively. Thus, our results show that such dominant pairwise particle configuration is still present at similar bulk concentrations but more than tenfold higher Re_T.

From $\phi = 10$ to 20% we observe yet another transition from preferential setting in a pairwise side-by-side motion at moderate bulk concentrations ($2\% \lesssim \phi \lesssim 10\%$) towards a more and more concentric ring-like distribution in the dense regime ($\phi \gtrsim 10\%$). This indicates a tendency towards a random "hard-sphere distribution" consistent with the observations of Yin and Koch [182] for $\phi = 20\%$ in the low and moderate Reynolds number regimes ($Re_T = 1$ and 10). They attributed the randomness of the distribution to chaotic motions from many-particle interactions. The layering in concentric rings originates from the restriction that hard spheres cannot overlap ('excluded volume effect') [64]. This causes a quasi-ordering of the distribution close to the reference particle, which quickly fades away over a distance of a few particle diameters related to increasingly uncorrelated motions of the spheres. We remark that at $\phi = 30\%$ the ring-like distribution is still not fully spherically symmetric, with a higher preference for horizontal than vertical particle alignment within the spherical shells, consistent with the local particle recirculation pattern. This suggests that weak DKT-type instabilities still play a role here.

Figure 3.4 presents the results for the PCA relative vertical fluid velocity as function of bulk concentration and Galileo number. The relative velocity is scaled with the difference between the mean fluid and mean sedimentation velocity, $V_r = V_f - V_s = -V_s/(1-\phi)$ using that $\phi V_s + (1-\phi)V_f = 0$ for zero bulk mixture velocity. We loosely characterize the vertical extent of the fluid wake by the 0.8 isocontour of the normalised relative velocity (i.e., the upper contour in the plots). At $\phi = 2\%$, the vertical wake extent is then approximately $3.5D_p$ for $Ga = 144$ and $Ga = 178$ and around $3D_p$ for $Ga = 210$. Interestingly, the tip of the 0.8 isocontour roughly matches with the local concentration maximum in the vertical clusters observed in Fig. 3.3. Furthermore, although the effect of Ga appears to be fairly small, the larger wake extent for $Ga = 144$ and $Ga = 178$ seems consistent with the observation from Fig. 3.3 that vertical clustering is more confined in the lateral direction for $Ga = 144$ and $Ga = 178$ (stronger wake trapping due to a more pronounced fluid wake), while the particle surplus region around $x/D_p \simeq 1.5$ is most pronounced for $Ga = 210$ (stronger DKT-type instabilities).

The extent of the fluid wake declines rapidly when increasing the bulk concentration from the dilute to the moderately dense regime, in line with a weakening of the wake trapping mechanism and stronger local instability mechanisms such as DKT based on hydrodynamic interactions between neighbouring particles. The decay of the wake extent continues when increasing the bulk concentration from the moderate to the dense regime, but at a much slower pace. Beyond $\phi \approx 10\%$, the extent of the wake is apparently so small that it can only facilitate weak DKT-type instabilities, while simultaneously short-range particle-particle interactions such as lubrication and collisions

start to dominate the particle dynamics. At $\phi = 25\%$ and 30% the wake structure is nearly identical and limited in extent to about one particle diameter.

3.4.3. MEAN PARTICLE SEDIMENTATION VELOCITY

The mean particle sedimentation velocity was obtained by averaging the time series of the particle-mean velocity for $t > 50\sqrt{D_p/g}$ for which the flow was in a fully developed state. The result is shown in a log-log plot in Fig. 3.5 as function of the bulk void fraction, $1-\phi$, and Galileo number. The figure clearly shows the effect of hindered settling: the sedimentation velocity drops rapidly with decreasing bulk void fraction and hence increasing bulk concentration. For each Ga and $\phi \gtrsim 10\%$, the data points lie approximately on a straight line, in agreement with the Richardson-Zaki power-law relation given by Eq. (3.1). The dashed lines show the fit of Eq. (3.1) to the DNS data for $\phi \geq 10\%$. The values for the correction factor, k, and the power-law exponent, n, are given in Table 3.4 along with the values for n estimated from the following correlations provided by Richardson and Zaki [142]:

$$n = \begin{cases} \left[4.45 + 18\frac{D_p}{D_{pipe}}\right] \cdot (kRe_T)^{-0.1} & , \quad 1 < kRe_T < 200\,, \\ 4.45 \cdot (kRe_T)^{-0.1} & , \quad 200 < kRe_T < 500\,, \end{cases} \tag{3.5}$$

where D_p/D_{pipe} is the particle-to-pipe diameter ratio in the experiments of Richardson and Zaki. As the flow domain in the DNS is a rectangular box with triply periodic boundary conditions, we evaluated Eq. (3.5) both for $D_p/D_{pipe} = 0$ and $D_p/D_{pipe} = 1/25$ based on the lateral extent of the flow domain of $25D_p$. The actual confinement effect from the finite lateral domain extent in the DNS is expected to be in between these two extreme cases. Indeed, this appears to be the case for $Ga = 144$ and 178, see Table 3.4. For $Ga = 210$, the Richardson-Zaki correlation predicts no confinement effect on the sedimentation velocity. The corresponding DNS value for n is in fairly good agreement with the correlation estimate (deviation of +14%). Note that the DNS values for n are varying in a non-monotonic manner with Ga. Nonetheless, in all cases the value is close to 3, which indicates a nearly Ga-independent exponent over the currently investigated Ga range.

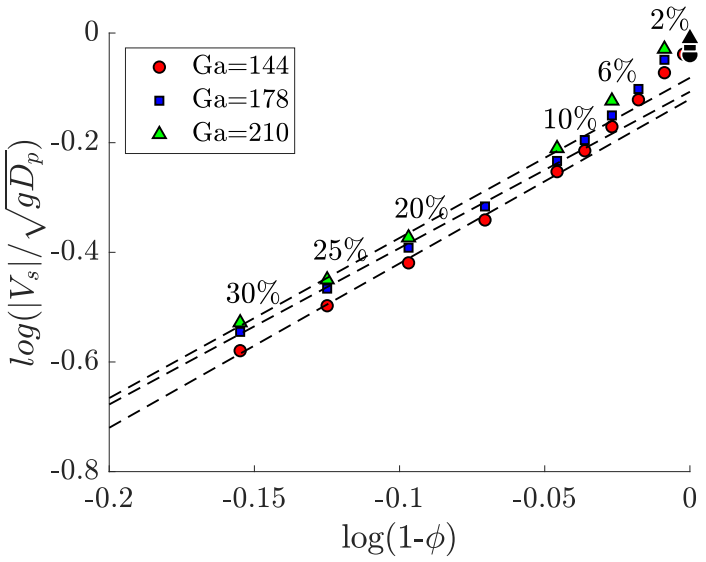

Figure 3.5: Double-log plot of the normalised mean particle sedimentation velocity, $|V_s|/\sqrt{gD_p}$, as function of bulk void fraction, $1-\phi$, and Galileo number. The dashed lines represent fits of the Richardson-Zaki relation, Eq. (3.1), to the data points for $\phi \geq 10\%$. The black symbols at $\phi = 0$ indicate the mean single-particle terminal settling velocity, see Table 3.3.

Table 3.4: Values for the correction factor, k, and the power-law exponent, n, in Eq. (3.1), obtained from fitting the DNS data for $\phi \geq 10\%$. The last two columns show estimates for n from the empirical Richardson-Zaki correlations given by Eq. (3.5).

Ga	k	n	n from Eq. (3.5) with $D_p/D_{pipe} = 0$	n from Eq. (3.5) with $D_p/D_{pipe} = 1/25$
144	0.83	3.00	2.69	3.12
178	0.82	2.85	2.62	3.05
210	0.85	2.92	2.57	2.57

From Fig. 3.5 it can be observed that the Richardson-Zaki relation underestimates the sedimentation velocity for $\phi < 10\%$. The deviation increases for smaller ϕ and is largest for $\phi = 0$. Indeed, the fitted value for the correction factor k is significantly smaller than one. This is well known from literature, see, e.g., Di Felice [54] and Yin and Koch [182]. Their reported values for k are in the range of 0.8-0.9, which is in good agreement with our DNS results. It is interesting to note that $\phi = 10\%$ marks the transition from the moderate concentration regime with an anisotropic microstructure towards the dense concentration regime with a more isotropic microstructure as discussed previously. Our results thus substantiate the suggestion of Yin and Koch [182] that the Richardson-Zaki relation is associated with a “hard-sphere distribution". This also implies that the underestimation of the sedimentation velocity for $\phi < 10\%$ can be attributed to anisotropy of the microstructure, which in turn is originating from hy-

drodynamic particle interactions in the inertial regime (wake trapping and DKT-type instabilities). Finally, it is worth mentioning that for $Ga = 144$ and $\phi = 0.5\%$ the mean sedimentation velocity is very close to the mean single-particle settling velocity at the same Ga (difference of 0.2%). Thus we do not observe enhanced settling at this Ga, consistent with the presumed threshold of $Ga \approx 155$ for this.

3.4.4. PARTICLE AND FLUID RMS VELOCITIES

Fluctuations in the vertical particle velocity are defined as temporal deviations in the vertical particle velocity around the mean sedimentation velocity, $v'_p = v_p - V_s$. Similarly, vertical velocity fluctuations of the fluid phase are defined as $v'_f = v_f - V_f = v_f + \phi V_s/(1-\phi)$. As mean velocities in the horizontal directions are very close to zero, as expected for sedimenting suspensions, horizontal velocity fluctuations are simply defined by the instantaneous horizontal velocity. Figures 3.6.a and 3.6.b depict the root-mean-square (rms) of the particle and fluid velocity fluctuations, respectively, both for the vertical (red symbols) and the lateral direction (blue symbols). Because of statistical symmetry, the horizontal rms velocities in x and z are nearly the same. Hence, they are represented by their average value, $\sqrt{(u^2_{p,rms} + w^2_{p,rms})/2}$.

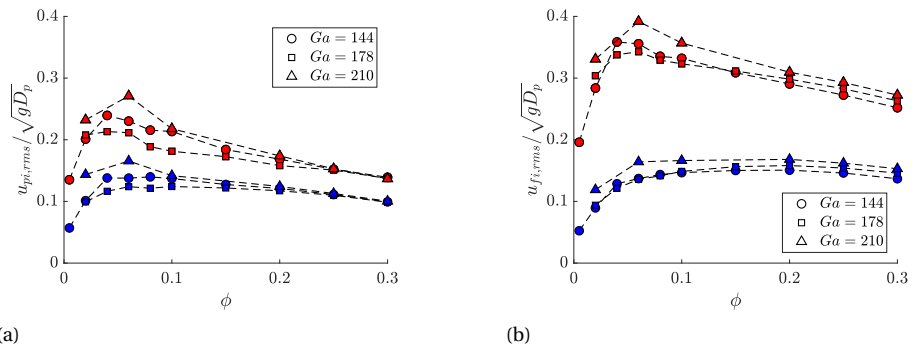

Figure 3.6: Root-mean-square velocity of ((a)) particles and ((b)) fluid, normalised with $\sqrt{gD_p}$, and shown as function of ϕ and Ga. Red and blue symbols refer to the vertical (y) and lateral (x and z) direction, respectively. Circles, squares and triangles correspond to $Ga = 144$, 178 and 210, respectively.

Focusing on the particle rms velocities, a clear Ga-dependent peak can be observed in the vertical and to a lesser extent also the lateral direction in the range of $\phi = 4-8\%$. The peak rms value varies in a non-monotonic fashion with Ga with the highest value for $Ga = 210$ and the lowest value for $Ga = 178$. On the other hand, when normalised with $\sqrt{gD_p}$, the particle rms velocities are nearly independent of Ga for $\phi \gtrsim 20\%$ and gradually decrease with increasing bulk concentration. The Ga-dependent peak in the particle rms velocity in the moderate concentration regime is consistent with contributions from hydrodynamic particle-particle interactions related to DKT-type instabilities. Conversely, the Ga-independent particle rms velocities in the dense concentration regime are consistent with short-range particle-particle interactions through

lubrication and particle collisions. For the fluid velocity rms we observe a peak in the moderate concentration regime too, though less distinct for the lateral fluid rms having an almost constant value for $\phi \gtrsim 8\%$. Also, different from the particle rms velocities, the fluid rms velocities exhibit a mild Ga dependency over the entire concentration range.

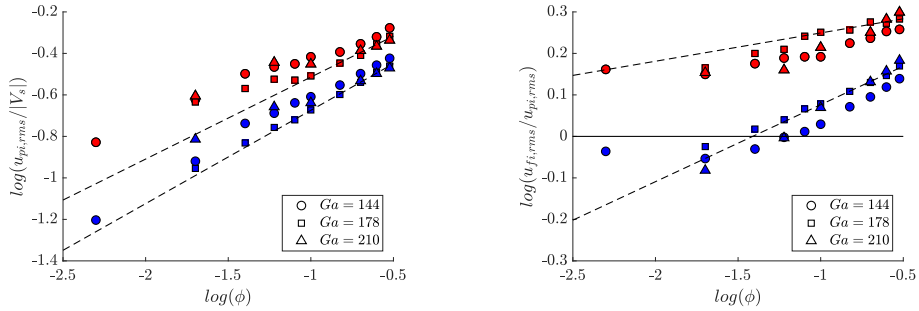

(a) (b)

Figure 3.7: Double-log plot of ((a)) the particle rms velocity normalised with $|V_s|$ and ((b)) the fluid/particle rms velocity ratio as function of ϕ and for the three different Galileo numbers. Red and blue symbols refer to the vertical (y) and lateral (x and z) direction, respectively. Circles, squares and triangles correspond to $Ga = 144$, 178 and 210, respectively. The dashed lines represent power-law fits of the DNS data to Eq. (3.6a) and (3.6b) for $Ga = 178$ and $\phi \geq 10\%$.

In Fig. 3.7a the particle rms velocities are plotted once again but now normalised with the mean sedimentation velocity and using logarithmic scales on both axes. Scaled in this manner, we observe that the particle rms velocities increase with increasing bulk concentration. In agreement with the DNS study of Zaidi [186], for sufficiently high concentration the trend can be fairly well approximated by the following power-law relation:

$$\frac{u_{pi,rms}}{|V_s|} = C\phi^m, \tag{3.6a}$$

where the subscript i denotes the velocity component in direction i, and C and m are constants. We find that also the rms of the fluid velocity follows a power-law scaling, and so does the fluid-to-particle rms velocity ratio as is clear from Fig. 3.7b:

$$\frac{u_{fi,rms}}{u_{pi,rms}} = \frac{C_{fi}}{C_{pi}}\phi^{(m_{fi}-m_{pi})}, \tag{3.6b}$$

where the subscripts p and f refer to the particles and fluid, respectively. We determined the power-law coefficients by fitting the DNS data to Eqs. (3.6a) and (3.6b) for $\phi \geq 10\%$. The fitted values are listed in Table 3.5.

Table 3.5: Values for the coefficients in Eqs. (3.6a) and (3.6b) for, respectively, the normalised particle rms velocity and the fluid/particle rms velocity ratio, obtained from fitting the DNS data for $\phi \geq 10\%$. Subscripts p, f, v and h refer to, respectively, the particles, the fluid, the vertical and the lateral direction.

Ga	m_{pv}	C_{pv}	m_{ph}	C_{ph}	$m_{fv}-m_{pv}$	C_{fv}/C_{pv}	$m_{fh}-m_{ph}$	C_{fh}/C_{ph}
144	0.29	0.72	0.39	0.60	0.14	2.16	0.23	1.80
178	0.40	0.76	0.45	0.57	0.07	2.08	0.19	1.83
210	0.23	0.60	0.35	0.52	0.18	2.43	0.23	1.99

Interestingly, our results contradict the findings from the DNS study of Zaidi [186], who reported approximately equal power-law exponents for the vertical and the horizontal particle rms velocity: $m_{ph/v} = 0$ for $Re_T = 200$ and $m_{ph/v} = -0.1$ for $Re_T \gtrsim 300$. For our range of $Re_T = 186-290$, we consistently find $m_{ph} > m_{pv} > 0$ (i.e., different exponents and a rising trend) with m_{ph} and m_{pv} in the range of 0.35-0.45 and 0.23-0.40, respectively. The reason for our different findings is unclear, though it might be related to a different particle/fluid density ratio considered by Zaidi [186] (2.5 vs 1.5 in our case).

normalised with the mean sedimentation velocity, the lateral particle rms velocity rises steeper with bulk concentration than the vertical particle rms velocity. A higher vertical than horizontal rms particle velocity has been reported in many previous studies [28, 183, 162, 187, 68, 51, 186, 171]. The anisotropy in the particle velocity fluctuations thus gradually decreases, though the power-law fits predict that it remains to exist in the very dense regime: assuming a maximum flowable packing fraction of $\phi \simeq 0.65$, the ratio of the vertical to the horizontal particle rms velocity approaches a value of approximately 1.2 for all three Galileo numbers. Finally, we observe from Fig. 3.7b that the ratio of the fluid to the particle rms velocity is increasing with ϕ and generally larger than one. The only exception is the lower bulk concentration range ($\phi \lesssim 8\%$) for the lateral direction, where the fluid rms velocity is a bit smaller than the particle rms velocity.

3.4.5. PDF OF PARTICLE VELOCITY

In Fig. 3.8 we show the normalised probability density function (pdf) of the particle velocity in the vertical (left) and the lateral (right) direction as function of bulk concentration and Galileo number (increasing from top to bottom). Note that $v_p - V_s < 0$ corresponds to particles falling faster than the mean sedimentation velocity as V_s is negative. For comparison, a Gaussian distribution is included in the plots. At first glance, the distribution of the particle velocities is close to Gaussian, in particular for $\phi > 6\%$, which agrees with the Gaussian distribution found for $\phi = 12\%$ in the simulations of Climent and Maxey [28]. Indeed, in the dense regime, the computed third and fourth standardized moment of the particle velocity, known as the skewness and kurtosis, are close to 0 and 3, respectively, as expected for a Gaussian distribution. The Ga-independent and Gaussian distribution at the higher bulk concentrations is consistent with a tendency towards a more random spatial arrangement of the particles and the dominant contribution of short-range particle-particle interactions to the particle dynamics. Furthermore, the collapse of the pdfs in the dense regime indicates that the velocity fluctuations scale with the rms velocity.

Although perhaps not immediately obvious from the pdfs, with increasing bulk concentration an increasing fraction of particles is instantaneously moving upwards. Using Eq. (3.6a), $v_p = 0$ corresponds to a standardized vertical velocity of $(v_p - V_s)/v_{p,rms} = (1/C_{pv})\phi^{-m_{pv}}$, which for $m_{pv} > 0$ indeed becomes smaller with increasing bulk concentration. For $Ga = 178$, we find that $v_p = 0$ corresponds to a standardized vertical velocity of 4.1 for $\phi = 6\%$, 2.5 for $\phi = 20\%$ and 2.1 for $\phi = 30\%$, which explains why at this Galileo number upward moving particles are hardly present for $\phi = 6\%$ but can be clearly observed for $\phi = 30\%$ in the snapshots of Fig. 3.2. The red dashed vertical line in Figs 3.8.a,c,e marks the value of $-V_s/v_{p,rms}$ ($v_p = 0$) at $\phi = 30\%$. A few percent of all particles are moving upward at this concentration with the fraction decreasing with increasing Ga for the currently examined Ga range (~ 3% at $Ga = 144$ vs less than 2% at $Ga = 210$).

Closer inspection for the lower concentration range reveals that the pdf of the vertical particle velocity is negatively skewed for $\phi = 0.5\%$ at $Ga = 144$ (Fig. 3.8a) and to a lesser extent also for $\phi = 2\%$ at $Ga = 178$ (Fig. 3.8c). The peak of the skewed pdf corresponds to particles falling a bit slower than the mean, while the longer left than right tail indicates that extreme events (say, $|v_p| > |V_s| + 2v_{p,rms}$) are more often associated with particles falling significantly faster than the mean. Skewed pdfs for the vertical particle velocity were also found in the previously mentioned sedimentation experiments by Huisman et al. [77], though much more pronounced and associated with a significantly enhanced mean settling speed with respect to settling of a single particle in free space. Huisman et al. attributed the skewed pdf to the tendency of particles to form vertical columnar clusters, caused by the inertial trapping of particles in the wake of other particles underneath. The particles that fall in tandem are less exposed to the fluid flow and hence they settle faster than the other particles. The latter was clearly shown by Uhlmann and Doychev [162] for the case of $Ga = 178$, $\rho_p/\rho_f = 1.5$ and $\phi = 0.5\%$.

Interestingly, we observe that the negatively skewed pdf for the vertical velocity corresponds to super-Gaussian behavior for the lateral velocity (a more peaky distribution with an enhanced kurtosis), which is most pronounced for $\phi = 0.5 - 4\%$ at $Ga = 144$ (Fig. 3.8b) and to a lesser extent for $\phi = 2\%$ at $Ga = 178$ (Fig. 3.8d). Similar behavior was reported by Fornari et al. [56] at $Ga \approx 145$, $\rho_p/\rho_f = 1.02$ and $\phi = 0.5$ and 1%. The higher peak around the origin is consistent with particles settling in rather stable vertical trains, whereas the longer tails might indicate strong horizontal particle excursions related to the initial formation or final breakup of the columnar structures. The skewed behavior of the vertical particle velocity and the super-Gaussian behavior for the lateral particle velocity both vanish with increasing bulk concentration. This is consistent with increasingly less stable columnar structures related to a smaller extent of the fluid wake (Fig. 3.4), disturbances from multi-particle interactions and more pronounced DKT-type instabilities in the moderate concentration range ($2\% \lesssim \phi \lesssim 10\%$).

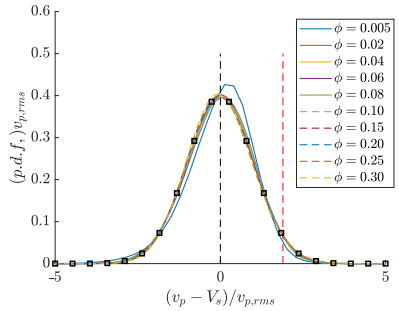

(a)

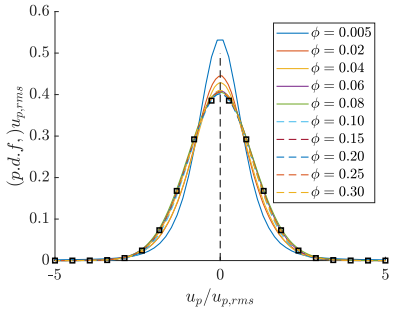

(b)

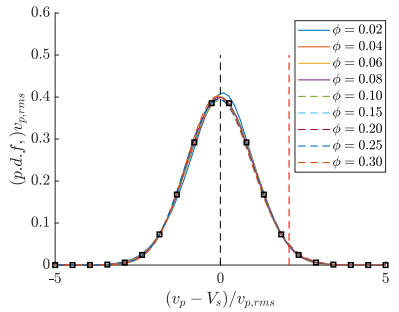

(c)

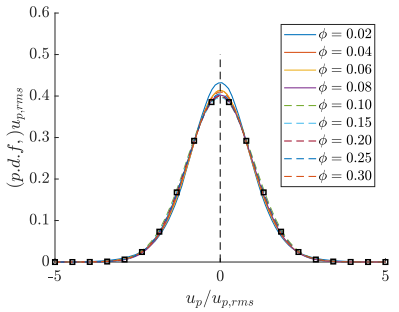

(d)

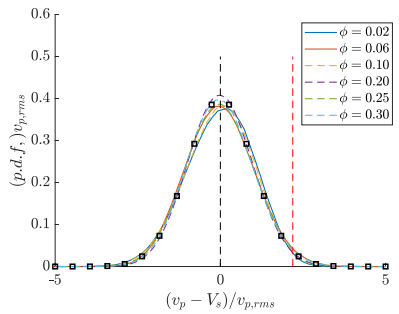

(e)

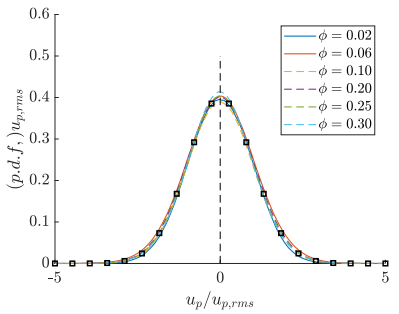

(f)

Figure 3.8: Probability density function of the vertical (v_p, left) and lateral (u_p and w_p, right) particle velocity as function of bulk concentration and Galileo number (increasing from top to bottom). The pdf is normalised with the rms particle velocity. Black squares represent a Gaussian distribution. ((a)) Vertical velocity, $Ga = 144$, ((b)) lateral velocity, $Ga = 144$, ((c)) vertical velocity, $Ga = 178$, ((d)) lateral velocity, $Ga = 178$, ((e)) vertical velocity, $Ga = 210$, ((f)) lateral velocity, $Ga = 210$. The red dashed vertical line in ((a)), ((c)) and ((e)) marks the value of $-V_s/v_{p,rms}$ ($v_p = 0$) at $\phi = 30\%$.

3.4.6. PARTICLE VELOCITY CORRELATIONS

Fig. 3.9 presents the temporal autocorrelations of the vertical (left) and lateral (right) particle velocity fluctuations as function of bulk concentration and Galileo number (increasing from top to bottom). For the vertical particle velocity, the autocorrelation is defined by:

$$\rho_{vv}(\tau) = \overline{v_p'(t)\, v_p'(t+\tau)} / \overline{v_p'^2}. \tag{3.7}$$

A first striking observation is the much slower decay of the autocorrelation of the vertical velocity fluctuations at $Ga = 144$ and $\phi = 0.5\%$ (Fig. 3.9a) as compared to the other autocorrelations of the vertical velocity at the same Ga but with higher bulk concentrations. The positive correlation at $\phi = 0.5\%$ up to $t = 400\sqrt{D_p/g}$ is consistent with the tendency of particles to settle preferentially in columnar structures. Also, a mild oscillatory behavior can be observed in this case with local minima near ~ 125 and $\sim 375\sqrt{D_p/g}$ and a local maximum in between at $\sim 225\sqrt{D_p/g}$, indicating an oscillation time period of $O(200-250)\sqrt{D_p/g}$. Interestingly, the autocorrelation of the corresponding lateral velocity fluctuations at $Ga = 144$ and $\phi = 0.5\%$ (Fig. 3.9b) gradually drops off to zero without signs of oscillatory behavior as seen for the vertical velocity component. Apparently, a recurrent instability mechanism is at work that affects only the vertical and not the lateral velocity component at $\phi = 0.5\%$ and $Ga = 144$. This hints at the possible presence of kinematic waves, which travel in the vertical and may potentially disturb the earlier mentioned "stable" columnar structures present at this bulk concentration. We will discuss this in more detail later.

A second striking observation is the presence of a clear negative correlation peak for the vertical velocity component around $O(40-60)\sqrt{D_p/g}$ and subsequent oscillatory behavior for $\phi = 2-20\%$ at $Ga = 144$, $\phi = 4-20\%$ at $Ga = 178$, and $\phi = 6-20\%$ at $Ga = 210$. The oscillation frequency varies with bulk concentration and Ga, but is equal to $\sim 120\sqrt{D_p/g}$ at $\phi = 6\%$ for all Ga, thus roughly twice as low as the frequency found for $\phi = 0.5\%$ and $Ga = 144$. Interestingly, a similar oscillation period was found by Fornari et al. [56] for $Ga \approx 145$, $\rho_p/\rho_f = 1.02$ and $\phi = 1\%$, at least when the oscillation period is normalised with $\sqrt{D_p/[(\rho_p/\rho_f - 1)g]}$, i.e., using the reduced gravity instead of gravity. This suggests that the use of the reduced gravity is preferred over gravity when the density ratio is varied, as may also be expected from the gravity term in Eq. (3.3a).

For all three Galileo numbers, the negative peak and oscillatory behavior in the correlation for the vertical velocity are absent at $\phi = 25$ and 30%. This again is reminiscent of a change in the particle dynamics, now from the moderate to the dense regime, consistent with the transition to a "hard-sphere distribution" dominated by short-range particle-particle interactions for dense sedimenting suspensions. The observations for the correlation of the vertical velocity component in the moderate and dense regime hold also largely for the horizontal velocity component: a negative correlation peak and oscillatory behavior for the moderate concentrations and the absence of this for the most dense cases. A more quantitative frequency analysis will be discussed later when we present frequency spectra of the velocity fluctuations.

From the autocorrelations we have computed the integral time scale, τ_L, defined as:

$$\tau_L = \int_0^\infty \rho(\tau)\, d\tau\,. \tag{3.8}$$

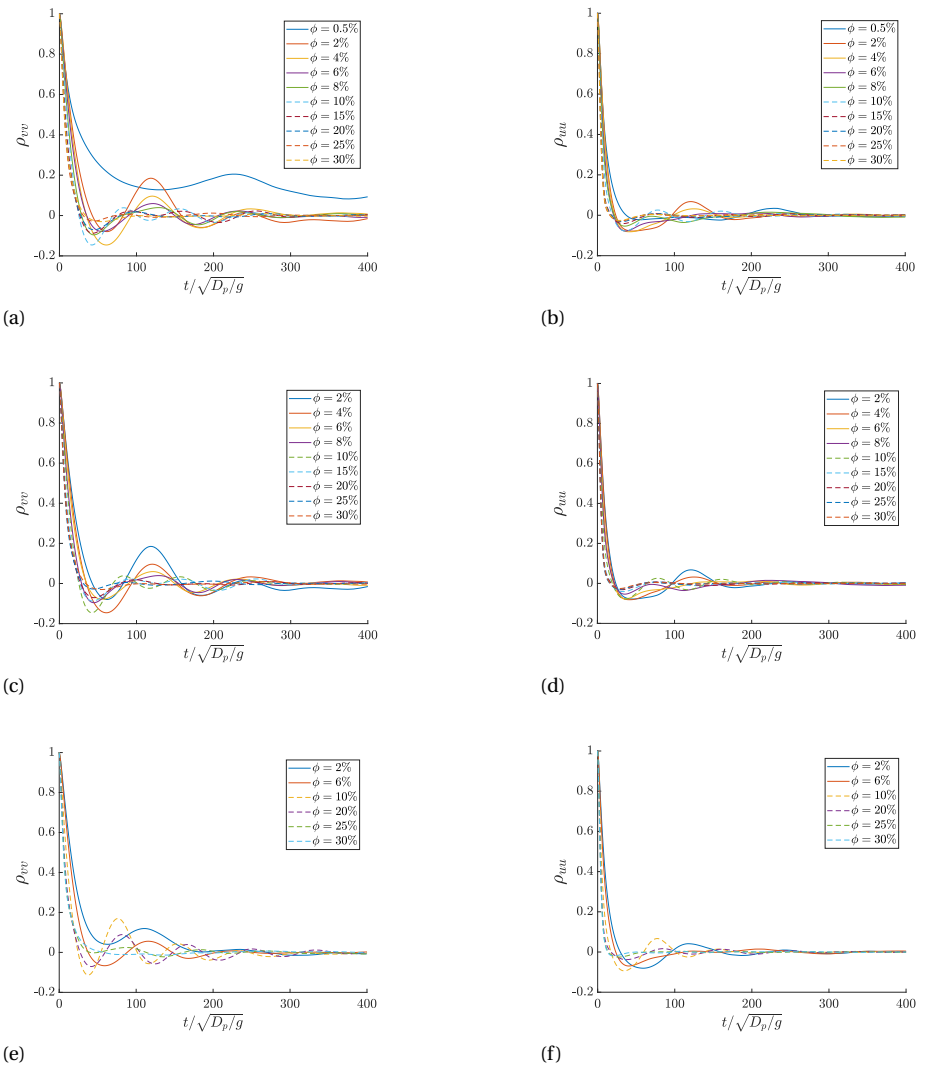

Figure 3.9: Temporal autocorrelation of the vertical (v_p', left) and lateral (u_p' and w_p', right) particle velocity fluctuations, shown as function of bulk concentration and Galileo number (increasing from top to bottom). Because of statistical symmetry, the correlations are shown only for positive time shifts and, for clarity, only up to $400\sqrt{D_p/g}$. ((a)) Vertical velocity, Ga = 144, ((b)) lateral velocity, Ga = 144, ((c)) vertical velocity, Ga = 178, ((d)) lateral velocity, Ga = 178, ((e)) vertical velocity, Ga = 210, ((f)) lateral velocity, Ga = 210.

This is a rough proxy of the largest time over which particle velocity fluctuations are still correlated. In our previous study [150] we multiplied it with the mean sedimentation velocity to estimate the corresponding vertical correlation distance. Fig. 3.10 shows $\tau_L/\sqrt{D_p/g}$ for the vertical (red) and lateral (blue) particle velocity fluctuations as function of ϕ and Ga. The normalised integral time scale rapidly drops off when increasing ϕ from the dilute to the moderate concentration regime, in particular for the vertical velocity, and then more gradually decreases towards a constant value of ~ 8 for the vertical and ~ 3 for the lateral velocity for $\phi > 10\%$. While the Galileo number has clearly some influence on τ_L in the dilute and moderate concentration regime, especially for the vertical velocity, it has almost no effect on τ_L in the dense regime. This is consistent with the importance of wake-related particle interactions for $\phi \lesssim 10\%$ and increasingly dominant short-range multi-particle interactions for $\phi \gtrsim 10\%$. The constant value of $\tau_L/\sqrt{D_p/g}$ in the dense regime implies that $\sqrt{D_p/g}$ is the relevant time scale for particle interactions in this regime, at least when the density ratio is kept constant as in our present study.

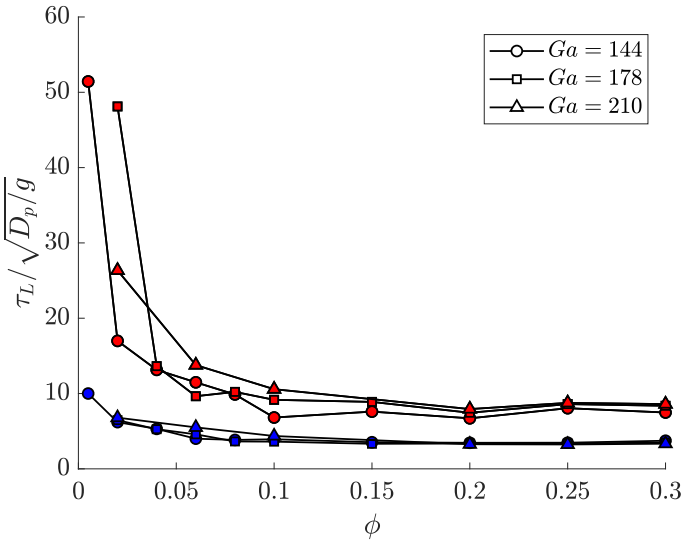

Figure 3.10: normalised integral time scale $\tau_L/\sqrt{D_p/g}$ for the vertical (v'_p, red) and lateral (u'_p and w'_p, blue) particle velocity fluctuations as function of ϕ and Ga.

Instead of using Eq. (3.8), the integral time scale can also be obtained from an analysis of particle dispersion by means of the mean square particle displacement as function of time [150]. Twice the integral time scale marks the transition from the ballistic to the diffusive particle transport regime [125]. Furthermore, it can be shown that in the diffusive regime (i.e., for $t \gtrsim 2\tau_L$) the vertical particle diffusivity, $\mathscr{D}_{yy}$, is given by

[125]:

$$\frac{\mathscr{D}_{yy}}{\sqrt{gD_p^3}} = 2\left(\frac{v_{p,rms}}{\sqrt{gD_p}}\right)^2\left(\frac{\tau_{L,vv}}{\sqrt{D_p/g}}\right). \tag{3.9}$$

A similar expression can be derived for the horizontal particle diffusivity. The diffusivity is higher in the vertical than in the horizontal direction, related to the higher rms velocity and integral time scale in the vertical. It is also higher for the dilute and moderate concentration regime than for the dense regime. As the normalised rms velocity and the normalised integral time scale are both independent of Ga in the dense regime, so does also the particle diffusivity: it scales with $\sqrt{gD_p^3}$ and gradually decreases with concentration in the dense regime.

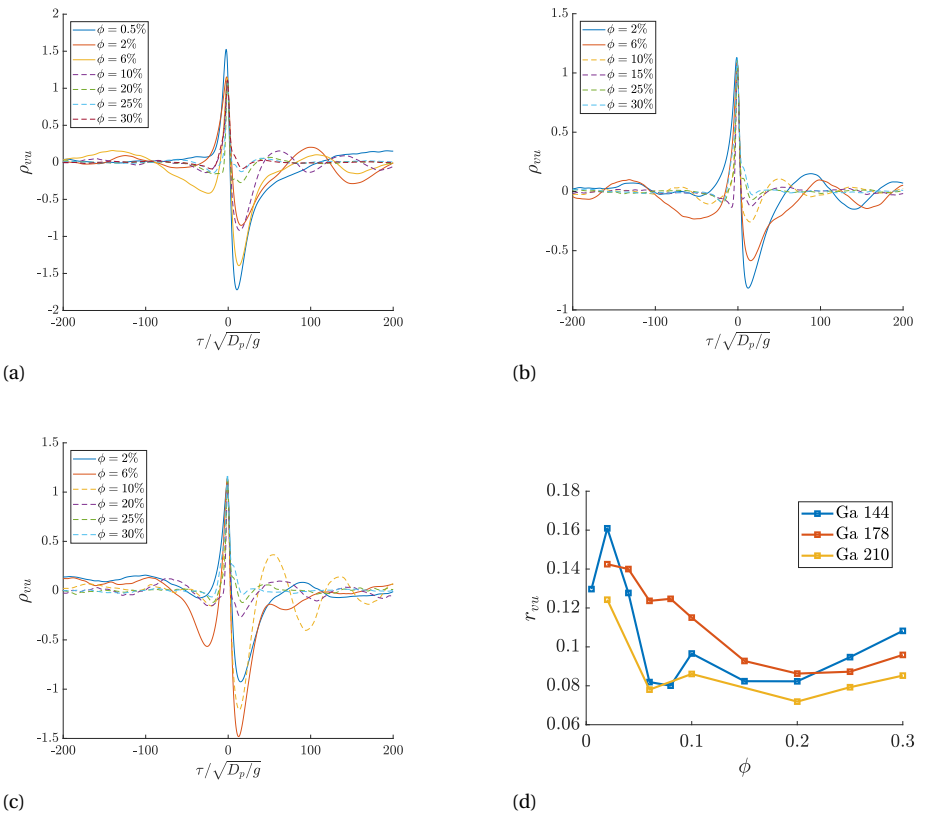

Figure 3.11: Temporal crosscorrelation of vertical velocity fluctuations with fluctuations in the horizontal velocity magnitude, shown as function of bulk concentration and Galileo number. For clarity, only a range of 400 time units is shown, centered around 0. ((a)) $Ga = 144$, ((b)) $Ga = 178$, ((c)) $Ga = 210$. ((d)) Correlation coefficient for fluctuations in the vertical velocity and in the magnitude of the horizontal velocity, shown as function of bulk concentration and Galileo number.

For DKT-type instabilities it may be expected that vertical and horizontal velocity fluctuations are related to each other. To investigate this, we have computed the cross-correlation defined by:

$$\rho_{vu}(\tau) = \frac{\overline{v'_p(t)u'_{ph}(t+\tau)}}{\overline{v'_p u'_{ph}}} \quad \text{with} \quad u_{ph} = \sqrt{u_p^2 + w_p^2}. \tag{3.10}$$

The crosscorrelation is shown in Figs 3.11.a-c as function of bulk concentration and Galileo number. For bulk concentrations of up to 10%, we observe a positive correlation peak larger than 1 at a slightly negative time lag followed by a strong anti-correlation peak for a positive time lag of $\tau/\sqrt{D_p/g} \approx 10-16$. The anticorrelation peak is even larger than the positive correlation peak for $\phi = 0.5$ and 6% at $Ga = 144$ and for $\phi = 6$ and 10% at $Ga = 210$. We attribute this behavior to DKT-type events in which a particle gets trapped in the wake of another particle and will display a more vertical path ("drafting" with faster settling and hence $v'_p < 0$, and $u'_{ph} < 0$), while directly after close contact with the leading particle ("kissing"), it will experience a strong perturbation in its horizontal velocity at a still enhanced fall velocity ("tumbling" with $u'_{ph} > 0$ and $v'_p < 0$). This also explains why the anti-correlation peak vanishes in the dense regime where short-range multi-particle interactions and collisions dominate the particle dynamics. The chaotic motions in the dense regime are responsible for a more symmetric crosscorrelation, which rapidly drops off to zero for non-zero time lag. As seen before for the autocorrelations, also the crosscorrelation exhibits oscillatory behavior for the lower concentration range, which in some cases is most pronounced for positive time lags (e.g., for $\phi = 2\%$ at $Ga = 144$ and 178 with an oscillation period of $O(100)$ time units, and for $\phi = 10\%$ at $Ga = 144$ and $Ga = 210$ with an oscillation period of $O(65)$ time units). We speculate that in these cases DKT-type instabilities might be responsible for the onset of large-scale instabilities such as kinematic waves. Conversely, the presence of slow oscillations for negative time lags, such as for $\phi = 6\%$ at all Ga, would then suggest that the opposite may also be true and that kinematic waves may trigger DKT-type instabilities by local compaction of the suspension along the vertically travelling waves. We will explore this in more detail later.

To assess the coupling of the vertical with the horizontal particle velocity fluctuations, we computed the corresponding zero-lag crosscorrelation coefficient from:

$$r_{vu} = \frac{\overline{v'_p u'_{ph}}}{v_{p,rms} u_{ph,rms}}. \tag{3.11}$$

The crosscorrelation coefficient is equal to ± 1 when the vertical and horizontal particle velocity fluctuations would be instantaneously fully coupled and is equal to 0 when they are completely uncorrelated with each other. The results are depicted in Fig. 3.11d as function of ϕ and Ga. The coupling of the velocity fluctuations is clearly strongest for $\phi = 2$ and 4%, where DKT-type instabilities are active. In the moderate concentration regime, it is highest for $Ga = 178$, except for $\phi = 2\%$ where a slightly higher peak is found for $Ga = 144$. For all bulk concentrations and Galileo numbers, the coupling

is smaller than 0.16 and thus seems relatively weak. This might indicate that chaotic particle interactions are interfering with DKT-type instabilities already in the moderate concentration regime. It is striking that at $Ga = 144$ the correlation coefficient is about a factor 1.5 smaller for $\phi = 0.5\%$ than for $\phi = 2\%$. However, note that the correlation coefficient is based on the covariance at zero time lag, while for $\phi = 0.5\%$ the anti-correlation peak corresponds to a lagged crosscorrelation of about -1.7. The corresponding lagged correlation coefficient is thus about $-1.7 \times 0.104 \approx -0.18$. Similarly, at $\phi = 2\%$ the crosscorrelation peaks around 1.15 at a slightly negative time shift, with a corresponding lagged correlation coefficient of about $1.15 \times 0.155 \approx 0.18$. Thus, the lagged correlation coefficients at $\phi = 0.5$ and 2% are comparable in magnitude.

3.4.7. FREQUENCY SPECTRA OF PARTICLE VELOCITIES

To investigate the presence of dominant frequencies in the particle velocity fluctuations, we have computed the frequency spectrum of the particle velocity from the Fourier transform of the temporal autocorrelation. For the vertical velocity component this is given by:

$$\frac{E_{vv}(\omega)}{R_{vv}(0)\sqrt{D_p/g}} = 2\Re\left(\frac{1}{2\pi}\int_{-\infty}^{\infty}\rho_{vv}(\tau)e^{-i\omega\tau}d\tau\sqrt{\frac{g}{D_p}}\right), \tag{3.12a}$$

where $\Re(..)$ denotes the real part of the transform and where we normalised the spectrum with the velocity variance ($R_{vv}(0) = \overline{v_p'^2}$) and the gravitational time ($\sqrt{D_p/g}$). Note that $\rho_{vv}(-\tau) = \rho_{vv}(\tau)$ at statistically steady state and this is how we obtained the autocorrelation for negative time lags. The frequency spectrum describes the contribution of the different frequency components of the velocity signal to the overall velocity variance and hence the one-sided integral over the normalised spectrum is equal to 1:

$$\int_0^{\infty}\frac{E_{vv}(\omega_*)}{R_{vv}(0)\sqrt{D_p/g}}d\omega_* = 1\,, \tag{3.12b}$$

where $\omega_* = \omega\sqrt{D_p/g}$. Also, the value of the frequency spectrum at zero frequency is related to the integral time scale defined by Eq. (3.8) according to:

$$\frac{E_{vv}(0)}{R_{vv}(0)\sqrt{D_p/g}} = \frac{2}{\pi}\frac{\tau_{L,vv}}{\sqrt{D_p/g}}\,. \tag{3.12c}$$

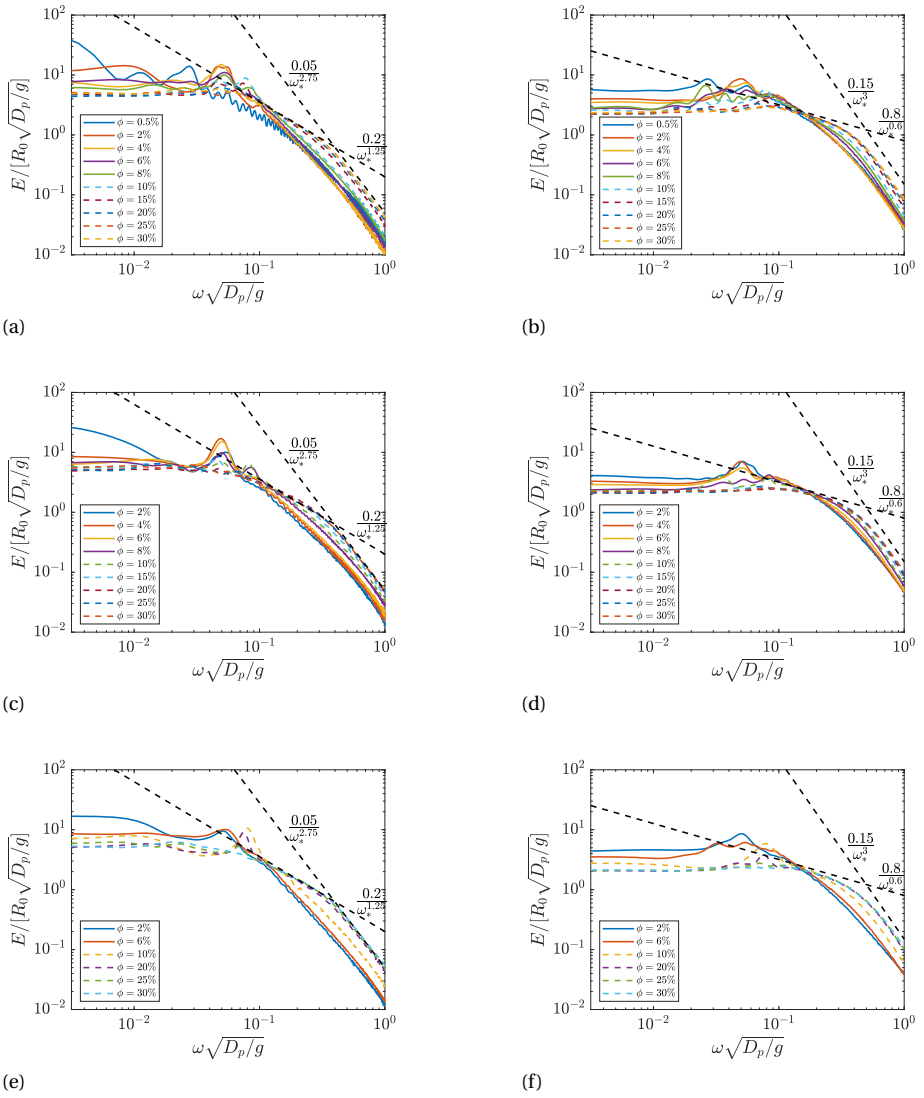

Figure 3.12: Double-log plots of the normalised frequency spectra of the vertical (v_p', left) and horizontal (u_p' and w_p', right) particle velocity fluctuations, shown as function of bulk concentration and Galileo number (increasing from top to bottom). Black dashed lines indicate power-law scaling of the normalised spectra in the normalised frequency for the most dense concentration cases in specific frequency ranges. ((a)) Vertical velocity, $Ga = 144$, ((b)) horizontal velocity, $Ga = 144$, ((c)) vertical velocity, $Ga = 178$, ((d)) horizontal velocity, $Ga = 178$, ((e)) vertical velocity, $Ga = 210$, ((f)) horizontal velocity, $Ga = 210$.

Fig. 3.12 presents the normalised frequency spectra for the vertical (left) and horizontal (right) particle velocity fluctuations as function of bulk concentration and Galileo number (increasing from top to bottom). At all Galileo numbers, clear peak frequen-

cies can be observed in the lower frequency range for $\phi \lesssim 10\%$, while no distinct peaks at all are present at $\phi = 25$ and 30%. This suggests that the frequency peaks for the lower concentration range can be attributed to wake-related hydrodynamic particle interactions. Focusing on $Ga = 144$, for $\phi = 0.5$ and 2% very low peak frequencies with $\omega_* < 0.01$ are present in the vertical velocity spectrum, which are likely related to the presence of persistent columnar structures in which particles settle at an enhanced velocity in these cases, especially for $\phi = 0.5\%$. For $\phi = 2-8\%$, where DKT-type instabilities are active, a clear peak is found in both the horizontal and the vertical velocity spectrum at $\omega_* \approx 0.05$ with a corresponding oscillation period of $\approx 126\sqrt{D_p/g}$. This agrees well with the oscillation period of $\sim 120\sqrt{D_p/g}$ observed earlier in the autocorrelation for the vertical particle velocity at $\phi = 6\%$ for all Ga. For $\phi = 10\%$, a dominant peak frequency is present at $\omega_* \approx 0.08$ in both spectra with a corresponding oscillation period of $\approx 79\sqrt{D_p/g}$. Upon further increasing the bulk concentration beyond 15%, no dominant peak frequencies can be observed anymore and the spectrum varies more gradually with frequency. The spectra for $Ga = 178$ and 210 are qualitatively similar to the spectra for $Ga = 144$. The same peak frequencies can be observed, though the height of the peaks depends on Ga. For $Ga = 210$ we also observe a significant frequency peak at $\omega_* \approx 0.08$ for $\phi = 20\%$.

Interestingly, for $\phi \gtrsim 20\%$, both the normalised horizontal and the normalised vertical velocity spectra collapse for $\omega_* \lesssim 0.02$ and $\omega_* \gtrsim 0.1$, independent of the Galileo number. For $\omega_* \lesssim 0.02$ the spectra are constant and approximately equal to 5 for the vertical velocity and 2 for the horizontal velocity. This is consistent with the values of approximately 8 and 3 for the normalised integral time scale of, respectively, the vertical and the horizontal velocity in the dense regime, see Fig. 3.10 and Eq. (3.12c). For $\omega_* \gtrsim 0.1$, the vertical velocity spectrum varies with the frequency as ${\omega_*}^{-1.25}$ between $0.1 \lesssim \omega_* \lesssim 0.4$ and as ${\omega_*}^{-2.75}$ for $\omega_* \gtrsim 0.4$. For the same frequency range, the horizontal velocity spectrum scales as ${\omega_*}^{-0.6}$ between $0.1 \lesssim \omega_* \lesssim 0.4$ and as ${\omega_*}^{-3}$ for $\omega_* \gtrsim 0.4$. Our results are consistent with an approximate -10/3 slope of the vertical particle velocity spectrum at high frequencies for $Ga = 4.6-153.6$ in Yao et al. [181], though no explanation was provided by them for the observed scaling.

The Ga-independent scaling of the velocity spectra in the dense regime suggests that the particle dynamics is dominated by multi-particle interactions by viscous lubrication and possibly particle collisions. Furthermore, the collapse of the spectra for the low and the higher frequency range indicates that in the dense regime the rms particle velocity and $\sqrt{D_p/g}$ are the characteristic velocity and the characteristic time scale of the particle velocity fluctuations. In fact, this is in line with the Gaussian distribution of the normalised particle velocity and the constant $\tau_L/\sqrt{D_p/g}$ in the dense regime, irrespective of the value of the Galileo number. The change in the power-law scaling exponent at $\omega_* \approx 0.4$, corresponding to an oscillation period of approximately $16\sqrt{D_p/g}$, indicates a change in the underlying dynamics. It is also striking that for $0.1 \lesssim \omega_* \lesssim 0.4$ the power-law scaling exponent for the horizontal velocity spectrum is approximately a factor 2 smaller than the power-law scaling exponent for the vertical velocity spectrum, while for $\omega_* \gtrsim 0.4$ the power-law scaling exponents are nearly the

same. In appendix A we propose a model that predicts an ${\omega_*}^{-3}$ scaling of the spectra for $\omega_* \gtrsim 0.4$. It is based on the inertial response of the particles to small-scale flow structures with a presumed k^{-3} wavenumber spectrum, as has been also observed for homogeneous bubble swarms [101, 144], that are advected by the mean relative fluid flow towards the particles and effectively impose high-frequency force perturbations on the particles. We also discuss the scaling behavior of the spectra for $0.1 \lesssim \omega_* \lesssim 0.4$. It is left for future research to investigate the physical origin of the power-law scalings in more detail and to what extent it can be generalized to other Galileo numbers and density ratios.

3.4.8. ROLE OF PARTICLE COLLISIONS

From Eq. (3.3a) it follows that at statistically steady state the mean vertical hydrodynamic drag force ($\overline{F}_d$) should balance the net gravity force (F_{ng}) acting on the particles:

$$\frac{\overline{F}_d}{\rho_f g D_p^3} = -\frac{\overline{F}_{ng}}{\rho_f g D_p^3} = \frac{\pi}{6}\left(\frac{\rho_p}{\rho_f} - 1\right)(1-\phi), \tag{3.13}$$

where the net gravity force is the downward gravity force minus the upward and concentration dependent Archimedes force related to the upward hydrostatic pressure gradient. Note that the mean collision force acting on the particles is zero as during a collision between two particles the same collision force acts on both particles but in opposite direction and hence their sum is zero. To assess the importance of particle collisions we have therefore evaluated the mean magnitude of the collision force, $\overline{|\mathbf{F}_c|} = \sqrt{\overline{F_{c,x}^2} + \overline{F_{c,y}^2} + \overline{F_{c,z}^2}}$. In Fig. 3.13a we show the mean vertical hydrodynamic drag force and the mean magnitude of the collision force as function of ϕ and Ga. The forces have been normalised with the net gravity force. From this figure we observe first that the normalised mean drag force is constant and equal to 1, which substantiates that the suspension is in a statistically steady state in all cases. Second, we observe that the effect of collision forces seems negligible for $\phi \lesssim 10\%$, in line with the dominant contribution of long-range hydrodynamic particle interactions to the overall particle dynamics (inertial wake suction and DKT-type instabilities). With increasing bulk concentration, collisions become gradually more important, though the mean magnitude of the collision force is still only about 20% of the net gravity force at the highest concentration. Third, we observe that the collision force is nearly independent of Ga, which might be related to the scaling with the net gravity force as this is ultimately the driving force responsible for sedimentation. Besides, in the dense regime, the relevant velocity and length scales are proportional to $\sqrt{gD_p}$ and D_p, respectively. Thus, when the collision force is scaled with gD_p^3 or, alternatively, with the net gravity force that is proportional to gD_p^3, it is expected that the collision force is independent of Ga, at least in the dense regime.

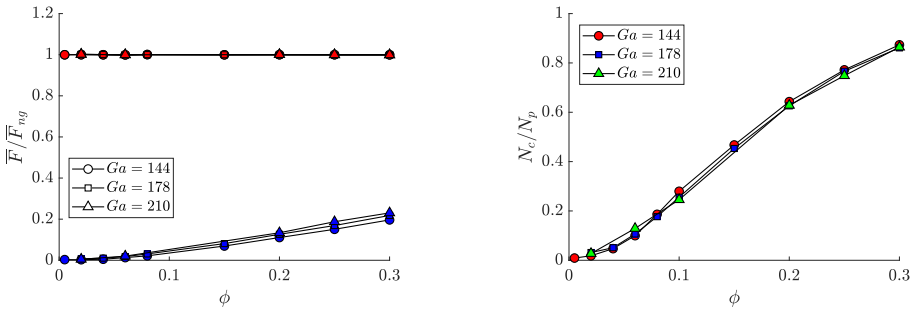

(a) (b)

Figure 3.13: ((a)) Mean vertical drag force ($\overline{F}_d$, red symbols) and mean magnitude of the collision force ($\overline{|\mathbf{F}_c|}$, blue symbols) normalised with the net gravity force ($\overline{F}_{ng}$) and shown as function of ϕ and Ga. Circles, squares and triangles correspond to Ga = 144, 178 and 210, respectively. ((b)) Average number of particles undergoing a collision during a computational time step (N_c), scaled with the total number of particles (N_p) and shown as function of ϕ and Ga.

To further assess the influence of collisions on the particle dynamics, we have also computed the average number of colliding particles by counting at every time instant the number of particles with a non-zero collision force and averaging this number over time. The average number normalised with the total number of particles is shown in Fig. 3.13b. We observe a gradual increase in the number of collisions as function of concentration, which is nearly independent of Ga. At the lowest concentration hardly any particle is colliding, at ϕ = 10% this is about 25% of the total number of particles and at ϕ = 30% this is nearly 90%. The high collision likelihood and the seemingly small mean magnitude of the collision force at ϕ = 30% suggest that collisions are frequent but gentle in the dense regime. This is likely related to viscous lubrication between particles that tends to reduce the relative velocity between two approaching particles prior to their collision. This can be further assessed by means of the impact Stokes number, a measure of the initial relative momentum of the approaching particles to the typical loss of their relative momentum by viscous lubrication [35]:

$$St = \frac{\rho_p \left(\frac{1}{6}\pi D_p^3\right) v_{rel}}{\frac{3}{2}\pi \rho_f \nu_f D_p^2}, \tag{3.14a}$$

where v_{rel} is the initial relative approach velocity. For $St \lesssim 10$ the particles will not rebound upon a collision due to strong viscous damping by lubrication, while $St \gtrsim 10^3$ corresponds to the granular regime where the particles will rebound with their initial approach velocity times the dry coefficient of restitution [106]. For simplicity, we restrict ourselves to collisions in the vertical as velocity fluctuations are strongest in this direction. We model the typical relative velocity between two particles by $v_{rel} = \sqrt{\overline{(v'_{p,1} - v'_{p,2})^2}} \approx \sqrt{2}\, v_{p,rms}$ based on the crude assumption that in the dense regime the chaotic motions of the particles are uncorrelated. Using Eqs. (3.1) and (3.6a) we

can then rewrite Eq. (3.14a) into the following form:

$$St = \frac{\sqrt{2}}{9} \cdot \frac{(\rho_p/\rho_f)\,Ga}{\sqrt{(\rho_p/\rho_f)-1}} \cdot \frac{k|V_T|}{\sqrt{gD_p}} \cdot C_{pv}\phi^{m_{pv}}(1-\phi)^n\,, \tag{3.14b}$$

where the values of $|V_T|/\sqrt{gD_p}$, C_{pv} and m_{pv}, and n, are listed as function of Ga in Table 3.3, 3.4 and 3.5, respectively. Evaluating St for $\phi = 10\%$, we find that $St \approx 10$, 10 and 15 for $Ga = 144$, 178 and 210, respectively. Similarly, for $\phi = 30\%$, we find that $St \approx 6$, 8 and 9, respectively. The low values of St are supporting evidence that in the dense regime particle interactions are indeed dominated by viscous lubrication rather than actual particle collisions, at least for the currently investigated range of Ga and density ratio of 1.5. Based on a similar analysis, Willen and Prosperetti [171] reached at the same conclusion for their simulations at $Ga = 49.7-99.4$ and $\rho_p/\rho_f = 2-5$.

The dominant contribution from viscous lubrication in the dense regime may also be understood from analyzing the Reynolds number based on the "mean collision distance", which we define as the typical distance travelled by two particles from the moment they start approaching each other till the moment that they collide. We estimate this distance by $\sqrt{2}\,\lambda_{\mathrm{mfp}}$, where λ_{mfp} is the "mean free path" travelled by a particle between two consecutive collisions (the collision distance is a factor $\sqrt{2}$ larger to account for the relative motion between particles). Based on kinetic theory of granular gases, see Eq. 13 in Willen and Prosperetti [171], the mean free path is modelled as:

$$\lambda_{\mathrm{mfp}} = \frac{D_p}{6\sqrt{2}\phi} \cdot \frac{2(1-\phi)^3}{(2-\phi)}\,. \tag{3.15}$$

The associated Reynolds number based on the collision distance and relative particle velocity can now be estimated from:

$$Re_{col} = \frac{(\sqrt{2}\lambda_{\mathrm{mfp}})(\sqrt{2}v_{p,rms})}{\nu_f} = \frac{1.5}{(\rho_p/\rho_f)\phi} \cdot \frac{2(1-\phi)^3}{(2-\phi)} \cdot St\,. \tag{3.16}$$

For $\phi = 10\%$, $Re_{col} \approx 75$, 80 and 116, for $Ga = 144$, 178 and 210, respectively. Similarly, for $\phi = 30\%$, we find that $Re_{col} \approx 9$, 11 and 13, respectively. For $\phi = 10\%$, the collision Reynolds number is thus well within the inertial regime, which leaves room for inertial interactions before lubrication starts to become dominant at close distance between the approaching particles. For $\phi = 30\%$, the collision Reynolds number is already in the weakly inertial regime, and thus lubrication sets in much sooner after particles start approaching each other.

3.4.9. KINEMATIC WAVES

As mentioned in the introduction, sedimenting suspensions may exhibit kinematic waves. They manifest themselves as vertically propagating waves in the horizontal plane average concentration, defined by $\Phi(y,t) = \langle\gamma\rangle_h$, where $\gamma(x,y,z,t)$ is the solid phase indicator function (equal to 1 in the solids and 0 in the fluid) and the brackets denote the average over the horizontal directions. To visualise the presence of kinematic waves in the present simulations, in Fig. 3.14a, 3.14c and 3.14e we have plotted

the plane-averaged concentration normalised by the bulk concentration as function of height and time at $\phi = 30\%$ for each Galileo number.

At first sight, the space-time diagrams in Fig. 3.14 look rather noisy. Significant variations in the plane average concentration can be observed of $O(25\%)$ of the bulk concentration. Note that $\phi = 30\%$ corresponds to an average number of $0.3L_xL_z/(\pi D_p^2/8) \approx 477$ spheres passing through a horizontal plane in the computational domain, where $\pi D_p^2/8$ is the average area of the circle formed when randomly cutting a sphere in the horizontal. Thus, a variation of $\pm 25\%$ in the local concentration corresponds to variations of $O(100)$ particles. Careful inspection of the space-time plots shows that there are two distinct wavy patterns present as indicated by the dashed and solid black lines in the panels. First, we observe a stripe pattern originating from small-amplitude waves with a wave length of $O(D_p)$, which are travelling downwards with an average speed equal to V_s as indicated by the black dashed lines. Recall from Fig. 3.2 that in the instantaneous snapshots of the spatial particle distribution relatively large structures are present with groups of particles moving collectively faster or slower than the mean sedimentation velocity. Because of the finite lateral domain size, there is also a finite number of such large structures passing through a horizontal plane. Random fluctuations in this number of passing structures will cause mild fluctuations in the local plane average velocity around the mean sedimentation velocity and, associated with this, mild fluctuations in the local plane average concentration. The stripe pattern is thus expected to gradually fade away when the horizontal dimensions of the computational domain are increased, though we have not tested this. Next to the stripe pattern, we observe larger-amplitude waves with a much larger wave length. We associate these waves with kinematic waves. They appear to travel upwards at a fraction of $|V_s|$ for $Ga = 144$ and 178, while moving slowly downwards for $Ga = 210$, as indicated by the black solid lines in the panels.

As already mentioned, the signal of Φ is rather noisy. The noise is responsible for a loss of spatio-temporal coherence of the kinematic waves. To isolate the component of Φ related to kinematic waves it seems therefore natural to apply an additional local time average that filters out the "high-frequency noise" while it preserves the low-frequency signal of the kinematic waves: $\widehat{\Phi} = \int_{-T/2}^{T/2} \Phi(t+\tau)d\tau/T$ with T the filter width. The filter width should satisfy $\tau_{L,vv} \ll T \ll T_{KW}$, where T_{KW} is the kinematic wave period. In appendix B we argue that $\widehat{\Phi}$ is approximately governed by the following transport equation:

$$\frac{\partial \widehat{\Phi}}{\partial t} + V_{KW}\frac{\partial \widehat{\Phi}}{\partial y} \approx \frac{\partial}{\partial y}\left(\mathscr{D}_{yy}\frac{\partial \widehat{\Phi}}{\partial y}\right), \tag{3.17a}$$

where $\mathscr{D}_{yy}$ is the particle diffusivity in the vertical given by Eq. (3.9) and $V_{KW} \approx \partial\left[V_s(\phi)\phi\right]/\partial\phi$ is the speed at which kinematic waves are propagating in the vertical [98]. Based on the Richardson-Zaki relation for V_s given by Eq. (3.1), which is valid for $\phi \gtrsim 10\%$, the kinematic wave speed can be further approximated by:

$$V_{KW} \approx \left[\frac{1-(n+1)\phi}{1-\phi}\right] V_s(\phi). \tag{3.17b}$$

where n is the power-law exponent in the Richardson-Zaki relation.

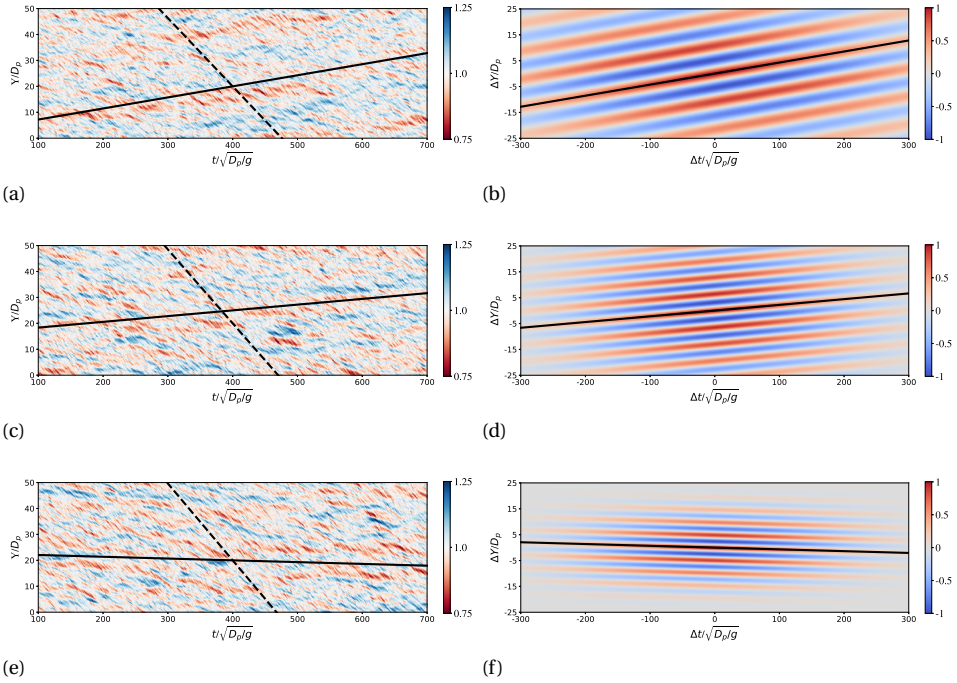

Figure 3.14: ((a)), ((c)) and ((e)) Space-time plot of the instantaneous horizontal plane average concentration normalised with the bulk concentration, $\Phi(y,t)/\phi$, at $\phi = 30\%$ for $Ga = 144$, 178 and 210, respectively. The slope of the black lines corresponds to $V_s/\sqrt{gD_p}$ (dashed) and $V_{KW}/\sqrt{gD_p}$ (solid). ((b)), ((d)) and ((f)) Space-time plot of the 7^{th} space-time autocorrelation of plane average concentration field shown in ((a)), ((c)) and ((e)), respectively. The slope of the black solid line corresponds to $V_{KW}/\sqrt{gD_p}$.

Instead of applying local time averaging to the space-time plots in Fig. 3.14, we use here the method of repeated space-time autocorrelations to visualise the spatio-temporal structure of the kinematic waves. The method is explained in detail in appendix C. The main principle of the method is that the spatio-temporal structure of travelling waves is preserved in a space-time autocorrelation. By performing repeated autocorrelations, the dominant wave component is amplified relative to other less dominant components and "noise" is filtered out. We define the first autocorrelation as the ordinary autocorrelation of the raw signal and the n^{th} autocorrelation as the autocorrelation of the $(n-1)^{th}$ autocorrelation. The rank n can be tuned to amplify the dominant travelling wave component to the desired degree, see appendix C. An advantage of the repeated autocorrelation technique is that no a priori assumption is required on the properties of kinematic waves as compared to filtering in time, space, frequency and/or wave number space [172].

The right panels in Fig. 3.14 show the 7^{th} space-time autocorrelation correspond-

ing to the space-time plots of the plane average concentration in the left panels. From the smooth fields thus obtained, we determined the wave speed of the dominant kinematic wave from the slope of the least-squares regression line through the correlation maxima. The results are shown in Fig. 3.15a. Kinematic waves travel always slower than the mean sedimentation velocity and their wave speed goes down with increasing concentration. Interestingly, in the range of $\phi = 20-30\%$ their velocity reduces to zero, corresponding to a standing wave, and they start to propagate upwards upon further increasing the bulk concentration as also visible from Figs. 3.14b and 3.14d. The agreement with the model predictions from Eq. (3.17b) is reasonably good, especially for $Ga = 178$. The model overpredicts the normalised wave speed in the lower concentration range as well as at $\phi = 30\%$. We note that less good agreement has to be expected for the lower concentration range anyway, as the model is based on Eq. (3.1) that underestimates the sedimentation velocity for $\phi \lesssim 10\%$. Differences between the model and the DNS may also be related to model assumptions such as the quasi-steady response of the settling speed of the particles to changes in the local concentration and the assumption that perturbations in the local concentration are small relative to the bulk concentration. We have also determined the wave length of the dominant kinematic wave from the average vertical distance between consecutive maxima in the 7^{th} space-time autocorrelation at zero time lag. Figure 3.15b shows the result. Large variations in kinematic wave length can be observed, varying from about 5 to 40 particle diameters. At each Ga, the lowest wave length is found for $\phi = 30\%$. No clear trend can be seen in the dependency of the wave length of Ga.

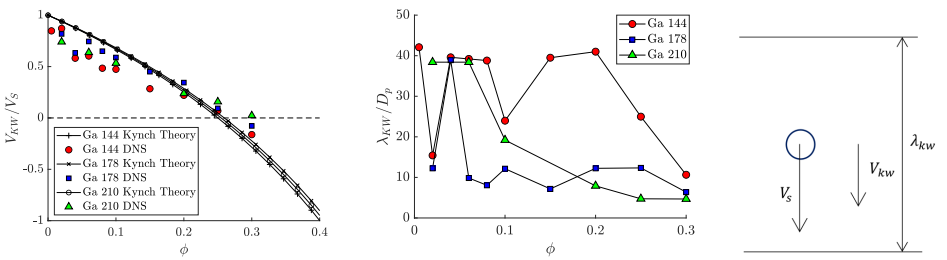

(a) (b) (c)

Figure 3.15: ((a)) Kinematic wave speed normalised by the mean sedimentation velocity and shown as function of ϕ and Ga. Positive (negative) values correspond to downward (upward) travelling waves. Black lines represent the model predictions from Eq. (3.17b). ((b)) Kinematic wave length normalised with the particle diameter and shown as function of ϕ and Ga. ((c)) Illustration of the perturbation of a particle by the passage of a kinematic wave. On statistical average, the particles are moving with the mean sedimentation velocity V_s. The presence of vertically propagating plane kinematic waves with a wave length λ_{KW} and speed V_{KW} will periodically perturb the particles with an oscillation period of $\lambda_{KW}/|V_s - V_{KW}|$.

In section 3.4.6 we suggested that the oscillatory behavior observed in some of the correlations can be related to the possible presence of kinematic waves. Figure 3.15c illustrates how the passage of vertically propagating, plane kinematic waves will periodically perturb the particles. The corresponding angular perturbation frequency is

given by:

$$\omega_{KW} = \frac{2\pi|V_s - V_{KW}|}{\lambda_{KW}}. \tag{3.18}$$

In Fig. 3.16 we have plotted the peak frequencies of the particle velocity spectra shown in Fig. 3.12 as function of the bulk concentration for each investigated Galileo number. For comparison we also plotted the expected perturbation frequency from the kinematic waves as given by Eq. (3.18.

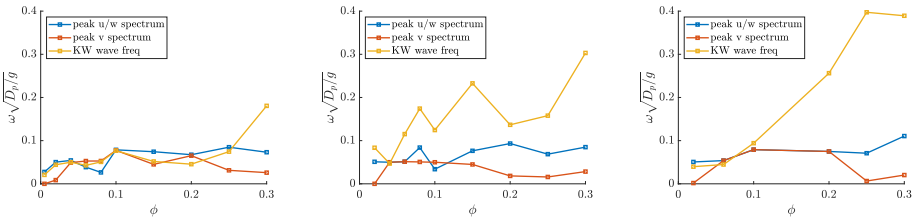

(a) (b) (c)

Figure 3.16: Normalised frequencies of dominant peak in the frequency spectra of the particle velocity shown in Fig. 3.12, plotted as function of the bulk concentration. In the legend, u/w and v refer to the spectrum for the horizontal and the vertical velocity, respectively. The purple line is the perturbation frequency from the passage of kinematic waves. ((a)) $Ga = 144$, ((b)) $Ga = 178$, ((c)) $Ga = 210$.

Interestingly, for $Ga = 144$ we find an almost perfect match of the expected kinematic wave frequency with the peak frequency of either the horizontal or the vertical velocity spectrum. For $\phi = 4$ and 10% there is a good match with both velocity spectra. Furthermore, when also considering the frequency of the second largest peak (not shown here), the match between the velocity spectra is further improved (e.g., for $\phi = 2\%$, the 2^{nd} peak in the vertical velocity spectrum coincides with the peak frequency of the horizontal velocity spectrum). At $\phi = 25$ and 30% the agreement of the peak frequencies with the kinematic wave frequency is poor, but recall that the corresponding spectra vary smoothly without any distinct frequency peak. Different from $Ga = 144$, for $Ga = 178$ only a good match of the peak frequencies with the kinematic wave frequency is found for $\phi = 4\%$. For $\phi \geq 6\%$, the normalised kinematic wave frequency is beyond 0.1, which is in the range where for $Ga = 178$ the velocity spectra vary smoothly with frequency. At $Ga = 210$, a good match is found only for the lower concentration range till and with $\phi = 10\%$. To conclude, for all Ga, a good match is found only in the lower concentration range, where we expect that wake trapping and DKT-type instabilities are active. Based on this, we hypothesize that kinematic waves may trigger such instabilities at particle level, while conversely such instabilities may be responsible for the onset of kinematic waves. This is in line with our previous analysis of the lagged crosscorrelations discussed in section 3.4.6.

Finally, we assess from Eq. (3.17a) the effect of particle dispersion on damping of kinematic waves. To this purpose, we define a "kinematic wave dispersive damping number", $\mathscr{P}$, as the ratio of the advection to the diffusion time scale based on

Eq. (3.17a):

$$\mathscr{P} = \frac{\lambda_{KW}/|V_{KW}|}{\lambda_{KW}^2/\mathscr{D}_{yy}} = \frac{v_{p,rms}^2 \tau_{L,vv}\, \omega_{KW}}{\pi |V_s - V_{KW}||V_{KW}|}. \tag{3.19}$$

We found that $\mathscr{P} < 0.47$ for $\phi \leq 20\%$, while $\mathscr{P} > 0.63$ at $\phi = 25$ and 30% for all Ga. Dispersive damping may thus explain why no significant imprint of kinematic waves is found on the particle velocity spectra in the dense regime.

3.5. CONCLUSIONS AND DISCUSSION

We presented DNS results for sedimenting suspensions of solid spheres in a viscous fluid. The particle/fluid density ratio was fixed at 1.5, while the bulk concentration was varied from 0.5-30% and three different Galileo numbers were considered in the range of 144-210. Based on our comprehensive analysis, our main conclusions are:

1. The suspension dynamics for $\phi = 2-30\%$ depends mostly on the bulk concentration, while at fixed bulk concentration qualitatively similar behavior is observed for all three Galileo numbers. In qualitative agreement with previous studies in literature [182, 162], three concentration regimes with a different microstructure can be distinguished: (i) the dilute concentration regime for $\phi \lesssim 2\%$ with preferential settling of particles in vertical trains, (ii) the moderate concentrations regime for $2\% \lesssim \phi \lesssim 10\%$ with a preference of particles to settle side-by-side in horizontal particle pairs at a distance of $\sim 1.5D_p$, and (iii) the dense concentration regime for $\phi \gtrsim 10\%$ with a nearly random ("hard-sphere") distribution of the particles in space. The transition across regimes is gradual. For instance, for $\phi = 2\%$ we found an enhanced likelihood for settling in both vertical trains of a few particles and in horizontal particle pairs.

2. The vertical trains in the dilute regime are formed by the wake-trapping mechanism. While for two isolated particles wake trapping is typically followed by a drafting-kissing-tumbling (DKT) instability, the vertical trains in dilute suspensions are rather stable, suggesting that "kissing" and "tumbling" is suppressed. The stability is reflected in the super-Gaussian pdf of the horizontal particle velocity. The negatively skewed pdf of the vertical particle velocity provides evidence of an enhanced settling speed of particles contained within the vertical trains. The formation of vertical trains is most pronounced for $Ga = 144$ and $\phi = 0.5\%$. At the same density ratio and bulk concentration, Uhlmann and Doychev [162] found no significant change in the settling speed for $Ga = 121$ and a 12% increase for $Ga = 178$. Our result for $Ga = 144$ does not show enhanced settling, consistent with the presumed threshold of $Ga \approx 155$ for this to happen [162]. With increasing concentration, the extent of the fluid wake behind the particles decreases rapidly and so does the extent of the vertical trains till they finally disappear at a bulk concentration of $2-4\%$. Multiparticle interactions might also contribute to destabilization and breakdown of the vertical clusters when the bulk concentration is increased.

3. The particle-conditioned mean concentration and particle velocity field indicate that in the moderate concentration regime the horizontal particle pairs origi-

nate from a DKT-type instability. The active role of DKT in this regime is further supported by the strong anti-correlation peak in the autocorrelation and crosscorrelation of the particle velocity fluctuations. The crosscorrelation coefficient exhibits a clear peak in the lower concentration range, though the relatively low value below 0.2 suggests that DKT is not a very strong mechanism and has to compete with chaotic motions from multiparticle interactions. The decreasing extent of the fluid wake behind the particles and the increasing importance of multiparticle interactions might be responsible for gradual weakening of the DKT mechanism with increasing bulk concentration. normalised with $\sqrt{gD_p}$ the particle rms velocity exhibits a Ga-dependent peak in the moderate concentration range, which underlines the importance of inertial hydrodynamic interactions between particles. The nearly Gaussian pdf of the particle velocity exhibits no sign of a significantly different average settling speed of the particle pairs compared to the mean sedimentation velocity.

4. In the dense concentration regime particle velocity fluctuations are dominated by short-range multiparticle interactions. The observed asymmetry in the concentric ring-like pattern of the particle-conditioned mean concentration, with a higher preference for horizontal than for vertical particle alignment, suggests that DKT-type instabilities are still present, though weak and confined in space to an interparticle distance of about 1-2 particle diameters at $\phi = 30\%$. The anti-correlation peak in the autocorrelation and crosscorrelation of the particle velocities is very small and consistent with weak and spatially confined DKT instabilities. The pdfs of the particle velocities exhibit a Gaussian distribution. The frequency spectra of the particle velocity fluctuations vary smoothly with frequency in the absence of distinct frequency peaks. Furthermore, they exhibit clear power-law scaling: the spectra of the vertical and horizontal velocity components scale with, respectively, ${\omega_*}^{-1.25}$ and ${\omega_*}^{-0.6}$ for $0.1 \lesssim \omega_* \lesssim 0.4$, and with, respectively, ${\omega_*}^{-2.75}$ and ${\omega_*}^{-3}$ for $\omega_* \gtrsim 0.4$. We proposed a model to explain the ${\omega_*}^{-3}$ scaling from the inertial response of the particles to small-scale fluid perturbations. It is left for future research to investigate the physical origin of the power-law scaling in more detail. The normalised frequency spectra are nearly independent of Ga in the dense regime, in particular for the low and the higher frequency range. The same holds for the particle rms velocities when normalised with $\sqrt{gD_p}$. This indicates that $\sqrt{gD_p}$ and $\sqrt{D_p/g}$ are the characteristic velocity and time scale for fluctuating particle motions in the dense regime, at least when the particle/fluid density ratio is kept constant. Particle collisions occur frequently but are gentle. Estimates of the impact Stokes number and the collision Reynolds number indicate that particle interactions are dominated by viscous lubrication rather than particle collisions.

5. Kinematic waves have been detected in all investigated cases, though overlaid with noise from unrelated particle motions. The noise is likely responsible for a loss of spatio-temporal coherence of the waves. The wave speed found from the method of repeated autocorrelations is in reasonable agreement with the prediction from Kynch theory using the Richardson-Zaki relation for the mean sed-

imentation velocity. The kinematic waves have a clear imprint on the frequency spectra of the particle velocity for concentrations till $\phi \approx 10\%$, being responsible for peak frequencies of roughly $O(0.05)\sqrt{g/D_p}$. The oscillatory behavior of the autocorrelation and especially the crosscorrelation of the particle velocity in the moderate concentration regime suggests that kinematic waves possibly trigger DKT-type instabilities, while conversely DKT-type instabilities might also generate kinematic waves. At the highest concentrations in the dense regime, we found no imprint of kinematic waves on the frequency spectra of the particle velocity. Weak DKT-type instabilities and strong dispersive damping might be the reason.

6. The Richardson-Zaki relation, Eq. (3.1), provides a good fit to the DNS data for $\phi \gtrsim 10\%$, while it underestimates the mean sedimentation velocity in the lower concentration range with the deviation increasing for decreasing concentration. This substantiates the hypothesis of Yin and Koch [182] that the Richardson-Zaki relation is associated with a "hard-sphere distribution" of the particles, and that DKT-type instabilities are responsible for the underestimation of the sedimentation velocity in the lower concentration range. We also found evidence of a power-law scaling in the bulk concentration of the particle rms velocity normalised with the mean sedimentation velocity, in particular for the dense regime.

It is striking that for given bulk concentration the suspension microstructure is qualitatively similar for all three Galileo numbers. While for a single settling particle the particle's wake structure is very different for the three investigated Galileo numbers (a steady axi-symmetric wake for $Ga = 144$, a steady planar oblique wake for $Ga = 178$, and an oscillating planar oblique wake for $Ga = 210$), in the moderate and dense concentration regime the fluid wake structure is actually very similar, see Fig. 3.4. This is likely related to physical obstruction and perturbation of the particle wake by nearby neighbouring particles. Based on this we hypothesize that the wake structure is controlled by the bulk concentration instead of the Galileo number beyond a Ga-dependent threshold concentration at which the particle mean free path is of the same order as the extent of the wake of an isolated settling particle. When the extent of the wake is roughly estimated by $O(10\,D_p)$, we find from Eq. (3.15) a threshold concentration of about $O(1\%)$, which seems quite plausible. Indeed, we find fairly little influence of Ga on the wake structure for $\phi = 2\%$, while the microstructure and suspension behavior for $Ga = 144$ and $\phi = 0.5\%$ is quite different from the case of $Ga = 178$ and $\phi = 0.5\%$ studied by Uhlmann and Doychev [162]. It remains to be seen to what degree our classification and characterization of the different settling regimes hold for Galileo numbers outside the presently studied range. More in particular, inertial hydrodynamic particle interactions associated with wake trapping and DKT are expected to ultimately vanish when the Galileo number is gradually lowered towards the Stokes regime. The DNS results of Yin and Koch [182] indicate that DKT and related preference for horizontal particle pair alignment are still present at $Ga = 11.5$ ($Re_T \approx 5$), while absent for $Ga \leq 6.3$ ($Re_T \lesssim 2$). Consequently, the range of the random "hard-sphere" distribution is extended towards significantly lower concentrations in the low (viscous-dominated and weakly inertial) Ga regime as compared to the $\gtrsim 10\%$ concen-

tration range for the higher (inertia-dominated) Ga regime presently studied.

Finally, it would be interesting to study the effect of varying the particle/fluid density ratio on the different settling regimes. The density ratio is known to affect the wake and path of a single settling path beyond the steady oblique regime and will thus likely have an effect on the suspension dynamics in the dilute concentration regime. The density ratio also influences the particle response time and hence will likely influence inertial hydrodynamic particle interactions too.

4

CHARACTERISTICS OF SLURRY TRANSPORT REGIMES: INSIGHTS FROM EXPERIMENTS AND INTERFACE-RESOLVED DIRECT NUMERICAL SIMULATIONS[1]

A common way to transport solids in large quantities is by using a carrier fluid to transport the solids as a concentrated solid/liquid mixture or slurry through a pipeline. Typical examples are found in dredging, mining and drilling applications. Dependent on the slurry properties and flow conditions, horizontal slurry pipe flow is either in the fixed-bed, sliding-bed or fully-suspended regime. In terms of non-dimensional numbers, the flow is fully characterized by the bulk liquid Reynolds number (Re), the Galileo number (Ga, a measure for the tendency of particles to settle under gravity), the solid bulk concentration (ϕ_b), the particle/fluid density ratio (ρ_p/ρ_f), the particle/pipe diameter ratio (D_p/D_{pipe}), and parameters related to direct particle interactions such as the Coulomb coefficient of sliding friction (μ_c). To further our fundamental understanding of the flow dynamics, we performed experiments and interface-resolved Direct Numerical Simulations (DNS) of slurry flow in a horizontal pipe. The experiments were performed in a transparent flow loop with $D_{pipe} = 4$ cm. We measured the pressure drop along the pipeline, the spatial solid concentration distribution in the cross-flow

[1] This chapter has been submitted to International Journal of Multiphase Flow in August 2023 as: T. Shajahan, T. Schouten, S.K. Raaghav, C. van Rhee (†), G.H. Keetels and W.-P. Breugem. Characteristics of Slurry Transport Regimes: Insights from Experiments and Interface-Resolved Direct Numerical Simulations. Available at SSRN 4556143. The experiments described in sections 4.3 and 4.5 of this chapter were performed by ir. T. Schouten under supervision of dr. ir. G.H. Keetels and late prof. dr. ir. C. van Rhee of the Dredging Engineering laboratory of TU Delft as part of a collaborative research program.

plane through Electrical Resistance Tomography (ERT), and used a high-speed camera for flow visualization. The slurry consisted of polystyrene beads in water with $D_p = 2$ mm, $\rho_p/\rho_f = 1.02$, Ga between 40-45 and ϕ_b between 0.26-0.33. The different flow regimes were studied by varying the flow rate, with Re varying from 3272 till 13830. The simulations were performed for the same flow parameters as in the experiments. Taking the experimental uncertainty into account, the results from the DNS and the experiments are in reasonably good agreement. The results for the pressure drop agree also fairly well with popular empirical models from literature. In addition, we performed a parametric DNS study in which we solely varied Re and Ga. In all flow regimes, a secondary flow of Prandtl's second kind is present, ascribed to the presence of internal flow corners and a ridge of densely packed particles at the pipe bottom during transition towards the fully-suspended regime. In the bulk of the turbulent flow above the bed, secondary flow transport of streamwise momentum dominates over turbulent diffusion in regions where the secondary flow is strong and vice versa where it is weak. The transition between flow regimes appears to be governed by the competition between the net gravity force on the particles and shear-induced particle migration from particle-particle interactions. This competition can be expressed by the Shields number, θ. For $\theta \lesssim 0.75$, gravity is dominant and the flow is in the fixed-bed regime. For $\theta \gtrsim 0.75$, shear-induced migration becomes progressively more important for increasing θ. Low-concentration zones flanking the sliding bed start to form at the top corners of the bed, and gradually expand downwards along the pipe wall till the pipe bottom is reached. For $\theta \gtrsim 1.5$, shear-induced migration is responsible for lifting the particle bed away from the wall, associated with the onset of the suspended regime. For $\theta \gg 1$, gravity is of minor importance and the mean flow eventually reaches axi-symmetry with a high-concentration particle core at the pipe center and negligible secondary flow.

4.1. INTRODUCTION

Slurry transport refers to the flow of a concentrated mixture of insoluble solid matter in a liquid. A thorough understanding of slurry flow physics is relevant to the design and operation of slurry pipelines in many applications such as the transport of domestic waste in sanitation systems [139], excavated soil in dredging [121], coal in mining [26], debris in drilling [66] and food and materials in process industry [102]. Slurries can also be observed in nature such as the transport of sediments in rivers. The fundamental challenges in studying slurry flows arise from, first, the carrier fluid, which is typically turbulent and characterized by a broad spectrum of 3D fluctuating motions and flow structures with different length and time scales [135]. Here, the principal mechanisms and coherent flow structures by which turbulence in slurry flows is maintained and how solids are distributed across the pipe [121], are still not fully understood. Second, the hydrodynamic particle-particle interactions (e.g., lubrication) and collisions are complex [155]. Third, the solids exhibit typically a distribution in shape, size and mass density. These features of the flow result in a multitude of non-linear fluid/solid (two-way) and solid/solid (four-way) interactions [8, 49]. Another complicating aspect is that slurries are generally opaque, which prohibits the use of optical diagnostics such as Particle Image Velocimetry [37].

In the present study, we focus our attention on the transport of slurries in horizontal pipelines. This is of relevance to the dredging industry in the Netherlands to maintain coastal and inland waterways and so historically the dynamics of slurry transport have been of long-standing interest. The behaviour of slurry flows can vary significantly depending on the operating conditions and slurry characteristics and may severely impact the operation of slurry pipelines. For instance, formation of stationary deposits may block the pipe and a sliding bed layer may increase wear of pipelines. Additionally, it is desired to estimate the pressure drop accurately to optimally position booster pumps along the pipeline.

Based on their behavior, slurry flows have been broadly classified into different slurry transport regimes. However, there has been a lot of ambiguity in defining the different transport regimes, ranging from three regimes defined by Doron and Barnea [41] to even nine regimes defined by Ramsdell and Miedema [140]. For simplicity we defer to the characterization of the three basic transport regimes as defined by Doron and Barnea [41], which are the fixed-bed regime (where most particles are settled at the pipe bottom and are at rest), the sliding-bed regime (where a fraction of the particles is suspended in the flow and a bed of particles slides along the pipe bottom), and the fully-suspended regime (where all particles are completely suspended in the flow).

The complexity in the dynamics of the flow regimes arises from the interplay between turbulence, buoyancy effects, and particle/particle and particle/wall lubrication and collision forces. In terms of non-dimensional numbers, the flow dynamics are governed by the bulk liquid Reynolds number $Re = v_{bl} D_{pipe}/\nu_f$, the Galileo number $Ga = \sqrt{(\rho_p/\rho_f - 1)|\tilde{\mathbf{g}}| D_p^3/\nu_f^2}$ that measures the tendency of particles to settle under gravity [138], the bulk solid volume concentratrion $\phi_b = (\pi N D_p^3/6)/(\pi D_{pipe}^2 L_{pipe}/4)$ with N the number of particles in a pipe segment of length L_{pipe}, the particle-to-pipe diameter ratio D_p/D_{pipe}, the solid-to-fluid density ratio ρ_p/ρ_f and parameters related to direct particle/particle interactions such as the Coulomb coefficient of sliding friction μ_c, where v_{bl} is the liquid bulk velocity, D_{pipe} is the pipe diameter, ν_f is the kinematic viscosity of the liquid, D_p is the particle diameter and $\tilde{\mathbf{g}}$ is the gravitational acceleration.

The early research on slurry transport in pipelines was focused on the development of empirical and semi-empirical models for the Limit Deposit Velocity (LDV) [44, 177, 159], often defined as the bulk mixture velocity below which a bed starts to form, and the pressure drop along the pipeline [43, 166, 42, 63]. Some models, such as proposed by Durand and Condolios [44] and Führböter [61] are still widely used in the industry. However, most models contain empirical coefficients obtained from a best fit with available experimental data and hence rely heavily on the accuracy of the experimental data used. Furthermore, they work reasonably well under conditions for which these coefficients have been determined, but may fail when applied to slurries with different characteristics and under other flow conditions [121].

In the later research on slurry transport, mechanistic layer models were developed, which treat different strata of the pipe as different layers having distinct physical dynamics. Wilson et al. [176] proposed a two-layer and a three-layer model based on force equilibrium for the bed. Doron et al. [42] introduced a two-layer model considering a bed layer at the bottom and a heterogeneous mixture above. This work was further extended by Doron and Barnea [40] to a three-layer model that included a stationary layer at the bottom, a moving bed layer, and a heterogeneous mixture layer on top. Furthermore, multicomponent models were proposed for slurries with a broad particle size distribution, in which distinction is made between, e.g., fluid, pseudo-homogeneous, and fully stratified components [174]. Since the layer models are bound by physical laws, their application may be extended beyond the parameters of any specific setup. However, the layer models are still strongly dependent on many assumptions and closure relations in their governing equations. An overview of the above described models is provided by Meidema [121].

Computational Fluid Dynamics (CFD) simulations facilitate a more detailed analysis of the flow regimes in slurry transport. In recent years, Eulerian-based continuum models have become increasingly popular to simulate liquid-solid flows, see, e.g., the review by Messa and Matoušek [119]. Ling et al. [110] proposed a simplified 3D Algebraic Slip Mixture (ASM) model combined with the Renormalisation Group (RNG) $k-\epsilon$ turbulence model, showing good predictions for the mean pressure gradient in fully developed turbulent flows. In other studies, the Two-Fluid Model (TFM) has been used for slurry flow modeling in which the solid and liquid phases are treated as two interpenetrating fluids. Ekambara et al. [48] conducted TFM simulations using the Kinetic Theory of Granular Flows (KTGF) for modelling the solids stress tensor, achieving overall good agreement with experimental data for slurry flow. Kaushal et al. [90] simulated slurry pipe flow using the ASM and TFM/KTGF models to test the performance of the different modelling approaches. Capecelatro and Desjardins [24, 25] developed an Euler-Lagrange Large Eddy Simulation (LES) framework. They model the fluid phase as a continuum as in the TFM approach, while a Discrete Particle Model (DPM) is used to track particles individually from the forces acting on them. The latter enables the treatment of particle collisions in a direct manner. Unlike the RANS approach, in their LES approach the large-scale turbulent motions are explicitly resolved. The same Euler/Lagrange LES framework was also applied in a later study on slurry pipe flow by Arolla and Desjardins [4]. Uzi and Levy [164] combined DPM for the particles with a RANS approach for the fluid phase using the $k-\epsilon$ turbulence model. The effect of the particles on the liquid flow was modelled through the inclusion of a liquid-particle interaction source term at the right-hand side of the momentum equations. Finally, Zhang et al. [189, 191, 190] employed an Euler-Lagrange framework to study the behavior of particle-laden gas-solid flows in a horizontal pipe. They used a fine computational grid for the fluid phase and referred to their approach as Direct Numerical Simulation (DNS) combined with four-way coupled Lagrangian Particle Tracking (LPT). However, the equations solved in their approach are similar as in the LES/DPM approach of Capacelatro and Desjardins [24] but with neglectance of the subfilter-scale Reynolds stress. This approximation is expected to hold only for sufficiently small

particles, in which case the implicit filter length associated with the Volume-Averaged Navier-Stokes (continuum) equations is small compared to the length scales of turbulence [21].

From the above brief overview of different CFD approaches used to simulate slurry pipe flow, it appears that the Euler-Lagrange LES/DPM approach of Capecelatro and Desjardins [25] and Arolla and Desjardins [4] is the most detailed one. An even more detailed approach would be interface-resolved Direct Numerical Simulation (DNS) [116] in which the flow is resolved completely by solving the Navier-Stokes and Newton-Euler equations for the fluid and the individual particles, respectively. Obvious advantages of interface-resolved DNS over LES are that (a) no turbulence modelling is required in DNS, and (b) the flow around the particles is explicitly resolved, avoiding the need of parameterizing the particle/fluid interaction forces as in LES. Interface-resolved DNS was used by Kidanemariam and Uhlmann [94, 95] to study sediment pattern formation in channel flow. However, to the best of the authors' knowledge, interface-resolved DNS has not been applied yet to slurry pipe flow.

An intriguing aspect of particle-laden pipe flows is the presence of a mean secondary flow [90, 191, 190, 111], i.e., mean fluid and particle motions perpendicular to the main flow direction. Secondary flows have been widely studied for single-phase flows. Commonly, a distinction is made between secondary flow of Prandtl's first kind, originating from centrifugal forces acting on the flow in a curved channel, and secondary flow of Prandtl's second kind in non-circular ducts related to the generation of mean streamwise vorticity by spatial gradients in Reynolds stresses [136, 17, 124, 103]. Nikitin et al. [126] provide a recent review of experimental, theoretical and numerical studies on secondary flows of the second kind in a number of different flow geometries and also discuss the effect of variations in surface roughness. For square ducts, the secondary flow in the vicinity of a corner is characterized by a pair of two counter-rotating streamwise vortices centered around the corner bisector. This can be explained from turbulent (fluctuating) fluid motions along arc-shaped paths near the corner, causing a mean excess pressure in the corner through centrifugal forces and which subsequently drives an outward-directed mean flow parallel to the adjacent walls [126].

For single-phase duct flows, turbulent motions are a prerequisite for the appearance of a secondary flow. Interestingly, for ducts flows laden with neutrally-buoyant particles, the interface-resolved DNS study of Kazerooni et al. [92] shows that a secondary flow is also present in the laminar regime. They ascribed this to spatial gradients in particle-induced stresses similar to the generation of secondary flow in the turbulent regime by spatial gradients in Reynolds stresses. This study was extended by Fornari et al. [58] to duct flow of neutrally-buoyant suspensions in the turbulent regime. The particles were found to preferentially accumulate near the duct corners and to enhance the secondary flow intensity at the lower bulk solid volume fractions (0.05 and 0.1) compared to the unladen case, while they accumulated preferentially in the core and reduced the secondary flow intensity at the highest bulk solid volume fraction (0.2). Similar findings are reported in the interface-resolved DNS study of Lin

et al. [108] for the low and moderate concentration range (0.0078−0.0707). In another study, Lin et al. [109] found that heavy particles break down the up-down symmetry of the secondary flow patterns. Sedimentation causes a stronger downward flow in the top-central region of the duct and an enhanced upward flow along the side walls. The breakdown of up-down flow symmetry and an enhanced upward flow along the side walls was also found by Zade et al. [185] in a combined experimental/numerical study of relatively heavy particles in turbulent duct flow. The enhanced upward secondary flow was likely responsible for a higher elevation of the suspended particles near the side walls.

Compared to particle-laden duct flows, the presence of a mean secondary flow in particle-laden pipe flows has received much less attention. Liu et al. [111] studied the behavior of heavy particles in a turbulent gas flow through a semi-circular pipe section using LES combined with one-way coupled Lagrangian Particle Tracking. The presence of a mean secondary flow was found to have a significant impact on the spatial particle distribution and on particle deposition and resuspension from the pipe floor. In two numerical studies of horizontal gas-solid pipe flow based on a four-way coupling Euler-Lagrange approach, Zhang et al. [191, 190] identified different flow regimes as function of the governing flow parameters and explored the characteristics and underlying mechanisms of the mean secondary flow in each regime. To our knowledge, secondary flow patterns have not yet been systematically explored for liquid-solid slurry pipe flows.

The aim of this work is to gain insight into the structure and dynamics of slurry pipe flow in the different transport regimes by means of both experiments and interface-resolved DNS. We want to address the following research questions: (1) How do the results from the experiments compare to the results from the DNS at the same flow conditions? (2) What are the main characteristics of the different flow regimes? (3) More specifically, how do mean secondary flow patterns evolve across the different flow regimes and what are the physical mechanisms responsible for their creation? (4) What is the relative importance of the mean secondary flow, the Reynolds stress (from turbulent motions) and the particle stress to transport of mean streamwise momentum across the pipe? (5) What is the effect of solely varying Re or Ga on the dynamics of slurry pipe flow? (6) What are the physical mechanisms governing the transition between flow regimes? And, related to this, what dimensionless number can be used as an appropriate metric for the transition between flow regimes?

The experiments were performed in a 4cm-diameter circulating slurry flow loop using 2mm-diameter polystyrene balls in water. The polystyrene/water density ratio is only slightly larger than one. Therefore a fully-suspended state could be reached at fairly low Reynolds number within the computational reach of DNS. For the DNS a computationally efficient Immersed Boundary method (IBM) was used for the fluid/solid coupling on a fixed grid. A frictional soft-sphere collision model was employed to model particle-particle interactions. The same flow conditions were used for the DNS as in the experiments to allow for a comparison of the numerical results with the ex-

perimental data.

The remainder of this manuscript is structured as follows. In sections 4.2, 4.3 and 4.4, we describe, respectively, the governing equations, the experimental slurry flow loop and the computational setup. Following which, a comparison of the experiments and the DNS is provided in section 4.5. Furthermore, results from additional DNS are provided in section 4.6 to study the influence of Re and Ga on the dynamics of slurry transport. Finally, the main conclusions and a discussion are given in section 4.7.

4.2. GOVERNING EQUATIONS

The particles in the present study are non-colloidal (non-Brownian) spheres, which are (nearly) monodisperse in size and density. The particles' motions are governed by the Newton-Euler equations. The carrier fluid is a Newtonian liquid and governed by the incompressible Navier-Stokes equations. The governing equations are made non-dimensional using D_p as a characteristic length scale, v_{bl} as a characteristic velocity scale and the ratio D_p/v_{bl} as a characteristic time scale. The non-dimensional Navier-Stokes equations are then given by:

$$\nabla \cdot \mathbf{u}_f = 0, \tag{4.1a}$$

$$\Big(\frac{\partial \mathbf{u}_f}{\partial t} + \nabla \cdot \mathbf{u}_f \mathbf{u}_f\Big) = -\nabla p_e - \nabla p + \Big(\frac{1}{Re}\frac{D_{pipe}}{D_p}\Big)\nabla^2 \mathbf{u}_f, \tag{4.1b}$$

where $\mathbf{u}_f$ is the fluid velocity vector, and p is the modified fluid pressure (i.e., the total fluid pressure $- p_e - \mathbf{g}\cdot\mathbf{x}$) with $\mathbf{g} = \tilde{\mathbf{g}} D_p/v_{bl}^2$, and ∇p_e is the externally imposed pressure gradient that drives the flow. We remark that the non-dimensional gravitational acceleration is related to the well-known Galileo number Ga for gravitational particle settling as:

$$|\mathbf{g}| = \Big(\frac{Ga}{Re}\frac{D_{pipe}}{D_p}\Big)^2 \frac{1}{(\rho_p/\rho_f - 1)}. \tag{4.2}$$

The non-dimensional Newton-Euler equations are given by:

$$\frac{\rho_p}{\rho_f}\frac{d\mathbf{u}_p}{dt} = \frac{6}{\pi}\Big(\oint_{\partial V}(\boldsymbol{\tau}\cdot\mathbf{n})dA + \frac{\pi}{6}\Big(\frac{\rho_p}{\rho_f} - 1\Big)\mathbf{g} - \frac{\pi}{6}\nabla p_e + \mathbf{F}_c\Big), \tag{4.3a}$$

$$\frac{\rho_p}{\rho_f}\frac{d\boldsymbol{\omega}_p}{dt} = \frac{60}{\pi}\Big(\oint_{\partial V}\mathbf{r}\times(\boldsymbol{\tau}\cdot\mathbf{n})dA + \mathbf{T}_c\Big), \tag{4.3b}$$

where $\mathbf{u}_p$ and $\boldsymbol{\omega}_p$ are the translational and rotational velocity of the particle, respectively, ρ_p and ρ_f are the solid and liquid mass density, respectively, $\mathbf{r}$ is the position vector with respect to the particle centroid, $\mathbf{n}$ is the unit normal vector directed from the surface (∂V) of the particle into the fluid, $\boldsymbol{\tau} = -p\mathbf{I} + (1/Re)(D_{pipe}/D_p)(\nabla\mathbf{u}_f + \nabla\mathbf{u}_f^T)$ is the stress tensor for a Newtonian fluid with $\mathbf{I}$ the unit tensor, and $\mathbf{F}_c$ and $\mathbf{T}_c$ are, respectively, the collision force and collision torque acting on the particle.

The Navier-Stokes and Newton-Euler equations are coupled with each other through the no-slip/no-penetration condition at the surface of the particles:

$$\mathbf{u}_f = \mathbf{u}_p + \boldsymbol{\omega}_p \times \mathbf{r} \quad \text{at } \partial V\,. \tag{4.4}$$

Finally, the fluid phase has to obey the no-slip/no-penetration condition at the pipe wall. The governing equations imply that the slurry flow dynamics are governed by the following non-dimensional numbers: Re, Ga, ϕ_b, D_p/D_{pipe}, ρ_p/ρ_f, and the parameters related to particle collisions discussed later.

4.3. EXPERIMENTAL SETUP

The experimental setup is shown in Fig. 4.1. It comprises an optically transparent plexiglass pipe with a diameter of 4 cm and 10 m long, and a 2 m high U-loop. The slurry consisting of water and polystyrene particles is driven by a centrifugal pump (A). The measuring section of the circuit is 4.65 m long and is equipped with a dual-plane Electric Resistance Tomography (ERT Z8000) sensor (B) to measure the spatial concentration distribution within the cross-flow plane. The ERT sensor is positioned at the end of the horizontal test section at a distance of 403 cm from the upstream bend and 23 cm before the downstream bend, which is well within the region where effects of both bends can be safely neglected. From the ERT data the bulk concentration ϕ_b in the test section was determined by integrating the spatial distribution over the cross-section. A high-speed camera with a frame rate of 1125 Hz (C) is placed at a distance of 214 cm from the upstream bend and thus in a well developed region of the flow. During operation, the bypass is opened and the inlet to the sump (D) is closed, allowing the polystyrene particles to enter the slurry loop by the action of gravity. Differential pressure measurements are taken (using Rosemount 1151 DP4S22 pressure transmitters) at 5 different positions along the measurement section at distances of 35 cm, 75 cm, 132 cm, 167 cm and 377 cm, respectively, from the reference point (R). The uncertainty in the pressure transmitters is 2.5 Pa. An EndressHauser promag 55S40 magnetic flow meter (E) is used to measure the liquid bulk velocity [16, 180] in the riser section of the U-loop with an instrumental uncertainty of 0.002 m/s.

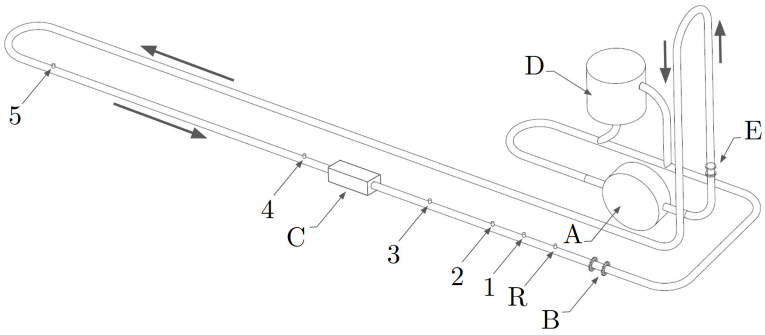

Figure 4.1: Experimental slurry loop setup, where A, B, C, D and E, indicate the locations of the centrifugal pump, ERT measuring planes, location where high-speed camera images were taken, sump and magnetic flow meter, respectively. The numbers 1-5 correspond to the locations of the pressure transmitters. The arrows indicate the flow direction.

Additional tilted flume experiments were performed to determine the static Coulomb coefficient of friction between the polystyrene balls and between the polystyrene balls and the plexiglass wall. In Appendix D we provide details of the measurements of the material properties. The density ratio of the polystyrene particles to water was determined to be $\rho_p/\rho_f = 1.02$. The ratio of the pipe diameter to the particle diameter is 20. The temperature in the three investigated cases was measured and this was used to determine the water viscosity and density. The experiments were conducted at different Re with the aim of accessing different transport regimes.

Originally, pressure sensors were placed in the riser and downcomer section of the U-loop with the intention of determining the bulk concentration from the difference in vertical pressure gradient between the riser and the downcomer, which could then be combined with the liquid bulk velocity measurement from the magnetic flow meter (E) to obtain the liquid flow rate. However, the obtained signal turned out to be too noisy as a result of the small density difference between the polystyrene spheres and water, and was therefore disregarded. The problem in determining the liquid flow rate was overcome by an estimate based on equating the solid and fluid volume fluxes in the *horizontal* test section and the corresponding fluxes in the *vertical* riser. The final estimation of the intrinsic liquid bulk velocity in the test section, v_{bl}, involved three steps. First, the solid volume flux in the test section was estimated using a combination of the velocity profile of the particles (estimated from the video recordings) and the concentration profile (obtained from the ERT sensor) as function of height in the pipe. Second, the solid volume flux balance over the horizontal test section and the vertical riser was used to estimate the concentration of particles in the riser. This was then used to estimate the fluid volume flux in the riser based on an empirical correlation for the macroscopic particle/fluid slip velocity. Third, the fluid volume flux balance over the test section and the riser was used to finally estimate the liquid bulk velocity in the test section. In Appendix E we provide a detailed description of the estimation and the assumptions used.

Case	Re	Ga	ϕ_b	Fr
D1/E1	3272	44.0	0.325	0.60
D2/E2	8513	43.6	0.284	2.00
D3/E3	13830	43.2	0.268	3.67
S1	2500	37.9	0.25	0.56
S2	5200	37.9	0.25	1.30
S3	7100	37.9	0.25	1.90
S4	12000	37.9	0.25	3.56
S5	12000	18.9	0.25	7.45

Table 4.1: Flow parameters in the experiments and the DNS: Re, Ga, ϕ_b and Fr, which correspond to the bulk liquid Reynolds number, the Galileo number, the solid bulk concentration and the densimetric Froude number, respectively. See main text for definitions of these numbers. E1-E3 refer to the experimental runs and D1-D3 are the corresponding DNS using the values of the governing dimensionless numbers estimated from the experiments. S1-S5 are additional DNS for a parametric study on the effect of Re and Ga on the flow dynamics where all other parameters were kept fixed. The particle to fluid density ratio is $\rho_p/\rho_f = 1.02$ and the pipe to particle diameter ratio is $D_{pipe}/D_p = 20$.

Though it was intended to maintain ϕ_b constant at a value of 0.25 (25%), it was observed *a posteriori* from the ERT measurements that the bulk concentration of particles in the test section was higher than originally planned due to an increased settling of particles in horizontal sections of the slurry loop when lowering the flow rate. The parameters Re, Ga and ϕ_b corresponding to the experimental runs are listed in table 4.1. This table also provides the values for the densimetric Froude number defined as $Fr = v_{mix}/\sqrt{(\rho_p/\rho_f - 1)|\tilde{\mathbf{g}}|D_{pipe}}$, where v_{mix} is the mixture bulk velocity defined as the sum of the liquid and solid flow rate divided by the pipe cross-sectional area. The densimetric Froude number is often used to assess whether particles will deposit on the bottom of the pipe. According to Miedema [121] (p. 156), the critical mixture velocity below which a bed will be present, corresponds to $Fr \approx 2$ for large particles as considered here. Based on the computed values we expect a bed for case E1 and possibly also for case E2.

4.4. COMPUTATIONAL SETUP

Interface-resolved Direct Numerical Simulations (DNS) were carried out in a cylindrical pipe filled with a viscous fluid and a prescribed bulk concentration of solid spheres, see Fig. 4.2. A Cartesian coordinate system was used where the axis of the pipe was aligned with the y direction and gravity was acting in the negative z direction. A total of eight simulations were performed, see table 4.1. The governing dimensionless numbers in cases D1-D3 were chosen to match the estimated dimensionless numbers from the corresponding experiments, cases E1-E3, respectively. In addition, a parametric study was performed to study the sole effect of varying the bulk liquid Reynolds number while all other numbers were kept fixed, see cases S1-S4. Finally, in case S5 we tested the sensitivity of the flow to a change in Galileo number at the highest investigated Reynolds number.

In the DNS the Navier-Stokes equations are solved using the finite-volume method

with a standard fractional step (predictor/corrector) scheme and the three-step Runge-Kutta method for the integration in time. Spatial gradients are approximated by the second-order accurate central-differencing scheme. The DNS makes use of two different grids: a fixed, staggered and isotropic Cartesian grid for the fluid phase and a uniform Lagrangian grid attached to the surface of every particle. The computationally efficient Immersed Boundary Method (IBM) of Breugem [18] is used for the fluid/solid coupling, which is a modified version of the original method introduced by Uhlmann [160]. The principle of the IBM is that the no-slip/no-penetration condition, Eq. 4.4, is not imposed in a direct manner, but that forces are locally added to the right-hand side of Eq. 4.1b in a thin spherical shell around each particle surface to enforce this condition by good approximation. Main advantage of the IBM is that a simple and continuous fluid grid can be used without the need of regridding every time particles have moved in space. The force distribution is computed from a combination of the regularized delta-function approach introduced by Peskin [130] and the direct-forcing approach of Fadlun et al. [53]. The fluid/solid coupling is explicit: first the Navier-Stokes equations are integrated to the next time level using the previous particle velocities and positions, then the Newton-Euler equations are integrated in time with the same Runge-Kutta method using the hydrodynamic force and torque computed from the IBM force distribution on the particle surface. As the Cartesian fluid grid did not conform to the cylindrical shape of the pipe, we used another IBM based on a volume-penalization approach to impose the no-slip/no-penetration condition for the fluid on the pipe wall. This method is described in more detail in Appendix F.

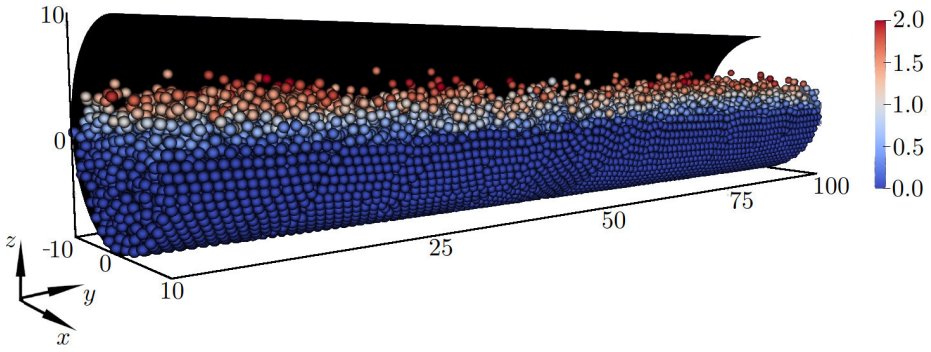

Figure 4.2: Computational setup used in the DNS (corresponding to case D1, see table 4.1). The particles are colored by the streamwise particle velocity v_p scaled with the liquid bulk velocity v_{bl}. The fluid is not shown in the figure for clarity. A periodic boundary condition in the streamwise (y) direction and a no-slip boundary condition at the pipe wall are imposed. The pipe-to-particle diameter ratio is $D_{pipe}/D_p = 20$ and the pipe has a length of 100 particle diameters.

The pipe length was set equal to five pipe diameters (100 particle diameters) and a periodic boundary condition is imposed in the streamwise direction. The flow is driven by a streamwise pressure gradient, which is adjusted every time step to maintain a constant intrinsic liquid bulk velocity, see Appendix F for more details. We used the same

grid resolutions in all DNS cases, corresponding to $D_p/\Delta x = 16$ ($D_{pipe}/\Delta x = 320$) and 746 Lagrangian grid points on the surface of the particles. This was sufficient to resolve both the turbulent flow structures in the carrier fluid as well as the flow around the particles. The DNS/IBM code has been extensively validated [18] and was used in many previous studies of, e.g., the rheology of dense neutrally-buoyant suspensions in plane Couette flow [133], the behavior of dense neutrally-buoyant suspensions in turbulent channel flow [132, 31, 30] and the sedimentation of heavy sphere suspensions in the inertial flow regime [150, 151]. In Appendix F we provide additional validation of the volume-penalization method for turbulent single-phase pipe flow.

Particle-particle and particle-wall collisions and contacts are treated using a soft-sphere collision model described by Costa et al. [29] which simulates a spring-damper interaction that accounts for the stick-slip nature of frictional collisions. Lubrication effects are automatically accounted for in the DNS, although underresolved at inter-particle distances smaller than a grid cell, for which a normal lubrication force correction is added to the right-hand side of Eq. 4.3a. The lubrication force is capped when the interparticle distance is smaller than a threshold distance of 0.2% of the particle diameter as to mimic the effect of particle roughness on lubrication. Due to the large pipe-to-particle diameter ratio ($D_{pipe}/D_p = 20$), the collision of a particle with the curved pipe wall is treated as a collision with the tangent plane to the pipe wall at the point of particle/wall contact. The collision model depends on three main parameters: the normal and tangential dry coefficients of restitution, e_n and e_t, respectively, and the Coulomb coefficient of sliding friction, μ_c. We have chosen $e_n = 0.97$ as this is a typical value for many materials [29] and $\mu_c = 0.39$ based on the tilted-flume experiments described in Appendix D. The value of $e_t = 0.1$ is an educated guess given that the particles appear rather smooth; the higher the value of e_t, the earlier the transition from stick to slip behavior [29].

The particles were initially randomly distributed in space and a laminar Poiseuille (parabolic) profile was prescribed for the streamwise fluid and solid phase velocity. The particles were also initialized with an angular velocity in the azimuthal direction equal to half the vorticity obtained from the prescribed Poiseuille flow. The computational time step was initially adjusted based on the von Neumann stability criteria for the three-step Runge-Kutta scheme used. After a few thousand time steps it was fixed in time at a value well below the maximum allowed value for stable integration in time. The temporal evolution of the flow was monitored by the time series of variables such as the averaged vertical position of the particles, the averaged streamwise velocity of all the particles and the driving streamwise pressure gradient. After the flow reached a fully-developed state, equidistant sampling of the DNS results was started for computing statistics with part of the statistics (e.g., spatial averages) computed and stored during runtime.

To evaluate whether the slurry flow is sufficiently resolved in space, two values for the normalized grid spacing are included in table 4.2: one based on the liquid viscosity $\Delta x\, v_\tau/\nu_f$ and one based on the effective suspension viscosity $\Delta x\, v_\tau/\nu_s$ calculated at

the prescribed bulk concentration and estimated from Eilers' correlation [46] with the coefficients taken from Costa et al. [31]. Here, the wall friction velocity v_τ is used as a first proxy for the typical velocity scale of the large eddies when a turbulent flow is present, given by:

$$v_\tau / v_{bl} = \sqrt{-\frac{1}{4}\left(\frac{D_{pipe}}{D_p}\right)\overline{\frac{dp_e}{dy}}}. \tag{4.5}$$

The effective suspension viscosity ν_s is estimated from:

$$\nu_s/\nu_f = \left(1 + 1.25\,\frac{\phi_b}{(1-\phi_b/0.64)}\right)^2. \tag{4.6}$$

While ν_f/v_τ may be used as a first estimate of the viscous wall unit for the stratified cases with the presence of a distinct bed and liquid flow region, ν_s/v_τ is deemed more appropriate for the fully-suspended cases in which the particles are mixed across the pipe [31, 30]. The values of $\Delta x\, v_\tau/\nu_f$ for the fixed-bed and sliding-bed cases, and of $\Delta x\, v_\tau/\nu_s$ for the fully-suspended cases are $\mathcal{O}(1)$ and hence the turbulent flow is deemed sufficiently resolved at the grid resolution used.

	$\frac{t_{obs} v_{bl}}{D_p}$	N_s	$\Delta t\,\frac{v_{bl}}{D_p}$	$\frac{v_{bs}}{v_{bl}}$	$\frac{v_\tau}{v_{bl}}$	$\Delta x\,\frac{v_\tau}{\nu_f}$	$\Delta x\,\frac{v_\tau}{\nu_s}$	Re_τ	$Re_{\tau,s}$	θ
D1	2000	200	0.0125	0.13	0.20	2.02	0.61	323.3	97.0	0.54
D2	2000	200	0.0125	0.71	0.11	2.97	1.11	474.8	176.9	1.19
D3	2000	200	0.0125	1.09	0.09	3.78	1.52	604.5	243.3	1.96
S1	800	80	0.02	0.06	0.17	1.24	0.54	197.8	86.4	0.27
S2	800	80	0.02	0.38	0.12	1.96	0.86	313.5	137.0	0.68
S3	800	80	0.02	0.63	0.11	2.37	1.04	379.5	165.8	1.00
S4	4500	300	0.03	1.02	0.09	3.23	1.41	516.8	225.8	1.86
S5	4500	300	0.03	1.20	0.08	3.07	1.34	491.4	214.7	6.76

Table 4.2: Additional parameters and computed numbers from the DNS where t_{obs} is the observation time over which statistics were collected, N_s is the number of samples, Δt is the time step, v_{bs} is the mean solid bulk velocity, v_{bl} is the mean liquid bulk velocity, v_τ is the average wall friction velocity, ν_f is the viscosity of the fluid, ν_s is the effective suspension viscosity of the solid/fluid mixture computed from Eilers' empirical model, Re_τ is the friction Reynolds number, $Re_{\tau,s}$ is the suspension friction Reynolds number and θ is the Shields number.

The proxy for the wall friction velocity was used to calculate a few other numbers whose values are listed in table 4.2. $Re_\tau = v_\tau R_{pipe}/\nu_f$ and $Re_{\tau,s} = v_\tau R_{pipe}/\nu_s$ are, respectively, the friction Reynolds number and the suspension friction Reynolds number with R_{pipe} the pipe radius. Finally, the Shields number is defined as $\theta = v_\tau^2/(\rho_p/\rho_f - 1)|\tilde{\mathbf{g}}|D_p$. The Shields number [152, 128] is another parameter that can be used to distinguish between the regimes, especially at low flow rates, where the onset of particle entrainment in slurry flow is characterized by the balance between shear-induced lift from turbulence and the particle stresses on the one hand and the immersed weight of the particles on the other hand [65]. The values of θ for cases D1-D3 are all well above the critical Shields number of 0.03−0.04 for the particles and flow conditions considered

in the present study [152, 143], suggesting that a significant portion of the particles will be suspended in all cases. In addition, the high value for θ in case D3 corresponds to the suspended regime according to the criteria given by Van Rijn [143].

In the post-processing of the raw DNS data, first the data was averaged over the streamwise direction and then time averaged. For example, the superficial volume and time average of the streamwise particle velocity v_p is defined as:

$$\overline{\langle v_p \rangle^s}(x,z) = \frac{1}{l_y} \int_y \overline{\gamma_p(x,y,z,t) v_p(x,y,z,t)} dy, \tag{4.7}$$

where the overline denotes the time or Reynolds average, l_y is the length of the pipe, and $\gamma_p \in [0,1]$ is the solid phase indicator function and measures the local solid volume fraction in a computational grid cell. Similarly, the macroscopic solid volume fraction is computed as:

$$\overline{\phi}(x,z) = \frac{1}{l_y} \int_y \overline{\gamma_p(x,y,z,t)} dy. \tag{4.8}$$

The intrinsic or phase-averaged streamwise solid velocity is computed by dividing the superficial average by the concentration:

$$\overline{\langle v_p \rangle}(x,z) = \frac{\overline{\langle v_p \rangle^s}}{\overline{\phi}}. \tag{4.9}$$

Finally, the intrinsic solid bulk velocity is computed from:

$$v_{bs} = \frac{\int_{A_{pipe}} \overline{\langle v_p \rangle^s} dA}{\int_{A_{pipe}} \overline{\phi} dA}, \tag{4.10}$$

where A_{pipe} denotes the cross-sectional area of the pipe.

4.5. COMPARISON OF EXPERIMENTS AND DNS

4.5.1. INSTANTANEOUS FLOW SNAPSHOTS

To facilitate a visual comparison, instantaneous snapshots from a side view of the slurry flow in the experiment (E1-E3) and DNS (D1-D3) are provided in Fig. 4.3. In both the DNS and experiment, we observe an increase in the number of particles in suspension with increasing Re. Further, from the video recordings we observed a fixed (static) bed in E1 and a nearly static bed in D1, a sliding bed in E2 and D2, and a suspension of particles without clear presence of a bed in E3 and D3. In E1 and D1, we observe an ordered packing arrangement of particles within the bed at the pipe wall. This is also clearly visible in the sliding bed cases E2 and D2, where the packing structure is somewhat skewed due to bed sliding. The ordered packing at the wall originates from the kinematic condition that the particles cannot overlap with the wall. This effect is reinforced by the high degree of monodispersity of the spheres in the experiments and the perfect monodispersity in the DNS. In cases E3 and D3 all particles are suspended, but the distribution is clearly heterogeneous with more particles in the lower than the

upper half of the pipe and moving at a lower velocity as well. Though the amount of particles in suspension and the bed height seems visually comparable between the experiments and corresponding DNS, it appears that there are more particles reaching the top of the pipe in cases E1 and E2 as compared to D1 and D2, respectively. The opposite holds for case E3 as compared to case D3.

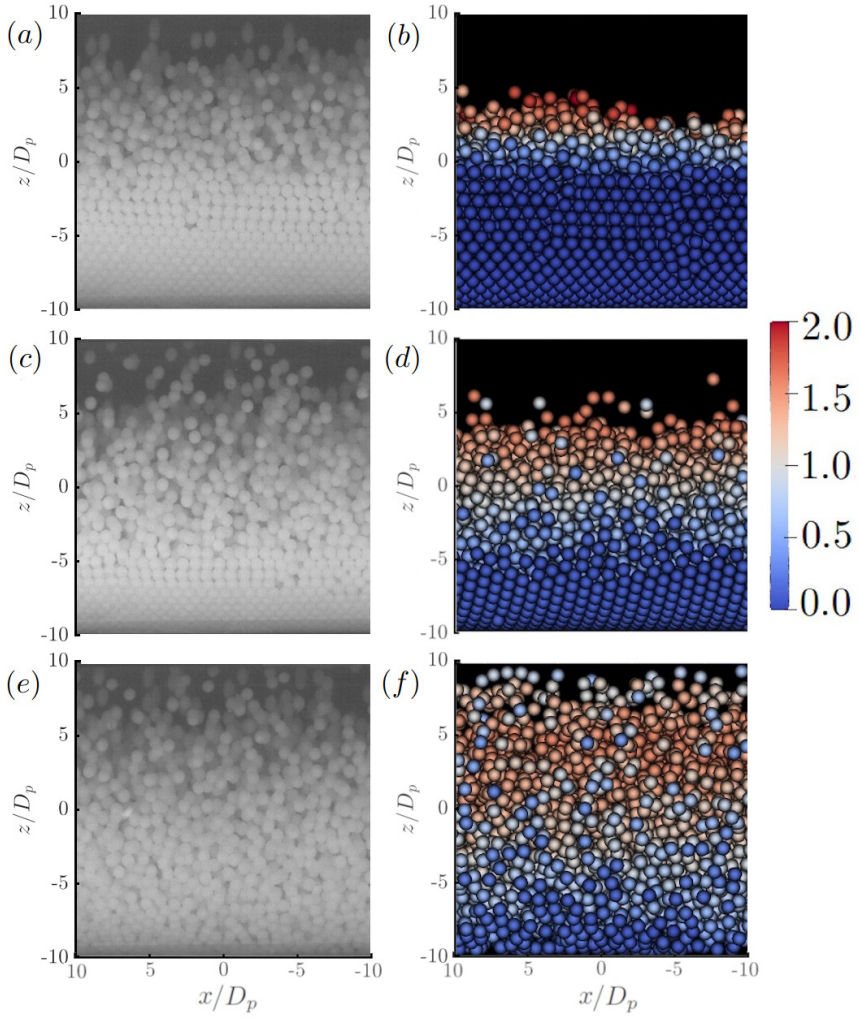

Figure 4.3: Instantaneous snapshots of the spatial distribution and velocity of the particles in the experiment (left) and DNS (right). The particles in the DNS are colored by their streamwise velocity v_p scaled with the fluid bulk velocity v_{bl}. Note that the snapshots provide a side view of the pipe along the y direction. (a) E1, (b) D1, (c) E2, (d) D2, (e) E3 and (f) D3.

For cases D1-D3, Fig. 4.4 presents snapshots of the streamwise fluid and solid velocity in two midplanes of the pipe, along with the 3D spatial particle distribution over

part of the pipe. It is visually apparent that the flow is turbulent in the upper half of the pipe where the particle concentration is zero or low, while strongly damped in the region where the particle concentration is high. Normalized with the liquid bulk velocity, the highest peak fluid velocity is seen in D1. The immobile particles block the lower half of the pipe in D1 and hence the fluid is funneled through a smaller cross-sectional area in the upper half of the pipe. In contrast to D1, in D2 the bed of particles in the lower half of the pipe has a nonzero velocity. In D3, we observe a suspension of particles, with particles even at the top of the pipe, and there no longer appears to be a clear presence of a particle bed at the pipe bottom.

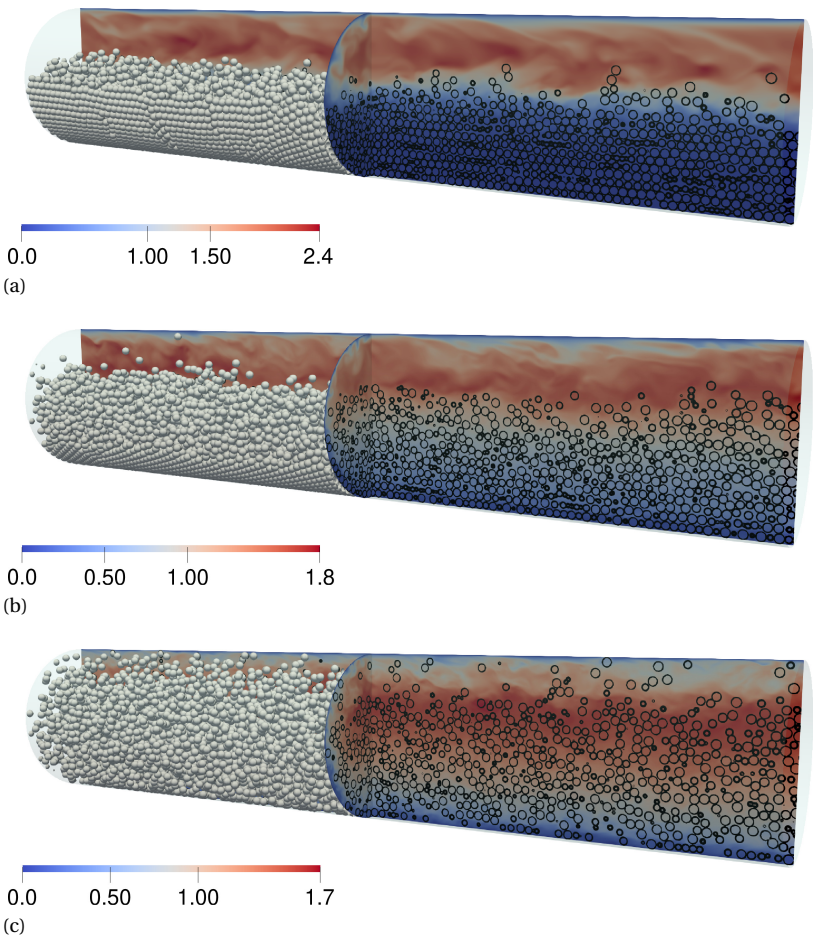

Figure 4.4: Instantaneous flow snapshots from the DNS in an xz and the yz plane along the pipe axis. The flow is going from left to right. The color denotes the streamwise velocity normalised with the liquid bulk velocity. Contours indicate the particle positions (local grid cell solid volume fraction equal to 0.5). The 3D spatial particle distribution is shown for part of the pipe in grey color. (a) D1, (b) D2, and (c) D3.

4.5.2. MEAN STREAMWISE PRESSURE GRADIENT

From the streamwise pressure gradient obtained from the DNS and experiments, the Darcy-Weisbach friction factor was computed according to:

$$f = -\frac{\overline{dp_e}}{dy}\frac{D_{pipe}}{\frac{1}{2}\rho_f v_{mix}^2}, \tag{4.11}$$

where here $\overline{dp_e/dy}$ is the dimensional mean pressure gradient, $v_{mix} = \phi_b v_{bs} + (1-\phi_b)v_{bl}$ is the bulk mixture velocity, and $\rho_f \approx 997.4\ kg/m^3$ is the density of water at 23.5°C in the experiments. Since v_{mix} was not explicitly measured in the experiments, v_{mix} from cases D1-D3 was used to determine the friction factor for cases E1-E3, respectively. In Fig. 4.5a the friction factor is plotted as function of the mixture Reynolds number defined as $Re_{mix} = v_{mix}D_{pipe}/\nu_f$. The DNS and experiment show good agreement for cases D3 and E3 ($Re_{mix} = 14164$), where the slurry flow is in the fully-suspended regime. However, the friction factor from the DNS underpredicts the experiment by −35% in case D1 compared to E1 and -21% in case D2 compared to E2 ($Re_{mix} = 7812$). The reason for this is not fully clear, but might be related to the uncertainty in the reconstructed liquid bulk velocity from the experiments, see the discussion in section 4.3.

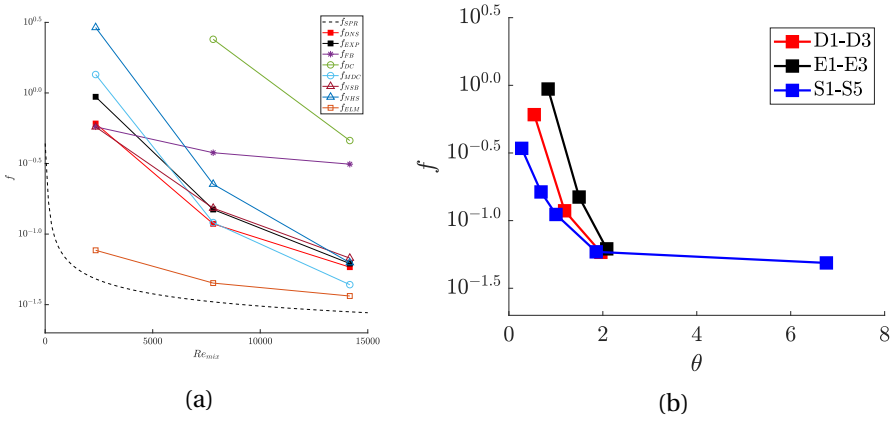

(a) (b)

Figure 4.5: (a) Darcy-Weisbach friction factor, f, as function of the bulk mixture Reynolds number, Re_{mix}. The red and black solid squares denote the data from the DNS (D1, D2 and D3) and experiments (E1, E2 and E3), respectively. Dashed line corresponds to the Haaland friction factor [67] for single-phase flow in a smooth pipe, f_{SPR}. Remaining symbols correspond to correlations proposed in literature: f_{DC} from Durand and Condolios [44], f_{MDC} a modified version of the Durand and Condolios model based on the use of the reduced gravity [123], f_{NHS} and f_{NSB} from Newitt et al. [123], f_{FB} from a fixed-bed model (Appendix G) and f_{ELM} from the equivalent liquid model. The estimated friction factor from the original Durand and Condolios model for cases D1/E1 is not shown as it falls out of range of the figure, see table G.1. (b) Darcy-Weisbach friction factor, f, as function of the Shields number θ.

In Fig. 4.5a the DNS and experimental data are compared with a number of friction factor models, each developed for a *specific* flow regime, see Appendix G for details of the models. The model for the fixed-bed regime (f_{FB}) closely matches with the DNS for case D1, while strongly overpredicts the friction factor for cases D2/E2 and D3/E3 as

may be expected since the flow is in a different regime. The original Durand and Condolios model (f_{DC}) [44] strongly overpredicts the DNS and experimental data, while the modified Durand and Condolios model (f_{MDC}) agrees very well with the sliding-bed case D2. This difference underlines the importance of using the *reduced gravity*, $(\rho_p/\rho_f - 1)|\tilde{\mathbf{g}}|$, in the friction factor model instead of *gravity*, $|\tilde{\mathbf{g}}|$, as suggested originally by Durand and Condolios, see Appendix G; this is especially relevant to our study where the density ratio is $\rho_p/\rho_f = 1.02$ and thus very different from the value of ≈ 2.65 in the experiments of Durand and Condolios. The model of Newitt et al. [123] for the sliding-bed regime (f_{NSB}) closely matches with the experiments for the sliding-bed case E2, while the model for the heterogeneous suspension regime best matches with the experiments for the fully-suspended case E3. Finally, the equivalent liquid model (f_{ELM}) strongly underpredicts both the DNS and experiments as particles are rather large in our study and not homogeneously mixed across the pipe.

Figure 4.5.b depicts the Darcy-Weisbach friction factor, f, as function of the Shields number, θ. As mentioned before, the Shields number is often used as a metric for the degree of particle entrainment into the flow and can thus be used to distinguish between the different regimes in slurry pipe flow. Figure 4.5.b shows that for each dataset (D1-D3, E1-E3, S1-S5), f drops off approximately with $1/\theta$ for $\theta \lesssim 2$. In the range between $\theta \simeq 2$ and 6.76, corresponding to case S5, f seems to level off and to become independent of θ; in fact, f is about three times larger for case S5 than predicted by the trend for cases S1-S4 for the smaller $\theta-$range. From the definition of the friction factor it can be shown that:

$$f = 8\theta\left(\frac{Ga}{Re_{mix}}\frac{D_{pipe}}{D_p}\right)^2. \tag{4.12}$$

For (nearly) constant Ga and D_{pipe}/D_p, it follows that $f \sim \theta/Re_{mix}^2$. Our results thus indicate that $\theta \sim Re_{mix}$ and $f \sim 1/Re_{mix}$ for $\theta \lesssim 2$, and suggest that $\theta \sim Re_{mix}^2$ and f constant for $\theta \gg 1$. Fig. 4.5a confirms that $f \sim 1/Re_{mix}$ for cases D1-D3 and E1-E3. This is a rather surprising result as it reminds of the behavior of the friction factor for laminar flows, while in all cases the slurry flow is clearly turbulent outside the bed and high particle concentration regions. The reason for this is not fully clear yet, but must be related to the change in flow regimes from fixed to sliding bed and to the suspended regime with increasing Re_{mix} and θ, which is associated with significant changes in the flow pattern and the amount of sediment carried by the flow. Finally, the constant friction factor for very high θ is intuitively expected based on the constant friction factor of a turbulent single-phase flow in a hydraulically rough pipe [135].

4.5.3. MEAN VELOCITY PROFILE

For the DNS cases D1-D3, Fig. 4.6 shows the mean velocity in the cross-flow plane. The top, middle and bottom row depict, respectively, the mean streamwise fluid velocity, $\overline{\langle v_f \rangle}$, the mean streamwise particle velocity, $\overline{\langle v_p \rangle}$, and the mean secondary fluid flow, $\overline{\langle u_f \rangle}$ and $\overline{\langle w_f \rangle}$. The streamwise fluid and particle velocity distributions appear nearly the same, macroscopic particle/fluid slip in the mean streamwise velocity is generally small. In all cases, but especially in case D1, the bulk flow happens through the top half

of the pipe.

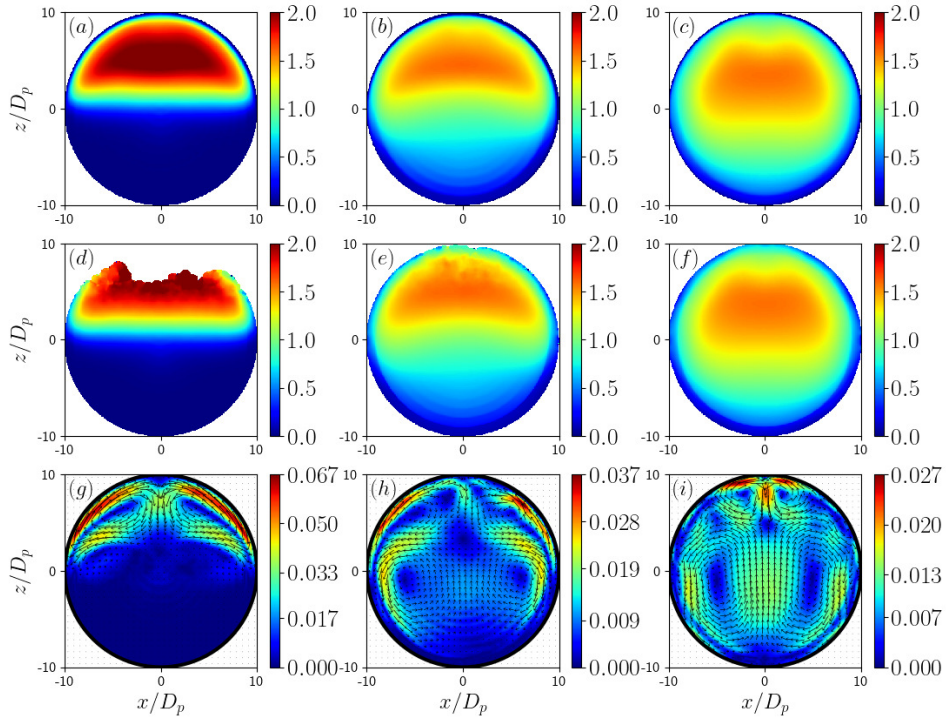

Figure 4.6: Mean velocity distribution across the pipe obtained from the DNS. From left to right results are depicted for cases D1-D3. (a)-(c) Mean intrinsic liquid velocity, $\overline{\langle v_f \rangle}/v_{bl}$. (d)-(f) Mean intrinsic solid velocity, $\overline{\langle v_p \rangle}/v_{bl}$, where white indicates areas where particles are absent. (g)-(i) Mean secondary fluid flow, $\overline{\langle u_f \rangle}/v_{bl}$ and $\overline{\langle w_f \rangle}/v_{bl}$. The color denotes the secondary flow magnitude, $\sqrt{\overline{\langle u_f \rangle}^2 + \overline{\langle w_f \rangle}^2}/v_{bl}$, and the vectors indicate the flow direction. The reference vector length has been rescaled for every case to optimize visibility.

In all cases a clear secondary flow of Prandtl's second kind is present. Relative to the liquid bulk velocity, the magnitude of the secondary flow is strongest in case D1 and weakest in case D3, with maximum values on the order of 7% and 3%, respectively. The high maximum value for case D1 is significantly higher than the maximum value of around 3% found for turbulent single-phase flows in semi-circular pipes in previous studies [103, 111]. This may be partially explained by our normalisation with the liquid bulk velocity based on the entire pipe cross-section, while for case D1 the liquid bulk velocity would be roughly twice as large when it would based on the upper half of the pipe only. As for turbulent single-phase flows in semi-circular pipes, in case D1 the secondary flow is characterized by two counter-rotating vortices near the flow corners at $z \approx 0$, suggesting a similar origin from centrifugal forces acting on curved paths of fluctuating fluid motions near the corners [126]. However, for case D1, the lower vortices of the vortex pairs are comparatively much weaker and spatially more confined,

while the upper vortices stretch over the entire upper part of the pipe and are responsible for a significant downflow underneath the top of the pipe. Since the lower vortices are located within the dense particle layer above the stationary bed (cf. Figs. 4.6g and 4.8d), damping by the particle stress (related to drag and a locally high suspension viscosity) is likely important. Furthermore, for case D1, the secondary flow is negligible inside the stationary sediment bed, presumably because of viscous drag which tends to damp any spatial inhomogeneity of the flow within the bed.

In case D2, the secondary flow is characterized by two main counter-rotating vortex pairs. The upper vortices bear a clear resemblance to the upper vortices in case D1. This suggests that they are dynamically similar and thus caused by turbulent fluctuating motions in the apparent presence of internal flow corners. Different from case D1, the lower vortex pair extends over the entire lower half of the pipe, including the sliding-bed region. Within the bed, both drag and the high suspension viscosity are likely responsible for damping of the secondary flow. A relatively strong downward secondary flow is present in the low-concentration regions flanking the sliding bed, which might be caused by turbulent fluctuations in a 'corner-like' geometry and is possibly amplified by particle-stress gradients [92, 58, 108] and local particle sedimentation [109]. The secondary flow pattern in case D2 exhibits a 'saddle' point at $x \approx 0$ and $z \approx 3D_p$, which is accompanied by a smooth 'dimple' in the streamwise fluid and particle velocity distributions in Figs. 4.6b and 4.6e, respectively. This suggests a mutual coupling between the mean streamwise and the mean secondary flow.

As in case D2, the secondary flow in case D3 is characterized by two main vortex pairs. Compared to case D2, in case D3 the upper, corner-induced, vortices are confined to a smaller region below the top of the pipe, which can be explained from the significantly higher elevation to which particles are suspended in this case (cf. Figs. 4.8e and 4.8f). The lower vortex pair extends over the entire lower half of the pipe. A fairly strong upward secondary flow is visible inside the dense particle core (cf. Figs. 4.6i and 4.8f), which contributes to the lifting of the particle core. The resemblance of the lower vortex pair in case D3 to the lower vortex pair in case D2, strongly suggests that they are dynamically similar and originate from similar physical mechanisms. Distinction should be made here between the primarily downward secondary flow inside the low-concentration zones flanking the particle core, of which the physical mechanism was discussed above, and the primarily upward flow inside the dense particle core. After the study of Kazerooni et al. [92] and based on the observation from Fig. 4.4c that turbulence is strongly damped inside the dense particle core, it is likely that spatial variations in the particle stresses are responsible for generating and maintaining the secondary flow inside the dense particle core. We hypothesize that this can be conceptually related to centrifugal forces acting on curved paths of fluctuating particle motions, similar to the mechanism by which secondary flow is generated in turbulent single-phase flow over longitudinal corners, ridges and riblets [126]. The fluctuating particle motions arise from interactions of adjacent particle layers under shear. For non-axisymmetric mean particle concentration and particle velocity distributions, the centrifugal forces from fluctuating particle motions are on statistical average responsi-

ble for mean particle-stress gradients that drive the secondary flow. We speculate that the 'wedge-shaped' high-concentration zone above the bottom of the pipe in cases D2 and D3 as observed from Fig. 4.8, might act as an apparent ridge to the particles around it and drives the particles along the wedge upwards.

Figure 4.7 shows mean streamwise fluid and particle velocity profiles as function of height obtained from both the DNS and experiments. While the DNS profiles were obtained from the streamwise-vertical midplane, the experimental profiles were reconstructed based on the camera recordings from a side view of the flow, see Appendix E, and thus represent the mean particle velocity as function of height *along the pipe wall in the side view of the pipe.* Nonetheless, since Fig. 4.6 shows that the mean streamwise particle velocity is rather homogeneous in x, the bias from the different way in which the experimental and DNS profiles were obtained, is deemed to be small.

In general, the DNS and experimental profiles show reasonable agreement, especially when the uncertainty in the estimation of the bulk velocity from the experimental data is taken into account as discussed in section 4.3. For the fixed-bed cases D1 and E1, the velocity within the bed region is close to zero. While in the experiment the bed is not moving at all, as observed from the high-speed camera recordings (cf. Fig. 4.3a), in the DNS the bed has a slight mean velocity of $\mathcal{O}(5{\cdot}10^{-3}\, v_{bl})$, see the inset in Fig. 4.7. Another striking observation is that the peak velocity at $z/D_p \approx 5-6$ is roughly 20% higher in the experiment than in the DNS. This might indicate that the actual bulk velocity in the experiment has been somewhat higher than we have estimated; this is also consistent with the higher friction factor for the experiment than for the DNS. In E2 and D2, we observe a non-stationary bed in both experiment and DNS. In the experiment, we observe a nearly constant velocity in the bed indicating that the bed moves as a single unit. However, in the DNS we observe a gradual increase in the velocity of the bed with increasing height, indicating a pronounced downward momentum transfer by shearing motion between adjacent particle layers within the sliding bed. Furthermore, the DNS underpredicts the peak velocity at $z/D_p \approx 5$ by roughly 10% as compared to the experiment. In the fixed and sliding-bed cases, we observe a distinct change in the slope of the velocity profile demarcating a diffuse interface between the bed of particles and the overlying fluid. This is not observed in E3 and D3 where a bed is absent, likely due to shear-induced migration of particles into the flow.

Finally, we note that the DNS results show that the mean streamwise particle and fluid velocity profiles are nearly identical over the entire height for all cases; small deviations are observed only for the top half of the pipe. The small macroscopic slip can be understood from a consideration of the particle Stokes number, $St = \tau_p/\tau_f$, with $\tau_p = (\rho_p/\rho_f + 1/2)\, D_p^2/(18\nu_f)$ the viscous particle response time to changes in the flow [8] and $\tau_p = R_{pipe}/v_\tau$ [135] a typical time scale for the large turbulent eddies in the bulk fluid. For cases D1-D3, St is in the range of $0.02-0.05$ and thus much smaller than one, indicating that the particles tend to follow the large-scale fluid motions and explaining the small slip.

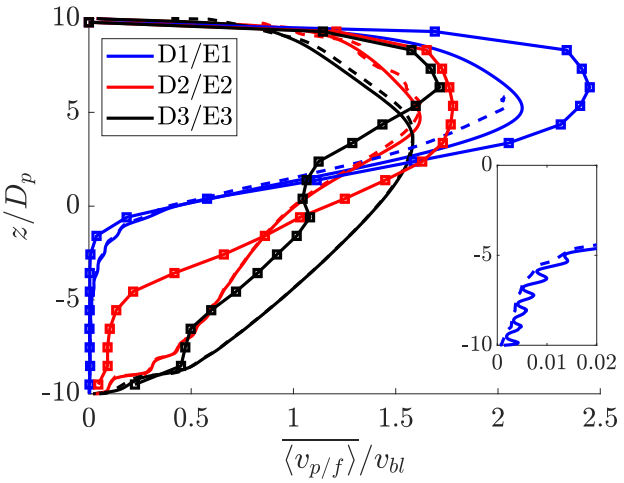

Figure 4.7: Mean streamwise velocity profile as function of height shown for the DNS (D1-D3) and experiments (E1-E3). The profiles from the DNS were taken from the streamwise-vertical midplane, while the experimental profiles represent the mean streamwise particle velocity as function of height *along the pipe wall in the side view of the pipe*. Solid lines with square symbols: experimental data for the mean streamwise particle velocity. Solid and dashed lines: DNS profiles for mean streamwise fluid and particle velocity. In case D1, the particle velocity profile reaches to $z/D_p \approx 6$ as beyond that height no particles are present in the flow. The inset shows an enlarged view of the bottom half of the pipe for case D1.

4.5.4. MEAN CONCENTRATION

In Fig. 4.8, we present the mean concentration distribution, $\overline{\phi}(x,z)$, in the cross-flow plane of the pipe for both the experiments and corresponding DNS. To ease the comparison of the different flow regimes, the concentration is normalised with the bulk concentration ϕ_b. The mean concentration distributions are qualitatively similar for the experiments and the corresponding DNS. For all cases the 2D mean concentration distribution appears intimately connected to the mean secondary flow pattern (cf. Figs. 4.8d-f and 4.6g-i). In the fixed-bed cases E1 and D1, the bed interface is flat and centered around $z = 0$. In case D1 we clearly observe a layered arrangement of the particles in concentric rings. This originates from the constraint that the perfectly monodisperse particles cannot overlap with the wall and tend to align parallel to the wall, as observed before from the flow snapshots shown in Fig. 4.3. This effect is likely also present in the experiment, though probably less pronounced as in the DNS due to a lesser degree of monodispersity. It is probably because of insufficient spatial resolution that the layering is not captured by the ERT sensor (cf. Figs. 4.8a and 4.3a).

In the sliding-bed cases E2 and D2, the bed interface is curved with the highest position of the interface in the middle. Highest concentrations are found in a 'wedge-shaped' zone in the lower circle quadrant centered around $x = 0$. Particle layering is visible in the DNS result, but mostly confined to this lower quadrant. Particle transport and drag from secondary flow likely contributed to the peculiar bed shape and solid volume distribution within the bed, cf. Figs. 4.6h and 4.8e.

In case E3 the particles are lifted upwards with respect to case E2. In the corresponding DNS case D3, the particles are lifted significantly higher than in E3 though. The lifted particle core in case D3 has a nearly uniform concentration with the absence of layering. Interestingly, two particle layers can still be observed near the bottom of the pipe, with a distinct fluid gap in between with a strongly reduced concentration. We attribute the origin of the lifted dense particle core and pronounced particle-wall layer to shear-induced migration [107, 105, 104] and a combined effect of gravity and particle lubrication at the pipe wall [104], respectively. The upward migration of the particles is associated with repulsive forces of lubricated and collisional contacts of adjacent particle layers in relative motion due to shear. The repulsive forces from particle-particle interactions already exist for suspensions in Stokes flow [107], but are amplified in the inertial regime due to particle inertia, a phenomenon dubbed as 'inertial shear thickening' by Picano et al. [133] (see also Fig. 3 and related discussion in Lashgari et al. [104]). From a continuum perspective, the repulsive forces are associated with a wall-normal gradient in the wall-normal particle stress [65]. The particle stress is higher for increasing shear rate and increasing concentration. Consequently, the repulsive forces between adjacent particle layers act such that particles tend to accumulate in low-shear regions. Since the secondary flow pattern closely matches with the particle concentration pattern, transport by secondary flow and viscous drag inside the particle core might also contribute to maintaining the shape and lifting of the particle core.

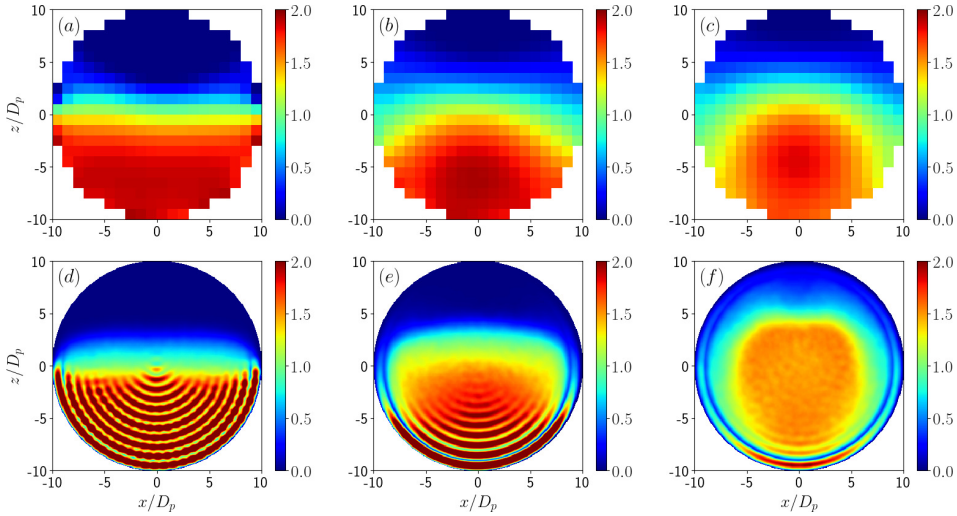

Figure 4.8: Normalised mean concentration distribution, $\overline{\phi}(x,z)/\phi_b$, in the cross-flow plane of the pipe. (a)-(c) Experimental cases E1-E3. (d)-(f) Corresponding DNS cases D1-D3.

We hypothesize that shear-induced particle migration is also responsible for the low-concentration zones flanking the sliding bed for $z/D_p \approx -4$ till 0 in case D2. With increasing shear rate, shear-induced migration becomes stronger and the low-concentration

zones will extend further downwards along the pipe wall untill the whole bed is lifted from the wall (which has nearly happened in case D3). This suggests that the angle of the wedge-shaped high-concentration zone at the pipe bottom might be set by a balance between the force from shear-induced particle migration directed upwards along the wedge edge and the component of the net gravity force on the particles directed downwards along the wedge edge. Within the sliding bed but outside the high-concentration zone at the pipe bottom, shear-induced migration is responsible for an apparent 'fluidisation' of the bed at a significantly lower concentration than of the bed packing in the high-concentration zone.

In Fig. 4.9 the mean concentration profiles from the experiments and corresponding DNS are shown in the streamwise-vertical midplane (i.e., at $x = 0$). Furthermore, a moving-mean filter of one particle diameter width is applied to the DNS data to approximately match the resolution of the ERT sensor. For cases D1/E1 and D2/E2 the profiles are in good quantitative agreement. However, as already noticed from Fig. 4.8, the agreement for cases D3 and E3 is not as good, with particles being mixed higher up in the pipe and with a lower concentration in the particle plug in case D3.

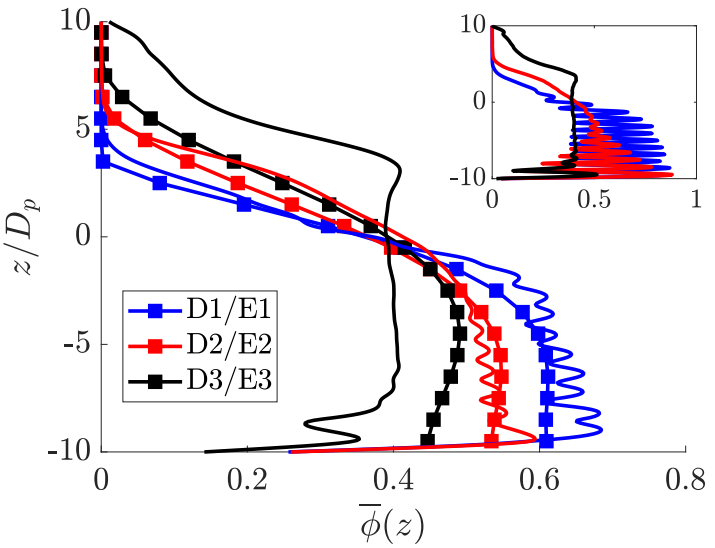

Figure 4.9: Mean concentration profile as function of height in the streamwise-vertical midplane, shown for the DNS (D1-D3, solid lines) and the experiments (E1-E3, solid lines with square symbols). A moving mean filter of 1 particle diameter was applied to the DNS profiles for the sake of comparison with the ERT data. The inset shows the unfiltered concentration profiles from the DNS.

The 2D mean concentration distributions of cases D2 and D3 bear a striking resemblance to the concentration distributions shown by Zhang et al. [189] (their figure 3) for horizontal gas-solid pipe flow in the so-called gravity-dominant and the particle-inertia-dominant regime, respectively. However, particle layering seems absent in their

simulations, probably because of the much lower solid bulk concentrations considered, which was varied in the range of $\phi_b = 5.3 \cdot 10^{-5}$ to $1.1 \cdot 10^{-3}$, and the neglectance of particle-wall lubrication. Zhang et al. [189] hypothesized that the wedge-shaped concentration distribution in the gravity-dominated regime is caused by a secondary flow pattern, although not analysed in further detail. This hypothesis is substantiated by the mean secondary flow pattern found for our case D2, see Fig. 4.6, indeed showing two circulation cells centered around the wedge-shaped high-concentration zone at the bottom of the pipe. As discussed before, we speculate that the wedge-shaped high-concentration zone might also act as an apparent ridge, which, in the presence of mean shear, drives a flow of particles along the ridge upwards. Furthermore, Zhang et al. postulated that the lifted particle core in the particle-inertia dominant regime originated from a Saffman lift force acting on the particles [147, 118], but without evaluating the requirements for the presence of this force. As the bulk solid volume fractions in our study are much higher, particle-particle interactions will dominate over particle-fluid interactions in the highly concentrated regions of the flow. Therefore, we deem it more likely that the lifted particle core in case D3 originated from shear-induced migration from particle-particle interactions as discussed before.

Interestingly, the presence of a lifted particle core was reported in a few other studies in literature, with different speculations about its origin. Campbell et al. [23] found experimental evidence of a lifted particle core in slurry flow through a rectangular channel. They speculated that it arose from multi-particle interactions, more specifically an attraction between particles from a 'Bernoulli interaction' in the presence of large particle-liquid slip. However, macroscopic particle-fluid slip is generally small in our simulations, see the collapse of the particle and fluid velocity profiles in Fig. 4.7, especially for case D3 with a lifted particle core. Wilson and Sellgren [175] attributed the presence of a lifted particle core to Kutta–Joukowski lift acting on particles with a size larger than the viscous sublayer, though it is questionable to apply results from potential flow theory to slurry flows, in particular in the presence of turbulence. Kaushal and Tomita [89] found evidence of a lifted particle core in γ-ray densitometer measurements, especially for coarser particles at higher concentrations and higher velocities. This was ascribed to a lift force related to the 'impact of the viscous-turbulent interface' on the bottom-most particle layer and a possible additional effect from particle-particle interactions. Furthermore, Kaushal et al. [89] observed particle lift in CFD/TFM simulations and related this to lift from particle-fluid slip near the pipe wall. However, the simulated concentration profiles differed significantly from their γ-ray densitometer measurements and the 2D concentration distributions appear quite different from our observation for case D3. Again, we consider it more plausible that shear-induced migration from particle-particle interactions has been responsible for the lifted particle core in our experiments and simulations, since turbulence near the bottom of the pipe is strongly suppressed by the high particle concentration.

Finally, Zhang et al. [189] mentioned that the degree of non-axisymmetry of the 2D mean concentration distribution or the 'gravity bias', is primarily controlled by the Froude number, which they defined as $v_{bl}/\sqrt{|\tilde{\mathbf{g}}|D_{pipe}}$. For comparison with the present

study on liquid-solid pipe flow, the densimetric Froude number (Fr) is more relevant as it is based on the reduced gravity instead of gravity itself, see our previous discussion in section 4.5.2. Using $\rho_p/\rho_f = 1000$ and $v_{mix} \approx v_{bl}$, the densimetric Froude number varied in the range of 0.27−1.08 in the simulations of Zhang et al., while $Fr = 0.60$, 2.00 and 3.67 in our cases D1, D2 and D3, respectively. The densimetric Froude numbers are thus having a similar order of magnitude, although we observe a fixed-bed regime for case D1 with $Fr = 0.60$ while this regime is not observed at all in the simulations of Zhang et al. As an alternative to the densimetric Froude number, the Shields number may be considered for comparison, but no information is provided on the values of the wall friction velocity in the study by Zhang et al. Instead, we compare the particle-based densimetric Froude number, defined here as $Fr_p = v_{mix}/\sqrt{(\rho_p/\rho_f - 1)|\tilde{\mathbf{g}}|D_p} = \sqrt{8\theta/f}$. In the simulations by Zhang et al., Fr_p is in the range of 5.7−22.8, while Fr_p = 2.7, 8.9 and 16.4 in our cases D1, D2 and D3, respectively. The match between the particle-based densimetric Froude numbers is closer than for the pipe-diameter-based densimetric Froude number; the low value of Fr_p for case D1 may explain why no fixed-bed regime is observed in Zhang et al. The above comparison suggests that the particle-based densimetric Froude number and likely also the Shields number are better metrics to distinguish between the different flow regimes than the pipe-diameter-based densimetric Froude number.

4.5.5. MEAN STREAMWISE MOMENTUM BALANCE

To gain insight in the dynamics of the mean flow and thus mechanisms behind pipe friction, pressure drop and energy loss, we applied spatial and Reynolds averaging to the governing equations in order to derive an equation for the mean streamwise (y) momentum balance of the mixture flow [13, 64, 132]:

$$-\overline{\frac{dp_e}{dy}} + T + D + R = 0\,, \tag{4.13a}$$

$$T = \Big(-\frac{\partial}{\partial x}\langle\overline{v_f u_f}\rangle^s - \frac{\partial}{\partial z}\langle\overline{v_f w_f}\rangle^s\Big) + \frac{\rho_p}{\rho_f}\Big(-\frac{\partial}{\partial x}\langle\overline{v_p u_p}\rangle^s - \frac{\partial}{\partial z}\langle\overline{v_p w_p}\rangle^s\Big)\,, \tag{4.13b}$$

$$D = \frac{1}{Re\,(D_p/D_{pipe})}\Big(\frac{\partial^2\overline{v}_m}{\partial x^2} + \frac{\partial^2\overline{v}_m}{\partial z^2}\Big)\,, \tag{4.13c}$$

$$R = \frac{\partial\overline{\Sigma}_{yx}}{\partial x} + \frac{\partial\overline{\Sigma}_{yz}}{\partial z}\,, \tag{4.13d}$$

where T represents the momentum transport by fluid and particle motions, D accounts for viscous diffusion with $\overline{v}_m = \overline{\langle v_f\rangle^s} + \overline{\langle v_p\rangle^s}$ the mixture velocity, and R is the momentum transport by superficial particle stresses, $\overline{\Sigma}_{yx}$ and $\overline{\Sigma}_{yz}$, related to the hydrodynamic particle stresslet and particle collisions/contacts [64]. The latter was not computed explicitly, but implicitly from $R = -(-\overline{dp_e/dy} + T + D)$, i.e., by using Eq. 4.13a.

The flow-induced momentum transport, Eq. 4.13b, is further decomposed into separate contributions from (a) the mean secondary flow and (b) turbulent fluctuations.

To this purpose, we decomposed the momentum fluxes in Eq. 4.13b according to:

$$\langle \overline{v_f u_f} \rangle^s = \langle \overline{v}_f \overline{u}_f \rangle^s + \langle \overline{v'_f u'_f} \rangle^s . \tag{4.14a}$$

Following Breugem and Boersma [20] (p. 10,11), the first term at the right-hand side can be further decomposed according to:

$$\langle \overline{v}_f \overline{u}_f \rangle^s \approx \frac{\langle \overline{v}_f \rangle^s \langle \overline{u}_f \rangle^s}{1-\overline{\phi}} + \langle \widetilde{\overline{v}}_f \widetilde{\overline{u}}_f \rangle^s , \tag{4.14b}$$

where the approximation holds under sufficient scale separation between the macroscopic and the subfilter-scale flow, and the second term at the right-hand side denotes the subfilter-scale contribution to the momentum flux from the mean secondary flow with $\widetilde{\overline{v}}_f = \overline{v}_f - \langle \overline{v}_f \rangle$ and $\widetilde{\overline{u}}_f = \overline{u}_f - \langle \overline{u}_f \rangle$. We can thus make the following decomposition:

$$\langle \overline{v_f u_f} \rangle^s \approx \frac{\langle \overline{v}_f \rangle^s \langle \overline{u}_f \rangle^s}{1-\overline{\phi}} + \langle \widetilde{\overline{v}}_f \widetilde{\overline{u}}_f \rangle^s + \langle \overline{v'_f u'_f} \rangle^s . \tag{4.14c}$$

The above decomposition inspired us to rewrite the flow-induced momentum transport, T, into the contributions from the macroscopic mean secondary flow, T_S, and from subfilter-scale mean secondary flow and turbulent motions, T_F, according to:

$$T = T_S + T_F , \tag{4.15a}$$

$$\begin{aligned} T_S = &\Big(-\frac{\partial}{\partial x}\left[\frac{\langle \overline{v}_f \rangle^s \langle \overline{u}_f \rangle^s}{1-\overline{\phi}} \right] - \frac{\partial}{\partial z}\left[\frac{\langle \overline{v}_f \rangle^s \langle \overline{w}_f \rangle^s}{1-\overline{\phi}} \right] \Big) \\ &+ \frac{\rho_p}{\rho_f} \Big(-\frac{\partial}{\partial x}\left[\frac{\langle \overline{v}_p \rangle^s \langle \overline{u}_p \rangle^s}{\overline{\phi}} \right] - \frac{\partial}{\partial z}\left[\frac{\langle \overline{v}_p \rangle^s \langle \overline{w}_p \rangle^s}{\overline{\phi}} \right] \Big) , \end{aligned} \tag{4.15b}$$

$$\begin{aligned} T_F = &\Big(-\frac{\partial}{\partial x}\left[\langle \overline{v_f u_f} \rangle^s - \frac{\langle \overline{v}_f \rangle^s \langle \overline{u}_f \rangle^s}{1-\overline{\phi}} \right] - \frac{\partial}{\partial z}\left[\langle \overline{v_f w_f} \rangle^s - \frac{\langle \overline{v}_f \rangle^s \langle \overline{w}_f \rangle^s}{1-\overline{\phi}} \right] \Big) \\ &+ \frac{\rho_p}{\rho_f} \Big(-\frac{\partial}{\partial x}\left[\langle \overline{v_p u_p} \rangle^s - \frac{\langle \overline{v}_p \rangle^s \langle \overline{u}_p \rangle^s}{\overline{\phi}} \right] - \frac{\partial}{\partial z}\left[\langle \overline{v_p w_p} \rangle^s - \frac{\langle \overline{v}_p \rangle^s \langle \overline{w}_p \rangle^s}{\overline{\phi}} \right] \Big) . \end{aligned} \tag{4.15c}$$

Since the typical length scale of the secondary flow patterns is on the order of the pipe radius and since the dimensions of the averaging volume used to compute the macroscopic stresses, are equal to one grid cell in the cross-stream directions, the contribution of the subfilter-scale secondary flow to T_F is likely negligible compared to the Reynolds stress contribution from turbulent motions.

The contributions from the four terms in Eq. 4.13 are shown in Fig. 4.10 as function of height for the streamwise-vertical midplane for the DNS cases D1-D3, along with the separate contributions from the mean secondary flow (T_S) and turbulent motions (T_F) to the flow-induced transport.

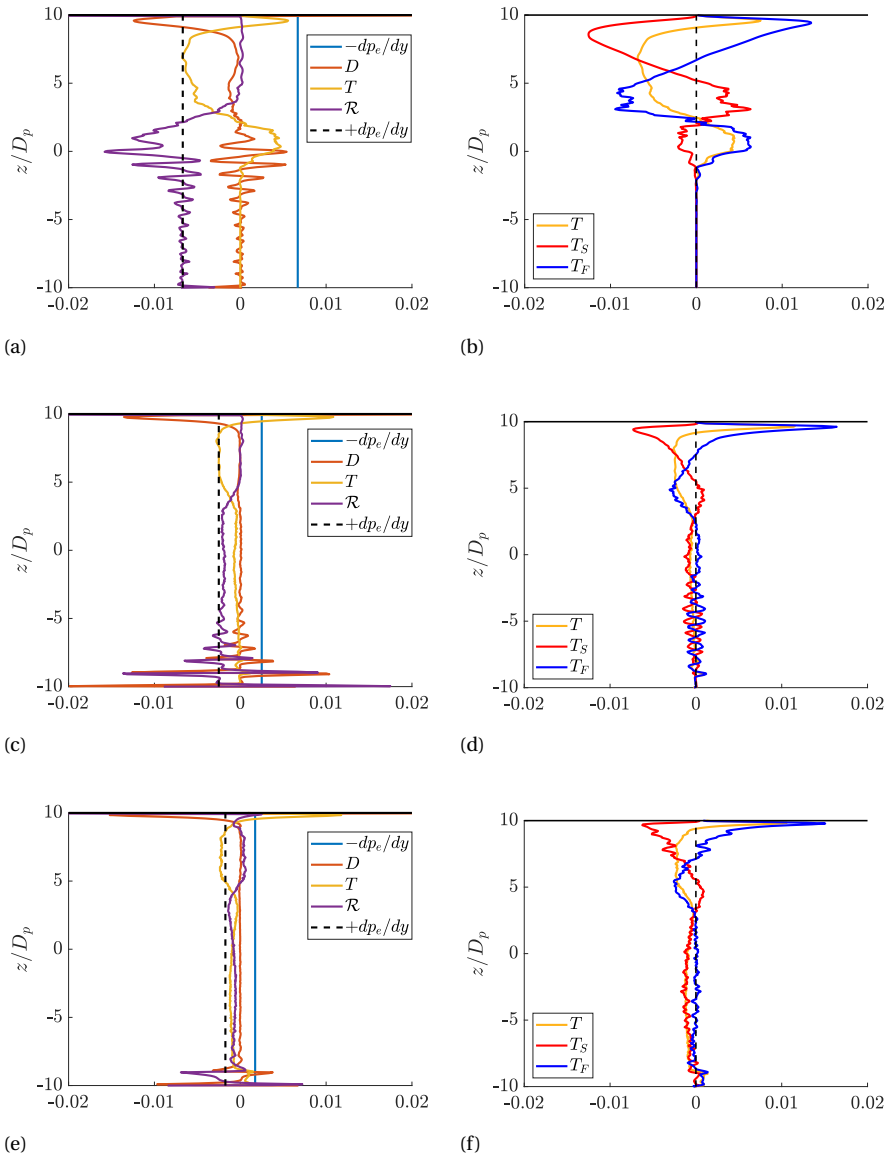

Figure 4.10: Mean streamwise momentum balance in the streamwise-vertical midplane (left) and decomposition of the flow-induced momentum transport into contributions from the mean macroscopic secondary flow and turbulent motions (right), shown for the DNS cases D1 (a,b), D2 (c,d) and D3 (e,f). $-\overline{dp_e/dy}$, D, T and R correspond to the external pressure gradient that drives the flow, viscous diffusion, transport of mean momentum by secondary flow (T_S) and turbulent stresses (T_F), and momentum transfer by particle stresses, respectively. In the left panels, $+\overline{dp_e/dy}$ is indicated with a black dashed line for visual comparison. The budget terms are normalised with $\rho_f v_{bl}^2/D_p$.

Focussing first on the fixed-case D1, we observe that inside the bed the streamwise pressure gradient is balanced by the particle-stress term. In fact, this is consistent with Darcy's law [21], as the particle-stress term should counterbalance the drag force within the bed (no net force on the particles):

$$0 = -\overline{\frac{dp_e}{dy}} - \frac{1}{Re(D_p/D_{pipe})}\frac{D_p^2}{\kappa}(1-\overline{\phi})\left[\overline{\langle v_f\rangle} - \overline{\langle v_p\rangle}\right], \tag{4.16}$$

where κ is the bed permeability. Estimating $\left[\overline{\langle v_f\rangle} - \overline{\langle v_p\rangle}\right]/v_{bl} \approx 0.0025$ from Fig. 4.7, the bed concentration $\overline{\phi} \approx 0.62$ from Fig. 4.9, and $-\overline{dp_e/dy} \approx 0.007$ (in units of $\rho_f v_{bl}^2/D_p$) from Fig. 4.10a, we find that $\kappa/D_p^2 \approx 8.3\times10^{-4}$. This is comparable to the prediction from the modified Ergun equation [113] with an uncertainty of ±50% for a random packed bed, $\kappa/D_p^2 = (1/180)(1-\overline{\phi})^3/\overline{\phi}^2 \approx 7.9\times10^{-4}$.

The particle-stress term in case D1 exhibits oscillations, which are accompanied with opposite oscillations in the diffusion term. This is a footprint of particle layering (cf. the insets of Figs. 4.7 and 4.9). In the top half of the pipe, the particle-stress term rapidly declines to zero and the flow-induced transport term becomes the dominant loss term, as may be expected for a turbulent flow and the absence of particles in this region. Interestingly, from Fig. 4.10b we observe that the contributions from secondary flow and turbulent motions to the overall flow-induced transport have the same order of magnitude and often have opposite sign, which seem typical features of secondary flows of Prandtl's second kind [126]. For the range of $z/D_p \approx 6-9$, the transport by secondary flow is the dominant contribution, being responsible for downward transport of low-momentum fluid from the region near the pipe top (cf. Fig. 4.6g), hence the negative sign of the transport term. For the range of $z/D_p \approx -1$ till 5, transport by turbulent motions is responsible for downward transport of high-momentum fluid towards the bed interface, consistent with the swap in sign of the transport term at $z/D_p \approx 2$. Close to the top wall, the overall flow-induced transport term in Fig. 4.10a swaps sign and becomes zero at the wall since there can be no transport across the wall. Furthermore, a thin viscous wall layer is present where viscous diffusion is the dominant loss term of momentum.

The momentum balance for case D2 is comparable to case D1. The particle-stress term is not only the dominant loss term inside the sliding bed ($z \lesssim 0$), but also in the dense suspension layer above the bed till $z/D_p \approx 3$ (cf. Fig. 4.8e). Oscillatory behavior in the particle-stress term is only significant close to pipe bottom, where particle layering is present. Figure 4.10.d shows that turbulence in the streamwise-vertical midplane is confined to the region $z/D_p \gtrsim 3$, indicating that turbulent motions are strongly suppressed in the dense suspension layer above the sliding bed.

In case D3, the particle-stress term is only dominant in the region close to pipe bottom due to particle layering and in a small region centered around $z/D_p \approx 3$. The latter corresponds approximately to the top of the lifted particle core (Fig. 4.8f), which is characterized by a rapid decline in the particle concentration with increasing height

and a local mean velocity maximum (Fig. 4.7). The flow-induced transport term is negative over most part of the streamwise-vertical midplane except near the pipe top and bottom and in a small region around the top of the lifted particle core at $z/D_p \approx 3$ where it is zero. Figure 4.10.f shows that this coincides with a transition from downward momentum transport by turbulent motions in the region directly above the lifted particle core to downward momentum transport by secondary flow within the particle core. Furthermore, within the lifted particle core, the zero turbulent transport indicates that turbulence is strongly suppressed. Interestingly, the transport from secondary flow is dominant over the particle-stress term in the bulk part of the lifted particle core ($z/D_p \approx -7$ till 0). This suggests that the upward directed secondary flow in the particle core likely contributes to the homogeneous concentration profile observed over the same region in Fig. 4.9 and acts in concert with shear-induced particle migration to counteract gravity.

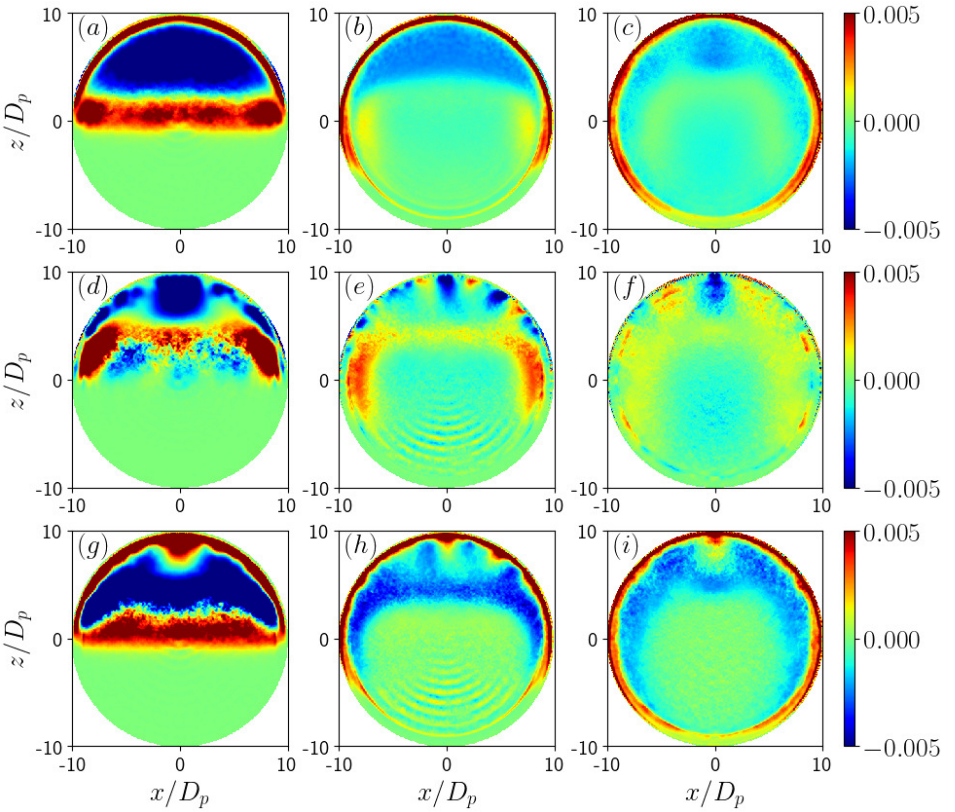

Figure 4.11: Spatial distribution of the flow-induced momentum transport defined by Eq. 4.13b (T, top row), and the contributions from the macroscopic mean secondary flow (T_S, middle row) and turbulent stresses (T_F, bottom row), shown for the cross-flow plane for cases D1-D3. (a,d,g) Case D1. (b,e,h) Case D2. (c,f,i) Case D3.

To gain additional insight in the contributions of the secondary flow and turbulence to streamwise momentum transport, Fig. 4.11 depicts the spatial distributions of T, T_S and T_F in the cross-flow plane. As observed before for the streamwise-vertical mid-plane, T_S and T_F have a similar magnitude and often opposite sign. The contribution from turbulent motions, T_F, is confined to the areas with comparatively low particle concentration. It is typically negative inside these areas, but flips sign and becomes positive near the pipe wall and near the bed interface for case D1, indicating turbulent transport of streamwise momentum down the mean velocity gradient. The transport by secondary flow clearly bears the imprint of the secondary flow pattern. In case D1, this is responsible for transport of high-momentum fluid towards the flow corners and downward transport of low-momentum fluid from the region near the pipe top. In case D2, the transport by secondary flow is dominant over turbulent transport in the low-concentration zones in between the pipe wall and the sliding bed. Finally, for case D3, turbulence appears strongly suppressed inside the entire lifted particle core given the zero transport from turbulent motions in this area. Note the significance of momentum transport by turbulent motions in the low-concentration zones flanking the dense particle core. This supports our previous hypothesis that the downward secondary flow in these zones is generated by turbulent motions and possibly augmented by particle-stress gradients and local particle sedimentation.

4.5.6. DISCUSSION

In general, the DNS results are in fairly good agreement with the corresponding experiments. Each of the three investigated cases resembles a different flow regime: the fixed-bed regime for case D1/E1, the sliding-bed regime for case D2/E2, and the suspended regime for case D3/E3, though the degree to which particles are suspended in the flow is significantly higher in the DNS (case D3) than in the experiment (case E3). The quantitative differences between the DNS and experiments are attributed primarily to two factors.

First, from Fig. 4.7 we observe a lower peak velocity in the DNS cases D1 and D2 than in the corresponding experiments, suggesting that the experimental value of the bulk liquid velocity and thus Re, which served as input parameter for the DNS, was underestimated. As discussed in section 4.3 and Appendix E, the liquid bulk velocity in the horizontal test section was not measured directly and had to be determined indirectly from available experimental data based on a number of assumptions and related uncertainty in the final estimate. An underestimation of the liquid bulk velocity in cases D1 and D2 is consistent with a lower friction factor in these DNS cases as compared to the corresponding experiments, see Fig. 4.5.

Second, another source of uncertainty relates to the actual value of the Galileo number: $Ga = 37.9 \pm 12.3$ at a reference temperature of $T = 25^{\circ}$C, see Appendix D. The relatively large uncertainty in Ga stems from the small relative density difference in the experiments, $(\rho_p/\rho_f - 1) \approx 0.02$, which strongly amplifies the uncertainty in the measured particle mass and particle diameter, see Eq. D.2. We hypothesize that the higher degree to which particles are suspended in case D3, might originate from an

underestimation of the actual Galileo number in the experiments and thus that the value used in the DNS was too low. Supporting evidence for this is given by the similar friction factor in Fig. 4.5 and similar peak velocity in Fig. 4.7 for cases D3 and E3, indicating a similar power input per unit pipe length from the driving pressure gradient, $(-\overline{dp_e/dy})\,(\pi D_{pipe}^2/4)\,v_{mix}$ with v_{mix} the bulk mixture velocity. If the power input is the same, part of which is needed to counteract gravity, then the higher degree to which particles are suspended in the DNS, is consistent with an underestimation of the relative density difference and thus the Galileo number in case D3.

Other possible causes for the observed discrepancies between the DNS and the experiments could be related to some, though limited, degree of polydispersity in size, shape and density of the particles used in the experiments, and experimental uncertainty in the parameters of the collision/contact model, see Appendix D. In particular, the Coulomb coefficient of sliding friction, μ_c, is deemed important for the sliding and suspended regime with frequent occurrence of particle/particle contact. Nonetheless, the spread in the measured values for μ_c is rather small, see Appendix D. In light of the above discussion, for future experiments we recommend to measure the liquid bulk velocity directly in the horizontal test section itself. Furthermore, we recommend to use PMMA particles with $\rho_p \approx 1200$ kg/m^3 in an aqueous glycerine solution. This will not only enhance the particle/fluid density contrast, but also provides flexibility in tuning the glycerol weight fraction for the desired fluid viscosity in order to keep the Galileo number around 40-45 as in the present experiments. As explained earlier, relatively low Galileo numbers are required to suspend the particles at moderate Reynolds numbers in reach of DNS. Finally, other measurement techniques such as Magnetic Resonance Imaging (MRI) may be considered too, which would enable simultaneous and accurate measurements of the local particle velocity and concentration field [74, 73].

4.6. PARAMETRIC DNS STUDY

The comparison between experiment and DNS was performed at different *Re*, *Ga* and ϕ_b. To investigate the influence of these parameters individually, an additional DNS study was performed. This consisted of five different cases, labelled S1-S5, of which the parameters are listed in tables 4.1 and 4.2. In cases S1-S4, only *Re* was varied, which is lowest for S1 and highest for S4. The parameters of case S5 are the same as for S4, except that *Ga* is twice as small.

4.6.1. INSTANTANEOUS FLOW SNAPSHOTS

Fig. 4.12 shows instantaneous flow snapshots in two different pipe cross-sections as well as the 3D particle distribution over the upstream part of the pipe. With increasing *Re* (S1-S4) and decreasing *Ga* (S4-S5), we observe that more particles are entrained into the flow. In case S1 we observe a fixed bed with clear particle layering, at least near the wall, and a turbulent flow above the bed as in cases E1/D1. In cases S2 and S3, the flow is in the sliding-bed regime as in cases E2/D2.

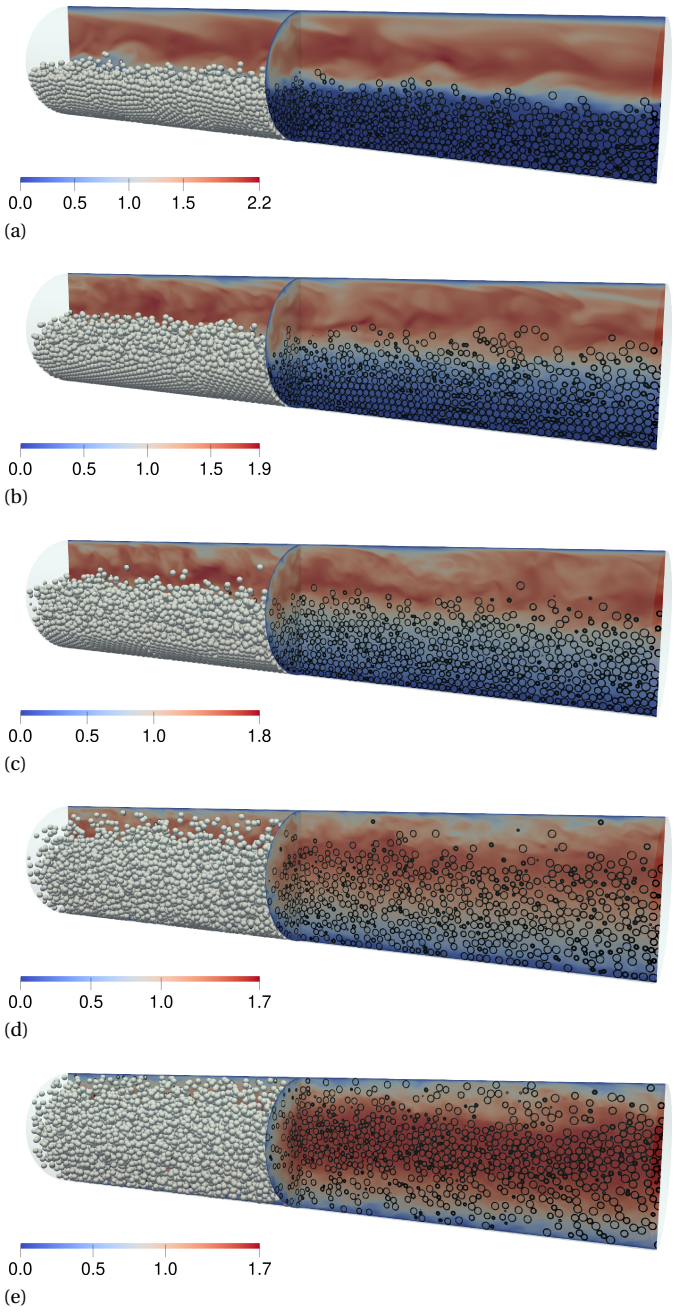

Figure 4.12: Instantaneous flow snapshots in two different pipe cross-sections as well as the 3D particle distribution over the upstream part of the pipe. The flow is going from left to right. The color denotes the streamwise velocity normalised with the liquid bulk velocity. Contours in the cross-sections indicate the particle positions (local grid cell solid volume fraction equal to 0.5). (a) S1, (b) S2, (c) S3, (d) S4, and (e) S5.

In cases S4 and S5, we observe a suspended-flow regime. Interestingly, while case S4 displays a clear heterogeneous particle distribution across the pipe, with more particles and slower flow at the pipe bottom than at the pipe top, in case S5 the particle distribution and flow appears nearly axisymmetric. In the latter case, a pronounced particle plug is present with a high particle concentration in the center of the pipe. While turbulence is fully damped inside the dense particle plug, the flow appears clearly turbulent outside the plug.

4.6.2. MEAN CONCENTRATION AND VELOCITY DISTRIBUTIONS IN CROSS-FLOW PLANE

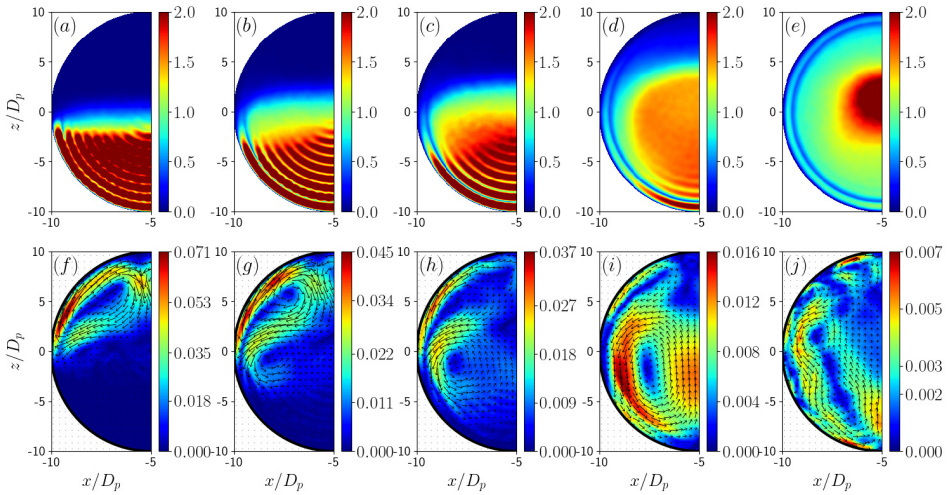

Figure 4.13: (a)-(e) Mean concentration field in the cross-flow section of the pipe for cases S1-S5. The color value indicates the mean concentration scaled with the bulk concentration ϕ_b. (f)-(j) Mean secondary fluid flow, $\overline{\langle u_f \rangle}/v_{bl}$ and $\overline{\langle w_f \rangle}/v_{bl}$, in the cross-flow section of the pipe for cases S1-S5. The color denotes the secondary flow magnitude $\sqrt{\overline{\langle u_f \rangle}^2 + \overline{\langle w_f \rangle}^2}/v_{bl}$ and the vectors indicate the direction of the secondary flow. The reference vector length has been rescaled for every case to optimize visibility.

Figure 4.13 shows the mean concentration and mean secondary flow in the cross-flow section of the pipe for cases S1-S5. Because of mirror-symmetry only half of the pipe is shown. A clear layered arrangement of particles in concentric rings can be observed for cases S1-S3 and to a lesser extent for case S4 near the pipe bottom. In case S4 we observe that the majority of the particles is lifted upwards in a plug between $z \approx -7$ till 3 with a fairly uniform concentration. In case S5 a large fraction of the particles even migrated towards the center of the pipe, where a distinct densely packed particle core can be seen with a diameter equal to $\sim 5D_p$. Furthermore, as already noticed from the flow snapshot of case S5 in Fig. 4.12, the mean particle concentration is nearly axisymmetric, though with a slightly upwards offset of the dense particle core and the presence of a more concentrated particle-wall layer at the pipe bottom as compared to

the pipe top due to gravity. As discussed before for case D3, we attribute the origin of the dense particle core and particle-wall layer in case S5 to shear-induced migration and particle-wall lubrication at the pipe wall, respectively. The very same flow features have been recently observed for dense neutrally-buoyant particle suspensions in pipe flow by Hogendoorn et al.[73]. Also, a similar concentration distribution was reported by Zhang et al. [189] for horizontal gas-solid pipe flow for their highest investigated Froude number, albeit with much less pronounced particle-wall layering. Obviously, in case S5, Re is sufficiently high and Ga is sufficiently low to reach a high value of the Shields number such that shear-induced particle migration towards the pipe core can overcome the tendency of particles to settle under gravity.

The radial force acting on the particles from shear-induced migration towards the pipe center (i.e., towards the low-shear zone) is expected to gradually increase with Re associated with the increase in shear rate. We argue that shear-induced migration is already significant in the sliding-bed regime and responsible for the gradual expansion of the low-concentration zones flanking the bed towards the pipe bottom as can be observed from Figs. 4.13b-d. Simultaneously, the wedge-shaped high-concentration zone at the bottom of the pipe becomes smaller. We associate this high-concentration zone with the region where shear-induced migration is too weak to 'fluidize' the bed, related to the weaker mean shear rate in this region and the larger component of gravity acting in the direction perpendicular to the pipe wall in this zone.

In all cases, a clear secondary flow is present, which is confined to the top half of the pipe in cases S1 and S2, but extends over the entire cross-section in cases S3-S5. Furthermore, as observed before for cases D1-D3, the secondary flow pattern is intertwinned with the spatial particle distribution. Albeit minor differences can be observed, the secondary flow patterns in cases S1, S3 and S4 are quite similar to the patterns observed before for cases D1, D2 and D3, respectively; this is probably because of the fairly similar Froude and Shields numbers, see tables 4.1 and 4.2. Normalised with the liquid bulk velocity, the strength of the secondary flow significantly drops from case S1 to S5.

In case S5, the secondary flow is weak (less than 1% of the liquid bulk velocity), which we ascribe to the near axisymmetry of the mean concentration and streamwise velocity distribution in this case, similar to the reason why a secondary flow is absent in single-phase turbulent pipe flow [126]. A weak upward flow is present from the bottom of the pipe towards the dense particle core and a downward flow near the pipe edges around $x/D_p \approx \pm 9$. Inside the dense particle core of case S5, the secondary flow is close to zero and hence not contributing to lifting of the core. Apart from the near axisymmetry of the flow, we ascribe the nearly zero secondary flow inside the core also to the locally high suspension viscosity and low permeability of the core packing.

While the concentration field in S5 is nearly axisymmetric in the core region, this is not the case near the wall, with more pronounced particle wall layering at the bottom than at the top. This is clearly visible in the mean concentration and mean velocity

profile along the streamwise-vertical midplane in Fig. 4.14a and b. The loss of axisymmetry near the pipe wall combined with the dense sphere packing in the pipe core, is ultimately responsible for the rather complex mean secondary flow pattern in Fig. 4.13j with a clear up-down asymmetry.

4.6.3. MEAN CONCENTRATION AND VELOCITY PROFILES

In Fig. 4.14a and b the mean concentration and velocity profiles are plotted as function of height in the streamwise-vertical midplane. The concentration profiles of cases S1-S3 are characterized by typical oscillations of about one particle diameter, related to regular particle layering within the bed. Peak concentrations well beyond 0.8 are observed, close to the value of approximately 0.91 for a hexagonal packing of circles in a plane (cf. the packing of the spheres near the wall in cases S1-S3 in Fig. 4.12). The uniform concentration plug in case S4 has a packing fraction somewhat less than 0.4. Different from case S4, where the concentration profile is non-axisymmetric and characterized by a large uniform plug, the profile in S5 is predominantly axisymmetric with a gradually varying concentration. The peak concentration in case S5 with a value of slightly less than 0.6, suggests a loose random sphere packing in the pipe center. The emerging picture is that shear-induced particle migration is responsible for 'filling' of the pipe core up to the maximum possible concentration for a loose random packing, after which the particle plug expands radially outwards [73]. We hypothesize that the growth of the particle plug stops once shear-induced migration (which is expected to weaken for decreasing concentration outside the plug) counterbalances turbulent particle diffusion in the region outside the particle plug.

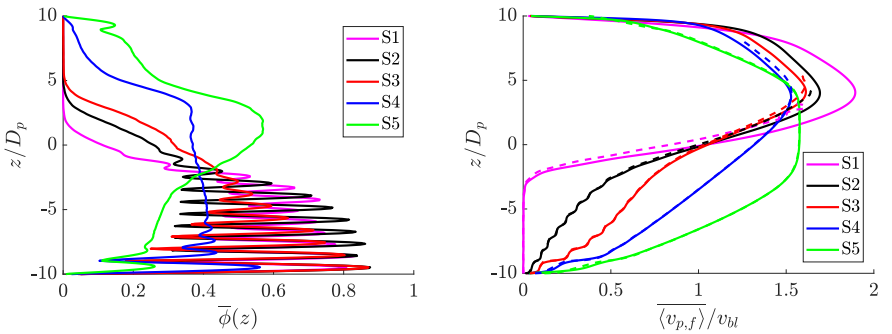

Figure 4.14: (a) Mean concentration and (b) mean velocity profiles in the streamwise-vertical midplane of the pipe for cases S1-S5. The solid and dashed lines in (b) denote the fluid and particle velocity profiles, respectively.

For case S5 the particle concentration at the pipe bottom is significantly higher than at the pipe top by a factor of 1.5−2, likely related to an effect of gravity. This asymmetry in the particle concentration near the wall is accompanied by a corresponding asymmetry in the mean velocity profile (cf. Fig. 4.14b). We speculate that this has been

responsible for enhanced wall friction and stronger shear-induced particle migration in the bottom half of the pipe as compared to the top half, which is consistent with the slight upward offset of the dense particle core with respect to the pipe centerline in this case.

The mean velocity profile in case S1 is similar to case D1 and characterized by a very slow (nearly zero) fluid flow through the fixed particle bed described by Darcy's law. The mean velocity profile in cases S2 and S3 is gradually increasing with height inside the sliding bed and the mild oscillations visible in the velocity profile are consistent with the oscillations in the corresponding concentration profiles. The mean velocity profile in case S5 is blunted in the core, which can be explained from the high concentration in the dense particle core and related high values of the particle shear stress and suspension viscosity. Finally, we note that the mean velocity profiles for the particles and fluid nearly coincide in all cases, indicating negligible macroscopic slip between the solid and fluid phase in the streamwise direction, in particular for cases S2-S4 in the lower half of the pipe and for case S5 away from the particle-wall layer. The particle Stokes number varies between $St = 0.04 - 0.11$ for cases S1-S5, and the low values may thus explain the negligible slip.

4.6.4. PARTICLE-MEAN VELOCITY AND HEIGHT

In Fig. 4.15a, the particle-mean streamwise velocity (red symbols) and the particle-mean height (black symbols) are shown as function of Re. Interestingly, normalized with the liquid bulk velocity, the particle-mean velocity increases close to linearly with Re between cases S1-S3 (i.e., the left three data points), suggesting that below $Re \approx 2000$ the particles would not move anymore at all. In case S4 the particle move on average with approximately the same velocity as the liquid phase. In case S5, where Ga is twice as low as in case S4 at the same Re, the particle-mean velocity is about 20% higher than the liquid bulk velocity, consistent with the high particle concentration in the core in this case where the velocity is maximum. Interestingly, this is accompanied by a drop of nearly 10% in the streamwise pressure gradient for case S5 (based on table 4.2 and given that the streamwise pressure gradient is proportional to v_τ^2), likely related to the much lower particle concentration near the bottom of the pipe compared to case S4 as can be observed from Fig. 4.14a. This is in line with the recent study of Hogendoorn et al. [73] on dense suspensions of neutrally-buoyant spheres in pipe flow, who reported drag reduction for core-peaking concentration distributions up to about 25% compared to the expected drag for a spatially uniform concentration distribution. They ascribed this to the relatively low concentration outside the dense particle core, which acts as an apparant lubrication layer with a relatively low viscosity between the dense and highly viscous particle core and the pipe wall.

The particle-mean vertical position in the pipe increases with Re in a clearly non-linear fashion. The lowest value found for case S1 is close to the limiting value corresponding to the case where all particles are settled in a bed at the pipe bottom and do not move at all. While in all cases the particle-mean position is negative, in case S5 the value is close to zero, indicating nearly negligible effect of gravity in this case.

In Fig. 4.15b the particle-mean (or solid bulk) streamwise velocity and particle-mean vertical position in the pipe are again depicted, but now as function of the Shields number, θ. The solid-to-fluid bulk velocity ratio, v_{bs}/v_{bl}, rises steeply with θ for the low θ-range, while beyond $\theta \approx 1$ the bulk velocity ratio inreases less steeply with θ and should ultimately become independent of θ for high θ when gravity effects are expected to be negligible. Interestingly, for cases S1-S3 (i.e., the lower θ-range), the bulk velocity ratio appears to scale as $v_{bs}/v_{bl} \approx 0.78 \cdot (\theta - 0.19)$, as indicated by the dashed line in the figure. This suggests a critical Shields number of about 0.19 beyond which particle transport is initiated by the flow over the bed, at least under the conditions chosen for the parametric DNS study. This is quite a bit higher than the critical value of 0.03−0.04 expected a priori from the original Shields diagram [152] given that the so-called grain Reynolds number of case S1 is equal to $v_\tau D_p/\nu_f \approx 20$. The reason for this is not fully clear. It might be related to non-linear scaling of v_{bs}/v_{bl} as function of θ just above the critical Shields number for incipient motion, which would thus invalidate our estimate based on the linear fit. Furthermore, we remark that the line fit would predict that $v_{bs}/v_{bl} \approx 0.27$ in case D1, while the actual value is 0.13 in this case (see table 4.2). This indicates that v_{bs}/v_{bl} depends also on Ga and/or ϕ_b as the values of these parameters were different in case D1 as compared to the parameter values chosen for the parametric DNS study. Finally, we remark that our flow geometry is different from the open-channel flow geometry studied by Shields and characterized by the presence of a secondary flow. We speculate that the downward-directed flow from the top of the pipe towards the bed as observed for the fixed-bed regime, see Fig. 4.13f, might have a stabilizing effect on the bed.

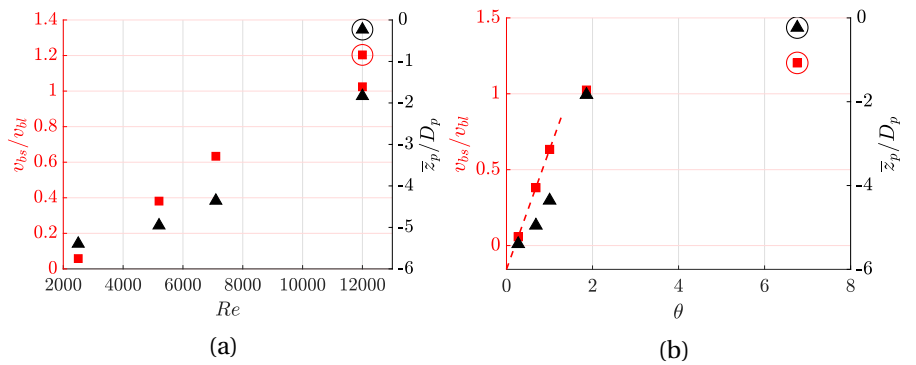

Figure 4.15: (a) Particle-averaged statistics for cases S1-S5 as function of Re. The left axis (red color and square symbols) shows the particle-mean streamwise velocity, v_{bs}, normalized with the liquid bulk velocity. The right axis shows the particle-mean vertical position in the pipe. The data points of case S5 are encircled. (b) Particle-averaged statistics for cases S1-S5 as function of θ. The dashed line is a linear fit through the particle-mean streeamwise velocity of cases S1-S3.

4.6.5. STREAMWISE MOMENTUM BALANCE

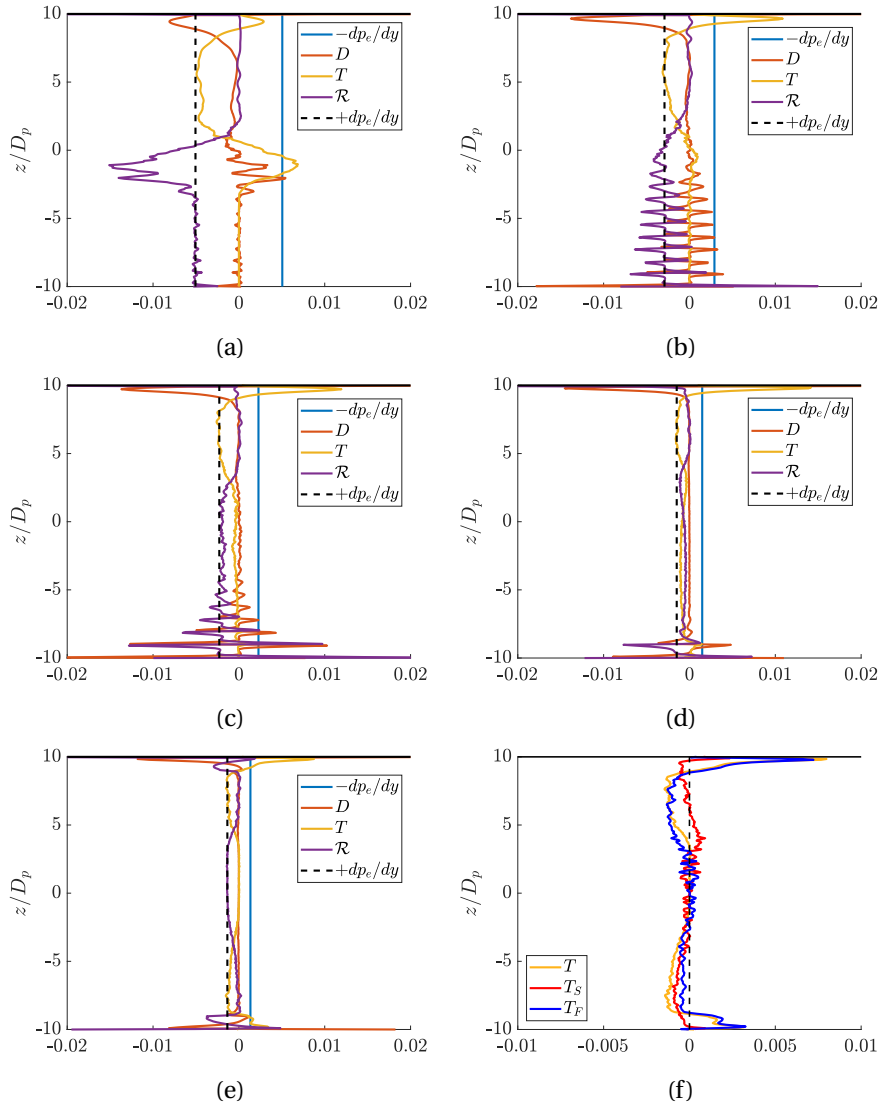

Figure 4.16: (a)-(e) Mean streamwise momentum balance in the streamwise-vertical midplane, shown for cases S1 (a), S2 (b), S3 (c), S4 (d) and S5 (e). $-\overline{dp_e/dy}$, D, T and R correspond to the external pressure gradient that drives the flow, viscous diffusion, flow-induced transport of mean momentum by secondary flow and turbulent fluctuations, and momentum transfer by particle stresses, respectively. $+\overline{dp_e/dy}$ is indicated with a black dashed line for visual comparison. The budget terms are normalised with $\rho_f v_{bl}^2/D_p$. (f) Decomposition of the flow-induced transport term, T, into the contribution from the mean secondary flow, T_S, and turbulent fluctuations, T_F, shown for case S5. Note the change in the range of the x-axis with respect to panels (a)-(e).

As before for cases D1-D3, also for cases S1-S5 we analyse the streamwise momentum balance given by Eq. 4.13a-d. The different contributions to the balance are presented in Fig. 4.16 for the streamwise-vertical midplane. From the comparison with Fig. 4.10 for cases D1-D3, it may be noticed that S1 is similar to D1 (fixed-bed regime), S2 and in particular S3 are similar to D2 (sliding-bed regime), and S4 is similar to D3 (heterogeneously suspended regime). Hence, cases S1-S4 are not discussed here for the sake of brevity and we focus on case S5.

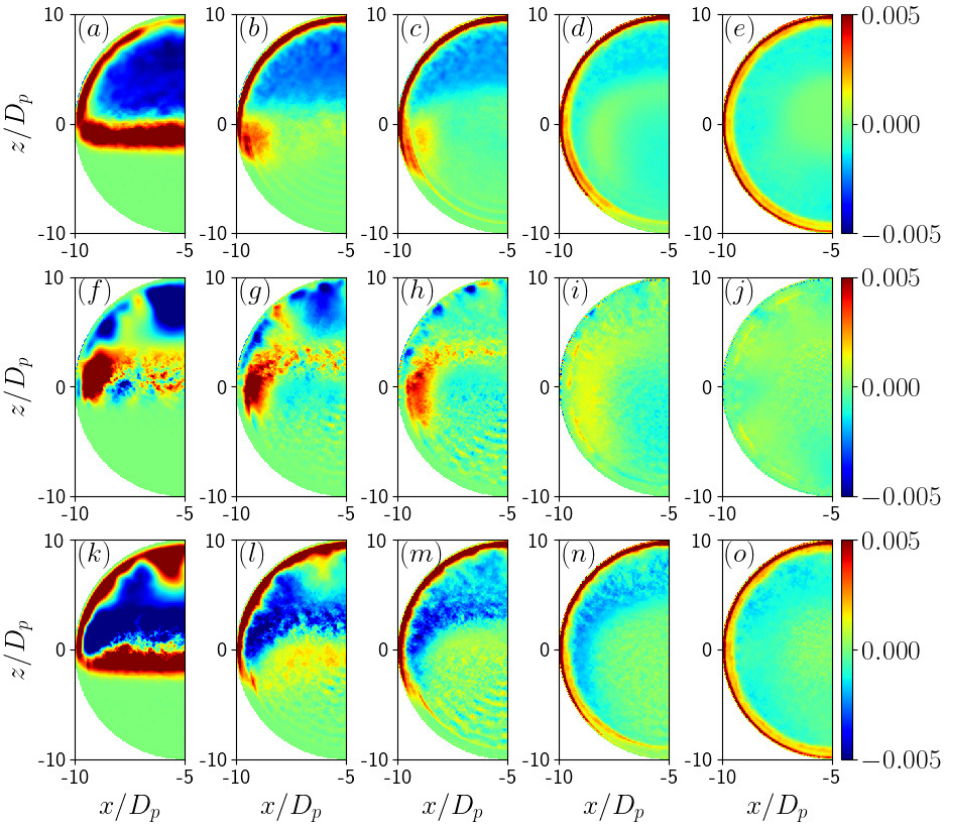

Figure 4.17: Spatial distribution of the flow-induced momentum transport defined by Eq. 4.13b (T, top row), and the contributions from the macroscopic mean secondary flow (T_S, middle row) and turbulent stresses (T_F, bottom row), shown for the cross-stream plane for cases S1-S5. (a,f,k) Case S1. (b,g,f) Case S2. (c,h,m) Case S3. (d,i,n) Case S4. (e,j,o) Case S5.

In case S5, we observe a near vertical symmetry about the center of the pipe, suggesting negligible influence of gravity. As discussed before, the observed deviation from perfect vertical flow symmetry is attributed to a still minor influence of gravity. In particular, the higher peak value of the particle-stress term at the pipe bottom relative to the pipe top, is consistent with the significantly more dense particle-wall layer near the pipe bottom (cf. Fig. 4.14a). For the core region, we observe that the pressure

gradient is balanced entirely by momentum transport from the particle stress, originating from the high local particle concentration (cf. Fig. 4.14a) and the related high suspension viscosity which tends to diverge near the maximum flowable packing limit (Eq. 4.6). While the flow-induced momentum transport is zero in the dense core region, indicating that turbulence is fully damped and secondary flow is absent here, it is the dominant loss term in the intermediate region of $4.5 \lesssim |z|/D_p \lesssim 8.5$ between the dense particle core and the pipe wall. The decomposition of the flow-induced transport in Fig. 4.16f shows that it originates almost fully from turbulent motions and related turbulent diffusion for $4.5 \lesssim z/D_p \lesssim 8.5$ in the upper part of the pipe, while it is the combined transport from secondary flow in the first place and turbulent diffusion in the second place for $-8.5 \lesssim z/D_p \lesssim -4.5$ in the lower part of the pipe. The dominance of the transport by secondary flow in the lower part of the pipe is rather suprising, given the weak secondary flow magnitude of less than 1% of the liquid bulk velocity (Fig. 4.13j). The negative sign of the transport by secondary flow is consistent with the upward flow in the bottom half of the pipe that transports low-momentum fluid from the bottom wall region towards the pipe core. Turbulent diffusion is negative for $4.5 \lesssim |z|/D_p \lesssim 8.5$, but swaps sign and becomes positive inside the particle layer ligning the pipe wall, related to the transport of high-momentum fluid by turbulent motions from the core region towards the wall. Within the particle-wall layer, the pressure gradient is balanced by the combined momentum transport from viscous diffusion, turbulent diffusion and the divergence from the particle stress. The contribution from the particle stress can be related to the local suspension viscosity (a diffusive effect) and a possible consequence from a slight macroscopic slip between the particles and the fluid in this layer (a drag effect), see Fig. 4.14b. Exactly at the wall, the streamwise pressure gradient is balanced by viscous diffusion and the divergence of the particle shear stress.

Finally, Fig. 4.17 depicts the spatial distributions of the flow-induced transport term, T, and the separate contributions from the mean secondary flow, T_S, and turbulent motions, T_F, for the cross-flow plane. The spatial distributions for cases S1-S4 by and large resemble the ones of cases D1-D3 previously discussed in section 4.5.5. For case S5, the negative flow-induced transport in the layer between the dense particle core and the particle-wall layer is mostly dominated by turbulent diffusion except in the regions directly below the core at $x = 0$ and sidewards of the core around $x/D_p \approx \pm 8$ where secondary flow contributes to the overall transport. Though the flow and concentration distributions in case S5 are nearly axisymmetric, the overall stronger turbulent diffusion in the upper part of the pipe indicates that turbulent motions are generally stronger here than in the bottom part of the pipe. An explanation for this might be the stronger turbulence production in the upper half of the pipe related to the generally steeper mean velocity gradient here from the upward offset of the dense particle core.

4.7. CONCLUSIONS AND DISCUSSION

We have studied the three basic transport regimes in horizontal slurry pipe flow by means of experiments in a slurry flow loop and interface-resolved DNS. In general, we found the DNS results in fairly good agreement with the experimental results, in partic-

ular given the experimental uncertainty in the actual values of the liquid bulk velocity and Galileo number. We also found fairly good agreement of the friction factor with popular empirical models from literature.

The experiments and simulations provided detailed insight into the characteristics of horizontal slurry transport through a small-diameter pipe. The densimetric Froude number, Fr, and in particular the Shields number, θ, are useful metrics to distinguish between the different flow regimes. Our main findings are summarized below.

- In the fixed-bed regime for $Fr \lesssim 1$ and $\theta \lesssim 0.75$, a rather sharp and flat interface exists between the overlying flow and the stationary bed. The bed is characterized by a regular packing of the spheres in circular rings. The particle alignment along the pipe wall originates from the constraint that the spheres cannot overlap with the wall. The perfect monodispersity of the spheres, at least in the DNS, is responsible for further layering deeper inside the bed. The flow inside the stationary bed is governed by Darcy´s law with the bed permeability comparable to the prediction from the modified Ergun model for slow flow through a packed bed. The turbulent flow above the bed is characterized by a secondary flow of Prandtl's second type and characterized by two main counter-rotating vortices related to the presence of two internal flow corners at the locations where the flat bed interface meets the pipe wall. The vortices stretch from the flow corners to the pipe top and are associated with a downflow from the pipe top into the bulk liquid above the bed. In the bulk of the turbulent flow above the bed, secondary flow transport and turbulent diffusion of streamwise momentum are balancing the streamwise pressure gradient. Here, secondary flow transport dominates over turbulent diffusion in regions where the secondary flow is strong, and vice versa in regions where the secondary flow is weak.

- In the sliding-bed regime for $1 \lesssim Fr \lesssim 2$ and $0.75 \lesssim \theta \lesssim 1.5$, the interface between the sliding bed and overlying turbulent flow is diffuse and curved down sideways. Turbulent low-concentration zones are flanking the top part of the bed. Furthermore, particle layering is still present within the bed, but confined to a wedge-shaped high-concentration zone above the pipe bottom. The secondary flow is characterized by a pair of counter-rotating vortices in the turbulent flow above the bed, with similar characteristics as in the fixed-bed regime, and another pair of counter-rotating vortices that extends over the lower half of the pipe though damped in the bed core. Inside the bed, the mean particle and fluid velocity gradually increase with height with negligible macroscopic slip. The streamwise pressure gradient is balanced here by the divergence of the particle shear stress associated with a high suspension viscosity from particle layers moving under shear.

- The suspended-flow regime for $Fr \gtrsim 2$ and $\theta \gtrsim 1.5$, is characterized by a dense lifted core of particles, which moves towards the pipe centerline with increasing Fr and θ. For very high Fr and θ, gravity has a minor influence on the flow dynamics, resulting in nearly axisymmetric distributions of the mean flow and concentration and a characteristic concentration peak near the pipe wall from

a particle layer lining the wall. The peak concentration in the core is about 0.6, characteristic for a random loose packing of spheres. The very high suspension viscosity in the core is responsible for a locally uniform velocity distribution and full damping of turbulence. Furthermore, the secondary flow has nearly disappeared in this limit as a result of the statistical axisymmetry of the flow. For the lower range of Fr and θ, when the lifted core of particles is still located significantly below the pipe centerline, the secondary flow pattern is similar to the pattern in the sliding bed regime, but the upper vortex pair is more confined to the pipe top and the lower vortex pair exhibits more pronounced upflow around the streamwise-vertical midplane. For $Fr \sim 3.5$ and $\theta \sim 2$, the upward secondary flow inside the particle core is found to be the dominant mechanism for transport of streamwise momentum across the core, with a secondary role for particle-induced diffusion related to the high suspension viscosity.

- For $\theta \lesssim 2$, the Darcy-Weisbach friction factor scales approximately as $f \sim 1/Re_{mix}$ and the Shields number as $\theta \sim Re_{mix}$. Since a turbulent flow is present in all cases, we ascribe this quasi-laminar behavior of the friction factor to changes in the flow topology and the amount of sediment carried by the flow. For $\theta \gg 1$, f seems to become approximately constant in Re_{mix} and $\theta \sim Re_{mix}^2$, consistent with the expectation for a turbulent flow in the presence of wall roughness related to a particle layer lining the wall.

Using the analogy of the flow above the bed with the flow in a circular pipe with the same hydraulic diameter and wall roughness, we proposed a model for the friction factor in the fixed-bed regime. Although this model does not account for secondary flow effects, still good agreement was found with the friction factor obtained from the DNS. For the sliding-bed regime, the friction factor is described well with the sliding-bed model of Newitt et al. [123] and the modified Durand-Condolios model [123]. The strong overprediction by the original Durand-Condolios model [44] underlines the importance of using the reduced gravity instead of gravity itself in the modelling of the friction factor, especially when the density ratio is strongly different from the value of ≈ 2.65 in the experiments of Durand and Condolios. For the heterogeneously suspended regime, the friction factor appears to be well described by the heterogeneous suspension model of Newitt et al. [123].

Our results on the influence of the Galileo number on the suspended flow regime at fixed bulk liquid Reynolds number (e.g., by simultaneously varying the bulk liquid velocity and the fluid viscosity), show that the axisymmetric core-peaking concentration distribution at high θ is accompanied by a reduction in drag and pressure drop relative to the non-axisymmetric concentration distribution at less high θ. This is ascribed to a higher particle concentration near the bottom wall for the non-axisymmetric case.

- All flow regimes are characterized by a secondary flow of Prandtl's second kind comprising mainly one counter-rotating vortex pair in the fixed-bed regime and

two main counter-rotating vortex pairs in the other regimes. The maximum strength of the secondary flow is on the order of a few percent of the liquid bulk velocity. In all flow regimes, the secondary flow patterns, the mean streamwise velocity and the spatial concentration distribution appear intimately related and mutually coupled with each other. Because of the resemblance to the secondary flow found for turbulent single-phase flow in semi-circular pipes, the upper vortex pair likely originated from turbulent motions in the apparent presence of internal flow corners. The origin of the lower vortex pair is more complex. We hypothesize that the downflow in the low-concentration zones flanking the bed, is primarily caused by turbulent motions in a corner-like geometry and possibly amplified by particle-stress gradients and local particle sedimentation. While the upflow in the core of the bed is weak in the sliding-bed regime due to the high suspension viscosity, it is significant in the suspended-flow regime. Since turbulence is fully damped here, we hypothesize that this upflow inside the lifted particle core originates from particle-stress gradients, which arise from centrifugal forces acting on curved paths of fluctuating particle motions near the wedge-shaped high-concentration zone at the pipe bottom.

- The prime physical mechanism for transition between the flow regimes is the competition in the bed region between the downward-directed net gravity force on the particles and shear-induced particle migration from particle-particle interactions towards a low-shear region. In this respect, the square root of the Shields number, $\sqrt{\theta}$, can be interpreted as the time scale ratio of gravity acting on a single particle within the bed, $\sqrt{D_p/(\rho_p/\rho_f - 1)g}$, to a time scale of the shear rate imposed by the overlying turbulent flow onto the hydraulically rough bed, D_p/v_τ. The definition of the Shields number thus seems to capture the relevant physics for flow transition in slurry pipe flow. This is less clear for the densimetric Froude number as it does not contain the particle diameter and is based on the mixture bulk velocity rather than the friction velocity related to the bed shear stress.

- The shear-induced particle migration can be understood from repulsive forces from lubricated and collisional contacts between adjacent particle layers under shear and thus in relative motion, resulting in a tendency of particles to accumulate in a region with low shear. Particle inertia may reinforce shear-induced migration. Assuming that the shear rate scales with v_τ/D_p and considering that ρ_p/ρ_f is nearly one in our study, this effect can be qualitatively assessed by means of the grain Reynolds number, $Re_p = v_\tau D_p/\nu_f$ [133, 152], which varies from approximately 30 in case S1 to approximately 50 in cases S4 and S5. This is thus well in the regime where 'inertial' shear thickening is expected to happen [133].

- The mechanism of shear-induced migration is already at work in the sliding-bed regime and responsible for (a) the formation of low-concentration zones flanking the upper part of the bed and (b) an apparent fluidisation of the particles in the upper part of the bed at a solid volume fraction significantly below that of the wedge-shaped high-concentration zone at the pipe bottom. With increasing θ, the low-concentration zones flanking the bed, extend further downwards

along the pipe wall untill the bed is fully lifted from the wall. The transition from the fixed-bed to the sliding-bed and ultimately the suspended regime for increasing θ, is thus a gradual transition process in which shear-induced particle migration becomes progressively more important. In the fixed-bed regime, gravity is strongly dominant and shear-induced migration negligible. The transition from the fixed-bed to the sliding-bed regime is marked by the formation of low-concentration zones flanking the bed and the subsequent formation of a secondary flow here. Shear-induced particle migration starts to dominate over gravity first at the top corners of the bed. It is here that the local shear rate is sufficiently large and the local component of gravity in the radial direction sufficiently small for shear-induced migration to dominate over gravity. The transition from the sliding-bed to the suspended regime corresponds to deepening of the low-concentration zones flanking the bed down to the bottom of the pipe. This is accompanied by the lifting of a dense particle core away from the wall and with a local maximum in the concentration (after filtering out the possible presence of particle layering). For very high Shields number, gravity will eventually become negligible, and shear-induced migration causes particles to accumulate in the pipe core untill it is counter-acted by turbulent diffusion outside of the dense particle core.

The results from our study have some important implications for CFD modelling of slurry pipe flow. For Reynolds-averaged continuum (mixture and two-fluid) models to accurately capture secondary flow patterns and related effects on the flow dynamics, the closure model for the Reynolds-stress tensor should account for the stress anisotropy as this is a prerequisite for existance of the secondary flow in zero and low-concentration regions [126]. Furthermore, because of the vital role played by shear-induced particle migration, accurate modelling of the particle stress is required, in particular particle stress gradients and, for capturing particle-induced secondary flow, anistropy of the particle-stress tensor (similar to the anistropy of the Reynolds-stress tensor required for generation of secondary flow by turbulence).

In the present study the particle/fluid density ratio was chosen close to 1 in order to obtain Shields numbers of $\mathcal{O}(1)$ at flow conditions in reach of DNS. To discuss this in more detail, we rewrite Eq. 4.12 into an the following expression for the Shields number:

$$\theta = \frac{f}{8}\left(\frac{Re_{mix}}{Ga}\frac{D_p}{D_{pipe}}\right)^2.$$

DNS is limited to moderate values of Re_{mix} as the required mesh width and computational time step to fully resolve the flow, both decrease with increasing Re_{mix}. Furthermore, interface-resolved DNS is also limited by the value of D_{pipe}/D_p as the computational costs scale with the number of particles in the domain and the flow has to be resolved both at the pipe and the particle scale. This leaves the Galileo number as the 'free' parameter that can be 'tuned' for the desired range of the Shields number, i.e., to simulate the fixed-bed, sliding-bed and suspended-flow regimes at moderate values of the mixture Reynolds number as in the present study. A sufficiently low value of the Galileo number can be accomplished in three different manners: (1) by choosing a particle/fluid density ratio close to 1 as in the present study where $(\rho_p/\rho_f - 1) \approx 0.02$ and

$Ga \approx 40-45$, (2) by increasing the kinematic fluid viscosity, and/or (3) by adopting a lower value for the gravitational acceleration. Though experimentally (nearly) impossible, the last option is numerically interesting as it enables to simulate for example sand/water slurries for realistic particle/fluid density ratio and fluid viscosity.

Through the present study, we hope to have sufficiently demonstrated the high potential of interface-resolved DNS to unravel the fundamental structure and dynamics of slurry pipe flow. To bridge the gap between idealized and real slurries, the present research may be extended towards investigating polydispersity effects in particle size, shape and density on the slurry flow dynamics and transition across flow regimes. We remark that polydispersity in size and shape may have a significant effect on the maximum (random) packing fraction [15, 39] and hence on the bed height in the fixed and sliding bed regime for given solid bulk concentration. Furthermore, polydispersity is also expected to reduce the tendency of particles to arrange themselves in a regular packing as observed in the present study for perfect monodisperse spheres.

5

CONCLUSIONS AND OUTLOOK

The primary objective of this research was to formulate a robust framework that harnesses particle-resolved Direct Numerical Simulation (DNS) to capture the intricate dynamics of 3D instationary flow in sediment transport within a horizontal pipe, encompassing scales ranging from the microscale of individual particles to the macroscale of the pipe. In our work, we related the particle-fluid and particle-particle interactions to their influence on the macroscopic dynamics of dense particulate suspensions, especially in the context of sedimentation and sediment transport. Furthermore, we compared our observations with other studies in literature and found them to be in agreement (see chapters 2 and 3). For example, the settling velocity measured in the direct numerical simulation (DNS) is in good agreement with the estimated settling velocity from correlations from Richardson and Zaki [142], Abraham [1] and Yin and Koch [182]. Next, in our study of sediment transport, we setup our DNS parameters to closely match an analogous experiment, thus, allowing us to make a direct comparison with the experiment. We were able to reproduce the different flow regimes observed in the experiments and we found the streamwise velocity profiles and the external pressure gradient measured in the DNS to be in good agreement with the experiment (see chapter 4). In summary, we demonstrate the ability of the numerical method to resolve individual particle-particle and particle-fluid interactions and reproduce trends observed in literature and experiment. Hence, providing confidence in the applicability of the (present) Immersed Boundary Method used for the particle/fluid coupling to dense heavy particulate suspensions. In the following sections, we discuss some of the critical insights from both our studies.

- Sedimentation
  Enhanced settling velocities of dilute sedimenting suspensions have been reported in literature where particles have been observed to settle preferentially in columns [163, 77]. It is conceivable that particles settling in these columns experience reduced drag, enabling them to settle at significantly higher velocities than a single settling particle under equivalent conditions. Notably, such enhanced settling velocities were observed particularly at Reynolds numbers (Re_T)

where isolated particles tend to settle in oblique trajectories [142], suggesting that the oblique settling trajectories facilitate particles being captured within the settling columns. Our investigation focused on the effect of inertia (of both the particle and fluid phase) on the dynamics of moderately dense and dense sedimenting suspensions. While we observed anticipated path instabilities for single settling particles, consistent with earlier findings, dense suspensions ($\gtrsim$ 10%) displayed consistent trends across different Re_T. Interestingly, even at Re_T where enhanced settling velocities were observed in dilute suspensions, the influence of Ga on the mean settling velocity in the dense regime was not pronounced (in contrast to the dilute regime). Furthermore, the conditioned averaged concentration and mean fluid flow field around a particle were remarkably similar across all Re_T at dense concentrations. This consistency aligns with expectations, where higher concentrations lead to smaller interparticular distances, curtailing the formation of large fluid structures. In such closely packed arrangements, collisions still play a minor role and for the most dense investigated cases, short-range, lubrication-type interactions between particles play a more pronounced role, dictating the macroscopic behavior of the sedimenting suspension. Another noteworthy observation was a preferentially higher concentration of particles in the lateral extent of each particle in the moderate concentration regime ($2\% \lesssim \phi \lesssim 10\%$), indicative of a preference for horizontal aggregation. This behavior can be attributed to the drafting-kissing-tumbling interaction between settling particles, where particles settle in a horizontal configuration due to the drafting effect [59, 80]. Further, we detected kinematic waves propagating through the sedimenting suspension and measured their velocity, which was found to be in good agreement with the correlation from Kynch theory [98]. For the moderate concentration regime, we found evidence that kinematic waves may trigger DKT instabilities, while conversely DKT instabilities may be responsible for the onset of kinematic waves.

- Sediment Transport
  The primary objective was to offer insights into the three basic transport regimes: the fixed-bed, the sliding-bed and fully-suspended regime in horizontal slurry pipe flow. Our exploration delves into the intricacies of interfacial drag force, particle stress, and turbulent stress, highlighting their roles in shaping slurry flow behavior. In the fixed-bed regime, a well-defined boundary separates a stationary bed of uniformly sized spheres from the flowing fluid above, with regular sphere packing influenced by the no-overlap constraint. Monodispersity within the bed leads to further layering, and the flow adheres to Darcy's law. The flow above the bed resembles turbulent flow in a non-circular, rough-walled channel, exhibiting a secondary flow pattern of Prandtl's second kind, consisting of two large recirculation cells. In the sliding-bed regime, the interface between the sliding bed and the fluid is diffuse, with particle layering in the lower pipe quadrant. A secondary flow pattern is present both in the fluid region above the sliding bed and inside the mobile particle layer in the upper bed region, intimately connected to the spatial particle distribution. The fully-suspended regime features a dense particle core, and for sufficiently low Ga, gravity has a minor influence and the

dense core at the pipe center likely results from shear-induced migration. Here, turbulence is suppressed within the particle core, where momentum transfer via particle stresses prevails, leading to a locally high suspension viscosity and a flattened velocity profile at the pipe center. Additionally, we also found fairly good agreement of the friction factor between the interface-resolved DNS and popular empirical models from literature.

The findings of this work offers insight conducive to enhancing the performance of slurry transport pipelines, aiming to boost operational efficiency and mitigate pipe wall abrasion. Noteworthy findings suggest that the optimal operational window for slurry pipelines potentially lies in the transitional region between a sliding bed and a fully-suspended regime. This strategic domain presents an opportunity for minimal bed wear and maximal solid flux, pivotal factors influencing pipeline performance. This determination is contextualized within the computational limitations arising from striving for high-resolution comparisons with operational conditions, particularly considering the higher Reynolds numbers that often apply in practice. Furthermore, with these insights at hand, there's a prospect of refining computational fluid dynamics models (for example the Two-Fluid model [119]) thereby advancing our comprehension of slurry transport dynamics and presenting actionable insights for optimizing practical pipeline operations.

RECOMMENDATIONS

The challenges encountered during our studies have provided valuable insights into improving our numerical simulations to better represent realistic particulate systems. In real-world scenarios, particles exhibit variations in size, shape, and density, which have a direct impact on various factors such as the terminal particle settling Reynolds number (Re_T), particle packing, inter-particle interactions, and settling path instabilities. For example, when analyzing sand samples from Oahu's beaches in Hawaii, it was found that the particles displayed around a 15% variation in mean density, diameters ranging from 0.2 to 7 mm, and a majority of particles being non-spherical in shape [154]. Although there are limited studies in literature considering the effects of polydispersity on dense particulate systems, there are some noteworthy works such as those by Kaushal et al. [91] and Vowinckel et al. [167]. Thus, incorporating the diversity of particle properties into Direct Numerical Simulations (DNS) appears to be a logical progression, especially since the present DNS methodology can potentially capture these effects with minimal adjustments. Further, the DNS approach's scope currently encompasses low-Reynolds (Re) turbulent flows. This limitation prompts contemplation on downscaling slurry flow conditions, possibly by lowering the Galileo number (Ga). However, for future experiments, we recommend considering a larger density contrast between the particle and fluid and a higher viscosity to access the suspended regime. For example, using PMMA particles in an aqueous glycerine solution.

In the evaluation of our simulations for single-phase turbulent pipe flow, agreement

with literature at the chosen grid resolution (as detailed in Chapter 4) is observed. However, a higher expected grid resolution is noted in light of Hogendoorn et al.'s recent study [73]. Despite satisfactory convergence at a lower grid resolution ($D_p/d_x = 16$) in previous studies on particle-laden flows, various factors, such as flow type and Reynolds number differences, must be considered. Notably, our study, featuring case D1 without moving particles over the pipe wall and a lower Reynolds number in case D3, is starkly different from the study of Hogendoorn et al. There are no moving particles over the pipe wall in our case D1 and the highest Reynolds number for our case D3 is significantly lower compared to the flow configurations in Hogendoorn et al. Nevertheless, the correct length scale to be resolved still remains an open question. In our study we argued that this is the 'standard' viscous wall unit in case D1 (based on the liquid viscosity and the wall friction velocity computed from the driving pressure gradient), while for homogeneous suspensions this should be the 'suspension' viscous wall unit based on the suspension viscosity (estimated from the bulk concentration) after the scaling found in previous studies by Costa et al. [31, 30].

Furthermore, it would be beneficial to explore additional aspects of sediment transport, such as the possibility of wavy motion of particles on bed surfaces or concentration waves within particle cores during fully-suspended regimes. Studies have shown that ripples or waves can significantly modify the arrangement of particles and consequently impact the transportation of sediment [158]. Research by Mazzuoli et al. demonstrated that secondary flows within recirculating cells can lead to ripple formation in oscillatory flow [117]. In our DNS of sediment transport, the observed recirculation cells suggest substantial particle mixing on bed surfaces or around suspended particle cores, underscoring the need for an in-depth investigation into the influence of secondary flows on ripple formation in sediment transport.

In light of the above findings and considerations, the following recommendations are put forth for future research:

1. **Analysis of Closure Models in TFM/RANS and LES/DEM Approaches:** Utilize the present DNS data to thoroughly examine and refine closure models used in Two-Fluid Models (TFM), Reynolds-Averaged Navier-Stokes (RANS) simulations, and Large Eddy Simulation coupled with Discrete Element Method (LES/DEM) approaches.

2. **Scour Studies Based on DNS Data:** Investigate scour phenomena by analyzing collision forces acting on walls and related work, thereby estimating the available power input that contributes to scouring processes.

3. **Exploration of Polydispersity Effects:** Delve into the effects of particle polydispersity by incorporating variations in particle size, shape, and density into simulations to better understand their impact on sediment transport.

4. **Colloidal Particle Interactions:** Explore the influence of colloidal particle interactions, including Brownian motion, Van der Waals forces, and electrostatic forces, on sediment behavior and transport.

5. **Investigation of Unsteady Flows:** Study the effects of unsteady flow conditions such as ramp-up, ramp-down, and oscillatory flows on sediment transport dynamics.

6. **Exploration of Non-Newtonian Carrier Fluids:** Extend the research to investigate how the presence of non-Newtonian carrier fluids affects particle behavior and sediment transport.

The interface-resolved DNS approach we have pursued not only addresses the challenges encountered in simulating sediment transport accurately but also holds the potential to unlock a wide array of phenomena relevant to dredging applications. Beyond its applicability to slurry transport, our methodology extends to the exploration of crucial processes such as excavation, cutting, and vertical transport. This not only enhances our understanding of sediment dynamics but also offers a comprehensive toolset for advancing various aspects of particle-laden flow simulations in diverse engineering contexts.

A

SCALING OF PARTICLE VELOCITY SPECTRA IN THE DENSE CONCENTRATION REGIME

We adopt the following simple model for particle velocity fluctuations in the dense concentration regime:

$$\frac{dv'_p}{dt} = \beta f' - \frac{(v'_p - v'_q)}{\tau_p}, \tag{A.1}$$

where the term on the left hand side accounts for the effect of particle inertia and added mass, the first term on the right hand side accounts for forcing by fluid pressure and viscous stress fluctuations, with β a dimensionless function of the particle-to-fluid density ratio and particle volume fraction and f' the fluctuating hydrodynamic force per unit particle mass, and the last term on the right hand side accounts for lubrication interactions with neighbouring particles with a typical velocity fluctuation v'_q and with τ_p an apparent time scale at which viscous lubrication acts.
Assuming that the particle velocity fluctuations are uncorrelated with the velocity fluctuations of neighbouring particles, the following equation can be derived for the temporal autocovariance of the particle velocity fluctuations:

$$\frac{d^2 R_{vv}}{d\tau^2} - \frac{R_{vv}}{\tau_p^2} = -\beta^2 R_{ff}, \tag{A.2}$$

where R_{ff} is the temporal autocovariance of f'. By taking the Fourier transform of this equation, we can relate the frequency spectrum of the particle velocity to the frequency spectrum of the fluid forcing:

$$E_{vv}(\omega) = \frac{\beta^2 \tau_p^2}{1 + (\omega \tau_p)^2} \cdot E_{ff}(\omega). \tag{A.3}$$

To model the forcing spectrum for the higher-frequency range, we assume that the forcing perturbations originate from small-scale fluid velocity perturbations ahead of the particle that are transported with the mean relative fluid velocity towards the particle and subsequently blocked and deflected by the particle. This yields a force perturbation on the particle of $f' = O(V_r \partial v_f'/\partial y)$ with $V_r = -V_s/(1-\phi)$ the mean relative fluid velocity. Similar to Taylor's hypothesis of frozen turbulence [125], we assume that the fluid velocity perturbations are rapidly advected past the particle compared to their lifetime. We can thus relate the forcing spectrum to the wavenumber spectrum of fluid velocity perturbations, $F(k)$, as follows:

$$E_{ff}(\omega) \propto \frac{(V_r k)^2 F(k)}{V_r}, \tag{A.4}$$

where the wavenumber k of the fluid perturbations relates to the frequency ω of particle perturbations as $k = \omega/V_r$.
For bubble-induced agitation of the fluid in homogeneous bubble swarms, Lance and Bataille [101, 144] used the spectral energy balance to argue that $F(k) \sim \epsilon k^{-3}/\nu_f$ for sufficiently large k, where ϵ is the viscous dissipation rate per unit fluid mass. A similar scaling based on the same argumentation is expected to hold for sedimenting sphere suspensions. Equation (A.3) then becomes:

$$E_{vv}(\omega) \propto \frac{\beta^2(\omega\tau_p)^2}{1+(\omega\tau_p)^2} \cdot \frac{\epsilon V_{fr}^2}{\nu_f \omega^3}. \tag{A.5}$$

Finally, two frequency limits can be considered:

$$\omega\tau_p \ll 1 : E_{vv}(\omega) \quad \propto \quad \left(\frac{\beta^2 \epsilon V_{fr}^2 \tau_p^3}{\nu_f}\right) \cdot \left(\omega\tau_p\right)^{-1}, \tag{A.6a}$$

$$\omega\tau_p \gg 1 : E_{vv}(\omega) \quad \propto \quad \left(\frac{\beta^2 \epsilon V_{fr}^2 \tau_p^3}{\nu_f}\right) \cdot \left(\omega\tau_p\right)^{-3}. \tag{A.6b}$$

In the dense concentration regime, the characteristic velocity and time scale are proportional to $\sqrt{gD_p}$ (Fig. 3.6.a) and $\sqrt{D_p/g}$ (Fig. 3.10), respectively. We thus expect that $\epsilon \propto \nu_f g/D_p$, $\tau_p \propto \sqrt{D_p/g}$ and the pre-factor at the right-hand side of the above equation to be proportional with $\sqrt{gD_p^3}$. In fact, the change in scaling behavior of the velocity spectra at $\omega\sqrt{D_p/g} \approx 0.4$ suggests that $\tau_p \approx 2.5\sqrt{D_p/g}$ for the currently investigated particle-to-fluid density ratio of 1.5. Thus, the above equation can be rewritten into the following form:

$$\omega\sqrt{D_p/g} \ll 0.4 : \frac{E_{vv}}{\sqrt{gD_p^3}} \quad \propto \quad \left(\omega\sqrt{D_p/g}\right)^{-1}, \tag{A.7a}$$

$$\omega\sqrt{D_p/g} \gg 0.4 : \frac{E_{vv}}{\sqrt{gD_p^3}} \quad \propto \quad \left(\omega\sqrt{D_p/g}\right)^{-3}, \tag{A.7b}$$

which for the high-frequency limit is in very close agreement with the observed scaling of the spectra in Fig. 3.12, though with a slightly less steep slope (-2.75 vs -3) for the vertical velocity fluctuations. For the lower-frequency range, the model prediction is less good, likely because the k^{-3} scaling of F does only hold for sufficiently large k [101]. For $0.1 \lesssim \omega \lesssim 0.4$ the fluid forcing seems anisotropic as the power-law scaling for the horizontal and vertical velocity spectra are different. The fact that their power-law exponents differ by a factor 2 suggests that the forcing of the two velocity components is still related to the same mechanism. We speculate that this could be a local DKT-type interaction between particles, but it is left for future study to test this hypothesis.

B

MASS BALANCE EQUATION FOR PLANE AVERAGE CONCENTRATION

We define the horizontal plane average concentration by $\Phi(y,t) = \langle \gamma \rangle_h$, where $\gamma(x,y,z,t)$ is the solid phase indicator function (equal to 1 in the solids and 0 in the fluid) and the brackets with subscript h denote the average over the horizontal directions in the computational domain (x and z). In a similar vein, we define the intrinsic plane average of the vertical particle velocity by $V_i = \langle \gamma v_p \rangle_h / \Phi$. Mass conservation requires that:

$$\frac{\partial \Phi}{\partial t} + \frac{\partial (V_i \Phi)}{\partial y} = 0 \,. \tag{B.1}$$

From Fig. 3.14 we observe that Φ is a rather noisy signal. To isolate the component of Φ related to kinematic waves, we introduce a local time average defined by $\widehat{\Phi} = \int_{-T/2}^{T/2} \Phi(t+\tau) d\tau / T$. We require that the filter width T is much larger than the integral time scale of the fluctuations in the vertical particle velocity ($\tau_{L,vv}$) on the one hand, while much smaller than the period of the kinematic waves (T_{KW}) on the other hand: $\tau_{L,vv} \ll T \ll T_{KW}$. When this condition is satisfied, the local time average preserves the signal related to low-frequency kinematic waves, while high-frequency "noise" is filtered out. We now decompose Φ and V_i according to $\Phi = \widehat{\Phi} + \widetilde{\Phi}$ and $V_i = \widehat{V}_i + \widetilde{V}_i$, where the tilde symbol denotes the deviation from the local time average. Application of the local time average to Eq. (B.1) yields the following result:

$$\frac{\partial \widehat{\Phi}}{\partial t} + \frac{\partial \left(\widehat{V}_i \widehat{\Phi} \right)}{\partial y} = - \frac{\partial \widehat{\widetilde{V}_i \widetilde{\Phi}}}{\partial y} \,. \tag{B.2}$$

Assuming that the local time and plane average particle velocity is in quasi-steady equilibrium with the local time and plane average concentration [98], we use the approximation $\widehat{V}_i \approx V_s(\widehat{\Phi})$ (i.e., $\widehat{V}_i$ is equal to the mean sedimentation velocity of a spatially uniform suspension with a concentration $\widehat{\Phi}$). Based on a similar analysis as in chapter

10 of Nieuwstadt et al. [125], we approximate the flux at the right-hand side by:

$$-\widetilde{\widetilde{V}_i\widetilde{\Phi}} \approx \mathscr{D}_{yy}\frac{\partial\widehat{\Phi}}{\partial y}, \tag{B.3}$$

where $\mathscr{D}_{yy}$ is the particle diffusivity in the vertical given by Eq. (3.9). Provided that there are no shock discontinuities and hence that $\widehat{\Phi}$ is smoothly varying in space, we may write Eq. (B.2) into the following form (cf. Eq. 3.18 in Batchelor [10]):

$$\frac{\partial\widehat{\Phi}}{\partial t} + V_{KW}\frac{\partial\widehat{\Phi}}{\partial y} \approx \frac{\partial}{\partial y}\left(\mathscr{D}_{yy}\frac{\partial\widehat{\Phi}}{\partial y}\right), \tag{B.4}$$

where $V_{KW} = \partial\left[V_s(\widehat{\Phi})\widehat{\Phi}\right]/\partial\widehat{\Phi}$ is the speed at which kinematic waves are propagating in the vertical [98]. Finally, we assume that variations in $\widehat{\Phi}$ are small compared to the bulk concentration ϕ, so that we may approximate V_{KW} by [10]:

$$V_{KW} \approx \left[\frac{1-(n+1)\phi}{1-\phi}\right] V_s(\phi). \tag{B.5}$$

where n is the power-law exponent in Eq. (3.1) for $V_s(\phi)$, valid for $\phi \gtrsim 10\%$.

C

METHOD OF REPEATED SPACE-TIME AUTOCORRELATIONS

The principle of the proposed method is that travelling wave characteristics of kinematic waves are preserved in the space-time autocorrelation of a space-time concentration field, while uncorrelated noise is filtered out. In addition, the "rank" of the autocorrelation can be tuned to amplify travelling wave modes when their contribution to the variance of the original signal is weak and to determine which wave mode is dominant. We define the first autocorrelation as the standard autocorrelation of a concentration field, and the second autocorrelation as the autocorrelation of the first autocorrelation. More in general, we define the n^{th} autocorrelation as the autocorrelation of the $(n-1)^{th}$ autocorrelation. To illustrate how the method works, we decompose the fluctuating, plane-averaged concentration, $\Phi'(y,t)$, into N travelling sine waves with amplitude A_l, wave speed c_l and phase θ_l, and a remaining term $\mathcal{N}$:

$$\Phi'(y,t) = \sum_{l=0}^{N-1} A_l \sin([y - c_l t]k_l + \theta_l) + \mathcal{N}(y,t)\,. \tag{C.1}$$

Note that for $c_l = 0$, $\mathcal{N} = 0$, and N equal to the number of grid cells in the periodic y-direction, Eq. (C.1) is essentially the Discrete Fourier Transform of Φ' at a given time. The variation of Φ' in time is thus accounted for by non-zero values of c_l and $\mathcal{N}$. Below we will determine the autocorrelations for the model signal given by Eq. (C.1) under the assumption that $\mathcal{N}$ can be modelled by white noise.

The first space-time autocorrelation of the above model signal can be computed by first computing the autocovariance, $R_1(\check{y},\check{t})$, with $\check{y}$ and $\check{t}$ denoting the spatial and temporal lag, respectively, and then normalizing it with the variance $R_1(0,0)$. In preliminary form, the autocovariance is given by:

$$R_1(\check{y},\check{t}) =$$

$$\frac{1}{TL}\int_{t=0}^{T}\int_{y=0}^{L}\sum_{l=0}^{N-1}\sum_{q=0}^{N-1}\Big[A_l A_q \sin\big([y - c_l t]k_l + \theta_l\big)\Big]\Big[\sin\big([y+\check{y} - c_q(t+\check{t})]k_q + \theta_q\big)\Big]\,dy\,dt$$

$$+R_{\mathcal{N}}(\check{y},\check{t}), \tag{C.2a}$$

where

$$R_{\mathcal{N}}(\check{y},\check{t}) = \begin{cases} \sigma^2_{\mathcal{N}} & \text{for } \check{y}=\check{t}=0, \\ 0 & \text{otherwise}. \end{cases} \tag{C.2b}$$

Here L is the height of the periodic domain and the integration time T is sufficiently large such that an integer number of periods of every wave component is captured. The integral in Eq. (C.2a) is only nonzero for $l = q$ and hence we can write R_1 as the sum of the following components:

$$R_1(\check{y},\check{t}) \quad = \quad R_{11}(\check{y},\check{t}) + R_{12}(\check{y},\check{t}) + R_{13}(\check{y},\check{t}) + R_{14}(\check{y},\check{t}) + R_{\mathcal{N}}(\check{y},\check{t}), \tag{C.3}$$

with the components R_{11} till and with R_{14} given by:

$$R_{11}(\check{y},\check{t}) =$$

$$\frac{1}{TL}\int_{t=0}^{T}\int_{y=0}^{L}\sum_{l=0}^{N-1} A_l^2\Big[\sin\big([y-c_l t]k_l\big)\Big]\cos(\theta_l)\Big[\sin\big([y-c_l t]k_l+\theta_l\big)\cos\big([\check{y}-c_l\check{t}\,]k_l\big)\Big]\,dy\,dt,$$

$$= \sum_{l=0}^{N-1}\frac{1}{2}A_l^2\cos^2(\theta_l)\cos\big([\check{y}-c_l\check{t}\,]k_l\big), \tag{C.4a}$$

$$R_{12}(\check{y},\check{t}) =$$

$$\frac{1}{TL}\int_{t=0}^{T}\int_{y=0}^{L}\sum_{l=0}^{N-1} A_l^2\Big[\cos\big([y-c_l t]k_l\big)\Big]\sin(\theta_l)\Big[\sin\big([y-c_l t]k_l+\theta_l\big)\cos\big([\check{y}-c_l\check{t}\,]k_l\big)\Big]\,dy\,dt,$$

$$= \sum_{l=0}^{N-1}\frac{1}{2}A_l^2\sin^2(\theta_l)\cos\big([\check{y}-c_l\check{t}\,]k_l\big), \tag{C.4b}$$

$$R_{13}(\check{y},\check{t}) =$$

$$\frac{1}{TL}\int_{t=0}^{T}\int_{y=0}^{L}\sum_{l=0}^{N-1} A_l^2\Big[\sin\big([y-c_l t]k_l\big)\Big]\cos(\theta_l)\Big[\cos\big([y-c_l t]k_l+\theta_l\big)\sin\big([\check{y}-c_l\check{t}\,]k_l\big)\Big]\,dy\,dt,$$

$$= -\sum_{l=0}^{N-1}\frac{1}{4}A_l^2\sin(2\theta_l)\sin\big([\check{y}-c_l\check{t}\,]k_l\big), \tag{C.4c}$$

$$R_{14}(\check{y},\check{t}) =$$

$$\frac{1}{TL}\int_{t=0}^{T}\int_{y=0}^{L}\sum_{l=0}^{N-1}A_l^2\Big[\cos\big([y-c_l t]k_l\big)\Big]\sin(\theta_l)\Big[\cos\big([y-c_l t]k_l+\theta_l\big)\sin\big([\check{y}-c_l\check{t}]k_l\big)\Big]\,dy\,dt\,,$$

$$=\sum_{l=0}^{N-1}\frac{1}{4}A_l^2\sin(2\theta_l)\sin\big([\check{y}-c_l\check{t}]k_l\big)\,. \tag{C.4d}$$

By summing up the contributions, we obtain the following expressions for the autocovariance and variance, respectively:

$$R_1(\check{y},\check{t}) = \sum_{l=0}^{N-1}\frac{1}{2}A_l^2\cos\big([\check{y}-c_l\check{t}]k_l\big)+R_{\mathcal{N}}(\check{y},\check{t})\,, \tag{C.5a}$$

$$R_1(0,0) = \sum_{l=0}^{N-1}\frac{1}{2}A_l^2+\sigma_{\mathcal{N}}^2\,. \tag{C.5b}$$

Finally, the first space-time autocorrelation is obtained by dividing Eq. (C.5a) by Eq. (C.5b):

$$\rho_1(\check{y},\check{t}) = \sum_{l=0}^{N-1}A_{l,1}\cos\big([\check{y}-c_l\hat{t}]k_l\big)+\rho_{\mathcal{N}}(\hat{y},\hat{t})\,, \tag{C.6a}$$

$$A_{l,1}=\frac{A_l^2}{\sum_{q=0}^{N-1}A_q^2+2\sigma_{\mathcal{N}}^2} \qquad \& \qquad \rho_{\mathcal{N}}=\frac{2R_{\mathcal{N}}}{\sum_{q=0}^{N-1}A_q^2+2\sigma_{\mathcal{N}}^2}\,. \tag{C.6b}$$

We remark that $\rho_{\mathcal{N}}(\hat{y},\hat{t})\neq 0$ only when $\hat{y}=\hat{t}=0$ as white noise correlates with itself only for zero displacement.
The second space-time autocorrelation is computed in a similar manner and is equal to:

$$\rho_2(\hat{y},\hat{t}) = \sum_{l=0}^{N-1}A_{l,2}\cos\big([\hat{y}-c_l\hat{t}]k_l\big)\,, \tag{C.7a}$$

$$A_{l,2} = \frac{A_{l,1}^2}{\sum_{q=0}^{N-1}A_{q,1}^2}=\frac{A_l^4}{\sum_{q=0}^{N-1}A_q^4}\,. \tag{C.7b}$$

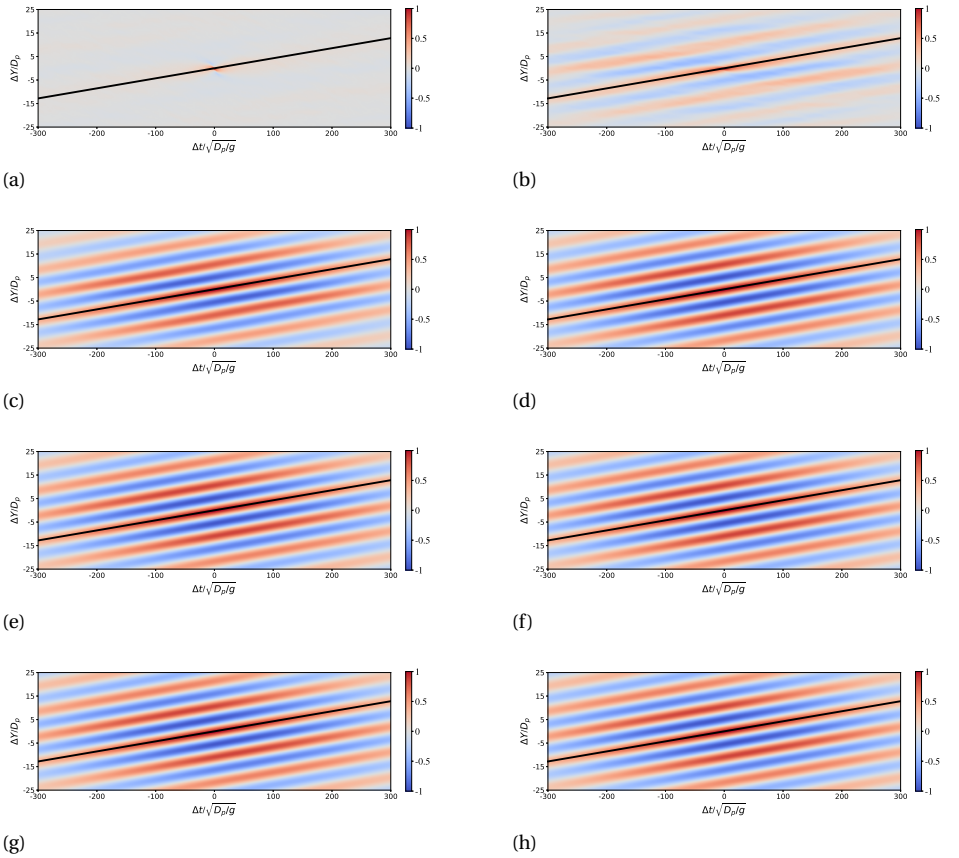

Figure C.1: Illustration of the method of repeated autocorrelations applied to the plane-averaged concentration field of the case with $Ga = 144$ and $\phi = 30\%$, see also Fig. 3.14.a,b. The slope of the black solid line corresponds to $V_{KW}/\sqrt{gD_p}$ determined from the 7th autocorrelation. ((a))-((h)) First till and with eighth autocorrelation.

The second autocorrelation can be readily generalized to the n^{th} space-time autocorrelation, which for $n > 1$ reads:

$$\rho_n(\hat{y},\hat{t}) = \sum_{l=0}^{N-1} A_{l,n}\cos\left([\hat{y} - c_l\hat{t}\,]k_l\right) \quad \text{for } n > 1\,, \tag{C.8a}$$

$$A_{l,n} = \frac{A_l^{(2^n)}}{\sum_{q=0}^{N-1} A_q^{(2^n)}}\,. \tag{C.8b}$$

The higher-rank autocorrelation maintains the travelling wave characteristics of the original signal. In addition, the higher the rank of the autocorrelation, the more the dominant travelling wave mode is amplified with respect to less dominant travelling wave modes. Let l_1 and l_2 be the dominant and second dominant travelling wave

mode, then the n^{th} autocorrelation amplifies the dominant travelling wave mode by a factor $(A_1/A_2)^{(2^n)}$ relative to the second dominant mode. So even in the presence of weak travelling wave modes and/or modes with nearly similar amplitude, the rank of the autocorrelation may be tuned to amplify travelling wave signals and to determine which mode stands out over other possibly present modes. Another benefit of the method of repeated autocorrelations is that it requires no a priori assumption on the range in wave number (k_l) and frequency ($c_l k_l$) of the dominant travelling wave modes as compared to, e.g., spectral band-pass filter methods. The method of repeated autocorrelations is illustrated in Fig. C.1 for $Ga = 144$ and $\phi = 30\%$, showing the first till and with the eighth space-time autocorrelation of the plane-averaged concentration field. As is clearly visible, the correlations are nearly identical for rank three and higher, as expected from the theoretical example discussed above. We picked the seventh autocorrelation for determining the kinematic wave velocity and wave length in the present study to make sure that only the most dominant wave mode was left in the data.

D

MEASUREMENTS OF MATERIAL PROPERTIES AND RELATED UNCERTAINTIES

Tilted flume experiments were performed to estimate the static Coulomb coefficient of sliding friction between (i) polystyrene particles, and (ii) between polystyrene particles and a plexiglass wall. The experimental setup is shown in Fig. D.1 and comprises a tiltable plexiglass box filled with tap water and a flat bed of particles. The Coulomb coefficient of friction between the polystyrene particles is measured from the tangent of the tilt angle at which there is initiation of motion of the bed of particles. The friction coefficient between polystyrene particles and the plexiglass bottom wall was measured in a similar manner, where (as opposed to a bed of particles) a number of polystyrene particles were glued to the bottom side of small plates and the tilt angle at which the plates began to slide was measured. The plates used are shown in Fig. D.2 and the measured friction coefficients are shown in Fig. D.3. From the measurements, we find that the friction coefficients for polystyrene-polystyrene contacts and for polystyrene-plexiglass contacts both have an overall mean value of close to 0.39. We adopted this value for the Coulomb coefficient of sliding friction in our interface-resolved DNS.

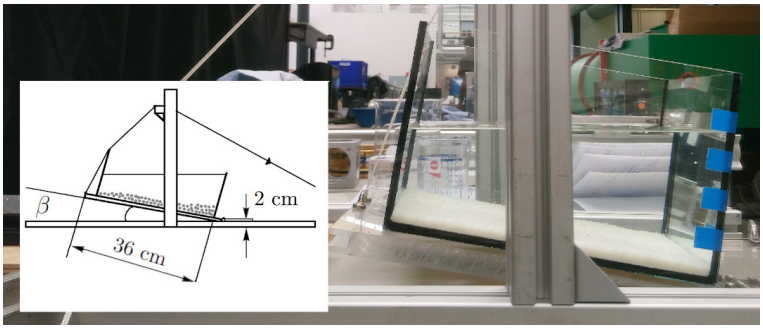

Figure D.1: Experimental setup used to measure the static Coulomb coefficient of sliding friction. The inset depicts a schematic of the setup. The coefficient of friction was estimated from the tangent of the angle β at which initiation of motion was observed.

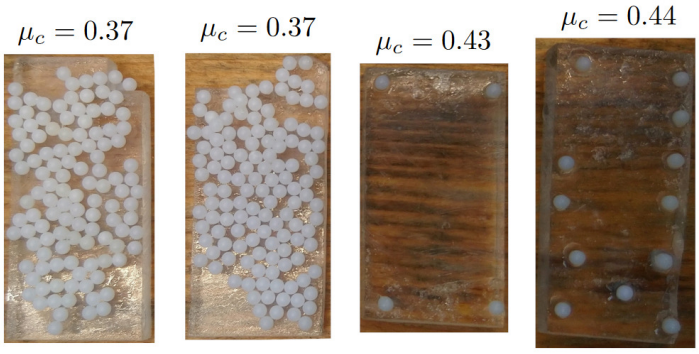

Figure D.2: Plates with polystyrene particles used to estimate the static Coulomb coefficient of sliding friction between the polystyrene particles and the plexiglass pipe wall.

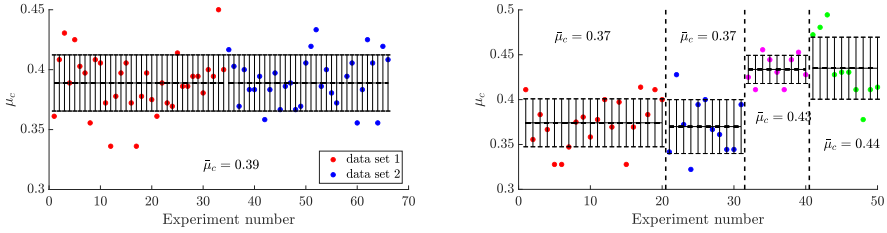

Figure D.3: Static Coulomb coefficient of sliding friction between (a) polystyrene particles and (b) polystyrene particles and a plexiglass wall. The solid bars show the standard deviation of the measurements.

Water absorption by the polystyrene particles over the course of the experiments is negligible. This was checked by comparing the weight of a sample batch of particles

after 1 week of immersion in water. To assess the effect of wear on the particles in the test loop, the particle diameter was remeasured after 40 hours of slurry flow loop operation. The distribution in particle size before and after operation is shown in Fig. D.4a where the particle diameters were measured from circle fitting of particle images by means of a circle Hough transform in MATLAB [6, 184]. The particles undergo some wear over the course of operation, as observed in the mean particle diameter which slightly decreased to 1.97 mm.

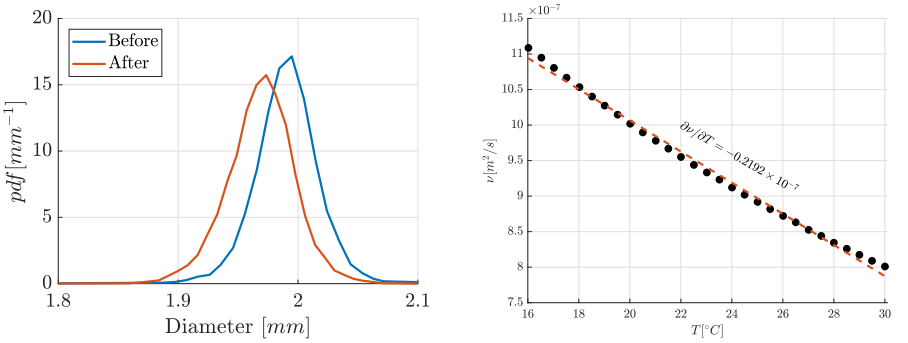

(a) (b)

Figure D.4: (a) Distribution in particle diameter before and after 40 hours of operation of the slurry flow loop indicated in blue and red, respectively. (b) Variation of kinematic viscosity of water as a function of temperature in the range where the experiments were performed, with the least squares line fit indicated by a red dashed line.

Uncertainty in the measured temperature yields an uncertainty in the value of the kinematic viscosity of the water as this was determined from the measured temperature: $\delta\nu_f = |\partial\nu_f/\partial T|\delta T$. Figure D.4b shows the variation in the viscosity of water as a function of temperature, from which $\partial\nu_f/\partial T$ was determined by means of a least squares line fit. The water density was determined also from the measured temperature where we assumed that the related uncertainty was negligible. The uncertainty in the mass and diameter of 20 individual particles was measured using a microgram weighing scale and a microscope (using again a circle Hough transform to fit circles to the particle images), respectively. The uncertainty in ρ_p was estimated from this by:

$$\delta\rho_p = \rho_p\sqrt{\left(\frac{\delta m}{m}\right)^2 + 9\left(\frac{\delta D_p}{D_p}\right)^2}. \tag{D.1}$$

Finally, the uncertainty in Ga was computed from:

$$\delta Ga = Ga\sqrt{\frac{1}{4}\left[\frac{\rho_p/\rho_f}{\rho_p/\rho_f - 1}\right]^2\left(\frac{\delta m}{m}\right)^2 + \frac{9}{4}\left[\frac{1}{\rho_p/\rho_f - 1}\right]^2\left(\frac{\delta D_p}{D_p}\right)^2 + \left(\frac{\delta\nu_f}{\nu_f}\right)^2}. \tag{D.2}$$

The uncertainty in particle diameter, mass, density and Ga of the particles are listed in table D.1, where the value of Ga was determined using the kinematic viscosity of water at a temperature of 25°C. The actual value of Ga was determined for each case

E1-E3 based on the corresponding water temperature during the experiment (listed in table 4.1).

D_p	2.02	$\pm$ 4.07 $\times$ 10^{-3} mm
m	4.39 $\times 10^{-6}$	$\pm$ 0.04 $\times$ 10^{-6} kg
ρ_p	1018	$\pm$ 11 kg/m^3
Ga	37.88	$\pm$ 12.27

Table D.1: Parameters related to the polystyrene spheres used in the slurry flow loop at $T = 25^{\circ}$C.

E

ESTIMATE OF INTRINSIC LIQUID BULK VELOCITY IN TEST SECTION OF SLURRY LOOP

The estimation of the intrinsic liquid bulk velocity in the test section, v_{bl}, involved three steps, which are discussed below in detail.

1. **Estimation of solid volume flux**
   Figure E.1 (left) shows a snapshot of the test section recorded at a frame rate of 1125 Hz. By scanning the row of pixels along the horizontal extent at each vertical pixel over all recorded frames, a $y-t$ diagram for each vertical pixel position was obtained. An example of such a $y-t$ diagram is depicted in Fig. E.1 (right), where the entire range of pixels in the horizontal is shown in the horizontal axis and the vertical axis shows the variation in pixel intensity over time. Here, the bright and dark pixels correspond to the particles and fluid, respectively.

   The mean particle velocity profile in the test section was estimated either by manually tracking lines corresponding to a particular intensity or by performing a temporal auto-correlation of each row of pixels in the video data. The two approaches yield comparable results, see Fig. E.2, and we decided to use the manual approach in the sequel. The video data presents a planar view of the pipe cross-section and therefore it is not possible to perceive depth from the video data. We expect that particles close to the center of the pipe will travel at a higher velocity than particles closer to the walls of the pipe. Hence, we might underpredict the depth-averaged particle velocity. Nevertheless, the solid volume flux in the test section, Q_p, was estimated using the expression:

$$Q_p = \int_0^{D_{pipe}} \bar{\phi}(z) 2 l(z) \overline{v}_p(z) dz, \tag{E.1}$$

where $\bar{\phi}(z)$ is the mean vertical concentration profile (averaged over x) obtained from the ERT sensor, $l(z) = \sqrt{z(D_{pipe} - z)}$ is the lateral half width of the pipe at a height z, and $\overline{v}_p(z)$ is the mean streamwise velocity profile of the particles.

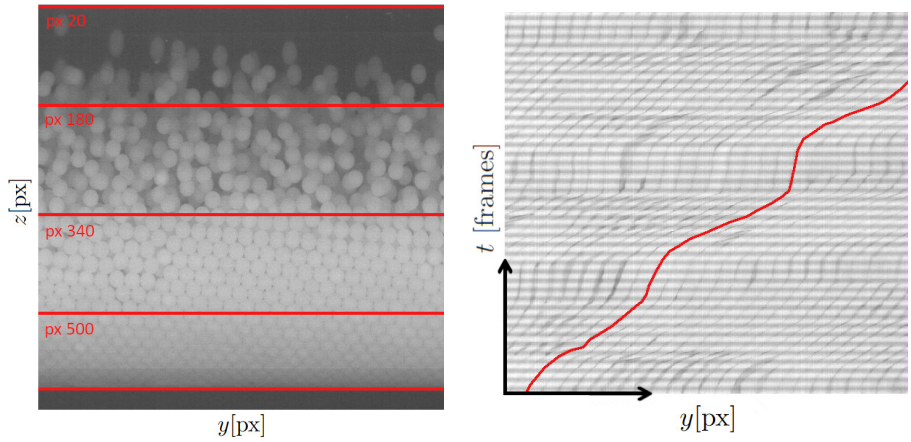

Figure E.1: Instantaneous snapshot (left) of the flow from the video recording at a frame size of 650×650 pixels. Some of the scanning lines along the horizontal at different vertical pixel heights are indicated in red. The evolution of the particle position with time along vertical pixel height 340 is shown on the right.

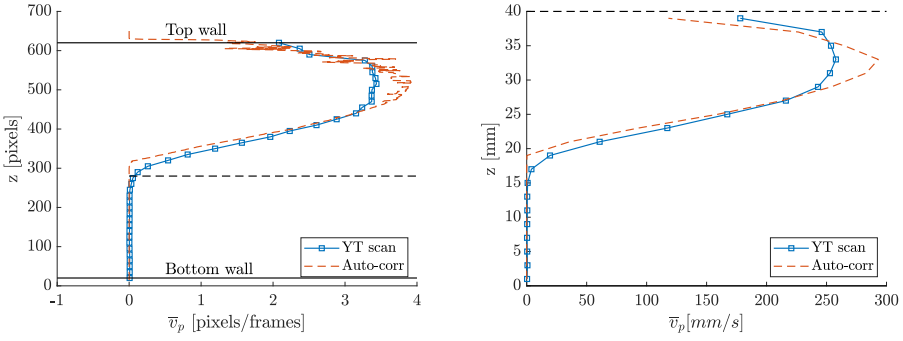

Figure E.2: Mean velocity of the particles in pixels/frames (left) and the same in mm/s (right). In the right figure, a moving mean filter with a width equal to one particle diameter was applied to the velocity profile. The blue and red dashed lines correspond to the estimation performed manually and using the temporal autocorrelation, respectively.

2. **Estimation of the particle concentration in the riser**
   For fully developed flow, the solid volume fluxes of the particles in the riser and the test section have to be equal to each other and are given by the expression:

$$c_r A_{pipe} v_{bs,r} = Q_p \,, \tag{E.2}$$

where c_r is the concentration of particles in the riser, $v_{bs,r}$ is the bulk velocity of

particles in the riser, and A_{pipe} is the cross-sectional area of the pipe. By rewriting $v_{bs,r}$ as the difference of the liquid bulk velocity and the sedimentation velocity of the particles in the riser, we estimated the riser concentration c_r using the expression:

$$c_r = (Q_p/A_{pipe})/(v_{bl,r} - v_{sed}(c_r, Re_T, D_p/D_{pipe})), \tag{E.3}$$

where $v_{bl,r}$, v_{sed} and Re_T are the liquid bulk velocity in the riser, the mean sedimentation velocity of particles in a quiescent fluid and the terminal Reynolds number of a single settling particle in free space, respectively. The liquid bulk velocity in the riser is known (from measurements using the magnetic flow meter installed in the riser). The sedimentation velocity was estimated using a correlation for the settling velocity of particles given by Richardson and Zaki [142]:

$$v_{sed} = v_T(1-c_r)^n, \tag{E.4}$$

where we calculated n based on a correlation from Richardson and Zaki for $1 < Re_T < 200$, given by:

$$n = (4.45 + 18D_p/D_{pipe})Re_T^{-0.1}. \tag{E.5}$$

The terminal settling Reynolds number of a particle was estimated from a balance between the net gravity force and the drag force acting on a settling particle [138], using Abraham's correlation for the sphere drag coefficient [1], given by :

$$Re_T = \frac{Ga}{\frac{\sqrt{3}}{2}\left(\sqrt{\frac{24}{Re_T}} + 0.5407\right)}. \tag{E.6}$$

Note that the Galileo number of the polystyrene particles is known. The terminal settling velocity of the particles was computed using the expression $v_T = Re_T \nu_f / D_p$.

3. **Estimation of the liquid bulk velocity in the test section**
For fully developed flow, the liquid volume flux in the riser and the test section have to be equal, from which the liquid bulk velocity in the test section was finally estimated using the relation $v_{bl,t} = ((1-c_r)/(1-c_t))v_{bl,r}$. The estimated liquid bulk velocity for E1-E3 is given in table E.1 and this estimate for the liquid bulk velocity was used to calculate the bulk liquid Reynolds number, Re, in the test section.

	c_r	c_t	$v_{bl,r}$ [mm/s]	$v_{bl,t}$ [mm/s]
E1	0.12	0.33	57	75
E2	0.14	0.28	164	196
E3	0.17	0.27	283	320

Table E.1: Table showing the estimated bulk concentration of particles in the riser, c_r, the measured bulk concentration in the test section, c_t, and the measured liquid bulk velocity in the riser, $v_{bl,r}$ and the estimated liquid bulk velocity in the test section $v_{bl,t}$.

F

VOLUME PENALIZATION METHOD AND DRIVING PRESSURE GRADIENT

The wall of the pipe is implemented by means of a volume-penalization method [88, 19]. The no-slip/no-penetration condition on the pipe wall is enforced by the projection:

$$\mathbf{u}^* \rightarrow \beta \mathbf{u}^* , \tag{F.1}$$

where $\mathbf{u}^*$ is a provisional velocity estimate obtained from Eq. 4.1b in the fractional step scheme and β is the local pipe wall volume fraction in a fluid grid cell. The latter is computed from a midpoint quadrature rule [93] to have a value of 1 in cells fully within the pipe, 0 in the cells fully outside it and an intermediate value for cells cut by the pipe wall:

$$\beta = \frac{\sum_{l=1}^{8} S_l H(S_l)}{\sum_{l=1}^{8} |S_l|} , \tag{F.2}$$

where l runs over the 8 corners of the fluid grid cell and H is the Heaviside function given by:

$$H(x) = \begin{cases} 1 & x \geq 0 \\ 0 & x < 0 \end{cases} .$$

S_l is the signed distance function to the pipe wall ($S_l > 0$ corresponds to the interior of the pipe), given by:

$$S_l = R_{pipe} - \sqrt{(x_l - x_c)^2 + (z_l - z_c)^2} , \tag{F.3}$$

where R_{pipe} is the pipe radius, and x_c and z_c are the coordinates of the centerline of the pipe.

The streamwise pressure gradient that drives the flow, is computed from the requirement that the non-dimensional intrinsic liquid bulk velocity has to be kept con-

stant at a value of 1. At Runge-Kutta level 1 it is computed from:

$$-\frac{dp_e}{dy}\Big|_{\alpha=1} = -\frac{dp_e}{dy}\Big|_{\alpha=0} + (1-\phi_b)\Big(\frac{1-v^*_{bl}|_{\alpha=1}}{RK_{\alpha=1}\Delta t}\Big), \tag{F.4}$$

where $\alpha = 0$ refers to the previous time step, Δt is the time step, RK_α is the Runge-Kutta coefficient at Runge-Kutta step α, and v^*_{bl} is the provisional phase-averaged fluid bulk velocity computed after the projection step (see Eq. F.1). The pressure gradient is kept constant at this value after the first Runge-Kutta step, i.e.:

$$-\frac{dp_e}{dy}\Big|_{\alpha=3} = -\frac{dp_e}{dy}\Big|_{\alpha=2} = -\frac{dp_e}{dy}\Big|_{\alpha=1}. \tag{F.5}$$

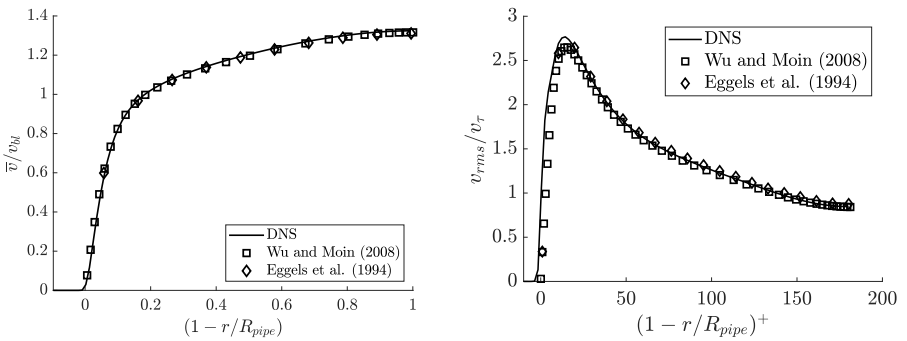

Figure F.1: DNS of single-phase pipe flow at $Re = 5300$ compared with results of Eggels et al. [45] and Wu and Moin [179]. (a) Mean streamwise velocity as function of radial distance from the pipe wall. (b) Streamwise root-mean-square (rms) velocity scaled with wall friction velocity v_τ and plotted as function of radial distance from the pipe wall measured in viscous wall units.

This method has been validated by performing DNS of a turbulent single-phase pipe flow at $Re = 5300$ and using the same grid resolution as in the slurry flow simulations ($\Delta x/D_{pipe} = 1/320$, corresponding to $\Delta x^+ = 1.13$ here, which is of the same order as the values given in table 4.2 for the DNS of slurry pipe flow). The results are compared with single-phase pipe flow simulations of Eggels et al. [45] and Wu and Moin [179]. Excellent agreement is found for the mean and rms streamwise velocity, see Fig. F.1.

G

FRICTION FACTOR MODELS FOR SLURRY PIPE FLOW

In this appendix, details are provided of the Darcy-Weisbach friction factor models for slurry pipe flow used for the comparison with the DNS and experimental data in Fig. 4.5.

MODEL FOR THE FIXED-BED REGIME

To model the friction factor for this regime, we assume first that the great majority of the liquid flow is confined to the channel region above the bed. The liquid bulk velocity in the channel region, v_{blc}, is approximated from the liquid bulk velocity through the entire pipe, v_{bl}, as:

$$v_{blc} \approx (1-\phi_b) A_{pipe} v_{bl} / A_c \,, \tag{G.1}$$

where A_{pipe} and A_c are the cross-sectional area of the pipe and channel region, respectively. Following the methodology described in chapter 6.8 of White (2011) [170], the streamwise pressure gradient for the channel region is estimated from the analogy of the flow through the non-circular channel with flow through a circular pipe with a hydraulic diameter $D_H = 4A_c/P_c$ with P_c the perimeter of the channel. The relative roughness height of the equivalent pipe is estimated by $\epsilon = D_p/D_H$. This yields the following model for the friction factor in the fixed-bed regime:

$$f_{FB} = f_{SPR}(Re_c, \epsilon) \cdot \frac{D_{pipe}}{D_H} \frac{v_{blc}^2}{v_{mix}^2} \,, \tag{G.2}$$

where $Re_c = v_{blc} D_H / \nu_f$ is the apparent Reynolds number for the equivalent pipe. f_{SPR} is the friction factor for the single-phase flow reference, which we estimated from the correlation of Haaland [67]:

$$f_{SPR} = \left(1.8 \, log_{10} \left[\frac{6.9}{Re} + \left(\frac{\epsilon}{3.7} \right)^{1.11} \right] \right)^{-2} . \tag{G.3}$$

Given that $\phi_b = 0.325$ in the fixed-bed case E1/D1 and assuming an average bed packing fraction of 0.64, we estimated that $A_c \approx A_{pipe}/2$ and $P_c \approx (\pi/2+1)D_{pipe}$.

DURAND AND CONDOLIOS MODEL (1953)

The original model for the friction factor proposed by Durand and Condolios [44] is given by:

$$f_{DC} = f_{SPR}\Big(1 + 176\phi_d\Big[\frac{v_{mix}^2}{|\tilde{\mathbf{g}}|D_{pipe}}\frac{\sqrt{|\tilde{\mathbf{g}}|D_p}}{v_T}\Big]^{-1.5}\Big), \tag{G.4}$$

where f_{SPR} is the estimated friction factor for pure liquid pipe flow, which is estimated here from the Haaland correlation for a hydraulically smooth pipe, see Eq. G.3, $\phi_d = \phi_b v_{bs}/(\phi_b v_{bs} + (1-\phi_b)v_{bl})$ is the so-called delivered concentration, and v_T is the terminal velocity of a single settling particle in free space. The latter can be calculated from the Galileo number according to $Re_T = \sqrt{\frac{4}{3C_d}}Ga$ [138], where $Re_T = v_T D_p/\nu_f$ is the terminal Reynolds number and $C_d = (\sqrt{24/Re_T}+0.5407)^2$ is the sphere drag coefficient estimated here from Abraham's drag correlation [1]. We note that the coefficient of 176 in Eq. G.4 was not given explicitly by Durand and Condolios, but it can be deduced from the line fit presented in Fig. 17b of their paper [44].

As discussed by Miedema [121], Durand and Condolios [44] normalised v_T with $\sqrt{|\tilde{\mathbf{g}}|D_p}$ and v_{mix} with $\sqrt{|\tilde{\mathbf{g}}|D_{pipe}}$. To account for the Archimedes force on the particles, it is deemed more appropriate to multiply $|\tilde{\mathbf{g}}|$ with the relative density difference between the particles and the fluid, $(\rho_p/\rho_f - 1)|\tilde{\mathbf{g}}|$, i.e., to replace the gravity by the *reduced* gravity. Since Durand and Condolios proposed their correlation based on a fit to experimental data for sand/water slurries with a fixed density ratio of $\rho_p/\rho_f \approx 2.65$, their correlation can be modified in a straightforward manner according to:

$$f_{MDC} = f_{SPR}\Big(1 + 121\phi_d\Big[Fr^2\frac{\sqrt{(\rho_p/\rho_f - 1)|\tilde{\mathbf{g}}|D_p}}{v_T}\Big]^{-1.5}\Big). \tag{G.5}$$

Eq. G.5 is precisely the form of the Durand and Condolios model as given by Newitt et al. [123] (p. 94), but we will refer to this correlation as the *modified* Durand and Condolios model as it is different from the original model when the density ratio is not equal to 2.65.

MODELS OF NEWITT ET AL. (1955)

Newitt et al. [123] distinguished between a sliding-bed and a heterogeneous suspension regime. For the sliding-bed regime, the authors assumed that the excess pressure gradient from the solids (with respect to single-phase pipe flow at the same mixture bulk velocity) can be modelled from the frictional contact force exerted by the pipe wall onto the moving bed. Based on this, they proposed the following model for the friction factor in the sliding-bed regime:

$$f_{NSB} = f_{SPR}\Big[1 + 66\phi_d\frac{1}{Fr^2}\Big], \tag{G.6}$$

where the coefficient of 66 was obtained from a best fit with their experimental data. For the heterogeneous suspension regime, the authors assumed that the suspended

solids are responsible for an excess pressure gradient needed to provide the required power for maintaining the solids suspended in the flow. Based on this, they proposed the following model for the friction factor in the heterogeneous suspension regime:

$$f_{NHS} = f_{SPR}\left(1 + 1100\phi_d \frac{1}{Fr^3} \frac{v_T}{\sqrt{(\rho_p/\rho_f - 1)|\tilde{\mathbf{g}}|D_p}} \sqrt{\frac{D_p}{D_{pipe}}}\right), \tag{G.7}$$

where the value of 1100 is an empirically determined coefficient to provide the best fit with their experiments.

EQUIVALENT LIQUID MODEL

The equivalent liquid model is based on the assumption that the particles are homogeneously suspended in the flow and very small (i.e., a small diameter and response time relative to the length and time scales of the liquid flow). In that particular case, it may be expected that the suspension behaves like an equivalent liquid based on the mixture density and suspension viscosity with a friction factor given by:

$$f_{ELM} = f_{SPR} \cdot \frac{\rho_{mix}}{\rho_f}, \tag{G.8}$$

where f_{SPR} is the friction factor for the single-phase flow reference based on Re_s, the suspension Reynolds number defined as $Re_s = \rho_{mix} v_{mix} D_{pipe}/\mu_s$ with $\rho_{mix} = \rho_s \phi_b + \rho_f(1-\phi_b)$ the mixture mass density and μ_s the suspension viscosity. We computed f_{SPR} from Haaland's correlation, Eq. G.3, for a hydraulically smooth pipe, and estimated Re_s using the suspension viscosity from Eilers' correlation, Eq. 4.6.

FRICTION FACTOR DATA

The above friction factor models have been evaluated for the conditions of cases D1/E1, D2/E2 and D3/E3. The data is provided in table G.1 and shown in Fig. 4.5.

Case	Re_{mix}	f_{DNS}	f_{EXP}	f_{FB}	f_{DC}	f_{MDC}	f_{NSB}	f_{NHS}	f_{ELM}
D1/E1	2347	0.607	0.939	0.576	35.7	1.351	0.575	2.909	0.077
D2/E2	7812	0.118	0.149	0.377	2.4	0.121	0.153	0.226	0.045
D3/E3	14164	0.058	0.062	0.313	0.46	0.044	0.068	0.063	0.036

Table G.1: Darcy-Weisbach friction factor f_{DNS}, f_{EXP}, f_{FB}, f_{DC}, f_{MDC}, f_{NSB}, f_{NHS} and f_{ELM} obtained from, respectively, DNS, experiment, proposed model for the fixed-bed regime, Durand and Condolios model [44], modified Durand and Condolios model based on the reduced gravity [123], Newitt et al. model for the sliding-bed regime [123], Newitt et al. model for the heterogeneous suspension regime [123], and equivalent liquid model.

BIBLIOGRAPHY

[1] F. F. Abraham. "Functional dependence of drag coefficient of a sphere on Reynolds number". In: *Physics of Fluids* 13.8 (1970), pp. 2194–2195.

[2] S. A. Altobelli, R. C. Givler, and E. Fukushima. "Velocity and concentration measurements of suspensions by nuclear magnetic resonance imaging". In: *Journal of Rheology* 35.5 (1991), pp. 721–734.

[3] M. P. Anderson and M. L. Jackson. "Sedimentation: Procedures and measurements". In: *Industrial & Engineering Chemistry* 49.1 (1957), pp. 89–96.

[4] S. K. Arolla and O. Desjardins. "Transport modeling of sedimenting particles in a turbulent pipe flow using Euler—Lagrange large eddy simulation". In: *International Journal of Multiphase Flow* 75 (2015), pp. 1–11.

[5] R. M. Ashley et al. *Solids in Sewers: Characteristics, Effects and Control of Sewer Solids and Associated Pollutants*. Vol. 4. IWA Publishing, June 2005.

[6] T. J. Atherton and D. J. Kerbyson. "Size invariant circle detection". In: *Image and Vision Computing* 17.11 (1999), pp. 795–803.

[7] F. Auguste and J. Magnaudet. "Path oscillations and enhanced drag of light rising spheres". In: *Journal of Fluid Mechanics* 841 (2018), pp. 228–266.

[8] S. Balachandar and J. K. Eaton. "Turbulent dispersed multiphase flow". In: *Annual Review of Fluid Mechanics* 42 (2010), pp. 111–133.

[9] E. Barnea and J. Mizrahi. "A generalized approach to the fluid dynamics of particulate systems: Part 1. General correlation for fluidization and sedimentation in solid multiparticle systems". In: *The Chemical Engineering Journal* 5.2 (1973), pp. 171–189.

[10] G. K. Batchelor. "A new theory of the instability of a uniform fluidized bed". In: *Journal of Fluid Mechanics* 193 (1988), pp. 75–110.

[11] G. K. Batchelor. *An introduction to fluid dynamics*. Cambridge University Press, 2000.

[12] G. K. Batchelor. "Sedimentation in a dilute dispersion of spheres". In: *Journal of Fluid Mechanics* 52.2 (1972), pp. 245–268.

[13] G. K. Batchelor. "The stress system in a suspension of force-free particles". In: *Journal of fluid mechanics* 41.3 (1970), pp. 545–570.

[14] G. K. Batchelor and C. -S. Wen. "Sedimentation in a dilute polydisperse system of interacting spheres. Part 2. Numerical results". In: *Journal of Fluid Mechanics* 124 (1982), pp. 495–528.

[15] A. Baule et al. "Mean-field theory of random close packings of axisymmetric particles". In: *Nature Communications* 4.1 (2013).

[16] R. N. Bernier and C. E. Brennen. “Use of the electromagnetic flowmeter in a two-phase flow”. In: *International Journal of Multiphase Flow* 9.3 (1983), pp. 251–257.

[17] P. Bradshaw. “Turbulent Secondary Flows”. In: *Annual Review of Fluid Mechanics* 19.1 (1987), pp. 53–74.

[18] W. -P. Breugem. “A Second-Order Accurate Immersed Boundary Method for Fully Resolved Simulations of Particle-Laden Flows”. In: *Journal of Computational Physics* 231.13 (May 2012), pp. 4469–4498.

[19] W. -P. Breugem, V. Dijk, and R. Delfos. “Flows Through Real Porous Media: X-Ray Computed Tomography, Experiments, and Numerical Simulations”. In: *Journal of Fluids Engineering* 136.4 (Feb. 2014).

[20] W.-P. Breugem and B. J. Boersma. “Direct numerical simulations of turbulent flow over a permeable wall using a direct and a continuum approach”. In: *Physics of Fluids* 17.2 (2005), p. 025103.

[21] W.-P. Breugem, B. J. Boersma, and R. E. Uittenbogaard. “The influence of wall permeability on turbulent channel flow”. In: *Journal of Fluid Mechanics* 562 (2006), pp. 35–72.

[22] D. Brinkerhoff, M. Truffer, and A. Aschwanden. “Sediment transport drives tidewater glacier periodicity”. In: *Nature Communications* 8.1 (2017), p. 90.

[23] C. S. Campbell, F. Avila-Segura, and Z. Liu. “Preliminary observations of a particle lift force in horizontal slurry flow”. In: *International Journal of Multiphase Flow* 30.2 (2004), pp. 199–216.

[24] J. Capecelatro and O. Desjardins. “An Euler–Lagrange strategy for simulating particle-laden flows”. In: *Journal of Computational Physics* 238 (2013), pp. 1–31.

[25] J. Capecelatro and O. Desjardins. “Eulerian–Lagrangian modeling of turbulent liquid–solid slurries in horizontal pipes”. In: *International Journal of Multiphase Flow* 55 (2013), pp. 64–79.

[26] L. Chen et al. “CFD simulation of coal-water slurry flowing in horizontal pipelines”. In: *Korean Journal of Chemical Engineering* 26.4 (2009), pp. 1144–1154.

[27] L. Chen et al. “Slip flow of coal water slurries in pipelines”. In: *Fuel* 89.5 (2010), pp. 1119–1126.

[28] E. Climent and M. R. Maxey. “Numerical simulations of random suspensions at finite Reynolds numbers”. In: *International Journal of Multiphase Flow* 29.4 (2003), pp. 579–601.

[29] P. Costa et al. “Collision model for fully resolved simulations of flows laden with finite-size particles”. In: *Physical Review E* 92 (5 2015), p. 053012.

[30] P. Costa et al. “Effects of the finite particle size in turbulent wall-bounded flows of dense suspensions”. In: *Journal of Fluid Mechanics* 843 (2018), pp. 450–478.

[31] P. Costa et al. “Universal Scaling Laws for Dense Particle Suspensions in Turbulent Wall-Bounded Flows”. In: *Physical Review Letters* 117 (13 2016), p. 134501.

[32] S. L. Dance and M. R. Maxey. “Incorporation of lubrication effects into the force-coupling method for particulate two-phase flow”. In: *Journal of Computational Physics* 189 (1 2003), pp. 212–238.

[33] R. H. Davis and A. Acrivos. “Sedimentation of noncolloidal particles at low Reynolds numbers”. In: *Annual Review of Fluid Mechanics* 17.1 (1985), pp. 91–118.

[34] R. H. Davis and K. H. Birdsell. “Hindered settling of semidilute monodisperse and polydisperse suspensions”. In: *AIChE Journal* 34.1 (1988), pp. 123–129.

[35] R. H. Davis, J. -M. Serayssol, and E. J. Hinch. “The elastohydrodynamic collision of two spheres”. In: *Journal of Fluid Mechanics* 163 (1986), pp. 479–497.

[36] T. Dbouk and D. Drikakis. “On coughing and airborne droplet transmission to humans”. In: *Physics of Fluids* 32.5 (2020), p. 053310.

[37] N. G. Deen, J. Westerweel, and E. Delnoij. “Two-Phase PIV in Bubbly Flows: Status and Trends”. In: *Chemical Engineering & Technology* 25.1 (2002), pp. 97–101.

[38] M. Denny. “Locomotion: The Cost of Gastropod Crawling”. In: *Science* 208.4449 (1980), pp. 1288–1290.

[39] K. W. Desmond and E. R. Weeks. “Influence of particle size distribution on random close packing of spheres”. In: *Physical Review E* 90.2 (2014), p. 022204.

[40] P. Doron and D. Barnea. “A three-layer model for solid-liquid flow in horizontal pipes”. In: *International Journal of Multiphase Flow* 19 (6 1993), pp. 1029–1043.

[41] P. Doron and D. Barnea. “Flow pattern maps for solid-liquid flow in pipes”. In: *International Journal of Multiphase Flow* 22.2 (1996), pp. 273–283.

[42] P. Doron, D. Granica, and D. Barnea. “Slurry flow in horizontal pipes - Experimental and modeling”. In: *International Journal of Multiphase Flow* 13.4 (1987), pp. 535–547.

[43] R. Durand. “Basic relationships of the transportation of solids in pipes—Experimental research”. In: *Proceedings 5th Minneapolis International Hydraulics Convention* (1953), pp. 89–103.

[44] R. Durand and E. Condolios. “Étude expérimentale du refoulement des matériaux en conduites, en particulier des produits de dragage et des schlamms”. In: *Journées de l’hydraulique* 2.1 (1953), pp. 29–55.

[45] J. G. M. Eggels et al. “Fully developed turbulent pipe flow: a comparison between direct numerical simulation and experiment”. In: *Journal of Fluid Mechanics* 268 (1994), pp. 175–210.

[46] H. von Eilers. “Die Viskosität von Emulsionen hochviskoser Stoffe als Funktion der Konzentration”. In: *Kolloid-Zeitschrift* 97.3 (1941), pp. 313–321.

[47] A. Einstein. *Investigations on the Theory of the Brownian Movement*. Dover Publications Inc., New York, 1956.

[48] K. Ekambara et al. “Hydrodynamic simulation of horizontal slurry pipeline flow using ANSYS-CFX”. In: *Industrial & Engineering Chemistry Research* 48.17 (2009), pp. 8159–8171.

[49] S. Elghobashi. “On predicting particle-laden turbulent flows”. In: *Applied Scientific Research* 52.4 (June 1994), pp. 309–329.

[50] B. Esse et al. “Quantification of ash sedimentation dynamics through depolarisation imaging with AshCam”. In: *Scientific Reports* 8.15680 (2018).

[51] A. Esteghamatian et al. “Particle resolved simulations of liquid/solid and gas/solid fluidized beds”. In: *Physics of Fluids* 29.3 (2017), p. 033302.

[52] D. Fabre, J. Tchoufag, and J. Magnaudet. “The steady oblique path of buoyancy-driven disks and spheres”. In: *Journal of Fluid Mechanics* 707 (2012), pp. 24–36.

[53] E. A. Fadlun et al. “Combined Immersed-Boundary Finite-Difference Methods for Three-Dimensional Complex Flow Simulations”. In: *Journal of Computational Physics* 161.1 (2000), pp. 35–60.

[54] R. D. Felice. “The sedimentation velocity of dilute suspensions of nearly monosized spheres”. In: *International Journal of Multiphase Flow* 25 (4 1999), pp. 559–574.

[55] R. D. Felice and E. Parodi. “Wall effects on the sedimentation velocity of suspensions in viscous flow”. In: *AIChE journal* 42.4 (1996), pp. 927–931.

[56] W. Fornari, F. Picano, and L. Brandt. “Sedimentation of finite-size spheres in quiescent and turbulent environments”. In: *Journal of Fluid Mechanics* 788 (2016), pp. 640–669.

[57] W. Fornari et al. “Reduced particle settling speed in turbulence”. In: *Journal of Fluid Mechanics* 808 (2016), pp. 153–167.

[58] W. Fornari et al. “Suspensions of finite-size neutrally buoyant spheres in turbulent duct flow”. In: *Journal of Fluid Mechanics* 851 (2018), pp. 148–186.

[59] A. F. Fortes, D. D. Joseph, and T. S. Lundgren. “Nonlinear mechanics of fluidization of beds of spherical particles”. In: *Journal of Fluid Mechanics* 177 (1987), pp. 467–483.

[60] I. Frankel and H. Brenner. “On the foundations of generalized Taylor dispersion theory”. In: *Journal of Fluid Mechanics* 204 (1989), pp. 97–119.

[61] A. Führbäoter. “Uber die Fäorderung von Sand-Wasser-Gemischen in Rohrleitungen”. In: *Mitteilungen des FranziusInstituts für Grund- und Wasserbau der Technischen Hochschule Hannover* 19 (1961).

[62] J. Garside and M. R. Al-Dibouni. “Velocity-Voidage Relationships for Fluidization and Sedimentation in Solid-Liquid Systems”. In: *Industrial & Engineering Chemistry Process Design and Development* 16.2 (1977), pp. 206–214.

[63] R. Gibert. “Transport hydraulique et refoulement des mixtures en conduites”. In: *Annales des Ponts et Chaussáees* 130.3 (1960), pp. 307–374.

[64] É. Guazzelli, J. F. Morris, and S. Pic. *A physical introduction to suspension dynamics*. Cambridge University Press, 2011.

[65] É. Guazzelli and O. Pouliquen. “Rheology of dense granular suspensions”. In: *Journal of Fluid Mechanics* 852 (2018), P1.

[66] A. Gurung et al. “Ultrasound image velocimetry for rheological measurements”. In: *Measurement Science and Technology* 27.9 (2016), 094008:1–9.

[67] S. E. Haaland. “Simple and Explicit Formulas for the Friction Factor in Turbulent Pipe Flow”. In: *Journal of Fluids Engineering* 105.1 (1983), pp. 89–90.

[68] A. Hamid, J. J. Molina, and R. Yamamoto. “Direct numerical simulations of sedimenting spherical particles at non-zero Reynolds number”. In: *RSC Advances* (96 2014).

[69] A. Hamid, J. J. Molina, and R. Yamamoto. “Sedimentation of non-Brownian spheres at high volume fractions”. In: *Soft matter* 9.42 (42 2013), pp. 10056–10068.

[70] J. Happel and H. Brenner. *Low Reynolds Number Hydrodynamics: With Special Applications to Particulate Media*. Springer Science & Business Media, 2012.

[71] S. Heitkam et al. “Speeding up of Sedimentation under Confinement”. In: *Physical Review Letters* 110 (17 2013), p. 178302.

[72] M. A. Hoef et al. “Multiscale Modeling of Gas-Fluidized Beds”. In: *Computational Fluid Dynamics*. Ed. by Guy B. Marin. Vol. 31. Advances in Chemical Engineering. Academic Press, 2006, pp. 65–149.

[73] W. Hogendoorn et al. “From nearly homogeneous to core-peaking suspensions: Insight in suspension pipe flows using MRI and DNS”. In: *Phys. Rev. Fluids* 8 (12 2023), p. 124302.

[74] W. J. Hogendoorn. “Suspension dynamics in transitional pipe flow, PhD thesis, Delft University of Technology”. PhD thesis. 2021.

[75] L. Hongying et al. “Airborne dispersion of droplets during coughing: a physical model of viral transmission”. In: *Scientific Reports* 11.4617 (2021), pp. 2045–2322.

[76] M. Horowitz and C. H. K. Williamson. “The effect of Reynolds number on the dynamics and wakes of freely rising and falling spheres”. In: *Journal of Fluid Mechanics* 651 (2010), pp. 251–294.

[77] S. G. Huisman et al. “Columnar structure formation of a dilute suspension of settling spherical particles in a quiescent fluid”. In: *Physical Review Fluids* 1 (7 Nov. 2016), p. 074204.

[78] R. Jackson. *The Dynamics of Fluidized Particles*. Vol. 12. 6. 2001, p. 755.

[79] R. Jackson. “The mechanics of fluidized beds: Part I: The stability of the state of uniform fluidization”. In: *Transactions of the Institution of Chemical Engineers* 41 (1963), pp. 13–28.

[80] K. O. L. F. Jayaweera, B. J. Mason, and G. W. Slack. “The behaviour of clusters of spheres falling in a viscous fluid Part 1. Experiment”. In: *Journal of Fluid Mechanics* 20.1 (1964), pp. 121–128.

[81] D. J. Jeffrey. “Low-Reynolds-number flow between converging spheres”. In: *Mathematika* 29.1 (1982), pp. 58–66.

[82] M. Jenny, J. Dušek, and G. Bouchet. “Instabilities and transition of a sphere falling or ascending freely in a Newtonian fluid”. In: *Journal of Fluid Mechanics* 508 (2004), pp. 201–239.

[83] J. Jeong and F. Hussain. “On the identification of a vortex”. In: *Journal of Fluid Mechanics* 285 (Feb. 1995), pp. 69–94.

[84] G. G. Joseph and M. L. Hunt. “Oblique particle-wall collisions in a liquid”. In: *Journal of Fluid Mechanics* 510 (2004), pp. 71–93.

[85] M. M. El-Kaissy and G. M. Homsy. “Instability waves and the origin of bubbles in fluidized beds: Part 1: Experiments”. In: *International Journal of Multiphase Flow* 2.4 (1976), pp. 379–395.

[86] T. Kajishima. “Influence of particle rotation on the interaction between particle clusters and particle-induced turbulence”. In: *International Journal of Heat and Fluid Flow* 25.5 (2004), pp. 721–728.

[87] T. Kajishima and S. Takiguchi. “Interaction between particle clusters and particle-induced turbulence”. In: *International Journal of Heat and Fluid Flow* 23.5 (2002), pp. 639–646.

[88] T. Kajishima et al. “Turbulence Structure of Particle-Laden Flow in a Vertical Plane Channel Due to Vortex Shedding”. In: *JSME International Journal Series B Fluids and Thermal Engineering* 44.4 (2001), pp. 526–535.

[89] D. R. Kaushal and Y. Tomita. “Experimental investigation for near-wall lift of coarser particles in slurry pipeline using γ-ray densitometer”. In: *Powder Technology* 172.3 (2007), pp. 177–187.

[90] D. R. Kaushal et al. “CFD modeling for pipeline flow of fine particles at high concentration”. In: *International Journal of Multiphase Flow* 43 (2012), pp. 85–100.

[91] D. R. Kaushal et al. “Effect of particle size distribution on pressure drop and concentration profile in pipeline flow of highly concentrated slurry”. In: *International Journal of Multiphase Flow* 31.7 (2005), pp. 809–823.

[92] H. T. Kazerooni et al. “Inertial migration in dilute and semidilute suspensions of rigid particles in laminar square duct flow”. In: *Phys. Rev. Fluids* 2 (8 2017), p. 084301.

[93] T. Kempe, S. Schwarz, and J. Frohlih. “Modelling of spheroidal particles in viscous flows”. In: vol. 845. KNAW, Amsterdam, The Netherlands, 2009.

[94] A. G. Kidanemariam and M. Uhlmann. “Direct numerical simulation of pattern formation in subaqueous sediment”. In: *Journal of Fluid Mechanics* 750 (2014), R2.

[95] A. G. Kidanemariam and M. Uhlmann. “Formation of sediment patterns in channel flow: minimal unstable systems and their temporal evolution”. In: *Journal of Fluid Mechanics* 818 (2017), pp. 716–743.

[96] M. Kliuev, C. Baumgart, and K. Wegener. “Fluid Dynamics in Electrode Flushing Channel and Electrode-Workpiece Gap During EDM Drilling”. In: *Procedia CIRP* 68 (2018). 19th CIRP Conference on Electro Physical and Chemical Machining, 23-27 April 2017, Bilbao, Spain, pp. 254–259.

[97] D. L. Koch. “Hydrodynamic diffusion in dilute sedimenting suspensions at moderate Reynolds numbers”. In: *Physics of Fluids A: Fluid Dynamics* 5.5 (1993), pp. 1141–1155.

[98] G. J. Kynch. “A theory of sedimentation”. In: *Transactions of the Faraday Society* 48 (0 1952), pp. 166–176.

[99] H. K. Kytomaa and C. E. Brennen. “Small amplitude kinematic wave propagation in two-component media”. In: *International Journal of Multiphase Flow* 17.1 (1991), pp. 13–26.

[100] A. J. C. Ladd. “Dynamical simulations of sedimenting spheres”. In: *Physics of Fluids A: Fluid Dynamics* 5.2 (1993), pp. 299–310.

[101] M. Lance and J. Bataille. “Turbulence in the liquid phase of a uniform bubbly air–water flow”. In: *Journal of Fluid Mechanics* 222 (1991), pp. 95–118.

[102] C. Lareo, P. J. Fryer, and M. Barigou. “The Fluid Mechanics of Two-Phase Solid-Liquid Food Flows: A Review”. In: *Food and Bioproducts Processing* 75.2 (1997), pp. 73–105.

[103] I. A. S. Larsson et al. “Secondary Flow in Semi-Circular Ducts”. In: *Journal of Fluids Engineering* 133.10 (2011), p. 101206.

[104] I. Lashgari et al. “Channel flow of rigid sphere suspensions: Particle dynamics in the inertial regime”. In: *International Journal of Multiphase Flow* 78 (2016), pp. 12–24.

[105] I. Lashgari et al. “Laminar, Turbulent, and Inertial Shear-Thickening Regimes in Channel Flow of Neutrally Buoyant Particle Suspensions”. In: *Physical Review Letters* 113 (25 2014), p. 254502.

[106] D. Legendre et al. “A note on the modelling of the bouncing of spherical drops or solid spheres on a wall in viscous fluid”. In: *Chemical Engineering Science* 61.11 (2006), pp. 3543–3549.

[107] D. Leighton and A. Acrivos. “The shear-induced migration of particles in concentrated suspensions”. In: *Journal of Fluid Mechanics* 181 (1987), pp. 415–439.

[108] Z. Lin et al. “Effects of finite-size neutrally buoyant particles on the turbulent flows in a square duct”. In: *Physics of Fluids* 29.10 (2017), p. 103304.

[109] Z.-W. Lin et al. “Effects of finite-size heavy particles on the turbulent flows in a square duct”. In: *Journal of Hydrodynamics, Ser. B* 29.2 (2017), pp. 272–282.

[110] J. Ling et al. “Numerical investigations of liquid–solid slurry flows in a fully developed turbulent flow region”. In: *International Journal of Heat and Fluid Flow* 24.3 (2003), pp. 389–398.

[111] M. Liu et al. “Particle behavior in a turbulent pipe flow with a flat bed”. In: *Particuology* 81 (2023), pp. 58–72.

[112] K. Luo et al. “Full-scale solutions to particle-laden flows: Multidirect forcing and immersed boundary method”. In: *Physical Review E* 76.6 (2007), p. 066709.

[113] I. F. Macdonald et al. “Flow through Porous Media-the Ergun Equation Revisited”. In: *Industrial & Engineering Chemistry Fundamentals* 18.3 (1979), pp. 199–208.

[114] I. Manzella et al. “The role of gravitational instabilities in deposition of volcanic ash”. In: *Geology* 43.3 (Mar. 2015), pp. 211–214.

[115] C. Marchioli, A. Soldati, and F. Porté-Agel. “Mechanisms for heavy particle clustering in homogeneous isotropic turbulence”. In: *Journal of Fluid Mechanics* 615 (2008), pp. 245–268.

[116] M. Maxey. “Simulation Methods for Particulate Flows and Concentrated Suspensions”. In: *Annual Review of Fluid Mechanics* 49.1 (2017), pp. 171–193.

[117] M. Mazzuoli, A. G. Kidanemariam, and M. Uhlmann. “Direct numerical simulations of ripples in an oscillatory flow”. In: *Journal of Fluid Mechanics* 863 (2019), pp. 572–600.

[118] J. B. McLaughlin. “Inertial migration of a small sphere in linear shear flows”. In: *Journal of Fluid Mechanics* 224 (1991), pp. 261–274.

[119] G. V. Messa and V. Matousek. “Analysis and discussion of two fluid modelling of pipe flow of fully suspended slurry”. In: *Powder Technology* 360 (2020), pp. 747–768.

[120] N. Michael. “Dealing with sediment transport in flood risk management”. In: *Acta Geophysica* 67.2 (2019), pp. 677–685.

[121] S. A. Miedema. *Slurry Transport: Fundamentals, A historical overview and the Delft Head Loss & Limit Deposit Velocity Framework*. Ed. by R. C. Ramsdell. 1st. S. A. Miedema / Delft University of Technology, 2016.

[122] R. -G. Mohammad et al. “Optimization of intraperitoneal aerosolized drug delivery using computational fluid dynamics (CFD) modeling”. In: *Scientific Reports* 12.6305 (2022), pp. 20145–2322.

[123] D. M. Newitt et al. “Hydraulic conveying of solids in horizontal pipes”. In: *Transactions of the Institution of Chemical Engineers* 33 (1955), pp. 93–113.

[124] I. Nezu. “Open-Channel Flow Turbulence and its Research Prospect in the 21st Century”. In: *Journal of Hydraulic Engineering* 131.4 (2005), pp. 229–246.

[125] F. T. Nieuwstadt, J. Westerweel, and B. J. Boersma. *Introduction to Theory and Applications of Turbulent Flows*. Springer, 2016.

[126] N. V. Nikitin, N. V. Popelenskaya, and A. Stroh. “Prandtl’s Secondary Flows of the Second Kind. Problems of Description, Prediction, and Simulation”. In: *Fluid Dynamics* 56.4 (July 2021), pp. 513–538.

[127] K. Nishino and H. Matsuhita. “Columnar particle accumulation in homogenous turbulence”. In: *Proceedings 5th International Conference Multiphase Flow* 248 (2004).

[128] M. Ouriemi et al. “Determination of the critical Shields number for particle erosion in laminar flow”. In: *Physics of Fluids* 19.6 (2007), p. 061706.

[129] G. Ovarlez, F. Bertrand, and S. Rodts. “Local determination of the constitutive law of a dense suspension of noncolloidal particles through magnetic resonance imaging”. In: *Journal of Rheology* 50.3 (2006), pp. 259–292.

[130] C. S. Peskin. “Flow patterns around heart valves: A numerical method”. In: *Journal of Computational Physics* 10.2 (1972), pp. 252–271.

[131] R. J. Phillips, J. F. Brady, and G. Bossis. “Hydrodynamic transport properties of hard-sphere dispersions. I. Suspensions of freely mobile particles”. In: *The Physics of fluids* 31.12 (1988), pp. 3462–3472.

[132] F. Picano, W. -P. Breugem, and L. Brandt. “Turbulent channel flow of dense suspensions of neutrally buoyant spheres”. In: *Journal of Fluid Mechanics* 764 (2015), pp. 463–487.

[133] F. Picano et al. “Shear Thickening in Non-Brownian Suspensions: An Excluded Volume Effect”. In: *Physical Review Letters* 111 (9 2013), p. 098302.

[134] C. Poelma. “Ultrasound Imaging Velocimetry: a review”. In: *Experiments in Fluids* 58.1 (2016), p. 3.

[135] S. B. Pope. *Turbulent flows*. Cambridge university press, 2000.

[136] L. Prandtl. *Essentials of fluid dynamics with applications to hydraulics, aeronautics, meteorology and other subjects*. Hafner Pub., 1952.

[137] A. Prosperetti and G. Tryggvason. *Computational Methods for Multiphase Flow*. Cambridge University Press, 2007.

[138] S. K. R. Raaghav, C. Poelma, and W. -P. Breugem. “Path instabilities of a freely rising or falling sphere”. In: *International Journal of Multiphase Flow* 153 (2022), p. 104111.

[139] A. K. Thota Radhakrishnan. *Domestic Slurry Hydraulics in Transport, PhD thesis, Delft University of Technology*. 2019.

[140] Robert C Ramsdell and Sape A Miedema. “An overview of flow regimes describing slurry transport”. In: *WODCON XX* (2013), p. 15.

[141] J. F. Richardson and W. N. Zaki. “Sedimentation and fluidization: Part I”. In: *Transactions of the Institution of Chemical Engineers* 32 (1954), pp. 35–53.

[142] J.F. Richardson and W. N. Zaki. “The sedimentation of a suspension of uniform spheres under conditions of viscous flow”. In: *Chemical Engineering Science* 3.2 (1954), pp. 65–73.

[143] L. C. van Rijn. “Sediment Transport, Part II: Suspended Load Transport”. In: *Journal of Hydraulic Engineering* 110.11 (1984), pp. 1613–1641.

[144] F. Risso. “Agitation, mixing, and transfers induced by bubbles”. In: *Annual Review of Fluid Mechanics* 50 (2018), pp. 25–48.

[145] A. M. Roma, C. S. Peskin, and M. J. Berger. “An adaptive version of the immersed boundary method”. In: *Journal of Computational Physics* 153.2 (1999), pp. 509–534.

[146] M. E. Rosti et al. “Fluid dynamics of COVID-19 airborne infection suggests urgent data for a scientific design of social distancing”. In: *Scientific Reports* 10.22426 (2020).

[147] P. G. Saffman. “The lift on a small sphere in a slow shear flow”. In: *Journal of Fluid Mechanics* 22.2 (1965), pp. 385–400.

[148] W. Sébastien et al. “Refractive-index and density matching in concentrated particle suspensions: a review”. In: *Experiments in Fluids* 50.5 (2011), p. 1183.

[149] A. Seyed-Ahmadi and A. Wachs. “Sedimentation of inertial monodisperse suspensions of cubes and spheres”. In: *Physical Review Fluids* 6.4 (2021), p. 044306.

[150] T. Shajahan and W. -P. Breugem. “Influence of Concentration on Sedimentation of a Dense Suspension in a Viscous Fluid”. In: *Flow, Turbulence and Combustion* 105.2 (Aug. 2020), pp. 537–554.

[151] T. Shajahan and W.-P. Breugem. “Inertial effects in sedimenting suspensions of solid spheres in a liquid”. In: *International Journal of Multiphase Flow* 166 (2023), p. 104498.

[152] A. Shields. “Anwendung der Aehnlichkeitsmechanik und der Turbulenzforschung auf die Geschiebebewegung”. In: *Mitt. Preuss. Versuchsanst. Wasserbau Schiffbau* 26.26 (1936).

[153] Y. T. Shih, D. Gidaspow, and D. T. Wasan. “Sedimentation of fine particles in nonaqueous media: Part I - experimental Part II - modeling”. In: *Colloids and Surfaces* 21 (1986), pp. 393–429.

[154] D. A. Smith and K. F. Cheung. “Empirical Relationships for Grain Size Parameters of Calcareous Sand on Oahu, Hawaii”. In: *Journal of Coastal Research* 18.1 (2002), pp. 82–93.

[155] J. J. Stickel and R. L. Powell. “Fluid Mechanics and Rheology of Dense Suspensions”. In: *Annual Review of Fluid Mechanics* 37 (2005), pp. 129–149.

[156] S. Sundaresan, L. R. Collins, and R. M. Lueptow. “Direct numerical simulation of particle-laden turbulent channel flow”. In: *Journal of Fluid Mechanics* 811 (2017), pp. 322–357.

[157] A. Ten Cate et al. “Particle imaging velocimetry experiments and lattice-Boltzmann simulations on a single sphere settling under gravity”. In: *Physics of Fluids* 14 (2002), pp. 4012–4025.

[158] L. Thibodeaux and J. Boyle. “Bedform-generated convective transport in bottom sediment”. In: *Nature* 325 (1987), pp. 341–343.

[159] R. M. Turian, F.-L. Hsu, and T.-W. Ma. “Estimation of the critical velocity in pipeline flow of slurries”. In: *Powder Technology* 51.1 (1987), pp. 35–47.

[160] M. Uhlmann. “An immersed boundary method with direct forcing for the simulation of particulate flows”. In: *Journal of Computational Physics* 209.2 (2005), pp. 448–476.

[161] M. Uhlmann and T. Doychev. “Direct numerical simulation of particle sedimentation at intermediate Galileo numbers”. In: *Journal of Fluid Mechanics* 868 (2019), pp. 766–793.

[162] M. Uhlmann and T. Doychev. “Sedimentation of a dilute suspension of rigid spheres at intermediate Galileo numbers: the effect of clustering upon the particle motion”. In: *Journal of Fluid Mechanics* 752 (2014), pp. 310–348.

[163] M. Uhlmann and J. Dušek. “The motion of a single heavy sphere in ambient fluid: A benchmark for interface-resolved particulate flow simulations with significant relative velocities”. In: *International Journal of Multiphase Flow* 59 (2014), pp. 221–243.

[164] A. Uzi and A. Levy. “Flow characteristics of coarse particles in horizontal hydraulic conveying”. In: *Powder Technology* 326 (2018), pp. 302–321.

[165] C. H. J. Veldhuis and A. Biesheuvel. “An experimental study of the regimes of motion of spheres falling or ascending freely in a Newtonian fluid”. In: *International Journal of Multiphase Flow* 33.10 (2007), pp. 1074–1087.

[166] J. J. Vocadlo and M. E. Charles. “Prediction of pressure gradient for the horizontal turbulent flow of slurries”. In: *Proceedings 2nd International Conference on the Hydraulic Transport of Solids in Pipes* (C1 1972), pp. 1–14.

[167] B. Vowinckel et al. “Settling of cohesive sediment: particle-resolved simulations”. In: *Journal of Fluid Mechanics* 858 (2019), pp. 5–44.

[168] M. S. Wertheim. “Exact solution of the Percus-Yevick integral equation for hard spheres”. In: *Physical Review Letters* 10.8 (1963), p. 321.

[169] P. Wesseling. *Principles of Computational Fluid Dynamics*. Springer-Verlag Berlin, 2001.

[170] F. M. White. *Fluid Mechanics*. 1st ed. Seventh Edition in SI Units. McGraw-Hill, 2011.

[171] D. P. Willen and A. Prosperetti. “Resolved simulations of sedimenting suspensions of spheres”. In: *Physical Review Fluids* 4.1 (2019), p. 014304.

[172] D. P. Willen et al. “Continuity waves in resolved-particle simulations of fluidized beds”. In: *Physical Review Fluids* 2 (11 2017), p. 114305.

[173] R. A. Williams et al. “Experimental techniques for monitoring sedimentation in optically opaque suspensions”. In: *Colloids and Surfaces* 43.1 (1990). Papers Presented at the Society of Chemical Industry Meeting, pp. 1–32.

[174] K. Wilson and A. Sellgren. “Developments in Slurry Flow Modelling in a Historical Perspective”. In: *The Canadian Journal of Chemical Engineering* 94 (2016), pp. 1019–1024.

[175] K. C. Wilson and A. Sellgren. “Interaction of particles and near-wall lift in slurry pipelines”. In: *Journal of Hydraulic Engineering* 129.1 (2003), pp. 73–76.

[176] K. C. Wilson et al. *Slurry transport using centrifugal pumps*. Springer Science & Business Media, 2006.

[177] W. E. Wilson. “Mechanics of flow with noncolloidal, inert solids”. In: *Transactions of the American Society of Civil Engineers* 107.1 (1942), pp. 1576–1586.

[178] J. Wu and R. Manasseh. “Dynamics of dual-particles settling under gravity”. In: *International Journal of Multiphase Flow* 24.8 (1998), pp. 1343–1358.

[179] X. Wu and P. Moin. “A direct numerical simulation study on the mean velocity characteristics in turbulent pipe flow”. In: *Journal of Fluid Mechanics* 608 (2008), pp. 81–112.

[180] J. Xu et al. “Measurement of Solid Slurry Flow Via Correlation of Electromagnetic Flow Meter, Electrical Resistance Tomography and Mechanistic Modelling”. In: *Journal of Hydrodynamics* 21.4 (2009).

[181] Y. Yao, C. S. Criddle, and O. B. Fringer. “The effects of particle clustering on hindered settling in high-concentration particle suspensions”. In: *Journal of Fluid Mechanics* 920 (2021), A40.

[182] X. Yin and D. L. Koch. “Hindered settling velocity and microstructure in suspensions of solid spheres with moderate Reynolds numbers”. In: *Physics of Fluids* 19.9 (2007), p. 093302.

[183] X. Yin and D. L. Koch. “Velocity fluctuations and hydrodynamic diffusion in finite-Reynolds-number sedimenting suspensions”. In: *Physics of Fluids* 20.4 (2008), p. 043305.

[184] H. K. Yuen et al. “Comparative study of Hough Transform methods for circle finding”. In: *Image and Vision Computing* 8.1 (1990), pp. 71–77.

[185] S. Zade et al. “Buoyant finite-size particles in turbulent duct flow”. In: *Phys. Rev. Fluids* 4 (2 2019), p. 024303.

[186] A. A. Zaidi. “Particle velocity distributions and velocity fluctuations of non-Brownian settling particles by particle-resolved direct numerical simulation”. In: *Physical Review E* 98 (5 2018), p. 053103.

[187] A. A. Zaidi, T. Tsuji, and T. Tanaka. “Direct numerical simulation of finite sized particles settling for high Reynolds number and dilute suspension”. In: *International Journal of Heat and Fluid Flow* 50 (2014), pp. 330–341.

[188] A. A. Zaidi, T. Tsuji, and T. Tanaka. “Hindered settling velocity & structure formation during particle settling by direct numerical simulation”. In: *Procedia Engineering* 102 (2015), pp. 1656–1666.

[189] X. Zhang et al. “Flow regimes within horizontal particle-laden pipe flows”. In: *International Journal of Multiphase Flow* 143 (2021), p. 103748.

[190] X. Zhang et al. “The dominant mechanisms for each regime of secondary flows in horizontal particle-laden pipe flows”. In: *Journal of Fluid Mechanics* 949 (2022), A10.

[191] X. Zhang et al. “The influence of the coefficient of restitution on flow regimes within horizontal particle-laden pipe flows”. In: *Physics of Fluids* 33.12 (2021), p. 123318.

[192] W. Zhou and J. Dušek. “Chaotic states and order in the chaos of the paths of freely falling and ascending spheres”. In: *International Journal of Multiphase Flow* 75 (2015), pp. 205–223.

ACKNOWLEDGEMENTS

I express my deepest gratitude to my supervisor, Wim-Paul Breugem, your unwavering support and insightful guidance has shaped my academic journey over the course of this project. Your curiosity for the work and your attention to detail is something that I really admire. I look back fondly at the DLES conference we attended in Madrid. I am also grateful for your patience and kindness towards me.

I extend my thanks to my promoter, Christian Poelma, whose incisive questions always kept me on my toes. Your encouragement to venture a comparison with ultrasound experiments expanded my academic horizons, thanks to the collaborative work with Amitosh Dash and Willian Hoogendoorn. The crux of my research, focused on sediment transport, owes much to the collaborative efforts with Thijs Schouten. Our close collaboration, combining experimental and numerical approaches, laid the foundation for much of my work. I am indebted to Geert Keetels for his invaluable insights into sediment transport. And also to Shravan Raaghav for your contributions to the work. The late Cees van Rhee's brief but impactful discussions in relation to our work is something I will look back on fondly. My brief encounter with Timo Overveld and Matias Duran Mutate at the Physics at Veldhoven conference, deserve my gratitude for our collaborative work. I also extend my appreciation to Pedro Costa who was instrumental in developing the numerical framework which formed the basis for my work.

Caroline Legierse, our daily chats provided a comforting sense of home within the lab, for which I am immensely grateful. To Mathieu Pourquie, your jovial demeanor left an indelible mark on me. Your assistance with the SARA grant proposals and our memorable experience at the Wildeman are among the highlights of my PhD. The weekly coffee talks within our lab was always something I looked forward to. The diverse perspectives I encountered during these discussions greatly enriched my work, and I'm thankful to the entire research group and staff, including Ruud Henkes, Gijs Ooms, Willem van de Water, Daniel Tam, Angeliki Laskari, Rene Delfos, Jerry Westerweel, Lorenzo Botto, Brian Tighe, Bendiks-Jan Boersma, and Johan Padding. Thanks also to technicians GertJan Mulder, Jasper Ruijgrok, and Edwin Overmars for their assistance in procuring equipment and facilitating one of the few experiments I performed.

Apart from research, my involvement with the PantaRhei board, alongside colleagues Parviz Ghoddoosi and Wout Cornel, provided a refreshing break. Organizing the lab trip to the Kaag was a delightful experience amid my academic pursuits.

This PhD would not be complete without mentioning my avid interest in bouldering that went hand in hand with this phd. Bouldering became an integral part of my life during this period, and I owe my thanks to Yavuz Kamis, Guillermo Amador, and

Florian Charruault for making those experiences memorable. In relation to bouldering I would also like to mention Rene Pecnic, I really enjoyed making your acquaintance. Likewise the same with Ellert Jelsma, Udhav Gawandalkar and Soren Schenke. To more concerts in the future. My office mates, Melika Gul, Andries van Eckeveld, and Mike van Meerkerk. Ankur Kislaya, grateful to have you as a partner in everything from Dutch lessons to filing out tax forms. Bob Mulder and Guillermo Amador, to all the amazing Formula 1 weekends. Our VrijMiBos not only encompassed scientific discussions but also delved into various aspects of life. I will always fondly remember our trip to India.

Manu Goudar and Saad Jahangir for your insightful advice. To my colleagues Abel John, Junaid Mehmood, Koen Muller, Cenk Cetin, Haoyu Li, Lyke van Dalen, Gem Rotte, Jesse Reijtenbagh, Yuk Man Lau, Teng Dong, Da Wei, Luuk Altenburg, Sowmya Kumar, Arnoud Greidanus, Henk Benscoop, Nagraj Nagalingam, Gosse Oldenziel, Wouter Peerbooms, Ernst Jan Grift and Lina Nikolaidou and others, I extend my gratitude for our camaraderie and shared experiences. Thank you Hessel van der Weide for being my travel companion in recent years. Likewise, my heartfelt thanks to Viktor Knoben for always being available since my very first days in the Netherlands.

Without a doubt I am grateful for the time I spent at Oostsingel 3 with my housemates Rishab Bhardwaj and Swaraj Nanda. I remember the COVID years, and I am lucky to have had your company to get through that time.

Lastly, to my family, your support throughout these years has been the bedrock of my journey.

List of Publications

4. **T. Shajahan and W.-P. Breugem**, *Influence of Concentration on Sedimentation of a Dense Suspension in a Viscous Fluid*, Flow Turbulence Combustion **105**, 537-554 (2020).

3. **T. J. J. M. van Overveld, T. Shajahan, W.-P. Breugem, H. J. H. Clercx, and M. Duran-Matute**, *Numerical study of a pair of spheres in an oscillating box filled with viscous fluid*, Physical Review Fluids **7**, 014308 (2022).

2. **T. Shajahan and W.-P. Breugem**, *Inertial effects in sedimenting suspensions of solid spheres in a liquid*, International Journal of Multiphase Flow **166**, 104498 (2023).

1. **T. Shajahan, T. Schouten, S. Raaghav, C. van Rhee, G. Keetels and W.-P. Breugem**, *Characteristics of slurry transport regimes: Insights from Experiments and interface-resolved Direct Numerical Simulations*, International Journal of Multiphase Flow (under review).

CURRICULUM VITÆ

Tariq SHAJAHAN

EDUCATION

2010–2014	Undergraduate in Mechanical Engineering National Institute of Technology, Karnataka
2014–2016	Master of Science in Aerospace Engineering Delft University of Technology, The Netherlands
2017–2024	PhD. Delft University of Technology, The Netherlands *Thesis:* Interface-resolved simulations of dense particulate flows: Studies on sedimentation and slurry pipe flow *Promotor:* Wim-Paul Breugem and Christian Poelma

AWARDS

2019	Young Scientist Award, Burgers Symposium 2019